# Jacobi No-Core Shell Model for P-shell Hypernuclei

Dissertation
zur
Erlangung des Doktorgrades (Dr. rer. nat.)
der
Mathematisch-Naturwissenschaftlichen Fakultät
der
Rheinischen Friedrich-Wilhelms-Universität Bonn

vorgelegt von

Hoai Le Thi

aus
Nam dinh

Bonn 2020

# Abstract

Understanding baryon-baryon (BB) interactions in the non-zero strangeness sectors is a crucial step toward one of the ultimate goals of nuclear physics - a unified theory describing interactions among baryons. Due to the scarcity of YN and practically complete lack of YY scattering data, BB interactions in the $S = -1$ and $S = -2$ sectors are ill-constrained and must be additionally confronted to hypernuclear observables such as the binding or excitation energies. The purpose of this thesis is to develop a many-body method than can accurately calculate observable properties of light p-shell hypernuclei (with single and double strangeness) and unambiguously connect these properties to that of the underlying YN and YY interactions. For that, we advance the J-NCSM approach that has been a successful tool for describing ordinary nuclei in the p-shell. The approach is an *ab inito* method that is based on an expansion in a many-body HO basis depending on relative Jacobi coordinates. We have generalized the J-NCSM formalism so that the extension to strangeness sectors other than $S = -1$ and $S = -2$ is straightforward.

With the numerical technique in hand, in the first part of the thesis, we study the predictions of the chiral NN and YN interactions for light hypernuclei up to the p-shell (A=7). In order the speed up the NCSM calculations, both NN and YN potentials are evolved via Similarity Renormalization Group (SRG) transformations. The influence of various chiral NN interactions as well as of the SRG evolutions on hypernuclear observables such as the $\Lambda$ separation or excitation energies are thoroughly investigated. The impact of the SRG YN evolution is uncomfortably large in all systems indicating the significance of the contributions from the SRG-induced YNN forces. Fortunately, we observe almost perfectly linear correlations between the separation energies of different systems. It turns out that the major part of the three-body forces (3BFs) due to the SRG can be effectively taken into account by tuning the SRG flow parameter such that $^{5}_{\Lambda}\text{He}$ is correctly described.

We also carefully study the predictions of the two practically phase-equivalent YN chiral interactions at NLO: NLO13 and NLO19. The latter predicts considerably larger separation energies for all considered systems except the $^{4}_{\Lambda}\text{He}(0^+)$ state. The energy spectra of $^{7}_{\Lambda}\text{Li}$ obtained with the two potentials are also slightly different. It follows that the chiral three-body YNN forces are also visible for both separation energies and level splittings in $A = 4 - 7$ hypernuclei.

The intriguing correlations of $B_{\Lambda}$ facilitate a study of possible consequences of a potentially more strong bound hypertriton that has been suggested in recent measurements by the STAR collaboration. It is found that increasing the hypertrinton separation energy leads to an improvement in the prediction for the ground-state separation energy as well as the doublet splitting in $^{4}_{\Lambda}\text{He}$. The separation energy of $^{7}_{\Lambda}\text{Li}$ is increased further away from the experimental value and its energy spectrum is also somewhat distorted. However, the overall effect is small as compared to the possible contributions from the 3BFs.

In the second part of the thesis, we investigate the *s*-shell double-$\Lambda$ hypernuclei using the YY chiral interactions at LO and NLO. At this point, only one parametrization has been used at each

order. The two potentials are also SRG evolved to a wide range of flow parameters to facilitate the convergence of the energy calculations. Unlike for the $S = -1$ systems, the SRG evolution of the YY forces has only minor influence on the $\Lambda\Lambda$ separation energies. We also find that the $^{6}_{\Lambda\Lambda}\mathrm{He}$ hypernucleus is fairly well described at NLO while it is slightly overbound at LO. Both interactions also yield a bound state for $^{5}_{\Lambda\Lambda}\mathrm{He}$ but predict that $^{4}_{\Lambda\Lambda}\mathrm{H}$ is particle-unstable with respect to the $^{3}_{\Lambda}\mathrm{H} + \Lambda$ breakup.

# Contents

## II Double Strangeness Hypernuclei 107

## 5 Jacobi NCSM for $S = -2$ systems 109

## 6 Results for $\Lambda\Lambda$ $s$-shell hypernuclei 117

## 7 Summary and Conclusions 127

## A The many-body Schrödinger equation in second quantization 131

## B Momentum distribution and correlation functions 145

## C Jacobi coordinates for an $A$-body system 151

# Introduction

The fundamental building blocks of hadron physics are quarks and gluons interacting through Quantum Chromodynamics (QCD) - the theory of the strong interaction - which can be treated perturbatively at high energies but is strictly non-perturbative for low-energy processes due to the running coupling constant $\alpha_s$ [1, 2]. The two lightest up and down quarks, being confined to a tight volume with the radius smaller than 1 fm, form the building blocks of all nuclei - the nucleons. The relatively small nuclear binding energy is understood as the residual effect of the strong interactions among constituent quarks mediated by gluons. A hyperon is obtained when substituting one (or more) quark(s) in nucleons by one (or more) strange quark(s). The former can exist in different strangeness: single strangeness $S = -1$ ($\Lambda, \Sigma$), or double strangeness $S = -2$ ($\Xi$) or even triple strangeness $S = -3$ ($\Omega$). The single- and double-strangeness hyperons together with nucleons form an octet of the lightest baryons, exhibiting SU(3) flavor symmetry of QCD in the limit of equal masses among up, down and strange quarks. The intrinsic properties of the octet baryons and their lifetimes are summarized in Table 1.1. These will be the main ingredients to our study. It is stressed that although hyperons are unstable (decaying via electroweak processes) their lifetimes are much longer compared to the typical time scale of the strong interaction of approximately $10^{-23}$ s.

| | Strangeness $S$ | Isospin $t$ | Isospin Project. $m_t$ | Mass $m[MeV]$ | Lifetime $\tau[s]$ |
|---|---|---|---|---|---|
| $p$ | 0 | 1/2 | 1/2 | 938.272 | - |
| $n$ | 0 | 1/2 | $-1/2$ | 939.565 | 885.7 |
| $\Lambda$ | -1 | 0 | 0 | 1115.683 | $2.6 \times 10^{-10}$ |
| $\Sigma^+$ | -1 | 1 | 1 | 1189.37 | $0.8 \times 10^{-10}$ |
| $\Sigma^0$ | -1 | 1 | 0 | 1192.642 | $7.4 \times 10^{-20}$ |
| $\Sigma^-$ | -1 | 1 | $-1$ | 1197.449 | $1.48 \times 10^{-10}$ |
| $\Xi^0$ | -2 | 1/2 | 1/2 | 1314.86 | $2.9 \times 10^{-10}$ |
| $\Xi^-$ | -2 | 1/2 | $-1/2$ | 1321.71 | $1.6 \times 10^{-10}$ |

Table 1.1: Intrinsic properties of the octet baryons. The data are taken from [3].

Being distinguishable from nucleons, a hyperon can penetrate deeply into a nucleus and resides on one of the energy levels to form a bound hypernucleus. The existence of other than $\Lambda$ hypernuclei, for example $\Sigma$ or $\Xi$ hypernuclei are considerably suppressed and the corresponding hypernuclear states will be rather broad due to the strong decay processes ($\Sigma + N \rightarrow \Lambda + N$, $\Xi + N \rightarrow \Lambda + \Lambda$). The recent experimentally claimed observations of deeply bound $\Sigma$ hypernuclei are still of considerable ambiguity [4]. The situation is different for $\Lambda$ hypernuclei. The first experiments of $\Lambda$ hypernuclei can be traced back to 1953 when Danysz and Pniewski observed the disintegration of hyperfragments in emulsion stacks exposed to energetic cosmic rays [5]. The event has opened up a new era for theoretical and experimental hypernuclear physics. Followed the 1953 discovery, many more light hypernuclei with $A \leq 16$ have been observed in emulsions or bubble chambers mainly through the strangeness exchange reactions ($K^-, \pi^-$) [6–8]. However, these experiments were still limited to the ground-state $\Lambda$-binding energies and very little information about the weak decay rates could be inferred. Since the counter techniques with magnetic spectrometers were developed, together with the introduction of associated production reactions ($\pi^+, K^+$), ($e, e\,K^+$) and hypernuclear $\gamma$-ray spectroscopy, a large realm of hypernuclei ranging from $^3_\Lambda$H to $^{208}_\Lambda$Pb have been investigated [7–9]. Experiments now have access not only to the binding energies but particularly to rather high-resolution hypernuclear energy spectra, providing great opportunities to study hyperon-nucleon interactions [10–12] as well as shedding light on so-far inaccessible deep-lying nuclear interiors [8, 13].

Experimental evidences of double $\Lambda$ hypernuclei have also slowly emerged. The first observation of $^6_{\Lambda\Lambda}$He was reported by Prowse with considerably large binding energy, $10.1 \pm 1.71$ MeV, implying a strongly attractive $\Lambda\Lambda$ interaction [14]. However, the authenticity of the event was put under questions [15]. The recent Nagara event has confirmed the existence of $^6_{\Lambda\Lambda}$He but with a smaller and probably more reasonable binding energy of $6.91 \pm 0.16$ MeV [16, 17]. The two other hypernuclei, $^{10}_{\Lambda\Lambda}$Be and $^{11}_{\Lambda\Lambda}$Be, have been also unambiguously detected in several experiments [15, 17]. The deduced $\Lambda\Lambda$ binding energies provide invaluable information for deepening our knowledge about hyperon-hyperon (YY) interactions since direct YY scattering data is practically absent. Although the current hypernuclear data are still rather limited in quantity and quality, ongoing experiments at international facilities as Jlab, BNL, KEK, J-PARC, MAMI, COSY and FAIR will provide promising results in very near future.

The discovery of hypernuclei has paved an essential path for achieving one of our ultimate goals of nuclear physics: a unified theory describing baryon-baryon interactions connected via SU(3) flavor symmetry. Initial attempts to construct such a theory from the scratch of the underlying QCD seem not feasible due the non-perturbative feature of QCD at low-energy scales. Lattice QCD overcomes this difficulty by means of computationally expensive simulations on finite discretized space-time lattices. It has been very successful in computing from first principles many important physical quantities, in particular the hadron mass spectrum [18]. Yet current Lattice QCD predictions for observables involving more than one baryon, such as scattering lengths or two-baryon bound states, are still limited to the unphysical mass of $\pi$, the barrier that can be removed in near future as the computational resources grow [19]. Nevertheless, the dynamics of the low-energy (hyper)nuclear processes that we are interested in are not sensitive to the underlying structures of the particles involved. Many traditional (meson or purely conventional) approaches are based on other than quark and gluons as degrees of freedom.

One therefore may argue that for describing the baryon-baryon (BB) interactions in this regime, other than quarks and gluons as degrees of freedom should be more adequate. The pioneering works based on pure phenomenology [20] or meson exchanges [21–23] have been quite successful

in describing the two-body BB interactions in the non-strangeness sector. The latter were also extended to the strangeness sectors [24–26]. These conventional approaches, however, are not firmly rooted in QCD, and more importantly, could not provide a proper way to systematically estimate the theoretical uncertainty and the contributions from higher-body forces. These drawbacks are comprehensively addressed in the new approach to (hyper)nuclear physics, chiral effective field theory ($\chi$EFT) [27–36] - an effective low-energy expansion of QCD. Since it developed, $\chi$EFT has become a tool-of-choice in *ab initio* nuclear structure calculations [37–39], as well as hypernuclear calculations [40, 41]. In the next section, we give an overview of the nuclear $\chi$EFT framework and summarize the up-to-date BB chiral interactions with special focuses on hyperon-nucleon (YN) and hyperon-hyperon (YY) potentials that are employed in the thesis.

## 1.1 Baryon-Baryon interactions in $\chi$EFT

The beautiful concept of $\chi$EFT for nuclear physics was first introduced by Weinberg almost thirty years ago in his groundbreaking works [27, 28]. Since then $\chi$EFT has been intensively studied by many different groups, for examples: Ordóñez, Ray and Van Kolck [29], the Munich group [30], the Bonn-Jülich-Bochum group [31, 42], the Idaho group [32, 33] and the Bochum group [34], resulting in very sophisticated and high-precision nucleon-nucleon (NN) potentials (with the latest version next-to-next-to-next-to-next-to-leading $N^4LO$ [34–36, 43]) which almost perfectly describe the abundant NN data and provide accurate predictions for nuclear observables [37, 38]. Recently, the Bonn-Jülich and Bonn-Jülich-Munich groups have also extended the $\chi$EFT for NN forces [42, 44] to the strangeness $S = -1$ [45–47] and $S = -2$ [46, 48] sectors. The developed chiral YN and YY potentials at the next-to-leading order (NLO) are well in line with meson-exchange models [25, 49, 50] in describing YN and YY data and especially yield plausible results for many-body hypernuclear calculations [47, 51].

The $\chi$EFT framework is directly rooted in QCD since it possesses all the underlying symmetries and symmetry-breaking patterns at low-energy as QCD. The essential difference is in the degrees of freedom. For low-energy processes, quarks and gluons are frozen into colorless hadrons. In the $\chi$EFT approach, one therefore adopts more appropriate degrees of freedom, namely hadrons instead of quarks and gluons. The unresolved dynamics associated with high-energy (short-distance) can be parameterized by a set of the so-called low energy constants (LECs). These parameters must be determined via a fit to the experimental data (or calculated from the underlying theory if it is possible) so that the theory is consistent with the data and therefore can be used to predict reliably other observables. The active degrees of freedom depend on systems studied as well as on the energy region of interest, and are associated with the approximate and spontaneously broken chiral symmetry of QCD. For examples, for ordinary nuclear processes (in the two-flavor sector) the adequate degrees of freedom are nucleons and three pseudo-scalar mesons $\pi^\pm, \pi^0$ (which are identified as the pseudo-Goldstone bosons arising due to the spontaneous breakdown of the chiral symmetry from $SU(2)_R \times SU(2)_L$ to $SU(2)_V$). The strangeness sectors require additional five pseudo-scalar mesons (Goldstone bosons) $K^\pm, K^0, \bar{K}^0$ and $\eta$, together with strange baryons, e.g. $\Lambda$ and $\Sigma$ for $S = -1$ or $\Lambda, \Sigma$ and $\Xi$ for $S = -2$.

The active degrees of freedom also set the separation of scales in $\chi$EFT: the soft scale $Q$ is naturally taken as an external momentum transfer $p$ or pion mass $m_\pi$, $Q \approx (p, m_\pi)$, and the hard scale $\Lambda_\chi$ is some large momentum scales at which the prediction ability of $\chi$EFT breaks down, e.g. $\Lambda_\chi = 4\pi F_\pi \approx 1$ GeV. It is also common that $\Lambda_\chi$ is taken as masses of the lowest-lying resonances,

for instance $\Lambda_\chi = m_\rho \approx 770$ MeV.

Based on the above ingredients, the most general chiral effective Lagrangian which consits of an infinite number of terms can be constructed. Hence, the number of Feynman diagrams contributing to the BB effective potential will certainly be infinite. Although the BB chiral Lagrangian is nonperturbative at low energy[1], there is an underlying power counting scheme that allows to assess the importance of each Feynman diagrams and categorize them according to the powers of $Q/\Lambda_\chi$ such that at a given order of accuracy only a finite number of graphs contribute to the effective potential. The latter can be then inserted into the Lippmann-Schwinger or Schrödinger equation and iterated to all orders in order to obtain bound states or scattering amplitudes. Furthermore, in $\chi$EFT the contributions from many-body forces are natural, and the power counting scheme ensures that they emerge harmonically with the hierarchy controlled by the expansion power, i.e., 2BF $\gg$ 3BF $\gg$ 4BF .... This is can be clearly seen in Fig. 1.1 where the hierarchy of the chiral nuclear forces based on the Weinberg counting scheme is shown. Here, the vertical axis indicates the expansion orders. When going downwards, each row can be seen as a correction to the previous one. At the leading order (LO, $\sim Q^0$), there are only two irreducible diagrams contributing to the effective potential: a tree diagram with two LECs and a static one-pion-exchange diagram. Those graphs proportional to $Q$ disappear because parity conservation. At next-to-leading order (NLO, $\sim Q^2$), the NN contact with two derivatives parameterized by seven new LECs and two-pion-exchange diagrams give contributions, and so on. One sees that up to NLO, only two-body forces contribute whereas the three- and four-body forces require much larger momentum in order to be significant and therefore appear later in the hierarchy expansion, namely at $N^2LO$ and $N^3LO$, respectively. Hence, Fig. 1.1 can be interpreted as a perturbative expansion of the important contributions to the nuclear effective potential.

Every effective theory requires regularization and renormalization, and $\chi$EFT is not an exception. Iterating the effective potential in the Lippmann-Schwinger or Schrödinger equation will unavoidably lead to ultraviolet divergent integrals, therefore, must be regularized (and renormalized). This is most practically done by introducing a regulator function that integrates out momenta larger than some specific cutoff $\Lambda_c$, typically of order of the chiral breaking scale $\Lambda_c \sim \Lambda_\chi$. Again, most of the contributions due to higher-energy dynamics that are removed by regularization can be absorbed into the LECs (being renormalized) that parameterize the effective potential. In that sense, it is said that the renormalization in $\chi$EFT is being performed at the potential level. In principle, the observables should be only mildly dependent on the regulator cutoff $\Lambda_c$. However, in practice this is not always true. When iterating the truncated expansion for the effective potential, one inevitably generates higher-order contributions whose divergences can not be completely regularized by the LECs present at the given order. Therefore, by varying the regulator cutoff, usually $\Lambda_c \sim 500 - 650$ MeV, one can roughly estimate a lower limit of the contributions from the left out higher-order forces.

So far, the LECs for nuclear interactions have been very successfully determined via a fit to the wealth of nuclear data (about 5000 NN scattering data, deuteron and hypertriton binding energies and *nd* doublet scattering). The two- and three-body nuclear forces have been derived up to very high levels of accuracy, $N^4LO$ [34, 36, 43] and $N^3LO$ [53, 54], respectively, and widely replaced the conventional potentials. With increasing chiral expansion orders, the number of new LECs need to be fixed from experiments quickly increase and it may possibly grow beyond the number of

---

[1] A notorious evidence is the existence of shallow-lying bound state of deuteron, for further discussions one can refer to [31, 52].

observables. At this point, $\chi$EFT on lattice, e.g. the so-called nuclear lattice EFT [55–57], or *ab initio* many-body approaches based on chiral forces such as the no-core shell model (NCSM)[38, 39] or the coupled cluster method [58], will be the most feasible ways in order to provide necessary constraints on these newly emerged LECs.
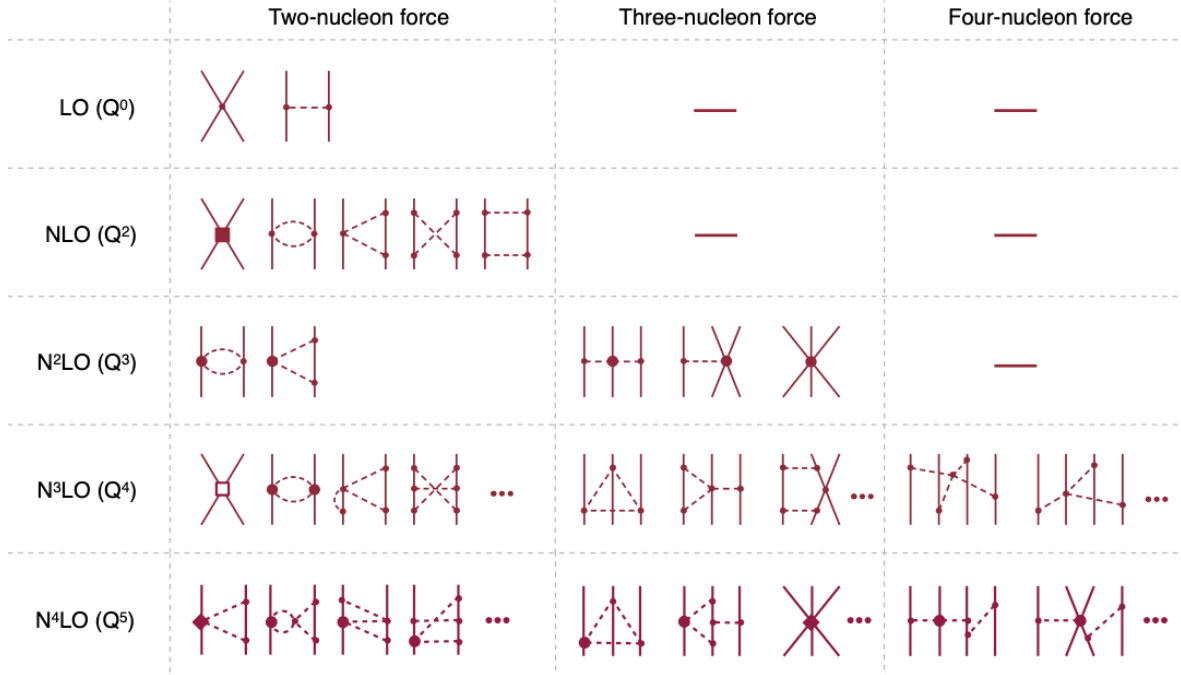


Figure 1.1: Hierarchy of nuclear forces up to N$^4$LO in $\chi$EFT using Weinberg counting scheme. The figure is from [34]

The situation is, however, much more severe for baryon-baryon interactions involving strangeness. Given extremely sparse scattering data (only about 35 YN data points for low-energy cross sections with very large uncertainty and essentially no YY scattering data at low-energy), it is practically not possible to uniquely determine the LECs in the strangeness sectors based solely on the available data (even at LO in the chiral expansion). One, therefore, often constraints these LECs by exploiting SU(3) flavor symmetry[2] but allows for the symmetry breaking through physical masses of the exchanged pseudo-scalar mesons ($\pi, K, \eta$) and of the active baryons as well. In doing so, the total number of LECs for the strangeness $S = -1$ channel at next-to-leading order (NLO) reduces to 23 [46], including 13 contact terms in the $S$-waves and the coupled $^3S_1 - ^3D_1$ partial waves, 9 LECs in the $P$-waves and a single low-energy coupling responding for the singlet-triplet transitions (such as $^1P_1 \leftrightarrow ^3P_1$). The latter, which arises due to the antisymmetric spin-orbit YN forces, is currently also set to zero. Additionally, because there are practically no polarization observables measured and in combination with the very limited number of differential cross sections that is predominantly determined by the $S$-waves, it is not possible to constrain all the nine $P$-wave LECs using only YN data. Therefore, parts of them (3 LECs) are currently determined from the NN $P$-wave phase shifts imposing strict SU(3) symmetry for the $P$-waves coupling constants. The remaining 6 LECs can then

---

[2] Note that this is also the main prerequisite in other meson-based models [22, 26] or constituent quark models [59].

be obtained via a fit to the available $\Lambda$p cross sections above the $\Sigma N$ threshold. Generally, in order to achieve a fairly good description of the $\Lambda$p cross sections, each of these $P$-waves contributions must be kept small. Concerning the 13 $S$-wave LECs, there are two possibilities to constrain them. In the first realization, referred to as NLO13 [46], these 13 $S$-wave coupling constants are fitted entirely to the YN experimental data. The resulting NLO13 potential describes the YN scattering almost perfectly even though there are still some correlations between the $^1S_0$ and $^3S_1$ low-energy contact terms. In the recent realization, labelled as NLO19 [47], parts of the $S$-wave LECs at NLO (namely 3 of them) are determined in the NN sector employing strict SU(3) symmetry for the coupling constants, while the remaining is constrained by information from YN observables[3]. It turns out that the two NLO13 and NLO19 versions differ essentially by the strength of the $\Lambda - \Sigma$ coupling, however, give completely equivalent descriptions for two-body observables [47]. It remains one of our aims here to comprehensively study the predictions of these two YN potentials for other heavier hypernuclear systems.

The contact terms in the strangeness $S = -2$ sector are determined in a very similar manner. Here, due to the nearly complete lack of YY scattering data, one has to even more strictly exploit SU(3) flavor symmetry in order to relate the $S = -2$ LECs at LO [61] and NLO [48] to the corresponding ones in the NN and YN sectors. In doing so, one is left with two undetermined contact terms, one in each expansion order, that are present only in the doubly strange channel and therefore must be constrained by the extremely scarce and uncertain YY data. There are a few upper limits of the elastic $\Xi^- p$ and inelastic $\Xi^- p \to \Lambda\Lambda$ cross sections [62], and some specific measurements of the $\Xi^- p$ total cross sections [63]. In addition, the relatively small $\Lambda$ separation energy recently extracted from the Nagara event [17] also hints at a weakly attractive YY force. Nevertheless, these YY data can provide only qualitatively constraints for the two additional contact terms. Further constraints, in principle, should be expected from YY scattering experiments which unfortunately are extremely difficult to carry out. Another resource is the separation energies of double-strangeness hypernuclei, for instance $^6_{\Lambda\Lambda}$He, which so far has not been employed in the $\chi$EFT approach yet. Our second goal here is to study double-$\Lambda$ hypernuclei using chiral YY forces at LO and NLO, and thereby, be able to provide meaningful constraints to the LECs in the $S = -2$ sector.

Although it is beyond the scope of our study, let us also mention that besides the direct connections to the underlying BB interactions in nuclear physics, hypernuclei also play an important role in astrophysics and in understanding neutron stars [64, 65]. It is believed that the presence of $\Lambda$ and $\Sigma$ (and other strange) hyperons in the interior of neutron stars softens the equation of state [66]. It is the current puzzle of astrophysics how this is consistent with the existence of neutron stars as massive as two solar masses that have been observed [67, 68].

In the following section, we will give an overview of the numerical methods that have been quite successfully implemented for hypernuclear calculations and motivate our approach

## 1.2 Theoretical approaches

Since the first discovery of hypernuclei numerous theoretical works have been devoted to study strangeness systems. Generally, most of the approaches have been an extension of the methods successfully employed in nuclear structure calculations. For very light $A = 3, 4$ hypernuclei, exact solutions of the Faddeev-Yakubovsky integral equation in momentum space can be obtained [69,

---

[3] A simultaneous description of YN and NN data imposing strict and consistent SU(3) on contact terms is not feasible. This is nevertherless consistent with the power counting which allows symmetry-breaking contact terms at LO [60].

70]. The method is accurate and also very flexible since it allows for calculations with almost all available NN and YN potentials. In fact, results obtained from the Faddeev-Yakubovsky calculations for $A = 4$ systems will be utilized to benchmark and validate our calculations.

Hiyama *et al.* developed the variational Gaussian expansion method (GEM) that can be applied to systems up to $A = 5$ baryons [71, 72]. As the name suggests, the method expands the many-body wavefunction in a basis of functions depending on the relative Jacobi coordinates, whose radial parts have a Gaussian dependence while the angular parts are described by spherical harmonics. The GEM does not employ bare YN interactions but rather a series of simulated Nijmegen-based potentials, SC97d(S)-f(S) and SC89(S), which have some Gaussian form factors in order to facilitate the calculations. Hiyama *et al.* also extent the GEM approach to heavier single- and double-strangeness hypernuclei up to $A = 13$ by exploiting the coupled cluster structures [73–75]. Here, instead of the bare interactions, the authors employ the *G*-matrix effective potentials (YNG) which are constructed in nuclear matter from the original Nijmegen YN potentials. The dependence of the YNG forces on the nuclear medium (often expressed in term of the nuclear Fermi momentum $k_F$) is adjusted to reproduce some experimental observables, e.g. the $\Lambda$-separation energy of $^5_\Lambda$He. The authors have successfully calculated not only the separation energies and the energy levels of a wide range of hypernuclei [74], but also comprehensively investigate the changes in dynamic structures of the core nuclei due to the presence of a $\Lambda$ hyperon like the shrinking effect [75], the glue-like and $\Lambda$-skin effects [73, 75]. The main disadvantage of the method is that there is no clear connection between the derived effective YNG potentials and the initial realistic YN interactions in free space. The derived potentials can not be employed in other many-body calculations, so it is difficult to benchmark the results especially given the situation where there are substantial differences among the predictions of various realistic YN interaction models.

Gal, Dalitz and Millener have also intensively studied the *p*- and *sd*-shell hypernuclei using the shell model, where only valence nucleons together with a hyperon are the active degrees of freedom [11, 12, 76, 77]. Within the approach, a hypernuclear system is usually considered exclusively in the configuration in which a $\Lambda$ hyperon in the *s*-shell is coupled to the shell-model ground state of the nuclear core. Also, the model does not utilize realistic but rather effective NN and YN interactions. The effective NN potentials are derived through the G-matrix procedure from a set of the Nijmegen potentials, while the YN interactions are parameterized in terms of some r-space functions (usually in Gaussian forms) with some variables depending on spins and orbital angular momenta of the hyperon and the nuclear core. Despite of that, the shell model has been quite successful in describing the energy spectra of the *p*- and *sd*-shell hypernuclei as well as in explaining some spin-dependence features of the YN interactions. Nevertheless, the vital link between the employed effective potentials and the original realistic interactions is hard to establish, furthermore, many dynamical effects like the distortion of the core nuclei due to the presence of a $\Lambda$ are difficult to incorporate.

In contrast to the shell-model approach, the no-core shell model (NCSM) treats all particles as active which, in principle, allows for a direct implementation of any baryon-baryon interaction. However, the NCSM bases on an expansion of the many-body wavefunctions in harmonic-oscillator (HO) states whose Gaussian long-distant tails are not well-suited for the description of the long-distance behavior of the wavefunctions. This manifests in the slow convergence of the binding energies (and other observables) calculated within the NCSM, especially when the initial potentials exhibit strong correlations due to the hard-core and strong tensor forces. Various transformations, e.g. $V_{lowk}$ or Okubo-Lee-Suzuki, have been exploited in order to soften the interactions hence speed up the convergence of the NCSM calculations [78]. But still, the applications of the approach are

somewhat limited to light nuclear systems. The situation has been significantly improved with the emerges of the $\chi$EFT forces and the powerful similarity renormalization group (which we will discuss in the following chapter), that make the NCSM nowadays a standard tool to study the p-shell nuclear structure [79–81]. Currently, the approach is widely implemented in two formulations differing essentially in the basis sets, the Jacobi-NCSM (J-NCSM) using the Jacobi basis [82, 83] and the m-scheme NCSM with the truncated Slater-determinant basis (also known as importance-truncated NCSM or IT-NCSM) [84, 85]. The Jacobi basis depends on relative Jacobi coordinates of all particles (with respect to which the HO functions are defined) and can be constructed by coupling relative angular momenta and intrinsic isospins in the $jj$-coupling scheme. By construction, the basis functions preserve the translational invariance of the Hamiltonian, and therefore, enable an explicit separation of the C.M. (center of mass) motions. Additionally, it is also possible to define the Jacobi basis for each physical states with definite angular momentum and isospin separately. The corresponding Hamiltonians are then decoupled, and hence, can be diagonalized independently. These factors together lead to much smaller dimensions in the J-NCSM as compared to the m-scheme full Slater-determinant realization for a given model space truncation. Furthermore, as shown in [82, 83], due to the flexibility of HO states expressed in relative Jacobi coordinates, the inclusion of higher-body forces in the J-NCSM approach is straightforward and does not require any further truncations. The trade-off of this formalism is that the antisymmetrization of the basis states is rather complicated and can be also very computationally demanding. However, the antisymmetrization procedure and ultimately the constructed Jacobi-basis functions are independent of HO frequencies and interaction models as well. These states thereby can be calculated very efficiently in a completely memory-distributed manner, independent of the Hamiltonian diagonalization procedure. With this great advantage, one can afford within the J-NCSM approach a series of calculations with different HO frequencies and also various interactions. The former makes it possible to systematically eliminate the HO-frequency dependence of the binding energies and at the same time reliably estimate the numerical accuracy of the final converged results. The latter allows for the most efficient way to study the impacts of different chiral forces with a range of chiral regulator cutoffs $\Lambda_c$ on the observables, in particular the binding energies.

In the Slater-determinant formalism, the basis functions are Slater determinants constructed from single-particle HO states. In this basis, the C.M. degrees of freedom can no-longer be explicitly separated out. Furthermore, it is not straightforward to construct the basis states with certain angular momentum and isospin in contrary to the Jacobi basis. As a result, the dimension of the linear equations need to be solved in the Slater-determinant basis is extremely large, which severely limits the applicability of the approach . Roth and Kruse have overcome this difficulty by ultilizing the importance-truncation, which perturbatively assesses the basis functions according to their contributions to the binding energies and filters the states out if their contributions are smaller than some criteria. This has reduced the dimension of the model space significantly and allows one to apply the IT-NCSM to heavy p-shell nuclei [84, 85]. However, such a truncation also leads to an explicit dependence of the truncated basis set on the HO frequency and the employed nuclear potential as well. That dependence is definitely undesired since it implies that one will need to generate a new basis set for each HO frequency or each chosen nuclear interactions. Therefore, in practice, in order to save substantial computational resources, one often performs calculations with only one presumably optimal HO frequency (that gives the lowest energy in all model space sizes, which is certainly a very rough approximation). Consequently, the final extracted binding energies may be still sensitive to the HO frequencies and the estimation of the numerical uncertainty may not be very trustable. Additionally, the Slater-determinant realization requires expensive transformations

of the matrix elements (of two-, three- and higher-body operators) from relative coordinates into single-particle coordinates. In case of two-body operators, in order to save computation time, the potential matrix elements are pre-calulated and stored. However, such strategy is not feasible for three- and higher-body matrix elements due to the severe memory constraints. So one has to repeatedly perform those computationally expensive transformations on the fly during the energy calculations.

Recently, Gazda *et al.* have incorporated the strangeness degree of freedom into the framework of the J-NCSM, and performed calculations for *s*-shell hypernuclei [86]. Wirth *et al.* has further extended the IT-NCSM for nuclei [84] to *p*-shell hypernuclei [41, 87, 88]. In this thesis, we want to advance the nuclear J-NCSM [83] to comprehensively study *s*- and light *p*-shell single strangeness hypernuclei (up to $A = 7$) as well as *s*-shell double strangeness hypernuclei (up to $A = 6$). Our ultimate goal is to unambiguously connect the observable properties of hypernuclei to that of the underlying YN and YY interactions.

The thesis is organized as follows: The first chapter started with a brief introduction to hypernuclear physics followed by an overview of baryon-baryon (NN, YN and YY) interactions derived from chiral effective field theory. We also gave an overview of the numerical techniques existing for many-body hypernuclear calculations and motivated our approach. In Chapter 2, the general concept of the Similarity Renormalization Group (SRG) is briefly discussed and exemplified with the YN and YY chiral interactions. The J-NCSM formalism for single-strangeness systems is described in details in Chapter 3. Here we also highlight some numerical difficulties and discuss our strategies to overcome these challenges. Results for $A = 4 - 7$ single-$\Lambda$ hypernuclei are presented in Chapter 4. We thoroughly investigate impacts of the SRG NN and SRG YN evolutions on the $\Lambda$-separation energies $B_\Lambda$, and compare the predictions of the two NLO13 and NLO19 YN chiral interactions for $B_\Lambda$ as well as the energy spectrum of $^7_\Lambda$Li. We close Chapter 4 with a comprehensive study about spatial distributions and the correlation functions in these hypernuclei. In Chapter 5, we construct the many-body Hamiltonian and the Jacobi bases for describing $S = -2$ systems. We also explain how one can generally relate the Hamiltonian matrix elements in the many-body bases to the matrix elements in the two-body sector. In Chapter 6, we investigate the predictions of the LO and NLO chiral YY interactions for the $^4_{\Lambda\Lambda}$H, $^5_{\Lambda\Lambda}$He and $^6_{\Lambda\Lambda}$He hypernuclei. Final conclusions and outlooks are given in Chapter 7.

# Similarity Renormalization Group (SRG)

$\chi$EFT potentials are softer than the conventional meson-exchange interactions due to smooth regulator functions and the lower cutoff on high-energy physics. Yet, the presence of large potential matrix elements coupling low- and high-momentum states is still significant. As a result, fully converged *ab initio* calculations can be achieved only for very light systems with $A \leq 4$ [70]. For larger systems, one often has to exploit some additional unitary transformations that can somehow renormalize the Hamiltonian such that it becomes more tractable. There are different approaches serving that purpose, for examples, $V_{lowk}$ which integrates out high-momentum components $k > \Lambda$ while preserving observables at low momenta $k \leq \Lambda$ [89, 90], Okubo-Lee-Suzuki transformation [91] (that was often employed in connection with the NCSM formalism before the SRG technique became available) which aims at constructing an $A$-body hermitian effective Hamiltonian whose eigenvectors approximate those of the original Hamiltonian in a small model space [78, 92, 93], or Unitary Correlation Operator Method that utilizes special transformations designed to eliminate the strong correlations due to the hard-core and tensor forces [94]. Although these methods can all successfully pre-diagonalize the Hamiltonian (hence improve the convergence) higher-body forces, however, can not be treated systematically. The Similary Renormalization Group approach can be equally successful in softening the interactions, and more importantly, provides a feasible way to handle many-body forces. The method was first proposed by Glazek, Wilson and Wegner [95, 96] to solid physics and recently employed by Bogner, Furnstahl and Perry [97] to nuclear interactions, and has become an indispensable tool for nuclear and hypernuclear many-body calculations especially in connection with chiral forces. Here, we will first summarize the general idea of the SRG and then discuss in some details the effects on $\chi$EFT potentials, specifically the LO and NLO YN and YY interactions.

## 2.1 SRG evolvement

We will follow the simple, but versatile, formalism developed by Wegner [96] which formulates the SRG in terms of a series of unitary transformations with respect to flow parameter $s$

$$H_s = U_s H_0 U_s^\dagger \equiv T_{rel} + V_s, \tag{2.1}$$

where $H_0 = H_{s=0}$ is the initial (bare) Hamiltonian, $T_{rel}$ is the intrinsic relative kinetic operator which also includes the mass term difference when one allows particle conversions in the Hamiltonian. The flow parameter $s$ has a unit of energy$^{-2}$ and varies continuously from 0 to $\infty$. Note that, although the flow equation is solved with respect to $s$, for characterizing the SRG-evolved potentials we will utilize a more intuitive variable, namely the SRG cutoff $\lambda = (\frac{4\mu^2}{s})^{1/4}$ with $\mu$ being the reduced mass (of the involved particles ). The new variable $\lambda$ has dimension of momentum (energy) and can qualitatively provide a measure of the suppression of off-diagonal matrix elements [97]. By differentiating the transformation Eq. (2.1), one obtains the evolution equation for the Hamiltonian $H_s$,

$$\frac{dH_s}{ds} = \frac{dV_s}{ds} = [\eta_s, H_s], \tag{2.2}$$

where the generator,

$$\eta_s = \frac{dU_s}{ds} U_s^\dagger = -\eta_s^\dagger,$$

is an anti-hermitian operator. Usually, $\eta_s$ is taken as a commutator of an arbitrary hermitian operator $G_s$ with the Hamiltonian, $\eta_s = [G_s, H]$, which leads to the following flow equation for the potential operator

$$\frac{dV_s}{ds} = [[G_s, H_s], H_s]. \tag{2.3}$$

The choice of $G_s$ is often done such that the final evolved Hamiltonian $H_s$ possesses a desired form. There are various possibilities of choosing $G_s$: the relative kinetic energy $G_s = T_{rel}$ (Wilson generator), momentum diagonal operators, for example $G_s = T_{rel}^2$, or running diagonal part of the evolved Hamiltonian $G_s = diag(H_s)$ (Wegner generator). In general, different choices of $G_s$ can lead to different speed of suppression of off-diagonal strength in different bases. For our purpose of decoupling the low- and high-momentum components, the simplest but yet very useful generator is the relative kinetic energy. We take,

$$G_s = \frac{p^2}{2\mu}, \tag{2.4}$$

with $p$ being particles relative momentum. Note that our chosen operator $G_s$ Eq. (2.4) and the relative kinetic energy $T_{rel}$ can slightly differ by the masses difference term induced by particle conversions. With $G_s$ defined in Eq. (2.4), the flow equation Eq. (2.3) now becomes

$$\frac{dV_s}{ds} = \left[\left[\frac{p^2}{2\mu}, V_s\right], H_s\right], \tag{2.5}$$

which is a universal operator equation independent of any basis. In order to solve the above equation for two-body systems, we will project the operator equation Eq. (2.5) onto a partial-wave relative momentum basis with states being denoted as

$$|p\,(ls)J;\, t_1 m_{t_1} S_1\; t_2 m_{t_2} S_2\rangle \equiv |p\alpha\rangle. \tag{2.6}$$

Here, $l$ is the orbital angular momentum which combines with the total spin $s$ to form the total angular momentum $J$, while $(t_i, m_{t_i}, S_i)_{i=1,2}$ are sets of the intrinsic quantum numbers: isoposin, isospin projection and strangeness, respectively, that distinguish different particle states. The normalization of the basis states Eq. (2.6) simply reads

$$\sum_{\alpha} \int dp p^2 \, |p\alpha\rangle\langle\alpha p| = 1. \tag{2.7}$$

Now, projecting the Eq. (2.5) onto the basis Eq. (2.6), one obtains the flow equation in form of an integro-differential equation

$$\frac{dV_s^{\alpha\alpha'}(pp')}{ds} = \Big[ T_{rel}^{\alpha}(p)\frac{p^2}{2\mu^{\alpha}} + T_{rel}^{\alpha'}(p')\frac{p'^2}{2\mu^{\alpha'}} - T_{rel}^{\alpha}(p)\frac{p'^2}{2\mu^{\alpha'}} - T_{rel}^{\alpha'}(p')\frac{p^2}{2\mu^{\alpha}} \Big]V_s^{\alpha\alpha'}(pp')$$

$$+ \sum_{\tilde{\alpha}} \int_0^{\infty} dk k^2 \Big[ \frac{p^2}{2\mu^{\alpha}} + \frac{p'^2}{2\mu^{\alpha'}} - \frac{k^2}{\mu^{\tilde{\alpha}}} \Big]V_s^{\alpha\tilde{\alpha}}(pk)V_s^{\tilde{\alpha}\alpha'}(kp'). \tag{2.8}$$

Note that, the reduced mass $\mu$ depends explicitly on the particle states $\alpha$ since physical masses are employed for the SRG evolution. We solve the flow equation Eq. (2.8) numerically using a non-equidistant momentum grid characterized by the ultraviolet momentum cutoff $p_{max}$ and $N$ Gauss-Legendre integration points $p_n$ with corresponding weights $w_n (n = 1, \cdots N)$. Since the initial potentials often vary at low momenta faster than at high momenta, it is useful to define the grid that is sparse at high momenta but denser at the low-momentum region. This can be achieved for example by performing a hyperbolic transformation on the Gauss-Legendre points $p_n$ and weights $w_n$. It is also important to stress that the momentum cutoff $p_{max}$ and the number of mesh points $N$ are rather sensitive to the original potentials and have to be chosen for each interactions carefully so that the SRG-evolved potential and ultimately the two-body observables (scattering phase shifts and binding energies) are independent of the momentum descretization. Generally, one may expect that potentials with very long tails in momentum space will require a large momentum cutoff and, consequently, many grid points which in turn can affect the efficiency of the numerical solvers.

Finally, by applying the Legendre-Gauss quadrature rule to the integral in Eq. (2.6), and discretizing the remaining terms on the defined momentum grid, we transform the integro-differential equation into a system of coupled ordinary differential equations

$$\frac{dV_s^{\alpha\alpha'}(p_i p_j)}{ds} = \Big[ T_{rel}^{\alpha}(p_i)\frac{p_i^2}{2\mu^{\alpha}} + T_{rel}^{\alpha'}(p_j)\frac{p_j^2}{2\mu^{\alpha'}} - T_{rel}^{\alpha}(p_i)\frac{p_j^2}{2\mu^{\alpha'}} - T_{rel}^{\alpha'}(p_j)\frac{p_i^2}{2\mu^{\alpha}} \Big]V_s^{\alpha\alpha'}(p_i p_j)$$

$$+ \sum_{\tilde{\alpha}} \sum_{n=1}^{N} p_n^2 w_n \Big[ \frac{p_i^2}{2\mu^{\alpha}} + \frac{p_j^2}{2\mu^{\alpha'}} - \frac{p_n^2}{\mu^{\tilde{\alpha}}} \Big]V_s^{\alpha\tilde{\alpha}}(p_i p_n)V_s^{\tilde{\alpha}\alpha'}(p_n p_j), \tag{2.9}$$

which are then solved using the advanced multi-step Adams PECE (Predict Estimation Correct Estimation) method.

## 2.2 SRG for $\chi$EFT YN and YY interactions

We first demonstrate the SRG evolutions of the two realizations of the YN interactions: the LO realization for a regulator of $\Lambda_Y = 700$ MeV (Fig. 2.1) and the NLO19 one with $\Lambda_Y = 650$ MeV (Fig. 2.2). The contour plots are the potentials of all particle channels with the charge $Q = 0$ and in the $^1S_0$ (upper left ), $^3S_1$ (upper right) and the coupling $^3S_1 - ^3D_1$ (lower figure) partial waves. The potentials are evolved to four different values of YN flow parameter: $\lambda_{YN} = 98$ fm$^{-1}$ (almost non-evolved, bare interaction), $\lambda_{YN} = 3$ fm$^{-1}$ (slightly evolved), $\lambda_{YN} = 1.6$ fm$^{-1}$ (commonly used ) and the extreme case $\lambda_{YN} = 0.946$ fm$^{-1}$ for LO and $\lambda_{YN} = 0.868$ fm$^{-1}$ for NLO19. It clearly sticks out that the SRG evolution steadily drives the potentials toward a diagonal form decoupling the low- and higher-momentum states. Qualitatively, the two initial (bare) YN interactions, LO and NLO19, and also their SRG-evolved versions are quite different from each other. The bare NLO19 shows a stronger repulsive behaviors in the partial waves $^1S_0$ and $^3S_1$ for almost all particle channels, but is more attractive in the coupling $^3S_1 - ^3D_1$ partial waves. One can also notice that the NLO19 seems to be driven towards a diagonal form faster than the LO. Also, there is a strong enhancement in the high-momentum part of the NLO19 potential during the evolution, see also Fig. 2.3 where only diagonal matrix elements are plotted. This enhancement becomes stiffer, even exhibits some oscillation behaviors when the cutoff on the SRG-YN flow parameter is small. This may reflect some sensitivity on the momentum-grid discretization of the potential when it is evolved to the extreme value of the flow parameter $\lambda_{YN}$. We have checked the discretization carefully to avoid any numerical instability around this high-momentum region. We also confirmed that the observables (binding energies) are not affected by the behavior of the potential in this region.

Very similar patterns are observed for the SRG evolutions of the EFT YY interactions. Here, we also show the evolution of the two chiral YY interactions, LO and NLO for a regulator of $\Lambda_{YY} = 600$MeV, for all particle channels with zero charge and in the $^1S_0$ partial wave, Figs. 2.4 to 2.6. The YY potentials are also evolved to four different values of flow parameter: $\lambda_{YN} = 98$ fm$^{-1}$ (almost non-evolved, bare interaction), $\lambda_{YN} = 3$ fm$^{-1}$ (slightly evolved), $\lambda_{YN} = 2.0$ fm$^{-1}$ and $\lambda_{YN} = 1.6$ fm$^{-1}$. Evidently, in the particle diagonal channels, both LO and NLO potentials exhibit a repulsive behaviour at the very beginning of the evolution and gradually become attractive at low momenta as the flow parameter decreases. The NLO potential also develops a slight enhancement at high momenta like in the case of the YN NLO potential. As one can clearly notice in Fig. 2.6, where the diagonal matrix elements in the $\Lambda\Lambda - \Lambda\Lambda$ channel is shown, the peak of the potential is shifted towards higher momentum and becomes narrower with decreasing flow parameter $\lambda_{YY}$.

By the examples of the SRG evolutions for $\chi$EFT YN and YY interactions, we have shown that the SRG indeed drives the interactions towards a diagonal form by decoupling the low- and high-energy physics, and hence (as one will see later), can tremendously facilitate the convergence of many-body calculations, in particular the NCSM [98]. However, one should keep in mind that the SRG will eventually shift the two-body strength to strengths of higher-body forces even if the initial Hamiltonian does not contain these higher-body forces [97, 99]. As a consequence, the binding energies and other observables in systems with $A > 2$ will be functions of the flow parameters when the SRG-induced many-body forces are not included. This dependence can then be used as a tool to assess the contributions from the missing terms.

Figure 2.1: Contour plot of the YN potential matrix elements for all possible particle channels with the charge $Q = 0$ in the $^1S_0$ (upper left), $^3S_1$ (upper right) and the coupled $^3S_1 - ^3D_1$ partial-wave channels. The potentials are evolved to four different values of the YN flow parameter: $\lambda_{YN} = 98$ fm$^{-1}$ (first column, almost non-evolved (bare) YN potential), $\lambda_{YN} = 3$ fm$^{-1}$ (second column, slightly evolved), $\lambda_{YN} = 1.6$ fm$^{-1}$ (third column) and $\lambda_{YN} = 0.868$ fm$^{-1}$ (last column). The initial potential is a chiral YN at LO with a regulator of $\Lambda_Y = 700$ MeV.

Figure 2.2: Contour plot of the YN potential matrix elements for all possible particle channels with the charge $Q = 0$ in the $^1S_0$ (upper left), $^3S_1$ (upper right) and the coupled $^3S_1 - ^3D_1$ (lower) partial-wave channels. The potentials are evolved to four different values of the YN flow parameter: $\lambda_{YN} = 98$ fm$^{-1}$ (first column, almost non-evolved (bare) YN potential), $\lambda_{YN} = 3$ fm$^{-1}$ (second column, slightly evolved), $\lambda_{YN} = 1.6$ fm$^{-1}$ (third column) and $\lambda_{YN} = 0.868$ fm$^{-1}$ (last column). The initial potential is a chiral YN at NLO with a regulator of $\Lambda_Y = 650$ MeV.

(a) $\lambda_{YN} = 98$ fm$^{-1}$

(b) $\lambda_{YN} = 3$ fm$^{-1}$

(c) $\lambda_{YN} = 1.6$ fm$^{-1}$

(d) $\lambda_{YN} = 0.868$ fm$^{-1}$
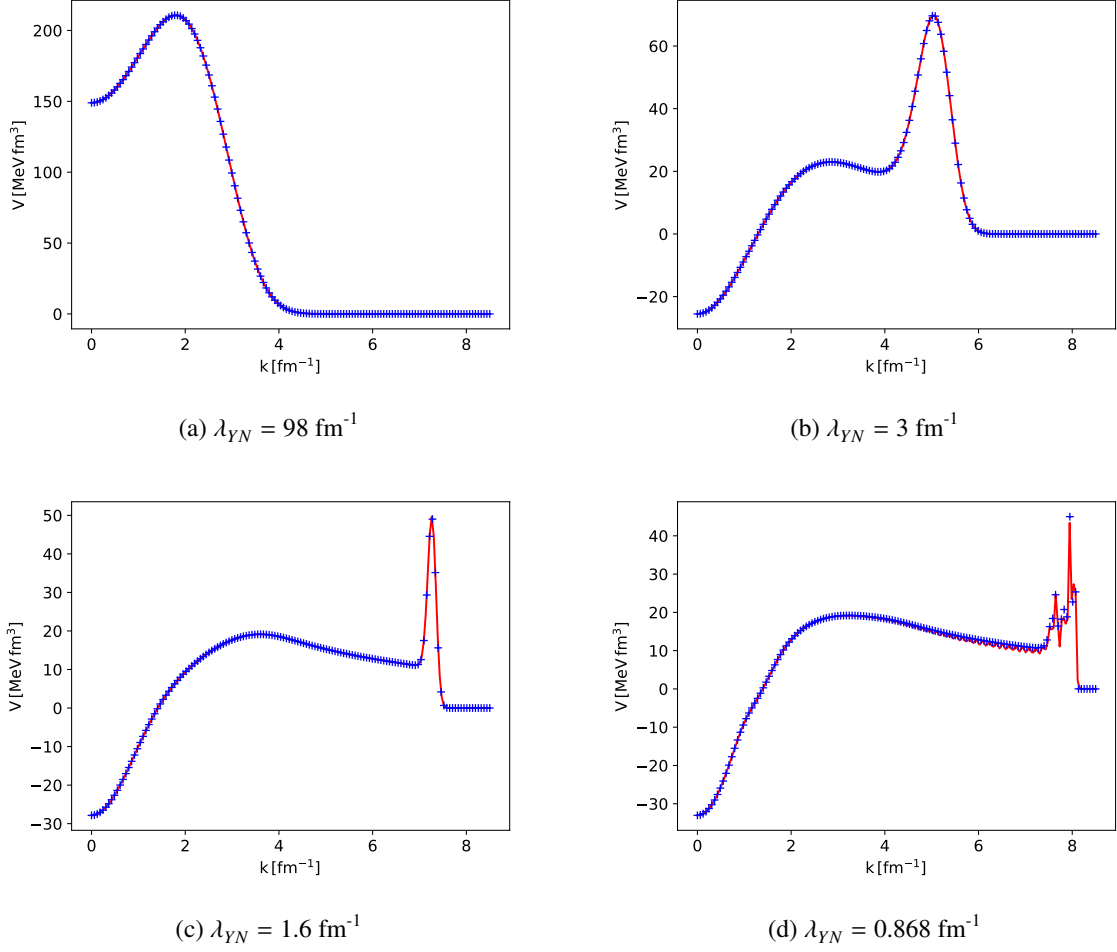
Figure 2.3: SRG evolutions of the diagonal matrix elements in the $\Lambda n - \Lambda n$ particle channel and the $^1S_0$ partial wave. The blue crosses are the SRG-evolved potentials on sparse momentum grid and red line is the interpolated results. The initial potential is a YN NLO19 with a chiral cutoff of $\Lambda_Y = 650$ MeV.
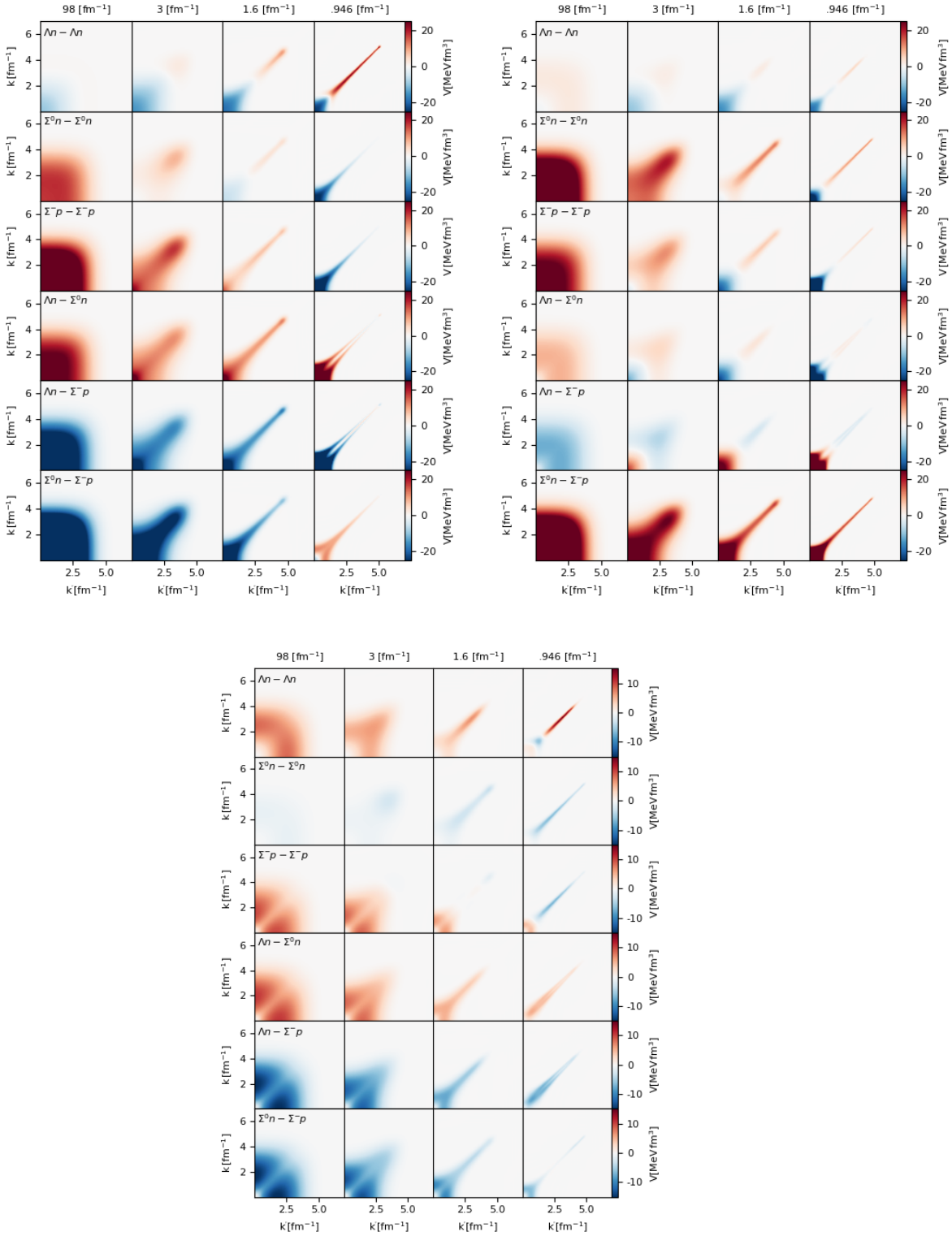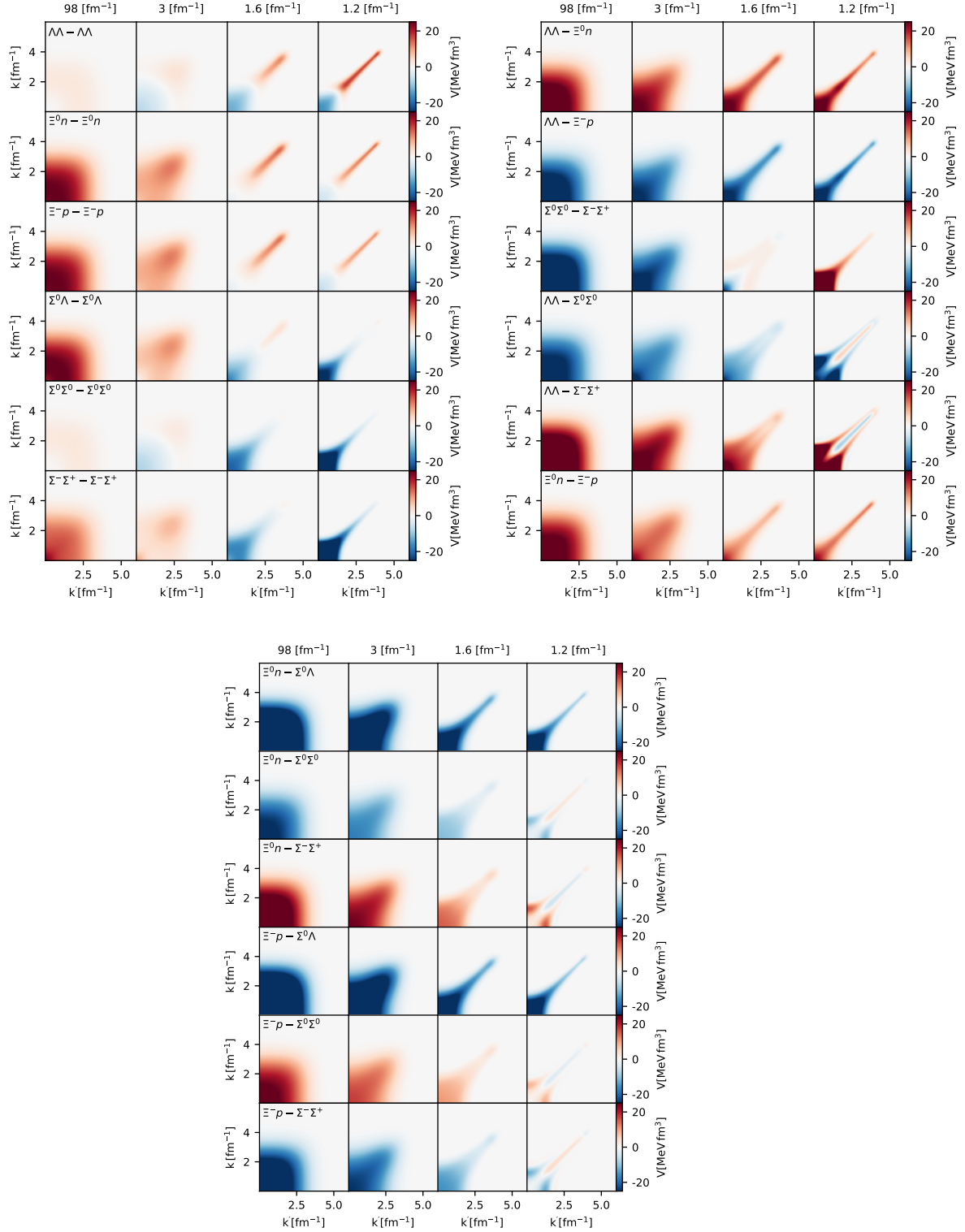
Figure 2.4: Contour plot of the YY potential matrix elements for all possible particle channels with the charge $Q = 0$ in the $^1S_0$ partial wave. The potential is evolved at four different values of the flow parameter: $\lambda_{YY} = 98$ fm$^{-1}$ (first column, almost non-evolved (bare) YY potential), $\lambda_{YY} = 3$ fm$^{-1}$ (second column, slightly evolved), $\lambda_{YY} = 1.6$ fm$^{-1}$ (third column) and $\lambda_{YY} = 1.2$ fm$^{-1}$ (last column). The initial potential is a chiral YY at LO with a regulator of $\Lambda_{YY} = 600$ MeV.
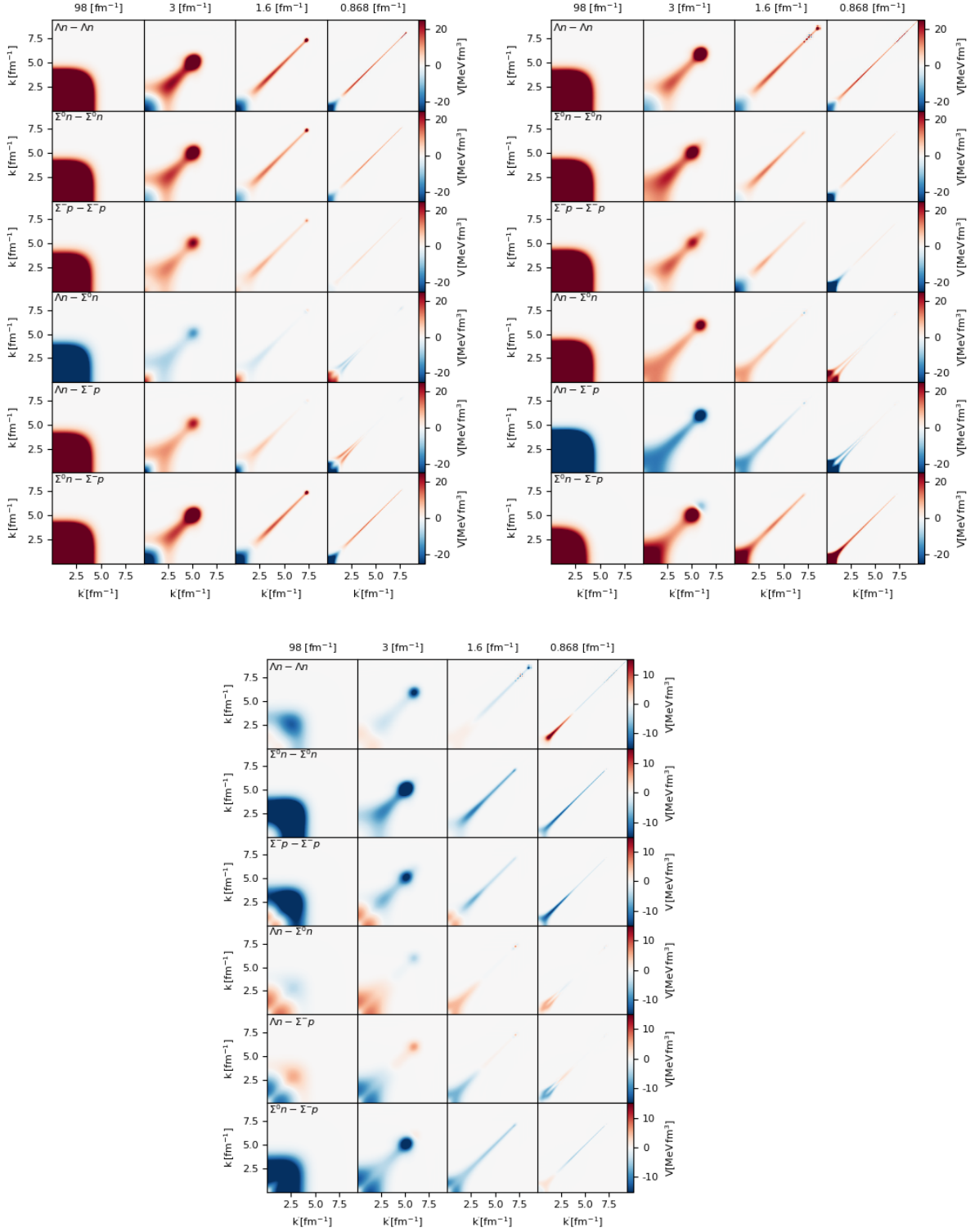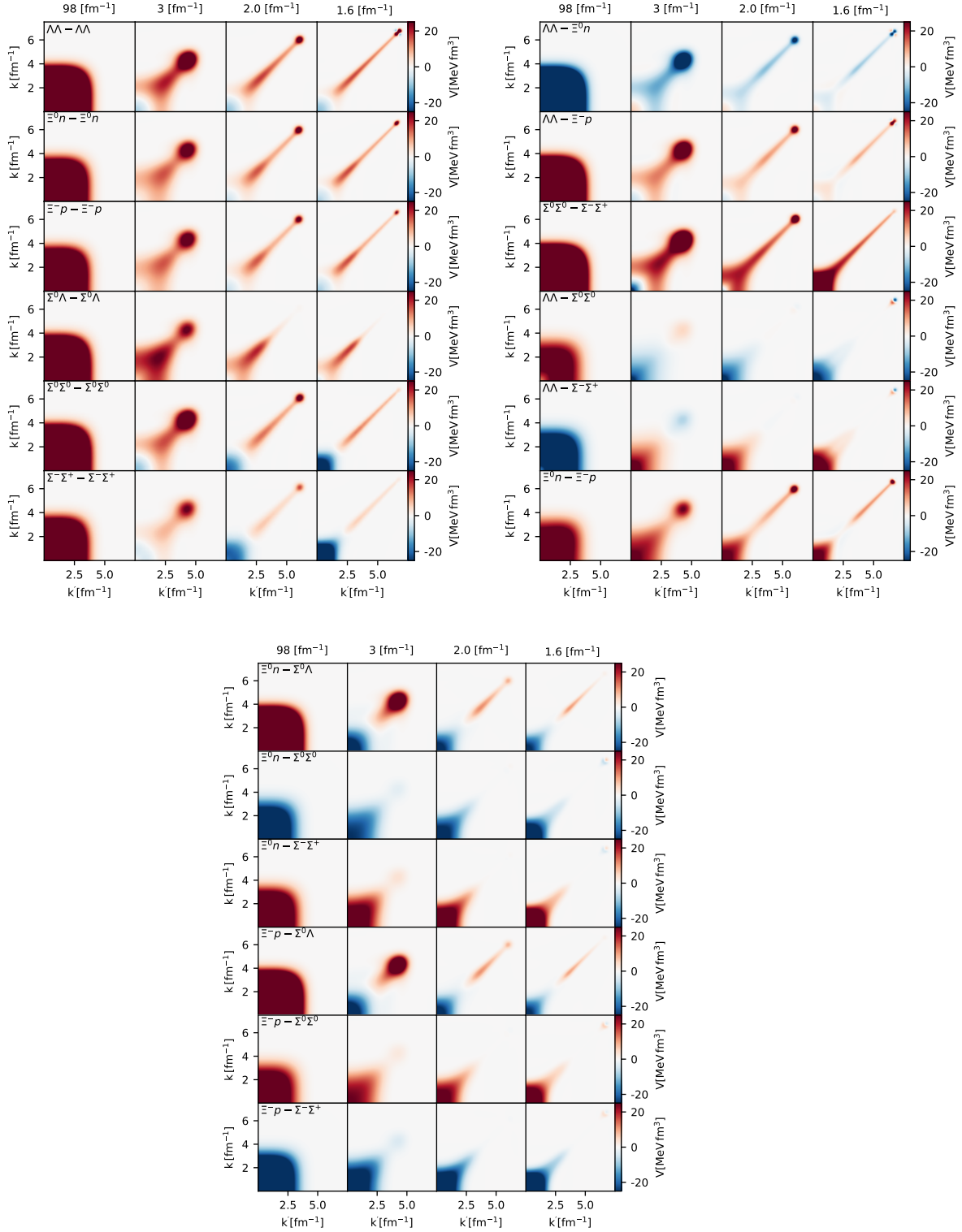
Figure 2.5: Contour plot of the YY potential matrix elements for all possible particle channels with the charge $Q = 0$ in the $^1S_0$ partial wave. The potential is evolved at four different values of the flow parameter: $\lambda_{YY} = 98$ fm$^{-1}$ (first column, almost non-evolved (bare) YY potential), $\lambda_{YY} = 3$ fm$^{-1}$ (second column, slightly evolved), $\lambda_{YY} = 1.6$ fm$^{-1}$ (third column) and $\lambda_{YY} = 1.2$ fm$^{-1}$ (last column). The initial potential is a chiral YY at NLO with a cutoff of $\Lambda_{YY} = 600$ MeV.

(a) $\lambda_{YY} = 98$ fm$^{-1}$

(b) $\lambda_{YY} = 3$ fm$^{-1}$

(c) $\lambda_{YY} = 2.0$ fm$^{-1}$

(d) $\lambda_{YY} = 1.6$ fm$^{-1}$

Figure 2.6: Diagonal matrix elements of the $\Lambda\Lambda - \Lambda\Lambda$ particle channel for $^1S_0$ partial wave at four different values of $\lambda_{YY}$. The blue crosses are the SRG-evolved potentials on sparse momentum grid and red line is the interpolated results. The initial potential is YY at NLO with a chiral cutoff of $\Lambda_Y = 600$ MeV.

# Part I

# Single Strangeness Hypernuclei

# Jacobi NCSM for $S = -1$ systems

In this chapter, we extend the nuclear J-NCSM [83] in order to incorporate a single strangeness hyperon ($Y = \Lambda, \Sigma$). We will explain how the Jacobi basis sets for hypernuclei as well as the many-body Hamiltonian matrix elements are constructed. We also discuss in detail the strategy that allows us to perform numerical calculations in the most efficient way regarding computational resources and memory constraints.

## 3.1 Jacobi basis for hypernuclei

The translationally invariant many-body Hamiltonian of a system consisting of $(A - 1)$ nucleons and a single-strangeness hyperon $Y$ (characterized by isospin $t_Y$) in relative Jacobi coordinates can be written as follows

$$
\begin{aligned}
H &= H^{S=0} + H^{S=-1} \\
&= \sum_{i<j=1}^{A-1} \Big( \frac{2p_{ij}^2}{M(t_Y)} + V_{ij}^{NN} \Big) + \sum_{i=1}^{A-1} \Big( \frac{m_N + m(t_Y)}{M(t_Y)} \frac{p_{iY}^2}{2\mu_{NY}} + V_{iY}^{YN} + \frac{1}{A-1}(m(t_Y) - m_\Lambda) \Big) + \dots \\
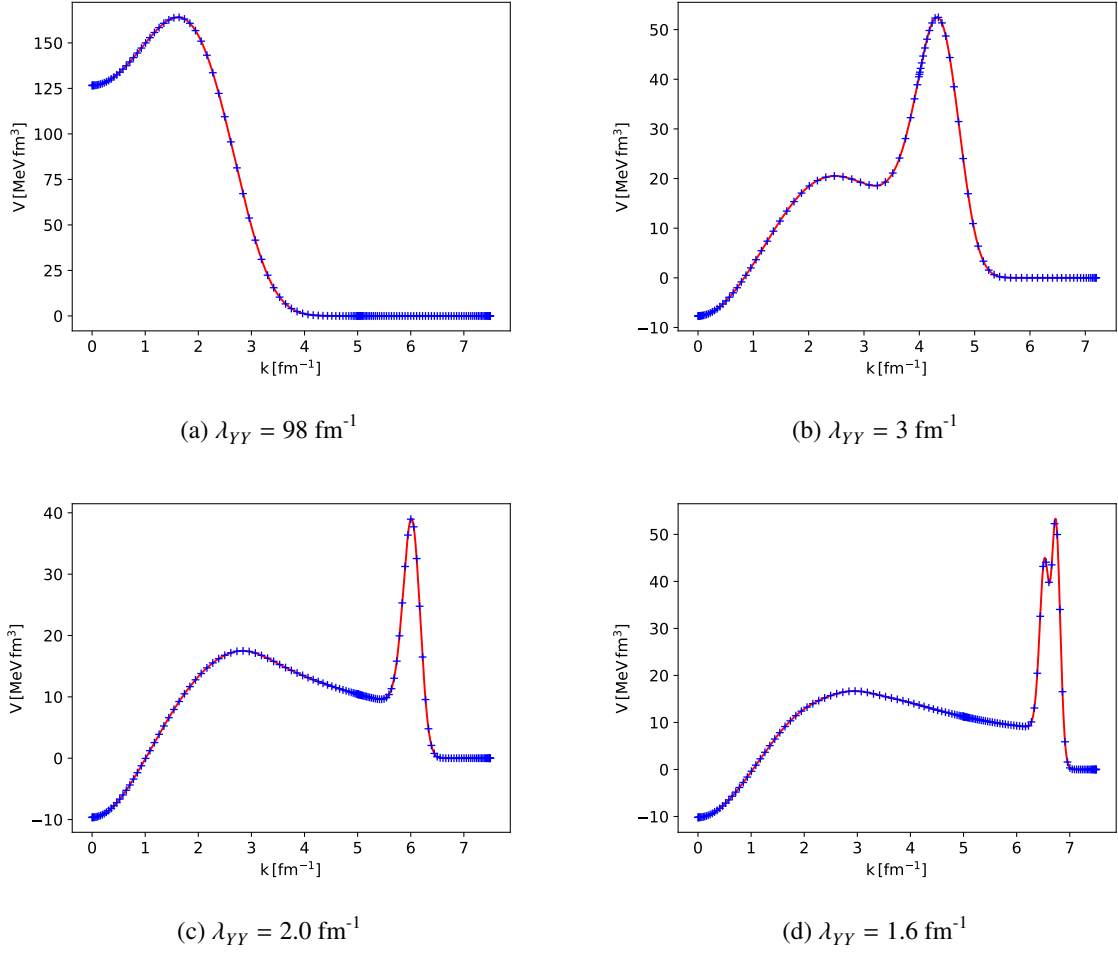&= \sum_{i<j=1}^{A-1} h_{ij}^{S=0} + \sum_{i=1}^{A-1} h_{iY}^{S=-1} + \dots,
\end{aligned}
\tag{3.1}
$$

where $m_N, m(t_Y)$ and $\mu_{NY}$ are nucleon, hyperon and their reduced masses, respectively. For simplicity, we follow the isospin formalism and assign $m_N = 2m_n m_p/(m_n + m_p)$ and $m(t_Y = 1) = (m_{\Sigma^+} + m_{\Sigma^-} + m_{\Sigma^0})/3$. A generalization to a formalism with unequal masses within the isospin multiplet of nucleons and of $\Sigma$'s is straightforward. Here, the total mass of the system, $M(t_Y) = (A-1)m_N + m(t_Y)$, depends explicitly on the hyperon isospin $t_Y$ because an explicit $\Lambda - \Sigma$ conversion is allowed. The term $m(t_Y) - m_\Lambda$ then accounts for the difference in the rest masses of the two hyperons. Also, $p_{ij} = \frac{1}{2}(k_i - k_j)$ and $p_{iY} = \frac{m(t_Y)}{m_N+m(t_Y)}k_i - \frac{m_N}{m_N+m(t_Y)}k_Y$ are relative Jacobi momenta of an NN and YN pairs, respectively, while $V_{ij}^{NN}$ and $V_{iY}^{YN}$ are the corresponding NN and YN potentials. Finally, the ellipsis stands for higher body forces that are omitted.

Since hyperons ($\Lambda, \Sigma$) and nucleons are distinguishable, the hypernuclear basis functions, denoted

as $|\alpha^{*(Y)}\rangle$, can be straightforwardly formed by coupling the hyperon HO states $|Y\rangle$, describing the relative motion of a single hyperon $Y$ with respect to the C.M. of the $(A-1)$N core, to the fully antisymmetrized states of the core $|\alpha_{(A-1)N}\rangle$. These basis states can be symbolically written as

$$
\begin{aligned}
\left|\alpha^{*(Y)}(\mathcal{N}JT)\right\rangle &= |\alpha_{(A-1)N}\rangle \otimes |Y\rangle \\
&= |\mathcal{N}JT, \alpha_{(A-1)N}\, n_Y I_Y t_Y; (J_{A-1}(l_Y s_Y)I_Y)J, (T_{A-1}t_Y)T\rangle \equiv \left|\,\begin{matrix}\bullet\!-\!\bullet\end{matrix}\,\right\rangle.
\end{aligned}
\tag{3.2}
$$

where $\alpha_{(A-1)N}$, following the same notation as in [83], denotes a complete set of all necessary quantum numbers characterizing the fully antisymmetrized states of an $(A-1)$N system: the total HO energy quantum number $\mathcal{N}_{A-1}$, total angular momentum $J_{A-1}$, isospin $T_{A-1}$ and the state indices $\zeta_{A-1}$ (that distinguish different $|\alpha_{(A-1)N}\rangle$ states with the same set of $\mathcal{N}_{A-1}, J_{A-1}$ and $T_{A-1}$). The superscript $(*Y)$ represents the separation of the hyperon $Y$ from the $(A-1)$N core. The relative motion of the hyperon $|Y\rangle$ is described by a similar set of quantum numbers: the HO energy quanta $n_Y$, orbital angular momentum $l_Y$ and spin $s_Y$ which combine together to form the relative angular momentum $I_Y$, and the isospin $t_Y$ as well. Here, the $jj$-coupling scheme is employed since angular momenta are good quantum numbers in nuclear interactions. The last line in Equation (3.2) demonstrates the ordering[1] in which the quantum numbers of the two subclusters are combined to form the total angular momentum and total isospin of the system, $J$ and $T$, respectively, whose values are deduced from the physical state of interest. The total HO quantum number $\mathcal{N}$ of each state $|\alpha^{*(Y)}\rangle$ (also referred to as the model space size) is given by $\mathcal{N} = \mathcal{N}_{A-1} + 2n_Y + l_Y$. Since parity $\pi = (-1)^{\mathcal{N}}$ is conserved in nuclear interactions, for each energy calculation, it is sufficient to consider only those basis states $|\alpha^{*(Y)}\rangle$ with same even $\mathcal{N}$ (for the positive-parity physical state) or odd $\mathcal{N}$ (for the negative-parity state). Note that the state index $\zeta$ that distinguishes different basis states $|\alpha^{*(Y)}\rangle$ with the same $J, T, \mathcal{N}$ is omitted in Eq. (3.2) to simplify the notations. Finally, we show on the right-hand side of Eq. (3.2) a graphical representation of the basis. The small red circle denotes a hyperon spectator while the big black circle represents the system of $A-1$ nucleons.

It should be clear that the most evolved part in constructing the Jacobi basis for a hypernuclear system is to obtain a complete antisymmetrized basis $|\alpha_{(A-1)N}\rangle$ of the $(A-1)$N system. Generally speaking, these states $|\alpha_{(A-1)N}\rangle$ can be constructed in an iterative manner with the starting point is a naturally antisymmetrized basis of two nucleons $|\alpha_{2N}\rangle$,

$$
|\alpha_{2N}\rangle = |n_{12}J_{12}T_{12}; (l_{12}s_{12})J_{12}(t_1t_2)T_{12}\rangle,
\tag{3.3}
$$

where the quantum numbers follow the same notations as for the antisymmetrized states $|\alpha_{(A-1)N}\rangle$ with $l_{12}, s_{12}$ and $T_{12}$ being restricted by the condition $(-1)^{l_{12}+s_{12}+T_{12}} = -1$. A third nucleon with all possibly allowable quantum numbers is coupled to $|\alpha_{2N}\rangle$ to form all possible three-body states $|\alpha_{3N}^{*(1)}\rangle$,

$$
|\alpha_{3N}^{*(1)}\rangle = |N_3J_3T_3, \alpha_{2N}\, n_3I_3t_3; (J_{12}(l_3s_3)I_3)J_3, (T_{12}t_3)T_3\rangle,
\tag{3.4}
$$

which are however only partially antisymmetrized (i.e. are antisymmetrized regarding the permutation of the two nucleons in the subcluster but are not antisymmetrized with respect to the exchanges between one of the nucleons of the two-nucleon subcluster and the spectator one). The

---

[1] The exact orderings are not important, however, they must be consistent for all basis states and the intermediate ones that we consider in the next section.

antisymmetrized states $|\alpha_{3N}\rangle$ can be then obtained with the help of an antisymmetrization operator

$$\chi = \frac{1}{3}(1 + \tau^- + \tau^+),\tag{3.5}$$

where $\tau^-, \tau^+$ are the anticyclic and cyclic permutations operators, respectively, which also satisfies the condition of a projection operator $\chi\chi = \chi$. When diagonalized the antisymmetrizer Eq. (3.5) in the basis Eq. (3.4), all eigenstates corresponding to the eigenvalue 1 will span the complete antisymmetrized three-nucleon subspace. Then, each antisymmetrized state $|\alpha_{3N}\rangle$ can be written as an expansion in the original basis Eq. (3.4)

$$|\alpha_{3N}\rangle = \sum_{\alpha_{3N}^{*(1)}} C_{\alpha_{3N}^{*(1)}}|\alpha_{3N}^{*(1)}\rangle.\tag{3.6}$$

Here, the expansion coefficients $C_{\alpha_{3N}^{*(1)}} = \langle\alpha_{3N}|\alpha_{3N}^{*(1)}\rangle$, obtained from the diagonalization, are referred to as the coefficients of fractional parentage (cfp). Based on the complete set of Eq. (3.6), one then proceeds further to construct a fully antisymmetrized basis for four nucleons and so on. For the details of the antisymmetrization procedure, one can refer to [83, 100, 101], and its numerical realization [102]. For systems with $A \geq 5$, the preparation of the antisymmetrizer matrix elements is a very time-consuming and memory-expensive task that involves the multiplications of extremely huge and usually sparse matrices. In general, the dimensions of these matrices are too large in order to fit into a single supercomputer node. Therefore, distributed memory parallelization (e.g. parallelization based on the Message Passing Interface (MPI) library) is definitely necessary. A good algorithm should be able to distribute all involved matrices over all MPI processes, meanwhile, avoid any global communications among the processes. This can be indeed achieved by employing the so-called Fox's matrix multiplication, the details of which will be discussed in Section 3.3.1. Let us mention that, for the current purpose, we have successfully generated the complete antisymmetrized bases for $A \leq 6$ nuclear systems with all $J, T$ blocks and model space sizes up to $\mathcal{N}_{max} = 12$, and for $A = 7, 8$ systems with $\mathcal{N}_{max} = 10$. We finally stress that although the antisymmetrization is rather challenging, it needs to be done only once for given $A$, $\mathcal{N}$, $J$ and $T$. Additionally, the calculations for each $\mathcal{N}$, $J$ and $T$ block can also be performed independently to reduce the total workload at each run.

With the basis functions defined by Eq. (3.2), the eigenstates of the Hamiltonian Eq. (3.1) with definite parity $\pi$, the total angular momentum $J$ and isospin $T$ can be easily expanded

$$\left|\Psi(\pi JT)\right\rangle = \sum_{\alpha^{*(Y)}} C_{\alpha^{*(Y)}}\left|\alpha^{*(Y)}(\mathcal{N}JT)\right\rangle.\tag{3.7}$$

The expansion coefficients $C_{\alpha^{*(Y)}}$ are obtained when diagonalizing the Hamiltonian Eq. (3.1) in the basis $|\alpha^{*(Y)}\rangle$. They are, in principle, independent of any NCSM parameters (namely the HO-$\omega$ frequency and the total HO energy number $\mathcal{N}$), provided that the model space is infinitely large $\mathcal{N} \to \infty$. Of course, for practical realization, one tries to make $\mathcal{N}$ as large as possible but finite by imposing a truncation on the largest possible value of the model space size $\mathcal{N}$: $\mathcal{N} = \mathcal{N}_{\alpha_{A-1}} + 2n_Y + l_Y \leq \mathcal{N}_{max}$. As a consequence, the dependence of the NCSM results (e.g binding energies, radii) on $\mathcal{N}_{max}$ and HO frequency $\omega$ is unavoidable. To obtain the final converged results (that are independent of any model parameters) one very often has to perform additional extrapolation procedures which we will

explain in detail in Section 4.1.

## 3.2 Evaluation of the Hamiltonian matrix elements

Having our basis states defined in Eq. (3.7), the next crucial step is to evaluate the Hamiltonian matrix elements with respect to this basis in the most efficient way. As it is seen in Eq. (3.1) both, the intrinsic kinetic operators and the two-body potentials, are expressed in terms of the relative momentum of the two particles involved. Our basis set $|\alpha^{*(Y)}\rangle$ is thereby not suitable for calculating the Hamiltonian matrix elements,

$$
\begin{aligned}
\langle \Psi(\pi JT) | H | \Psi(\pi JT) \rangle = &\sum_{\alpha^{*(Y)}, \alpha'^{*(Y)}} C_{\alpha^{*(Y)}} C_{\alpha'^{*(Y)}} \langle \alpha^{*(Y)} | H^{S=0} | \alpha'^{*(Y)} \rangle \\
&+ \sum_{\alpha^{*(Y)}, \alpha'^{*(Y)}} C_{\alpha^{*(Y)}} C_{\alpha'^{*(Y)}} \langle \alpha^{*(Y)} | H^{S=-1} | \alpha'^{*(Y)} \rangle,
\end{aligned}
\tag{3.8}
$$

as they do not depend explicitly on the relative coordinates of the involved NN or YN pairs. In order to facilitate the evaluation of Eq. (3.8), one will need to expand the states $|\alpha^{*(Y)}\rangle$ in two additional bases of intermediate states $|(\alpha^{*(2)})^{*(Y)}\rangle$ and $|\alpha^{*(YN)}\rangle$ that explicitly single out an NN or YN pair, respectively. Here, the superscripts represent subsystems that are singled out. Clearly, the former states $|(\alpha^{*(2)})^{*(Y)}\rangle$ are needed for evaluating the first part in Eq. (3.8) involving the non-strangeness Hamiltonian $H^{S=0}$, while the latter ones are required for the evaluation of the second part that involves the singly-strange Hamiltonian $H^{S=-1}$.

### 3.2.1 Separation of an NN pair

We first consider the construction of the intermediate states $|(\alpha^{*(2)})^{*(Y)}\rangle$. As the notation suggests, these states can be formed by directly coupling the hyperon states $|Y\rangle$, depending on Jacobi coordinates of a hyperon relative to the C.M. (A-1)N, to the states of an $(A-1)$N system that consist of antisymmetrized subclusters of $(A-3)$N and 2N

$$
\begin{aligned}
\left|(\alpha^{*(2)})^{*(Y)}\right\rangle &= |\alpha^{*(2)}_{(A-1)N}\rangle \otimes |Y\rangle \\
&= \left|\tilde{N}JT, \alpha^{*(2)}_{(A-1)N} \tilde{n}_Y \tilde{l}_Y \tilde{t}_Y; (J^{*(2)}_{A-1}(\tilde{l}_Y s_Y)\tilde{I}_Y)J, (T^{*(2)}_{A-1}\tilde{t}_Y)T\right\rangle \\
&\equiv \left|\; \raisebox{-0.5ex}{\includegraphics[height=1em]{diagram}} \;\right\rangle .
\end{aligned}
\tag{3.9}
$$

Here, in the second line, $\alpha^{*(2)}_{(A-1)N}$ stands for the total HO energy quantum number $\mathcal{N}_{\alpha^{*(2)}_{(A-1)}}$, the total angular momentum $J^{*(2)}_{A-1}$, isospin $T^{*(2)}_{A-1}$ and state index $\zeta^{*(2)}_{A-1}$, as introduced in [83]. Note that a finite truncation is also applied to the total HO energy quantum number $\tilde{N}$ in Eq. (3.9), i.e. $\tilde{N} \leq \mathcal{N}_{max}$. It is obvious that the subspace spanned by the basis set $|\alpha^{*(Y)}\rangle$ is less extended than that spanned by the intermediate set $|(\alpha^{*(2)})^{*(Y)}\rangle$. In other word, a set of all possible states $|(\alpha^{*(2)})^{*(Y)}(\tilde{N}JT, \tilde{N} \leq \mathcal{N}_{max})\rangle$ is complete with regard to the set of basis functions $|\alpha^{*(Y)}(\mathcal{N}JT, \mathcal{N} \leq \mathcal{N}_{max})\rangle$. This completeness

allows an exact expansion,

$$\left|\alpha^{*(Y)}\right\rangle = \sum_{(\alpha^{*(2)})^{*(Y)}} \left\langle (\alpha^{*(2)})^{*(Y)} \middle| \alpha^{*(Y)} \right\rangle \left|(\alpha^{*(2)})^{*(Y)}\right\rangle, \tag{3.10}$$

where the expansion coefficients

$$\left\langle (\alpha^{*(2)})^{*(Y)} \middle| \alpha^{*(Y)} \right\rangle = \langle \; \rangle = \delta_{\mathcal{N},\tilde{\mathcal{N}}} \, \delta_{Y\tilde{Y}} \delta_{core} \; {}_{(A-1)N}\langle \; \rangle, \tag{3.11}$$

are essentially given by the transition coefficients of an (A-1)N system, ${}_{(A-1)N}\langle \; \rangle$, for which an explicit expression has been derived in [83, 102]. The Kronecker symbols $\delta_{Y\tilde{Y}}$ and $\delta_{core}$ in Eq. (3.11) are to ensure the conservation of the quantum numbers of the hyperon and $(A-1)$N system, respectively,

$$\delta_{Y\tilde{Y}} = \delta_{n_Y\tilde{n}_Y}\delta_{l_Y\tilde{l}_Y}\delta_{I_Y\tilde{I}_Y}\delta_{t_Y\tilde{t}_Y}; \qquad \delta_{core} = \delta_{\mathcal{N}_{A-1}\mathcal{N}_{A-1}^{*(2)}}\delta_{J_{A-1}J_{A-1}^{*(2)}}\delta_{T_{A-1}T_{A-1}^{*(2)}}. \tag{3.12}$$

An algorithm to calculate the nuclear transition coefficients in a partially-distributed manner[2] has been well explained in [83, 102]. Here, we have further improved the algorithm with the help of Fox's algorithm for matrix multiplications (Algorithm 1). This allows one to completely distribute all the involved matrices (i.e. distribute both row and column indices of all matrices) and hence significantly reduce the memory usage. As a result, we are able to perform calculations with much larger model space sizes. So far, we have already generated the transition coefficients for $A \leq 6$ nuclear systems with all model spaces up to $\mathcal{N}_{max} = 12$, and $A = 7, 8$ with model space sizes up to $\mathcal{N}_{max} = 10$ and all possible $J$ and $T$ blocks.

Let us further remark that the completeness of $|(\alpha^{*(2)})^{*(Y)}\rangle$ with respect to $|\alpha^{*(Y)}\rangle$ can also be expressed in terms of the following orthogonality condition of the expansion coefficients,

$$\sum_{(\alpha^{*(2)})^{*(Y)}} \left\langle \alpha^{*(Y)} \middle| (\alpha^{*(2)})^{*(Y)} \right\rangle \left\langle (\alpha^{*(2)})^{*(Y)} \middle| \alpha'^{*(Y)} \right\rangle = \delta_{\alpha^{*(Y)}\alpha'^{*(Y)}}. \tag{3.13}$$

In practice, we have employed the above relation as a primary check for the correctness of our implementations. Indeed, the orthogonality condition Eq. (3.13) is fulfilled with an accuracy of $10^{-4}$. Now, exploiting the completeness relation and then taking into account Eq. (3.11), the matrix element of the non-strangeness Hamiltonian $H^{S=0}$ in Eq. (3.8) becomes

$$\langle \alpha^{*(Y)}|H^{S=0}|\alpha'^{*(Y)}\rangle = \langle \; \rangle\langle \;|H^{S=0}|\; \rangle\langle \; \rangle$$
$$= \delta_{\mathcal{N}\tilde{\mathcal{N}}} \, \delta_{YY'}\delta_{core}\delta_{core'}\langle \; \rangle \, \langle \;| H^{S=0} |\; \rangle_{(A-1)N} \, \langle \; \rangle. \tag{3.14}$$

The summations over the two intermediate states $|\!\!-\!\!\bullet\rangle$ and $\langle\bullet\!\!-\!\!|$ are implied in Eq. (3.14). The remaining unknown term, $\langle \;| H^{S=0} |\; \rangle_{(A-1)N} \equiv \langle \alpha_{(A-1)N}^{*(2)}| H^{S=0} |\alpha'^{*(2)}_{(A-1)N}\rangle$, is simply the matrix elements of the many-nucleon Hamintionian $H^{s=0}$ in the basis of (A-1)N, which can be easily reduced to the matrix elements of the free space two-nucleon Hamiltonian $h_{NN}^{S=0}$ in the two-particle basis $|\alpha_{2N}\rangle$, multiplied with some combinatorial factor. In the isospin formalism, it can be quickly

---

[2] Only row or column indices of the matrices are distributed over mpi-processes, the remaining index is kept global

shown that the latter is simply given by the binomial coefficient of $\binom{A-1}{2} = (A-2)(A-1)/2$. Hence,

$$\langle \alpha^{*(2)}_{(A-1)N} | H^{S=0} | \alpha'^{*(2)}_{(A-1)N} \rangle = \frac{(A-2)(A-1)}{2} \delta_{core_{(A-3)}} \langle \alpha_{2N} | h_{NN}^{S=0} | \alpha'_{2N} \rangle. \tag{3.15}$$

We evaluate the two-nucleon matrix elements in Eq. (3.15) using the full two-body Hamiltonian $h^{NN}$ for those $|\alpha_{2N}\rangle$ and $|\alpha'_{2N}\rangle$ states with the total angular momentum $J_{NN} \leq 6$. For channels with higher $J_{NN}$ only the two-nucleon kinetic operator contributes.

## 3.2.2 Separation of a YN pair

Similarly, in order to construct the intermediate states $|\alpha^{*(YN)}\rangle$, needed for evaluating the matrix elements of the singly strange Hamiltonian $H^{S=-1}$, one combines the states describing an YN pair, $|YN\rangle$, with the antisymmetrized basis of an $(A-2)$N system, $|\alpha_{(A-2)N}\rangle$

$$\begin{aligned}
|\alpha^{*(YN)}\rangle &= |\alpha_{YN}\rangle \otimes |\alpha_{(A-2)N}\rangle \\
&= |\mathcal{N}JT, \alpha_{YN} n_\lambda \lambda \alpha_{(A-2)N}; ((l_{YN}(s_Y s_N)S_{YN})J_{YN}(\lambda J_{A-2})I_{A-2})J, \\
&\qquad ((t_Y t_N)T_{YN}T_{A-2})T\rangle \\
&\equiv |\ \vcenter{\hbox{⊶●}}\ \rangle.
\end{aligned} \tag{3.16}$$

Here, $\alpha_{YN}$ represents a complete set of quantum number characterizing a YN subcluster: the total HO energy quantum numbers $\mathcal{N}_{YN}$, total angular momentum $J_{YN}$, isospin $J_{YN}$ and state index $\zeta_{YN}$. Note that, in contrary to an NN subcluster, there is no antisymmetry requirement for the $|\alpha_{YN}\rangle$ states. Likewise, $\alpha_{(A-2)N}$ stands for a set of quantum numbers describing an antisymmetrized state of the $(A-2)$-nucleon subcluster: the total HO quanta number $\mathcal{N}_{A-2}$, total angular momentum $J_{A-2}$, isospin $T_{A-2}$ and state index $\zeta_{A-2}$. The relative motion of the $(A-2)$-nucleon subcluster with respect to the C.M. of the separated out YN pair is described by the HO energy number $n_\lambda$ together with the orbital angular momentum $\lambda$. The completeness of the set of all the intermediate states $|\alpha^{*(YN)}\rangle$ with regard to the basis set $|\alpha^{*(Y)}\rangle$ also allows for an exact expansion as in Eq. (3.10)

$$\left|\alpha^{*(Y)}\right\rangle = \sum_{\alpha^{*(YN)}} \langle \alpha^{*(YN)} | \alpha^{*(Y)} \rangle | \alpha^{(*YN)} \rangle. \tag{3.17}$$

For calculating the overlap $\langle \alpha^{*(Y)} | \alpha^{*(YN)} \rangle$, we need to introduce another set of auxiliary states $|(\alpha^{*(1)})^{*(Y)}\rangle$ in which the HO hyperon states $|Y\rangle$ are coupled with the nuclear states consisting of an antisymmetrized (A-2)-nucleon subcluster and a single nucleon

$$\begin{aligned}
\left|(\alpha^{*(1)})^{*(Y)}\right\rangle &= |\alpha_{A-1}^{*(1)}\rangle \otimes |Y\rangle \\
&= |\tilde{\mathcal{N}}JT, \alpha_{(A-1)N}^{*(1)} n_Y I_Y \tilde{t}_Y; (J_{A-1}^{*(1)}(l_Y s_Y)I_Y)J, (T_{A-1}^{*(1)} \tilde{t}_Y)T\rangle \\
&\equiv |\ \vcenter{\hbox{●⊷}}\ \rangle,
\end{aligned} \tag{3.18}$$

with

$$|\alpha^{*(1)}_{(A-1)N}\rangle = |\mathcal{N}^{*(1)}_{(A-1)} J^{*(1)}_{A-1} T^{*(1)}_{A-1}, \tilde{\alpha}_{(A-2)N} \, n_N I_N t_N;$$

$$(\tilde{J}_{A-2}(l_N s_N) I_N) J^{*(1)}_{A-1}, (\tilde{T}_{A-2} t_N) T^{*(1)}_{A-1}\rangle \tag{3.19}$$

$$\equiv |\mathbf{O}\!\!-\!\!\rangle.$$

Since the auxiliary states Eq. (3.18) are less constrained by the antisymmetry requirement than both $|\alpha^{(Y)}\rangle$ and $|\alpha^{*(YN)}\rangle$ states, the auxiliary basis is complete with respect to the two bases, $|\alpha^{(Y)}\rangle$ and $|\alpha^{*(YN)}\rangle$. Hence,

$$\langle\alpha^{*(Y)}| = \sum_{\left(\alpha^{*(1)}\right)^{*(Y)}} \langle\alpha^{*(Y)}|(\alpha^{*(1)})^{*(Y)}\rangle\langle(\alpha^{*(1)})^{*(Y)}|$$

$$|\alpha^{*(YN)}\rangle = \sum_{\left(\alpha^{*(1)}\right)^{*(Y)}} \langle(\alpha^{*(1)})^{*(Y)}|\alpha^{*(YN)}\rangle|(\alpha^{*(1)})^{*(Y)}\rangle. \tag{3.20}$$

With the completeness relations in Eq. (3.20) the transition coefficient $\langle\alpha^{*(Y)}|\alpha^{*(YN)}\rangle$ can be now calculated via a two-step procedure as follows

$$\langle\alpha^{*(Y)}|\alpha^{*(YN)}\rangle = \langle\alpha^{*(Y)}|(\alpha^{*(1)})^{*(Y)}\rangle\langle(\alpha^{*(1)})^{*(Y)}|\alpha^{*(YN)}\rangle$$

$$\equiv \langle\mathbf{O}\!\!-\!\!|\mathbf{O}_{\!\top}\!\!\cdot\rangle\langle\mathbf{O}_{\!\top}\!\!\cdot|\!\!\cdot\!\!-\!\!\mathbf{O}\rangle \tag{3.21}$$

$$= \delta_{YY}\langle\mathbf{O}|\mathbf{O}\!\!-\!\!\rangle_{\mathrm{cfp}(A-1)}\langle\mathbf{O}_{\!\top}\!\!\cdot|\!\!\cdot\!\!-\!\!\mathbf{O}\rangle.$$

where an explicit summation over $|(\alpha^{*(1)})^{*(Y)}\rangle$ is required. One quickly sees that the first overlap $\langle\alpha^{*(Y)}|(\alpha^{*(1)})^{*(Y)}\rangle$ is essentially given by the cfp $\langle\mathbf{O}|\mathbf{O}\!\!-\!\!\rangle$, of an $(A-1)$N system, which basically determine the antisymmetrized basis of $(A-2)$ nucleons in terms of the states in Eq. (3.19). Hence, in the preparation step only the second transition $\langle\mathbf{O}_{\!\top}\!\!\cdot|\!\!\cdot\!\!-\!\!\mathbf{O}\rangle$ in Eq. (3.21) needs to be taken care of. This transition can be interpreted simply as a transformation between different Jacobi coordinates. We can therefore make use of the general Jacobi-coordinate transformation formula in [83]. Since this formula is widely used here, we also provide the explicit expression in Appendix C (Eq. (C.6)). In order to utilize the formula Eq. (C.6), we first need to specify the directions of the relative motions of particles (subclusters) in the two states $|\alpha^{*(YN)}\rangle$ and $|(\alpha^{*(1)})^{*(Y)}\rangle$. These directions are depicted in Figs. 3.1 and 3.2.

$$\mathcal{N}_{YN} J_{YN} T_{YN} \overset{2}{\underset{1}{\vert}}\overset{\lambda, n_\lambda}{\longrightarrow}\overset{3}{\bigcirc} \quad \alpha_{A-2}, \mathcal{N}_{A-2} J_{A-2} T_{A-2} \zeta_{A-2}$$
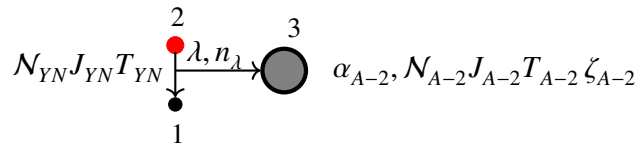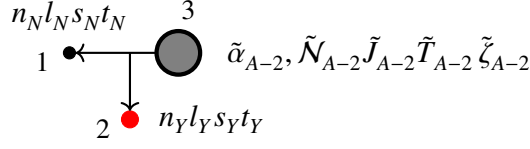
Figure 3.1: $|\alpha^{*(YN)}\rangle$ state with directions of momenta

Comparing the definitions of our two states $|\alpha^{*(YN)}\rangle$ and $|(\alpha^{*(1)})^{*(Y)}\rangle$ with the two states defined

Figure 3.2: $\left|(\alpha^{*(1)})^{*(Y)}\right\rangle$ state with directions of momenta

in Appendix C.1, $|\alpha\rangle_{(12)3}$ and $|\alpha\rangle_{(13)2}$, respectively, one notices that the directions of the relative momenta are the same, however, the ordering of the coupling of the angular momenta and isospins in $\left|(\alpha^{*(1)})^{*(Y)}\right\rangle$ and $|\alpha\rangle_{(13)2}$ are different. The recoupling from $\left|(\tilde{J}_{A-2}(l_N s_N)I_N)J_{A-1}^{*(1)}\right\rangle$ to $\left|(l_N(s_N \tilde{J}_{A-2})S_{A-1})J_{A-1}^{*(1)}\right\rangle$ can be done with the help of $6j$-symbols [103]

$$
\left|(\tilde{J}_{A-2}(l_N s_N)I_N)J_{A-1}^{*(1)}\right\rangle = (-1)^{I_N+2\tilde{J}_{A-2}+l_N+s_N} \sum_{S_{A-1}=\tilde{J}_{A-2}+s_N} \hat{I}_N \hat{S}_{A-1} \begin{Bmatrix} \tilde{J}_{A-2} & s_N & S_{A-1} \\ l_N & J_{A-1}^{*(1)} & I_N \end{Bmatrix}
$$
$$
\times \left|(l_N(s_N \tilde{J}_{A-2})S_{A-1})J_{A-1}^{*(1)}\right\rangle,
$$
(3.22)

where the abbreviation $\hat{I}_N = \sqrt{2I_N + 1}$ is introduced. Changing the coupling $|(\tilde{T}_{A-2} t_N)T_{A-1}^{*(1)}$ to $(t_N \tilde{T}_{A-2})T_{A-1}^{*(1)}$ introduces an additional phase factor,

$$
(\tilde{T}_{A-2} t_N)T_{A-1}^{*(1)}\rangle = (-1)^{\tilde{T}_{A-2}+t_N-T_{A-1}^{*(1)}}\left|(t_N \tilde{T}_{A-2})T_{A-1}^{*(1)}\right\rangle.
$$
(3.23)

Now taking into account Eqs. (3.22) and (3.23) and then making use of Eq. (C.6) one obtains

$$
\langle(\alpha^{*(1)})^{*(Y)}|\alpha^{*(YN)}\rangle = \delta_{\mathcal{N}\tilde{\mathcal{N}}} \, \delta_{t_Y \tilde{t}_Y} \, \delta_{\tilde{T}_{A-2}T_{A-2}} \delta_{\tilde{J}_{A-2}J_{A-2}} \delta_{\tilde{\mathcal{N}}_{A-2}\mathcal{N}_{A-2}} \delta_{\tilde{\zeta}_{A-2}\zeta_{A-2}}
$$

$$
\times \hat{I}_N \hat{I}_Y \hat{J}_{YN} \hat{S}_{YN} \hat{I}_{A-2} \hat{J}_{A-1}^{*(1)} \hat{T}_{A-1}^{*(1)} \hat{T}_{YN}
$$

$$
\times (-1)^{3J_{A-2}+2T_{A-2}+T_{YN}+S_{YN}+\lambda+t_Y+l_Y+t_N+l_N+I_N+1}
$$

$$
\times \sum_{S_{A-1}=\tilde{J}_{A-2}+s_N} (-1)^{S_{A-1}}\hat{S}_{A-1}^2 \begin{Bmatrix} J_{A-2} & s_N & S_{A-1} \\ l_N & J_{A-1}^{*(1)} & I_N \end{Bmatrix}
$$

$$
\times \sum_{L,S} \hat{L}^2\hat{S}^2 \begin{Bmatrix} l_N & S_{A-1} & J_{A-1}^{*(1)} \\ l_Y & s_Y & I_Y \\ L & S & J \end{Bmatrix} \begin{Bmatrix} l_{YN} & S_{YN} & J_{YN} \\ \lambda & J_{A-2} & I_{A-2} \\ L & S & J \end{Bmatrix}
$$
(3.24)

$$
\times \langle n_N \, l_N \, n_Y \, l_Y : L \,|\, n_{YN} \, l_{YN} \, n_\lambda \, \lambda : L\rangle_d
$$

$$
\times \begin{Bmatrix} s_Y & s_N & S_{YN} \\ J_{A-2} & S & S_{A-1} \end{Bmatrix} \begin{Bmatrix} t_Y & t_N & T_{YN} \\ T_{A-2} & T & T_{A-1}^{*(1)} \end{Bmatrix},
$$

where $\langle n_N \, l_N \, n_Y \, l_Y : L \,|\, n_{YN} \, l_{YN} \, n_\lambda \, \lambda : L\rangle_d$ is the HO bracket that was initially introduced as Talmi-Brody-Moshinsky orthogonal transformation [104]. We follow here the same conventions as

employed in [105] and the mass ratio is given by

$$d = \frac{(A-2)\,m(t_Y)}{(A-1)\,m_N + m(t_Y)}. \tag{3.25}$$

In the second step, we need to perform a summation over the auxiliary states $|\!-\!\bullet\rangle$ in Eq. (3.21) which essentially is the multiplication of two very large matrices. The practical realization of this step will be discussed in the next section. We finally note that the expansion coefficients $\langle \alpha^{*(Y)} | \alpha^{*(YN)} \rangle$ also satisfy the following orthogonality condition,

$$\sum_{\alpha^{*(YN)}} \langle \alpha^{*(Y)} | \alpha^{*(YN)} \rangle \langle \alpha^{*(YN)} | \alpha'^{*(Y)} \rangle = \delta_{\alpha^{*(Y)}\,\alpha'^{*(Y)}}, \tag{3.26}$$

which again serves as an important criterion for checking the correctness of our implementation. With the help of the expansion Eq. (3.17), the matrix element of the singly strange Hamiltonian $H^{S=-1}$ becomes

$$\langle \alpha^{*(Y)} | H^{S=-1} | \alpha'^{*(Y)} \rangle = \langle \bullet\!\!-\!\!\bullet |\!-\!\bullet \rangle \langle \bullet\!-\!| H^{S=-1} |\!-\!\bullet \rangle \langle \bullet\!-\!| \bullet\!-\!\bullet \rangle, \tag{3.27}$$

where the summations over the two intermediate states $|\!-\!\bullet\rangle$ and $\langle \bullet\!-\!|$ are also imposed. The remaining term $\langle \bullet\!-\!| H^{S=-1} |\!-\!\bullet\rangle \equiv \langle \alpha^{*(YN)} | H^{S=-1} | \alpha'^{*(YN)} \rangle$ in Eq. (3.27) can be easily related to the matrix elements of the two-body Hamiltonian $h_{YN}^{S=-1}$ (see Eq. (3.1)) in the basis $|\alpha_{YN}\rangle$

$$\langle \alpha^{*(YN)} | H^{S=-1} | \alpha'^{*(YN)} \rangle = \delta_{core_{A-2}} (A-1) \langle \alpha_{YN} | h_{YN}^{S=-1} | \alpha'_{YN} \rangle, \tag{3.28}$$

with the combinatorial factor of $(A-1)$ simply given by the total number of possible $YN$ pairs in the system. Like in the case of the non-strange Hamiltonian $H^{S=0}$, the YN potential matrix elements in the basis $|\alpha_{YN}\rangle$ are also restricted to partial waves $J_{YN} \leq 6$. For higher partial-wave channels, only the YN kinetic operator contributes to Eq. (3.28).

It should be now clear from Eqs. (3.14) and (3.27) that the evaluations of the matrix elements $\langle \alpha^{*(Y)} | H^{S=0} | \alpha'^{*(Y)} \rangle$ and $\langle \alpha^{*(Y)} | H^{S=-1} | \alpha'^{*(Y)} \rangle$ are essentially the multiplications of very large matrices. Because we solve the eigenvalue problem using Lanczos iterations, we will need to perform those matrix multiplications again and again. Therefore, an efficient method to evaluate the product matrices will be extremely important. We come back to this issue in the following section.

Before closing this section, let us also provide here the transition coefficients between the basis function $|\alpha^{*(Y)}\rangle$ and the state $|(\alpha^{*(Y)})^{*(1)}\rangle$ in which a nucleon is coupled to a subsystem consisting of an $(A-2)N$ antisymmetrized subcluster and a hyperon

$$\begin{aligned}
\left| (\alpha^{*(Y)})^{*(1)} \right\rangle &= \left| \mathcal{N}' JT \alpha_{A-1}^{*(Y)} \, n'_N I'_N t_N; (J'_{A-1}(l'_N s_N)I'_N)J, (T'_{A-1}t_N)T \right\rangle \\
&= \left| \mathcal{N}' JT \, \alpha'_{A-2} \, n'_Y I'_Y \, t'_Y \, n'_N I'_N t_N; \right. \\
&\qquad \left. ((J'_{A-2}(l'_Y, s_Y)I'_Y)J'_{A-1}(l'_N s_N)I'_N)J, ((T'_{A-2}t'_Y)T'_{A-1}t_N)T \right\rangle \\
&\equiv \left| \bullet\!\!\top\!\!\bullet \right\rangle.
\end{aligned} \tag{3.29}$$

The coefficients $\langle \alpha^{*(Y)} | (\alpha^{*(Y)})^{*(1)} \rangle$ will be useful for calculating the proton (neutron) momentum distributions in hypernuclei. Similar to Eq. (3.21), the final expression for $\langle \alpha^{*(Y)} | (\alpha^{*(Y)})^{*(1)} \rangle$ can be

derived exploiting the completeness of the intermediate states $|(\alpha^{*(1)})^{*(Y)}\rangle$

$$\langle\alpha^{*(Y)}|(\alpha^{*(Y)})^{*(1)}\rangle = \langle \bullet\!\!-\!\!\bigcirc|\bigcirc_{\!\!\top}\!\bullet\rangle = \langle \bullet\!\!-\!\!\bigcirc|\bigcirc_{\!\!\top}\!\bullet\rangle\langle\bigcirc_{\!\!\top}|\bigcirc_{\!\!\top}\!\bullet\rangle$$

$$= \delta_{YY'}\langle\bigcirc|\bigcirc\!\!-\!\!\rightarrow\rangle_{\mathrm{cfp}(A-1)}\langle\bigcirc_{\!\!\top}|\bigcirc_{\!\!\top}\!\bullet\rangle. \tag{3.30}$$

The unknown overlap $\langle\bigcirc_{\!\!\top}|\bigcirc_{\!\!\top}\rangle$ in the last line of Eq. (3.30) can be considered as the Jacobi-coordinate transformation similar to Eq. (3.24). We therefore skip the detailed deviation but provide the final expression here

$$\langle\underset{3}{\overset{\overset{1\ \ 2}{\bigcirc_{\!\!\top}}}{}}\,|\,\underset{3}{\overset{\overset{1\ \ 2}{\bigcirc_{\!\!\top}}\bullet}{}}\,\rangle = \delta_{\mathcal{N}\mathcal{N}'}\,\delta_{t_Y t'_Y}\,\delta_{\tilde{\mathcal{N}}_{A-2},\mathcal{N}'_{A-2}}\,\delta_{\tilde{J}_{A-2}J'_{A-2}}\,\delta_{\tilde{T}_{A-2}T'_{A-2}}\,\delta_{\tilde{\zeta}_{A-2}\zeta'_{A-2}}$$

$$\times (-1)^{2\tilde{J}_{A-2}+l_N+I_N+l'_Y+I'_Y+t_Y+t_N+T^{*(1)}_{A-1}+T'_{A-1}+s_N+s_Y}$$

$$\times \hat{I}_N\hat{I}'_Y\,\hat{T}^{*(1)}_{A-1}\,\hat{T}'_{A-1}\,\hat{J}^{*(1)}_{A-1}\,\hat{J}'_{A-1}\,\hat{I}_Y\hat{I}'_N$$

$$\times \sum_{\substack{S_{A-1}=(s_N\tilde{J}_{A-2})\\ S'_{A-1}=(s_Y\tilde{J}_{A-2})}} (-1)^{2S_{A-1}+2S'_{A-1}}\,\hat{S}^2_{A-1}\,\hat{S}'^2_{A-1}$$

$$\times \begin{Bmatrix} l_N & s_N & I_N \\ \tilde{J}_{A-2} & J^{*(1)}_{A-1} & S_{A-1} \end{Bmatrix} \begin{Bmatrix} l'_Y & s_Y & I'_Y \\ \tilde{J}_{A-2} & J'_{A-1} & S'_{A-1} \end{Bmatrix} \tag{3.31}$$

$$\times \sum_{L,S} \hat{L}^2\hat{S}^2 \begin{Bmatrix} l_N & S_{A-1} & J^{*(1)}_{A-1} \\ l_Y & s_Y & I_Y \\ L & S & J \end{Bmatrix} \begin{Bmatrix} l'_Y & S'_{A-1} & J'_{A-1} \\ l'_N & s_N & I'_N \\ L & S & J \end{Bmatrix}$$

$$\times \langle n_N\,l_N\,n_Y\,l_Y : L\,|\,n'_Y\,l'_Y\,n'_N\,l'_N : L\rangle_d$$

$$\times \begin{Bmatrix} s_Y & \tilde{J}_{A-2} & S'_{A-1} \\ s_N & S & S_{A-1} \end{Bmatrix} \begin{Bmatrix} t_Y & \tilde{T}_{A-2} & T'_{A-1} \\ t_N & T & T^{*(1)}_{A-1} \end{Bmatrix},$$

with the mass ratio given by

$$d = \frac{m(t_Y)}{(A-2)((A-1)m_N + m(t_Y))}. \tag{3.32}$$

## 3.3  Numerical realization

As we have discussed in previous section, calculating the transition coefficients and the Hamiltonian matrix elements involve multiplications of huge (and sparse) matrices. The memory required to store each of the involved matrices generally exceeds the storage capacity of a single supercomputer node. Therefore, parallelization on distributed memory is necessary. A highly efficient parallelization algorithm that enables a complete distribution of the involved matrices without a need of global communications is crucially important in particular for the problems where the memory constraint is

the biggest obstacle. In this section, we shall demonstrate that this, indeed, can be efficiently achieved by exploiting the versatile Fox's algorithm and the standard MPI (Message Passing Interface) library.

The MPI library provides various possibilities to group different processes into the so-called MPI communicators. Within a communicator, each process can be uniquely labelled by its rank (id). It is important that the communications (exchange data) among processes belonging to the same communicator is independent of any operations in other communicators. This allows for the most practical way of parallel transferring data, and therefore, significantly reduces the communication time. Now, let us assume that there are total $np$ processes available. For distributing two-dimensional matrices, it is convenient to arrange these $np$ processes in a two-dimensional Cartesian grid. Thus, each process can be identified with two Cartesian coordinates, namely *rowid* and *colid*. The Fox's algorithm specifically requires that the numbers of processes in each dimension, $np_{row}$ and $np_{col}$, are equal, meaning that $np = np_{row} \times np_{col} = np_{row}^2$. Furthermore, all processes with the same *colid* (*rowid*) coordinate can be grouped in a so-called *commrow* (*commcol*) local communicator. Fig. 3.3 shows the example of a $(2 \times 2)$ Cartesian process grid together with the defined local communicators.
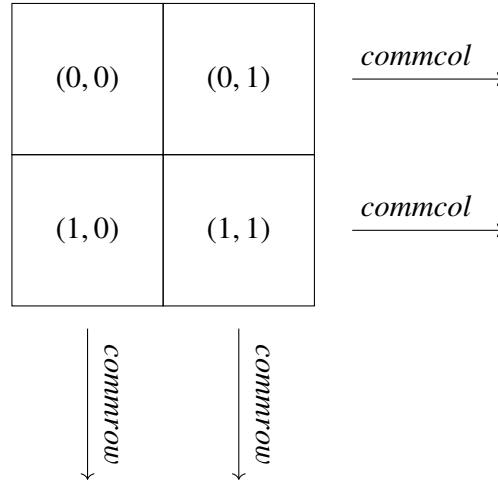


Figure 3.3: 2-dimensional cartesian grid for $2 \times 2$ processes.

### 3.3.1 Fox's algorithm for matrix multiplications

Let us now perform the following matrix multiplication

$$C_{mn} = A_{mk} \times B_{kn}, \tag{3.33}$$

where $A_{mk}$ and $B_{kn}$ are huge matrices calculated on the fly or read in from the input files. We assume that all matrices are distributed on the above defined Cartesian process grid so each process only needs to store its local input matrices $A_{rowcol}^{loc}$ and $B_{rowcol}^{loc}$ and the resulting matrix $C_{rowcol}^{loc}$. The subscript *rowcol* indicates that the first dimension of the matrix is distributed over $np_{row}$ processes (in *commrow* communicators), and the second dimension is distributed over $np_{col}$ processes (in *commcol* communicators). Of course, the other distribution, namely *colrow* (the first index is over $np_{col}$ while the second one is over $np_{row}$), is also possible. We stress that it is not important how the

two matrices $A_{mk}$ and $B_{kn}$ are distributed on the process grid (element-wise or block-wise), but it is crucial that both local matrices are either *rowcol* or *colrow*-distributed. The main idea of Fox's algorithm [106] is to efficiently calculate the product matrix $C_{rowcol}^{loc}$ locally on each MPI process without any global communications among all processes or the necessity to store the entire $C_{mn}, A_{mk}$ or $B_{kn}$ matrices on each process.

Ideally, all processes can independently perform the multiplication in Eq. (3.33) using their local matrices $A_{rowcol}^{loc}$ and $B_{rowcol}^{loc}$ which yields also a local product matrix $C^{loc}$,

$$C^{loc} = A_{rowcol}^{loc} \times B_{rowcol}^{loc}. \tag{3.34}$$

Apparently, $C^{loc}$ is not yet the final product matrix $C_{rowcol}^{loc}$ since some data is still missing on each MPI process. In order to be able to compute $C_{rowcol}^{loc}$, each process needs the information about $A_{rowcol}^{loc}$ and $B_{rowcol}^{loc}$ from all other processes on the Cartesian grid. The locally missing data can be recovered step by step using only local communications, for example by broadcasting $A_{rowcol}^{loc}$ among the processes in the same local *commcol* communicator while shifting $B_{rowcol}^{loc}$ to the neighbor process in the same local *commrow* communicator. Furthermore, in order for all processes to recover all of its missing pieces of data, this procedure must be iterated $np_{row} = \sqrt{np}$ times. The just described algorithm can be summarized in the following pseudo code with the local inputs $A_{rowcol}^{loc}$ and $B_{rowcol}^{loc}$ and the local output $C_{rowcol}^{loc}$. For further explanations of MPI subroutines one can refer to [106].

---

**Algorithm 1** Fox's algorithm for matrix multiplication

---

1: **procedure** FOXMULTIPLICATION($A_{rowcol}^{loc}, B_{rowcol}^{loc}, C_{rowcol}^{loc}$)

2:      $A_{rowcol}^{temp} \leftarrow A_{rowcol}^{loc}; \ C_{rowcol}^{loc} \leftarrow 0$

3:      $source \leftarrow \textbf{mod}(rowid + 1, npe_{row})$

4:      $dest \leftarrow \textbf{mod}(rowid, npe_{row})$

5:      **for** $iter = 0, npe_{row} - 1$ **do**

6:          $root \leftarrow \textbf{mod}(rowid + iter, npe_{row})$

7:          **if** $root = colid$ **then**

8:              **MPI_Bcast**($A_{rowcol}^{loc}, root, commcol$)

9:              $C_{rowcol}^{loc} \leftarrow C_{rowcol}^{loc} + A_{rowcol}^{loc} \times B_{rowcol}^{loc}$

10:         **else**

11:              **MPI_Bcast**($A_{temp}^{loc}, root, commcol$)

12:              $C_{rowcol}^{loc} \leftarrow C_{rowcol}^{loc} + A_{rowcol}^{temp} \times B_{rowcol}^{loc}$

13:         **MPI_Sendrecv_Replace**($B_{rowcol}^{loc}, dest, source, commrow$)

---

The similar idea of Fox's algorithm can be readily applied to the multiplications of three or more matrices, or to the matrix-vector multiplications as well. As one can see, there are no global MPI communications involved throughout the entire calculation despite the fact that all matrices remain local and, at each step, all operations (calculations) are performed in parallel. This feature makes Fox's algorithm particularly useful to very large calculations where memory constraints are the

biggest issue. Parallel computing ideally involves scaling in computing time and memory usage. Thus, complete distributions of data but avoiding global communications are always desirable. This powerful Fox's method is thereofore widely employed in all our calculations that involve either matrix-matrix or matrix-vector multiplications. For illustrations, in the next two subsections we shall explain the applications of Fox's algorithm for calculating the transition coefficients in Eq. (3.21) and performing the Lanczos iteration as well. One will see that the method not only provides the most optimal way of distributing data but also significantly speeds up the calculations.

### 3.3.2 Transition coefficients for $S = -1$ Hamiltonian

As we already mentioned in Section 3.2.2, one of the most challenging tasks in the preparation steps for hypernuclear energy calculations within the J-NCSM is to obtain the transition coefficients Eq. (3.21), which can be regarded as a product of two extremely large but sparse matrices (with dimensions up to $10^6 \times 10^6$, see also Table 3.1)

$$\langle \alpha^{*(Y)}|\alpha^{*(YN)}\rangle = \langle \alpha^{*(Y)}\big|(\alpha^{*(1)})^{*(Y)}\rangle\langle(\alpha^{*(1)})^{*(Y)}\big|\alpha^{*(YN)}\rangle$$

$$\equiv \langle \bullet\!\!-\!\!\bullet_\top\!\!\cdot\rangle\langle\bullet_\top\!\!\cdot\!\!\!-\!\!\bullet\rangle \tag{3.35}$$

$$= \delta_{YY}\langle\bullet|\bullet\!\!\!-\!\!\!\rightarrow\rangle_{A-1}\langle\bullet_\top\!\!\cdot\!\!\!-\!\!\bullet\rangle.$$

We, therefore, shall make use of Fox's algorithm to perform the summation over the auxiliary states $|(\alpha^{*(1)})^{*(Y)}\rangle$. The challenge here is then to find the most efficient way to distribute all final states $|\alpha^{*(Y)}\rangle$ and $|\alpha^{*(YN)}\rangle$, as well as the auxiliary ones over the $np_{row}$ and $np_{col}$ processes. Remember that the nuclear cfp of an $(A-1)$N system, $\langle\bullet|\bullet\!\!\!-\!\!\!\rightarrow\rangle_{A-1} \equiv \langle\alpha_{(A-1)}|\alpha^{*(1)}_{(A-1)}\rangle$, present in Eq. (3.35) are calculated beforehand and stored in each $(\mathcal{N}_{A-1}J_{A-1}T_{A-1})$-block in the machine-independent HDF5 format. The HDF5 library provides very advanced subroutines that enable all MPI processes to efficiently read every $(\mathcal{N}_{A-1}J_{A-1}T_{A-1})$-block of data in parallel, provided that the the specific information about how the cfp are going to be distributed on the Cartesian process grid is given. For example, it can be chosen that the $|\alpha_{(A-1)}\rangle$ states of each $(\mathcal{N}_{A-1}J_{A-1}T_{A-1})$-block are distributed over $np_{row}$ processes while the $|\alpha^{*(1)}_{(A-1)}\rangle$ states are distributed over $np_{col}$ processes. We refer to this distribution pattern as a regular distribution. This, however, has the disadvantage that then both, the basis states $|\alpha^{*(Y)}\rangle$ and the auxiliary ones $|(\alpha^{*(1)})^{*(Y)}\rangle$, are also needed to be distributed over $np_{row}$ and $np_{col}$ processes in the same manner as the $|\alpha_{(A-1)}\rangle$ and $|\alpha^{*(1)}_{(A-1)}\rangle$ states of the $(A-1)$N core, respectively. That is, each col-process will calculate and store only those $|\alpha^{*(Y)}\rangle$ states which are constructed from the $|\alpha_{(A-1)}\rangle$ that are available in this col-process. Similarly, each row-process needs to calculate and store only those $|(\alpha^{*(1)})^{*(Y)}\rangle$ that are directly related to the available $|\alpha^{*(1)}_{(A-1)}\rangle$ states. We refer to these ways of distributing the $|\alpha^{*(Y)}\rangle$ and $|(\alpha^{*(1)})^{*(Y)}\rangle$ states as irregular distributions. Note that the intermediate states $|\alpha^{*(YN)}\rangle$, on the other hand, can be distributed over $np_{col}$ processes independently. The irregular distribution of $|\alpha^{*(Y)}\rangle$ will of course lead to some complications when one needs to store the coefficients $\langle\alpha^{*(Y)}|\alpha^{*(YN)}\rangle$ to the HDF5 files. For that we have to manually keep track of every local $np_{row}$-distributed $|\alpha^{*(Y)}\rangle$ states. Nevertheless, it is doable and our effort has paid off by a significant reduction of the memory-per-node usage as well as total runtime, as one can clearly seen in Fig. 3.4. This in turn enables us to extend the calculations to significantly larger model space sizes otherwise it would impossible. Let us again emphasize that both, the basis
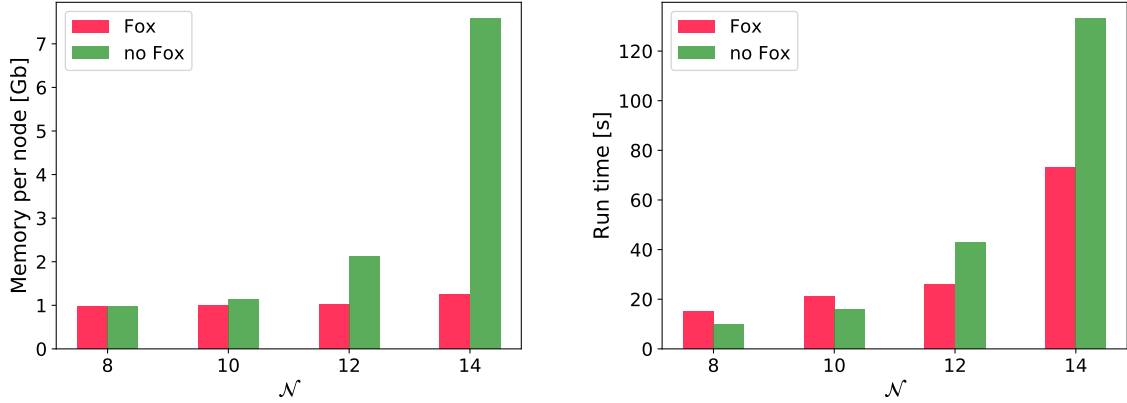
Figure 3.4: Memory usage (left figure) and total runtime (right figure) when calculating the transition coefficients with Fox's algorithm (red bars) and without Fox's algorithm (green bars) for different blocks $(\mathcal{N}, J^\pi = \frac{1}{2}^+, T = 0)$ in $^5_\Lambda$He. The calculations are performed on the JURECA-Booster supercomputer with 64 nodes for $\mathcal{N} = 8, 10$ and with 128 nodes for $\mathcal{N} = 12, 14$.

states as well as transition coefficients for the $H^{S=0}$ and $H^{S=-1}$ Hamiltonians, are HO-frequency and interaction-model independent. They therefore need to be calculated only once and can be also stored in the machine independent HDF5-format files, which makes the parallelization of the write-out and read-in data very efficient. Finally, we summarize in Tab. 3.1 the largest model spaces (second column) together with the total dimensions (*Dim*) of the basis and the two intermediate states of the hypernuclear systems which that will be studied in the following chapter. Generally, for the ground states, one we notice that $Dim_{\alpha^{*(YN)}}/Dim_{\alpha^{*(Y)}} \approx A - 1$ and $Dim_{(\alpha^{*(2)})^{*(Y)}}/Dim_{\alpha^{*(Y)}} \approx (A - 1)(A - 2)/2$, which follow the similar ratios observed for the basis and intermediate states in in the parent nuclei [102].

### 3.3.3 Applying Fox's algorithm to Lanczos iterations

We have mentioned earlier that the Jacobi basis allows one to perform calculations for a specific physical state at a time which can tremendously reduce the dimensionality of the huge sparse symmetric Hamiltonian matrix needed to be diagonalized. But still, the basis sizes are significant (especially for $A \geq 6$ hypernuclei, see also Table 3.1) as compared to the memory capacity of the up-to-date supercomputers. Therefore, an efficient scheme to obtain the lowest eigenvalues and the corresponding eigenstates is crucially important. In this aspect, the powerful Lanczos eigenvalue iterations [107] will be the most suitable diagonalization tool to our problems. Here, we employ the parallel Lanczos eigensolver available as a part of the advanced PARPACK library - a parallel version of the popular ARPACK software [108]. The basic idea of the method is to iteratively

| system | $(\mathcal{N}_{max}\, J^{\pi}\, T)$ | $\alpha^{*(Y)} \equiv \big\|\text{●-}\big\rangle$ | $\alpha^{*(YN)} \equiv \big\|\text{-●}\big\rangle$ | $(\alpha^{*(2)})^{*(Y)} \equiv \big\|\text{-●}\big\rangle$ |
|---|---|---|---|---|
| ${}^{4}_{\Lambda}\text{He}/{}^{4}_{\Lambda}\text{H}$ | $(22\, 0^{+}\, \tfrac{1}{2})$ | 118,149 | 355,008 | 319,221 |
| | $(22\, 1^{+}\, \tfrac{1}{2})$ | 343,490 | 1,031,424 | 1,923,957 |
| ${}^{5}_{\Lambda}\text{He}$ | $(14\, \tfrac{1}{2}^{+}\, 0)$ | 186,155 | 748,480 | 1,119,873 |
| ${}^{6}_{\Lambda}\text{He}/{}^{6}_{\Lambda}\text{Li}$ | $(13\, 1^{-}\, \tfrac{1}{2})$ | 1,452,047 | 7,513,728 | 15,098,199 |
| ${}^{7}_{\Lambda}\text{Li}$ | $(12\, \tfrac{1}{2}^{+}\, 0)$ | 871,102 | 5,782,144 | 13,843,348 |
| | $(12\, \tfrac{3}{2}^{+}\, 0)$ | 1,004,129 | 9,987,776 | 17,782,800 |
| | $(10\, \tfrac{5}{2}^{+}\, 0)$ | 408,084 | 2,589,910 | 6,693,764 |
| | $(10\, \tfrac{7}{2}^{+}\, 0)$ | 407,770 | 2,5948,32 | 6,716,857 |
| | $(10\, \tfrac{1}{2}^{+}\, 1)$ | 363,963 | 2,332,047 | 6,057,652 |

Table 3.1: Total dimensions of the basis and the intermediate states for the $S = 0$ and $S = -1$ Hamiltonians. The second column shows the largest model space sizes for each system.

construct an orthonormal Lanczos basis $\{\mathbf{v}, \mathbf{v}^1, \cdots, \mathbf{v}^{m-1}\}$ of a *Krylov* subspace [109],

$$\mathcal{K}_m(H, \mathbf{v}) = span\{\mathbf{v}, H\mathbf{v}, H^2\mathbf{v}, \cdots, H^{m-1}\mathbf{v}\}, \tag{3.36}$$

where $H$ is a Hermitian matrix of size $n \times n$, $\mathbf{v}$ is an arbitrary starting vector of dimension $n$ and $m$ is some integer number $m \ll n$ (typically $m$ is of order of 100 or several hundreds at most) that specifies the dimensionality of the *Krylov* space. The Lanczos vectors $\mathbf{v}^k$, $k = 1, m-1$ are constructed (usually in combination with an implicit restart process) such that in this basis the Hamiltonian $H$ becomes a tridiagonal matrix whose the lowest eigenvalue provides the best approximation to the ground-state binding energy of $H$ in the full Hilbert space. The main input to the parallel Lanczos eigensolver is a function that can calculate the matrix-vector product,

$$H_{ij}v_j^{k-1} \rightarrow v_i^k, \tag{3.37}$$

at each $k - th$ iteration with the two vectors, $\mathbf{v}^{k-1}$ and $\mathbf{v}^k$, being either *col-* or *row*-distributed. It turns out that computing Eq. (3.37) is the most time-consuming part of every Lanczos iteration, hence, it should be performed with very high efficiency. Furthermore, in order to reduce the memory usage, it is necessary that the Hamiltonian matrix $H$ is completely over the process grid. In that sense, the standard matrix-vector algorithm is no longer the optimal one since it certainly involves global communications among all processes. The desired efficiency can, however, be attained by exploiting the beautiful idea of Fox's algorithm. For that, let us distribute the matrix $H_{ij}$ on the $np_{row} \times np_{col}$ process grid and the vector $v_j^{k-1}$ over $np_{row}$ processes. Each process now stores a local *rowcol* matrix $H_{rowcol}^{loc}$ and a local *row* vector $v_{row}^{k-1,loc}$. At every Fox's iteration, each process will first need to perform the matrix-vector multiplication on its local data, $H_{rowcol}^{loc}$ and $v_{row}^{k-1,loc}$, resulting in a temporary *row*-distributed vector $v_{row}^{temp,loc}$,

$$H_{rowcol}^{loc}v_{row}^{k-1,loc} \rightarrow v_{row}^{temp,loc}, \tag{3.38}$$

and then shift its *row* vector $v_{row}^{k-1,loc}$ to its neighbour process in the same *commrow* communicator in order to prepare for the next Fox's iteration. At the end, a localized mpi-collective operator *mpi_allreduce* on $\mathbf{v}_{row}^{temp,loc}$ must be carried out in every *commcol* communicator, yielding a final *row*-distributed product vector $v_{row}^{k,loc}$. The pseudo code for the Fox's matrix-vecctor multiplication with the input $H_{rowcol}^{loc}, v_{row}^{k-1,loc}$ and the ouput $v_{row}^{k,loc}$ is shown below.
We are now ready to apply the described Fox's matrix-vector multiplication to the hypernuclear eigenvalue problems. As an example, we will explicitly show the Lanczos procedure that involves only the strange part ($S = -1$) of the Hamiltonian $H^{S=-1}$,

$$H^{S=-1}\big|\Psi^{k-1}\big\rangle = \big|\Psi^k\big\rangle. \tag{3.39}$$

Here, $\big|\Psi^{k-1}\big\rangle$ and $\big|\Psi^k\big\rangle$ are the wavefunctions at $(k-1)$-th and $k$-th Lanczos iterations, which can be expanded in the *col*-distributed basis states $|\alpha^{*(Y)}\rangle$ as follows

$$\big|\Psi^{k-1}\big\rangle = \sum_{\alpha^{*(Y)}} C_\alpha^{k-1}\big|\alpha^{*(Y)}\big\rangle; \qquad \big|\Psi^k\big\rangle = \sum_{\alpha^{*(Y)}} C_\alpha^k\big|\alpha^{*(Y)}\big\rangle. \tag{3.40}$$

---

**Algorithm 2** Fox's algorithm for vector-matrix multiplication

---

1: **procedure** Fox_matrixvector_multiplication($H_{rowcol}^{loc}, v_{row}^{k-1,loc}, v_{row}^{k,loc}$)

2:      $v_{row}^{temp} \leftarrow 0$

3:      $source \leftarrow \mathbf{mod}(myrowid + 1, npe_{row})$

4:      $dest \leftarrow \mathbf{mod}(myrowid, npe_{row})$

5:      **for** $iter = 0, npe_{row} - 1$ **do**

6:          $root \leftarrow \mathbf{mod}(myrowid + iter, npe_{row})$

7:          **if** $root = mycolid$ **then**

8:              $v_{row}^{temp} \leftarrow v_{row}^{temp} + H_{rowcol}^{loc} \times v_{row}^{k-1,loc}$

9:          **MPI_Sendrecv_Replace**($v_{row}^{k-1,loc}, dest, source, commrow$)

10:      **MPI_Allreduce**($v_{row}^{temp}, v_{row}^{k,loc}, dest, source, commcol$)

---

Automatically, the expansion coefficients $C_\alpha^{k-1}$ and $C_\alpha^k$ are also distributed over $np_{col}$ processes in the same manner as the states $|\alpha^{*(Y)}\rangle$. After projecting the equation Eq. (3.39) onto the basis $|\alpha^{*(Y)}\rangle$ and then making use of the completeness of the intermediate states $|\alpha^{*(YN)}\rangle$ in Eq. (3.26), we obtain

$$\sum_{\alpha'^{*(Y)}} \sum_{\substack{\alpha^{*(YN)} \\ \alpha'^{*(YN)}}} \langle \alpha^{*(Y)} | \alpha^{*(YN)} \rangle \langle \alpha^{*(YN)} | H^{S=-1} | \alpha'^{*(YN)} \rangle \langle \alpha'^{*(YN)} | \alpha'^{*(Y)} \rangle \langle \alpha'^{*(Y)} | \Psi^{k-1} \rangle = \langle \alpha^{*(Y)} | \Psi^k \rangle. \tag{3.41}$$

Now, by inserting the expansion in Eq. (3.40) into Eq. (3.41), one arrives at a set of linear equations Eq. (3.42) for the Lanczos iterations

$$\sum_{\alpha'^{*(Y)}} \sum_{\substack{\alpha^{*(YN)} \\ \alpha'^{*(YN)}}} \langle \alpha^{*(Y)} | \alpha^{*(YN)} \rangle \langle \alpha^{*(YN)} | H^{S=-1} | \alpha'^{*(YN)} \rangle \langle \alpha'^{*(YN)} | \alpha'^{*(Y)} \rangle C_{\alpha'}^{k-1} = C_\alpha^k. \tag{3.42}$$

It is obvious that, during the Lanczos iterations, only the expansion coefficients $C_\alpha^{k-1}$ and $C_\alpha^k$ are updated, while the other terms in Eq. (3.42) remain unchanged. It is therefore advisable to prepare the matrix elements $\langle \alpha^{*(YN)} | H_Y | \alpha'^{*(YN)} \rangle$ as well as the overlap $\langle \alpha'^{*(YN)} | \alpha'^{*(Y)} \rangle$ and have them stored in the desired *row*- and *col*-distribution before entering the iterations. Since our basis states $|\alpha^{*(Y)}\rangle$ are distributed over $np_{col}$ processes, the overlap matrix $\langle \alpha'^{*(YN)} | \alpha'^{*(Y)} \rangle$ should also be distributed in the $\alpha'^{*(YN)}$-*row* and $\alpha'^{*(Y)}$-*col* manner. Then the first summation over the $|\alpha'^{*(Y)}\rangle$ states can be straightforwardly performed with the help of the standard matrix-vector multiplication, which yields an intermediate *row*-distributed vector

$$v_{row}^{inter}(\alpha'^{*(YN)}) = \sum_{\alpha'^{*(Y)}} \langle \alpha'^{*(YN)} | \alpha'^{*(Y)} \rangle_{rowcol} C_{\alpha',col}^{k-1} \tag{3.43}$$

We employ Fox's matrix-vector multiplication algorithm for the second summation that involves $\langle \alpha^{*(YN)} | H^{S=-1} | \alpha'^{*(YN)} \rangle$ and $v_{row}^{inter}(\alpha'^{*(YN)})$. Since the latter is *row*-distributed, it is necessary that the matrix $\langle \alpha^{*(YN)} | H^{S=-1} | \alpha'^{*(YN)} \rangle$ is also $\alpha^{*(YN)}$-*row* and $\alpha'^{*(YN)}$-*col* distributed. Applying the Fox's
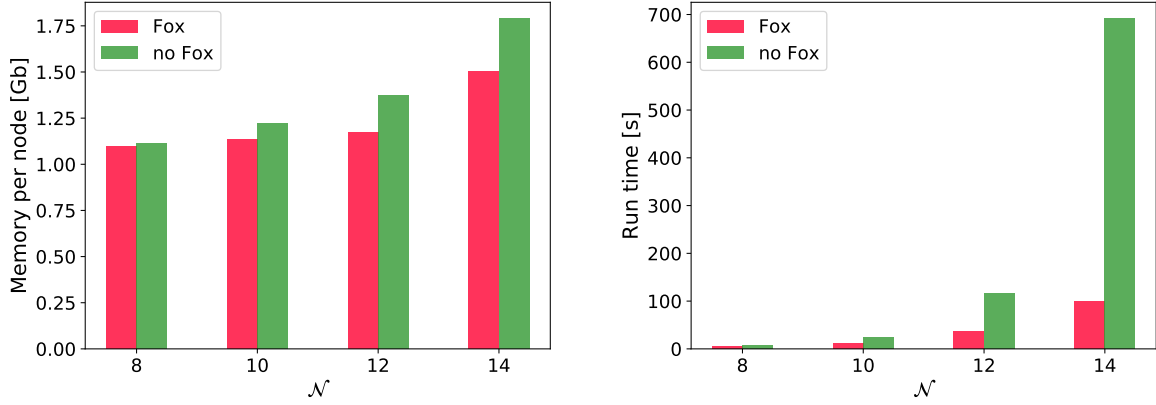
Figure 3.5: Memory usage (left figure) and total runtime (right figure) when calculating the ground-state binding energy in $^5_\Lambda$He with Fox's algorithm (red bars) and without Fox's algorithm (green bars) for different model space sizes $\mathcal{N}$. The calculations are performed on the JURECA-Booster supercomputer with 64 nodes.

algorithm 2 to the summation over $|\alpha'^{*(YN)}\rangle$ then results in another *row*-distributed intermediate vector

$$v_{row}^{inter2}(\alpha^{*(YN)}) = \sum_{\alpha'^{*(YN)}} \langle \alpha^{*(YN)}|H^{S=-1}|\alpha'^{*(YN)}\rangle_{rowcol}\, v_{row}^{inter}(\alpha'^{*(YN)}). \tag{3.44}$$

Finally, the third summation over the $|\alpha^{*(YN)}\rangle$ states

$$C_{\alpha,col}^k = \sum_{\alpha^{*(YN)}} \langle \alpha^{*(Y)}|\alpha^{*(YN)}\rangle_{colrow}\, v_{row}^{inter2}(\alpha^{*(YN)}), \tag{3.45}$$

is nothing but a normal matrix-vector multiplication, hence, can be performed in the same way as the first summation in Eq. (3.43). The Lanczos procedure involving the non-strange Hamiltomian $H^{S=0}$ can be performed in a similar manner as for $H^{S=-1}$. In order to illustrate the benefits of using Fox's matrix-vector multiplication in the Lanczos iterations, in Fig. 3.5 we compare the memory usage per node (left figure) and total runtime (right figure) when calculating the binding energy of $^5_\Lambda$He with Fox's algorithm (red bars) and without Fox's algorithm (green bars) for different model space sizes[3]. One clearly sees that the implementation of the Fox's multiplication leads to a slight reduction in memory usage and tremendously speeds up the calculations especially for large model space sizes.

---

[3] In binding energy calculations, when saying model space $\mathcal{N}$ we mean that all the basis states with the same $J^\pi$ and $T$ and with all allowable HO energy quantum numbers up to $\mathcal{N}$.

# Results for $A = 4 - 7$ Hypernuclei

In this chapter we explore light hypernuclear systems ranging from $^{4}_{\Lambda}\text{He}$ ($A = 4$) to $^{7}_{\Lambda}\text{Li}$ ($A = 7$) using our Fortran based J-NCSM code. We will first explain the extrapolation procedure employed in order to extract the infinite model-space binding (and $\Lambda$-separation) energies together with the theoretical uncertainties. In Section 4.2 we carefully study the separation energies $B_{\Lambda}$ of these light hypernuclei focusing on the effects of different NN chiral interactions as well as the SRG evolutions. The energy spectrum of $^{7}_{\Lambda}\text{Li}$ is presented in Section 4.3. Intriguing correlations between $B_{\Lambda}$ of different systems are discussed in Section 4.4. The impacts of various YN (chiral) interaction models on hypernuclear observables are comprehensively investigated in Sections 4.5 and 4.6. The next section, Section 4.7, is devoted to study possible CSB in the $A = 7$ isotriplet hypernuclei, $^{7}_{\Lambda}\text{Li}(T = 1)$, $^{7}_{\Lambda}\text{He}$ and $^{7}_{\Lambda}\text{Be}$. Finally, we report our J-NCSM results for other interesting quantities like nucleon and hyperon radii, together with NN and YN correlation functions in Section 4.8. As it has been mentioned earlier, for all our calculations presented here the NN and YN potentials with partial waves higher than 6 ($J > 6$) are left out. And, for simplicity, the electromagnetic NN interactions [110] as well as Coulomb point-like YN interactions are not included in the SRG evolutions, but only added afterwards. We observed that evolving these interactions changes hypernuclear binding energies only by few keV.

## 4.1 Extrapolation of the binding energies

Due to the finite truncation in the single-particle Hilbert space, results from the NCSM calculations are dependent on the HO frequency $\omega$ as well as the model space size $\mathcal{N}$. In order to obtain the converged binding energies, and at the same time, be able to systematically estimate the numerical uncertainties, we shall follow a two-step procedure as employed in [83]. The first step is to minimize (eliminate) the HO-$\omega$ dependence. For each model space size $\mathcal{N}$, we first calculate the binding energies, $E(\omega, \mathcal{N})$, for a wide range of HO-$\omega$ and then utilize the following ansatz,

$$E(\omega, \mathcal{N}) = E_{\mathcal{N}} + \kappa(\log(\omega) - \log(\omega_{\text{opt}}))^{2}, \tag{4.1}$$

to extract the lowest binding energy $E_{\mathcal{N}}$ for the considered model space $\mathcal{N}$ and the corresponding optimal HO frequency $\omega_{\text{opt}}$. Here, $\kappa$ is a constant to be determined from the parabolic fitting for all $E(\omega, \mathcal{N})$. As an example, we show in Fig. 4.1 the HO-$\omega$ dependence of $E(^{4}_{\Lambda}\text{He}, 0^{+})$ for model space
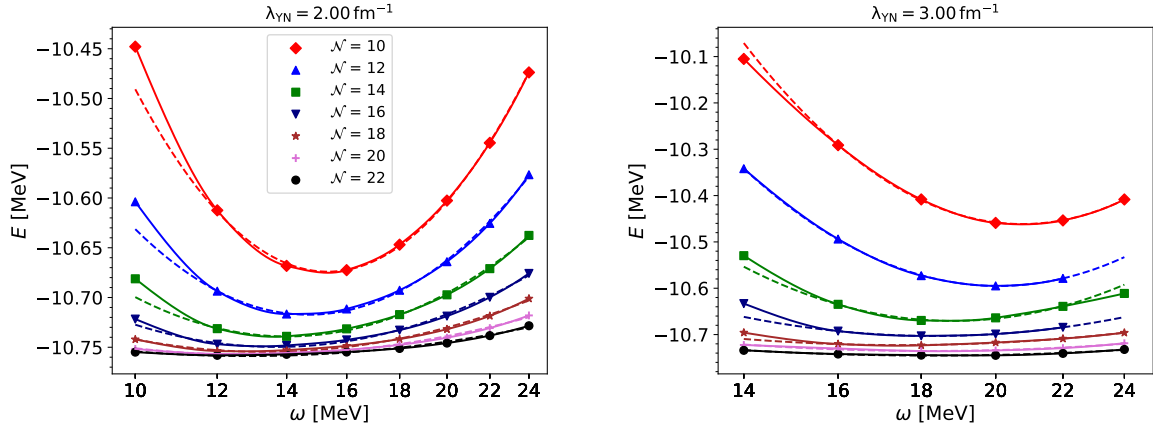
Figure 4.1: $E(^4_\Lambda \text{He}, 0^+)$ as a function of HO $\omega$. Solid lines with different colors and markers are the numerical results for different model space $\mathcal{N}$. Dashed lines are obtained using the ansatz Eq. (4.1). The calculations are based on the NN Idaho-N$^3$LO(500) potential evolved to $\lambda_{NN} = 1.6$ fm$^{-1}$ and the NLO19 with a regulator of 600 MeV for YN potential evolved to two SRG flow values $\lambda_{YN} = 3.00$ fm$^{-1}$ (right figure) and $\lambda_{YN} = 2.0$ fm$^{-1}$ (left figure).

$\mathcal{N}$ varying from 10 to 22 with a step of 2, computed at two values of the SRG-YN flow parameters: $\lambda_{YN} = 3.0$ (right figure) and $\lambda_{YN} = 2.0$ fm$^{-1}$ (left figure). Generally, the optimal frequency $\omega_{\text{opt}}$ corresponding to each model space $\mathcal{N}$ becomes smaller when $\lambda_{YN}$ decreases. We further notice that $\omega_{\text{opt}}$ also shifts to smaller values as $\mathcal{N}$ increases, and the $\omega$-dependence energy curves of sufficiently large model spaces are practically flat. This basically reflects the intrinsic properties of the HO basis. With increasing $\mathcal{N}$, the basis functions contain many more higher-order polynomials that can efficiently describe the high-momentum (short-distance) part of the wavefunction. The HO basis then can afford smaller HO frequencies so that the resolution at low-momentum (large-distance) can be improved. We note that a similar trend is observed for all investigated hypernuclei hinting at good convergence patterns in all these systems. In the second step, the binding energies with the minimal $\omega$-dependence, $E_\mathcal{N}$, are used for extrapolating to a converged result in infinite model space assuming an exponential ansatz

$$E_\mathcal{N} = E_\infty + A e^{-B\mathcal{N}}. \tag{4.2}$$

The confidence interval for each $E_\mathcal{N}$ in (4.2) can be determined either from the spread of the energy in the vicinity of $\omega_{\text{opt}}$ or from the slope between two successive energies, $E_\mathcal{N}$ and $E_{\mathcal{N}+2}$. The latter is widely employed in our calculations. We, however, stress that the two ways of assigning confidence intervals are equivalent and lead to the same results within the numerical uncertainties. This determined intervals will serve as a weight for each $E_\mathcal{N}$ in the model-space fit with the ansatz Eq. (4.2). In Fig. 4.2 we illustrate the model-space extrapolation for $E(^4_\Lambda \text{He}, 0^+)$ for the two chosen SRG cutoffs $\lambda_{YN}$. Here, the red lines are the extrapolated binding energies $E_\infty$ while the shaded areas are the estimated uncertainties which are taken as differences between the $E_\infty$ and $E_{\mathcal{N}_{max}}$. One clearly sees that, in both cases, the ground state binding energies $E(^4_\Lambda \text{He})$ calculated using model space up to $\mathcal{N}_{max} = 22$ converge very nicely, with lower SRG cutoff leading to a faster convergence rate (note the energy scale difference on the y-axes of the two plots).
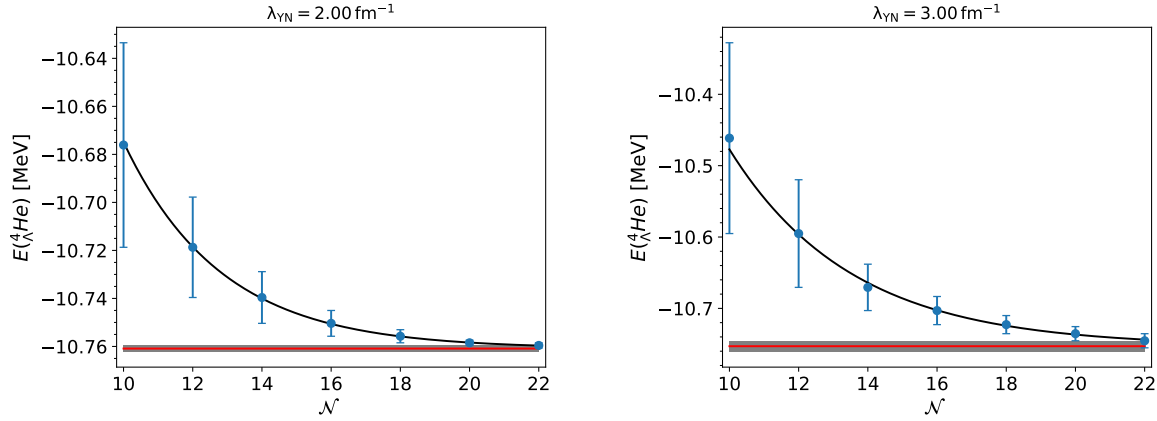
Figure 4.2: $E({}^{4}_{\Lambda}\text{He}, 0^{+})$ as a function of model space size $\mathcal{N}$. Solid line is the $\mathcal{N}$-extrapolated result. Red line with shaded area indicates the converged result and its uncertainty. The calculations are based on the Idaho-N$^3$LO(500) interaction evolved to $\lambda_{NN} = 1.6$ fm$^{-1}$ and the NLO19 with a regulator of 600 MeV for YN potential evolved to two SRG flow values $\lambda_{YN} = 3.00$ fm$^{-1}$ (right figure) and $\lambda_{YN} = 2.0$ fm$^{-1}$ (left figure).

In hypernuclear physics, a more interesting quantity is, however, the so-called $\Lambda$−separation energy, $B_\Lambda$, which is defined as the difference of the binding energies of a hypernucleus and the corresponding parent nucleus. Thus, for $B_\Lambda({}^{4}_{\Lambda}\text{He})$ can be calculated as

$$B_\Lambda({}^{4}_{\Lambda}\text{He}) = E({}^{3}\text{He}) - E({}^{4}_{\Lambda}\text{He}). \tag{4.3}$$

Following the definition Eq. (4.3), one in principle can subtract the separation energy for each $\omega$ and $\mathcal{N}$,

$$B_\Lambda({}^{4}_{\Lambda}\text{He}, \omega, \mathcal{N}) = E({}^{3}\text{He}, \omega, \mathcal{N}) - E({}^{4}_{\Lambda}\text{He}, \omega, \mathcal{N}), \tag{4.4}$$

and then employ the above mentioned two-step procedure to extrapolate the converged $B_\Lambda$. We have, however, observed that, for each model space size $\mathcal{N}$, the useful ranges of $\omega$ and hence the optimal frequencies $\omega_{\text{opt}}$ for the nuclear core ${}^{3}\text{He}$ and hypernucleus ${}^{4}_{\Lambda}\text{He}$ are not the same. It is therefore advisable to eliminate the $\omega$-dependence of the binding energies of ${}^{3}\text{He}$ and ${}^{4}_{\Lambda}\text{He}$ separately. After that, one subtracts $B_\Lambda(\mathcal{N})$ for every model space $\mathcal{N}$

$$B_\Lambda({}^{4}_{\Lambda}\text{He}, \mathcal{N}) = E({}^{3}\text{He}, \mathcal{N}) - E({}^{4}_{\Lambda}\text{He}, \mathcal{N}), \tag{4.5}$$

and employs the ansatz Eq. (4.2) to extract the converged result $B_\Lambda({}^{4}_{\Lambda}\text{He})$ in infinite model space together with its uncertainty. For demonstration, we also show in Fig. 4.3 the model-space extrapolation of the separation energy in ${}^{4}_{\Lambda}\text{He}$. As expected, evolving the YN potential to low SRG cutoffs indeed speeds up the calculations significantly. When comparing Figs. 4.2 and 4.3, we also notice a faster convergence rate of $B_\Lambda({}^{4}_{\Lambda}\text{He})$ than that of the binding energy $E({}^{4}_{\Lambda}\text{He})$.

It should be stressed that, while the binding energies are strictly monotonic (variational), it is not necessarily true for $B_\Lambda$ especially in large systems like ${}^{7}_{\Lambda}\text{Li}$. Nevertheless, one will see later that the separation energies always converge faster than the individual binding energies of the hypernucleus and of the corresponding nuclear core. In many cases, one can even use a straight line instead of
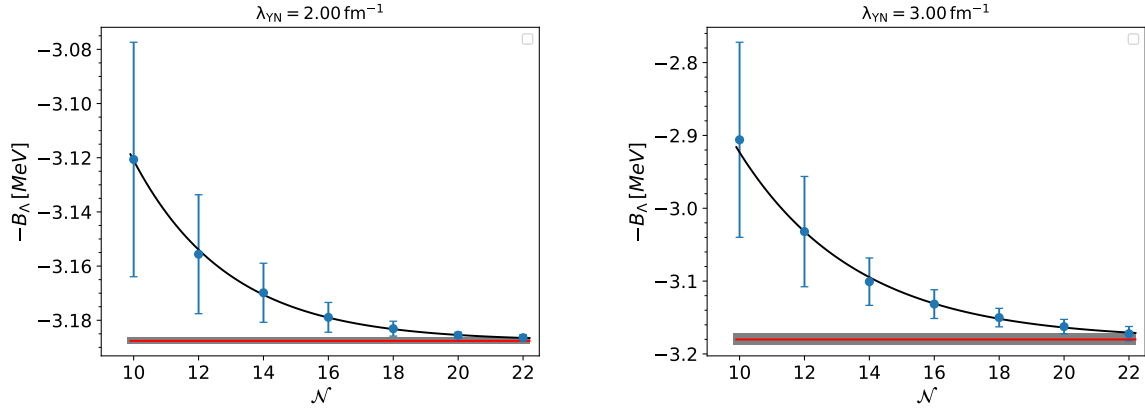
Figure 4.3: $B_\Lambda(^4_\Lambda\mathrm{He}, 0^+)$ as a function of model space size $\mathcal{N}$. Same descriptions of lines and symbols as in Fig. 4.2.

the exponential decay function as in Eq. (4.2) for extrapolating $B_\Lambda$. Let us further emphasize that, although the described procedure is rather expensive, it allows for a systematic and very reliable extraction of the final results of the NCSM calculations. hypernuclear calculations present in the thesis. Importantly, within the Jacobi-basis formalism such robust extrapolation scheme is doable and yields plausible results for light p-shell hypernuclei as one will see in the following section.

## 4.2  Separation energies in $A = 4 − 7$ hypernuclei

We are now at a position to study the $\Lambda$ removal energies in some light systems. The SRG evolutions soften NN and YN potentials via decoupling the low- and high-momentum states, and thereby, tremendously speed up binding energy calculations which are essentially driven by low-energy physics. The evolutions, however, unavoidably shift strength of two-body forces to higher-body forces that are omitted in our current study. In the nuclear sector, it is shown that binding energies then depend on the SRG evolution parameter, the variations from which can be attributed to the contributions of the missing SRG-induced higher-body forces [99, 111]. It is important that the latter preserves the hierarchy of many-body forces in chiral EFT [112]. The situation is even more complicated in hypernuclear calculations. Here, one can expect that the dependences on the SRG evolution and on the nuclear interaction models will carry over to the hypernuclear binding energies in combination with possibly strong variations due to the YN-SRG evolution. Nonetheless, it is believed that the impact of NN forces on the $\Lambda$-separation energies is considerably smaller than on the binding energies. These aspects will be the main focus of this section. Most of the results present in this section are obtained using the YN NLO19 interaction for a chiral cutoff of $\Lambda_Y = 600$ MeV [47] combined with two NN potentials: the Idaho N$^3$LO with $\Lambda_N = 500$ MeV [32] and the chiral semilocal momentum-spaced regularized (SMS) N$^4$LO+ for a regulator of $\Lambda_N =$450 MeV [35].

Before going into details, let us first mention the benchmark between the binding energies of $^4_\Lambda$He computed within the J-NCSM model with those obtained by solving the Faddeev-Yakubovsky equations [69]. These binding energies for the ground state $(0^+)$ and first excited state $(1^+)$ are tabulated in Table 4.1. We see that within the numerical accuracy of less than several keV the two

| $\lambda_{YN}$ | $0^+$ | | $1^+$ | |
| :---: | :---: | :---: | :---: | :---: |
| [fm$^{-1}$] | J-NCSM | Yakubovsky | J-NCSM | Yakubovsky |
| 1.6 | -10.700(1) | -10.70 | -9.863(3) | -9.86 |
| 3.0 | -10.751(6) | -10.77 | -9.81(1) | -9.82 |
| 14.0 | -9.27(8) | -9.31(3) | | |

Table 4.1: Ground state and excited state energies of $^4_\Lambda$He obtained from the Faddeev-Yakubovsky and J-NCSM approaches. The calculations are based on the Idaho-N$^3$LO(500) for the NN interaction that is evolved to $\lambda_{NN}$ = 1.6 fm$^{-1}$ and the YN NLO19(600) potential evolved to three different SRG flow values of $\lambda_{YN}$ = 1.6, 3.0 and 14.0 fm$^{-1}$.

approaches, J-NCSM and Faddeev-Yakubovsky, indeed agree very nicely.

## 4.2.1 $^4_\Lambda$He$(0^+, \frac{1}{2})$

The $A = 4$ hypernuclear systems are always of huge interest. They are the smallest hypernuclei where two spin states $0^+$ and $1^+$ are observed which serve as an important laboratory for studying the spin-dependence of the YN forces. In addition, there is a considerable difference between the $\Lambda$-separation energies of the isospin mirror pair $^4_\Lambda$He and $^4_\Lambda$H, approximately about 233 keV for the ground state [113]. This is a charge symmetry breaking (CSB) effect whose the underlying causes are not completely understood yet despite numerous theoretical studies have been devoted to it [40, 71, 113]. Since the YN interactions considered here do not contain any CSB except a tiny effect from the Coulomb interactions (and some small SRG-YN induced effects due to the mass differences among $\Sigma^\pm, \Sigma^0$ hyperons, see also Section 4.7), we obtain almost identical results for $^4_\Lambda$He and $^4_\Lambda$H. In the following, we will therefore concentrate only on the $^4_\Lambda$He hypernucleus. It is known that the nuclear binding energy $E(^3\text{He})$ and therefore $E(^4_\Lambda\text{He})$ are very sensitive to the employed NN interaction models because three- and higher-body forces are missing. This is also easily noticed for our binding energies of the $^4_\Lambda$He$(0^+)$ state, see left plot in Fig. 4.4, which are calculated using various NN forces: the Idaho-N$^3$LO(500), the improved chiral N$^2$LO and N$^4$LO with a configuration-space regulator of 0.9 fm [43, 114] and the SMS N$^4$LO+(450). All NN forces are evolved to an SRG parameter of $\lambda_{NN}$ = 1.6 fm$^{-1}$ while the YN potential is evolved to a wide range of flow parameters, $1.0 \leq \lambda_{YN} \leq 3.0$ fm$^{-1}$. One can see that the binding energy variations due to different NN chiral forces can be as large as 270 keV. However, being evolved to the same $\lambda_{NN}$ = 1.6 fm$^{-1}$, these NN interaction models have a much smaller influence on the $\Lambda$ removal energy, in particular for low SRG-YN flow parameters $\lambda_{YN} \leq 1.6$ fm$^{-1}$ where there is practically no difference in $B_\Lambda(^4_\Lambda\text{He}, 0^+)$, see also right plot in Fig. 4.4. For higher $\lambda_{YN}$, the discrepancies among the computed values of $B_\Lambda(^4_\Lambda\text{He}, 0^+)$ somewhat increase but still remain small, about 50 keV at most. These variations are again negligible if one leaves aside results from the N$^2$LO potential which slightly overbinds the
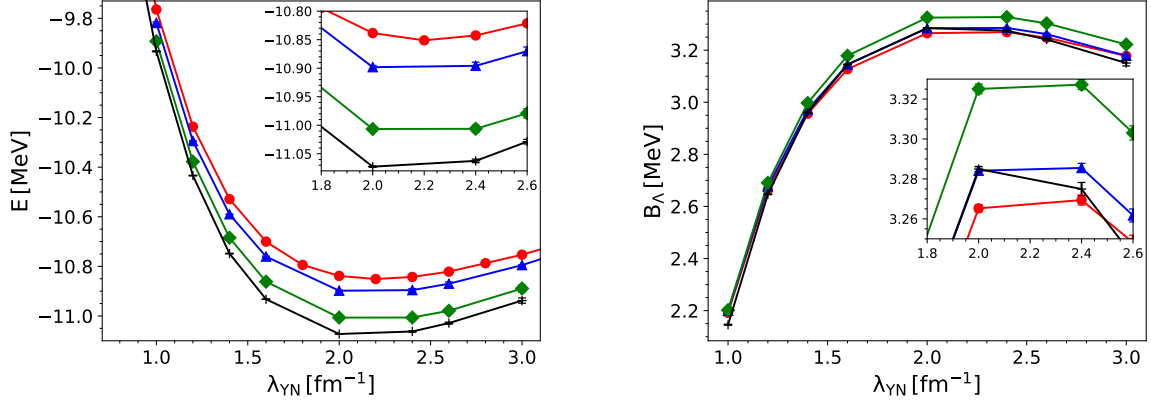
Figure 4.4: Binding energy (left figure) and $\Lambda$-separation energy (right figure) in $^4_\Lambda$He($0^+$) as functions of the SRG YN flow parameter $\lambda_{YN}$. The calculations are based on the YN NLO19(600) potential and three chiral NN interactions: the Idaho-N$^3$LO(500) (red circles), two improved chiral-N$^4$LO (blue triangles) and Chiral-N$^2$LO (green diamonds) regulated in configuration space with a cutoff $R = 0.9$ fm [43, 114], and the SMS N$^4$LO+(450) (black crosses). All NN potentials are evolved to a flow parameter of $\lambda_{NN} = 1.6$ fm$^{-1}$. The error bars show the estimated numerical uncertainties.
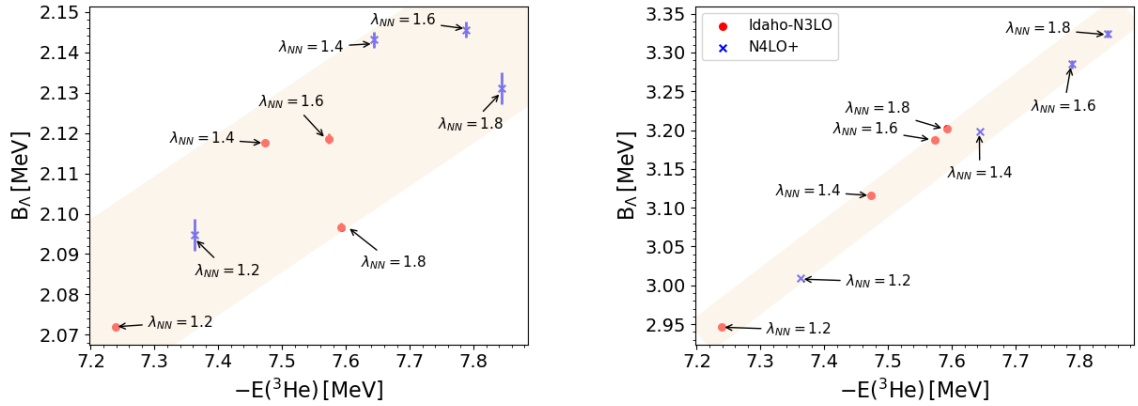


Figure 4.5: $\Lambda$-separation energy in $^4_\Lambda$He($0^+$) with respect to the $^3$He binding energies. The calculations are based on the chiral NN Idaho-N$^3$LO(500) (red circles) and the SMS N$^4$LO+(450) (blue asterisks) evolved at several values of $\lambda_{NN}$ together with the YN NLO19(600) evolved to two SRG flow parameters $\lambda_{YN} = 1.0$ fm$^{-1}$(left figure) and $\lambda_{YN} = 2.0$ fm$^{-1}$(right figure). The error bars show the estimated numerical uncertainties.

deuteron [43, 114]. In order to examine the effects of the SRG-NN evolution on the $\Lambda$-separation energy in $^4_\Lambda$He($0^+$), we compute $B_\Lambda(^4_\Lambda$He, $0^+)$ using the two most accurate NN potentials, namely the Idaho-N$^3$LO(500) and SMS N$^4$LO+(450), evolved to several $\lambda_{NN}$ flow variables. Note that, although these two NN potentials describe the available NN scattering data almost perfectly, they indeed have very different matrix elements particularly in the high-momentum region. It is therefore interesting to study their predictions for $B_\Lambda$ more carefully. In order to speed up the convergence of $B_\Lambda$, we evolve the YN NLO19(600) to two flow parameters of $\lambda_{YN} = 1.0$ and 2.0 fm$^{-1}$. The latter choice of $\lambda_{YN} = 2.0$ fm$^{-1}$is based on results shown in Fig. 4.4 which indicate that the largest $B_\Lambda$ discrepancy is observed at that flow parameter. In Fig. 4.5 we show the $\Lambda$-separation energies, $B_\Lambda(^4_\Lambda$He), plotted against the binding energy of the core nucleus $^3$He. The results obtained with the Idaho-N$^3$LO(500) and SMS N$^4$LO+(450) are denoted by red squares and blue crosses, respectively. Also, the error bars are added to indicate the estimated numerical uncertainties which in many case are hardly noticeable. The light colored bands are results from a linear fit of all the computed $B_\Lambda(^4_\Lambda$He). It is quickly observed that stronger nuclear binding energies generally lead to larger $\Lambda$-separation energies. There is probably a simple explanation for that as mentioned in [115]. Usually, larger binding energies of the core nucleus implies also smaller radii or higher nucleon density in the nuclear interior, which in turn leads to a stronger interaction between a $\Lambda$ hyperon and the core (i.e. larger $B_\Lambda$). Furthermore, for a low value of $\lambda_{YN} = 1.0$ fm$^{-1}$(left plot), the overall variations of $B_\Lambda$ due to SRG-NN evolutions are insignificantly small, about 50 keV at most (left figure), but become noticeable at higher value of $\lambda_{YN} = 2.0$ fm$^{-1}$(right plot), which can be as large as 350 keV (right plot). Nonetheless, it also clearly sticks out from the two plots in Fig. 4.5 that, the width of the linear fitting bands in both cases are negligibly small (of order of 40 keV only). This may imply that the variation of $B_\Lambda(^4_\Lambda$He, $0^+)$ will probably become negligible once the $^3$He core is properly described by the chosen NN interactions. This is indeed in consistent with the observation by Nogga that the two chiral NN potentials, Idaho-N$^3$LO(500) and SMS N$^4$LO+(450), have minor effect on $B_\Lambda(^4_\Lambda$He, $0^+)$ [40, 47] .

Furthermore, it is also visible from Fig. 4.4 that the dependence of $B_\Lambda(^4_\Lambda$He, $0^+)$ on the YN flow parameter $\lambda_{YN}$ is considerably larger, of order of 1 MeV, implying the significant contribution to $B_\Lambda$ of the SRG-YN induced higher-body forces. The latter is believed to be tightly related to probabilities of finding $\Sigma$ particles in hypernuclear wavefunctions [87]. Our calculated $\Sigma$-probability in $^4_\Lambda$He, shown in Fig. 4.6(a), also indicates a strong correlation between $P_\Sigma$ and the SRG YN evolution. Evidently, at the beginning of the SRG-YN evolution the $\Sigma$ probability is quite large, e.g. $P_\Sigma = 1.8\%$ for $\lambda_{YN} = 14$ fm$^{-1}$, however, it is quickly reduced to the smallest value of about 0.2% at $\lambda_{YN} = 1.0$ fm$^{-1}$. Surprisingly, we observe a slight increase in $P_\Sigma$ as the YN potential being evolved further, which indicates that the SRG evolution affects the $\Sigma$-components in a rather complicated way. We finally remark that the NN interactions have a minor effect on the $\Sigma$-components which is different for the $E(^4_\Lambda$He).

The $\Lambda$-separation energy of $^4_\Lambda$He($0^+$) calculated for the same range of $\lambda_{YN}$ ($0.83 \leq \lambda_{YN} \leq 14$ fm$^{-1}$) exhibits a similar interesting behaviour with respect to the SRG evolution, see Fig. 4.6(b). For high values of the evolution parameter, $\lambda_{YN} \geq 3$ fm$^{-1}$, the SRG-induced YNN forces are attractive since one observes a continuous increase in $B_\Lambda$ as the YN potential being evolved from $\lambda_{YN} = 14$ fm$^{-1}$ to a much smaller flow parameter of $\lambda_{YN} = 3.0$ fm$^{-1}$. When the evolution parameter is below 3.0 fm$^{-1}$, the SRG-induced higher-body forces seem to be strongly repulsive which lead to a steady decrease in $B_\Lambda(^4_\Lambda$He). So, there is clearly no simple one-to-one correlation between the $\Sigma$-probabilities and SRG-induced YNN forces. This is somewhat different from the general observation for the
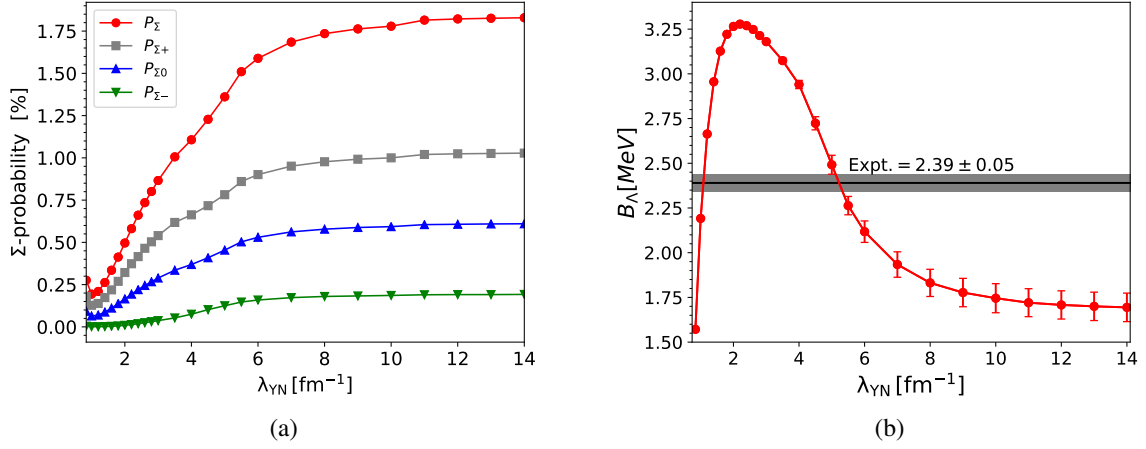
Figure 4.6: (a): Probabilities of finding a $\Sigma^+$ (grey squares), $\Sigma^0$ (blue up triangles) and $\Sigma^-$ (green down triangles) in $^4_\Lambda$He($0^+$) as functions of the SRG YN flow parameter $\lambda_{YN}$. Red circles are the total $\Sigma$ probability, $P_\Sigma = P_{\Sigma^+} + P_{\Sigma^-} + P_{\Sigma^0}$. The differences among $P_{\Sigma^+}$, $P_{\Sigma^-}$ and $P_{\Sigma^0}$ are simply driven by some Clebsch Gordan coefficients. (b): $\Lambda$-separation energy as a function of flow parameter $\lambda_{YN}$. The calculations are based on the YN NLO19(600) potential and the Idaho-N³LO(500) for the NN interaction that is evolved to a flow parameter of $\lambda_{NN} = 1.6$ fm⁻¹.

phenomenological YNN forces. Indeed, Bodmer *et al.* [116] have found in their study using variational methods that an explicit removal of the $\Sigma$ degrees of freedom would lead to strongly repulsive three-body $\Lambda NN$ forces.

## 4.2.2 $^4_\Lambda$He($1^+, \frac{1}{2}$)

In the next step, we study the excited state of the $^4_\Lambda$He hypernucleus. Here, we also perform calculations with model space sizes up to $\mathcal{N}_{max} = 22$ which are apparently sufficient for obtaining well-converged results as demonstrated in Figs. 4.7 and 4.8. It is noted that the total numbers of the basis states as well as of the intermediate ones for $^4_\Lambda$He($1^+$) are almost three times larger than those for $^4_\Lambda$He($0^+$) (see Table 3.1). This also clearly manifests in a faster convergence speed for the ground-state binding (separation) energy calculations, compare Figs. 4.1 and 4.7 (Figs. 4.3 and 4.8).

Fig. 4.9 demonstrates the uncomfortably large dependence of $B_\Lambda(^4_\Lambda$He, $1^+)$ on the SRG-YN evolution. The results are shown for the Idaho-N³LO(500) interaction with flow variables, $\lambda_{NN} = 1.6$ fm⁻¹ (red circles) and $\lambda_{YN} = 2.4$ fm⁻¹(blue triangles). Apparently, the SRG-YN evolution has quite similar effect on the $\Lambda$-separation energies of the two spin-doublet $0^+$ and $1^+$ states. Likewise, at low values of $\lambda_{YN}$, the overall variation of $B_\Lambda(^4_\Lambda$He, $1^+)$ due to different chiral NN models as well as the SRG-NN evolution is negligible. It, however, becomes noticeable (of the order of 300 keV) at higher $\lambda_{YN}$ flow parameters, as it is clearly seen in Fig. 4.10 where the $\Lambda$-separation energies computed for an SRG cutoff of $\lambda_{YN} = 2.0$ fm⁻¹ are plotted against the ³He-core binding energies. Nonetheless, it can be quickly deduced from Fig. 4.10 that the with of the linear fitting band (light colored band) is quite small, of order of 50 keV, which is practically the same as for the ground
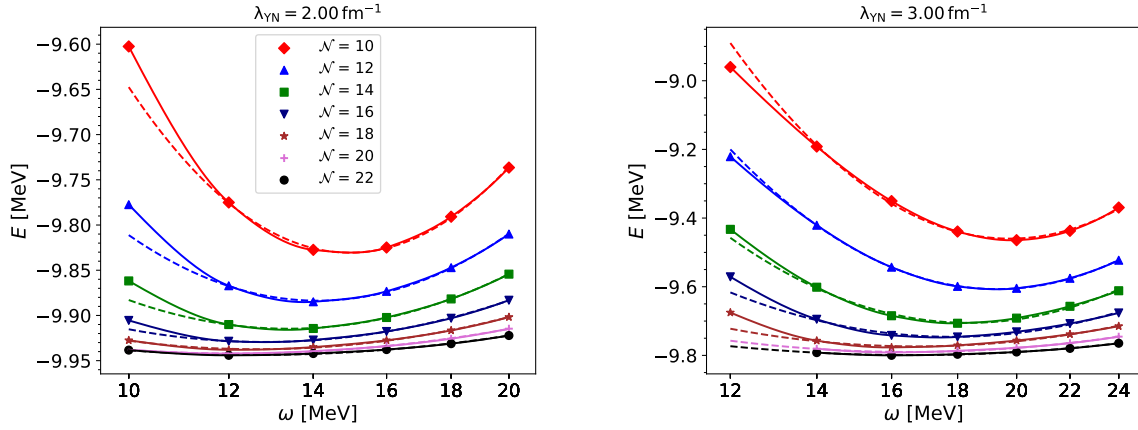
Figure 4.7: $E(^4_\Lambda \text{He}, 1^+)$ as a function of HO $\omega$. The same description of lines and symbols as in Fig. 4.1
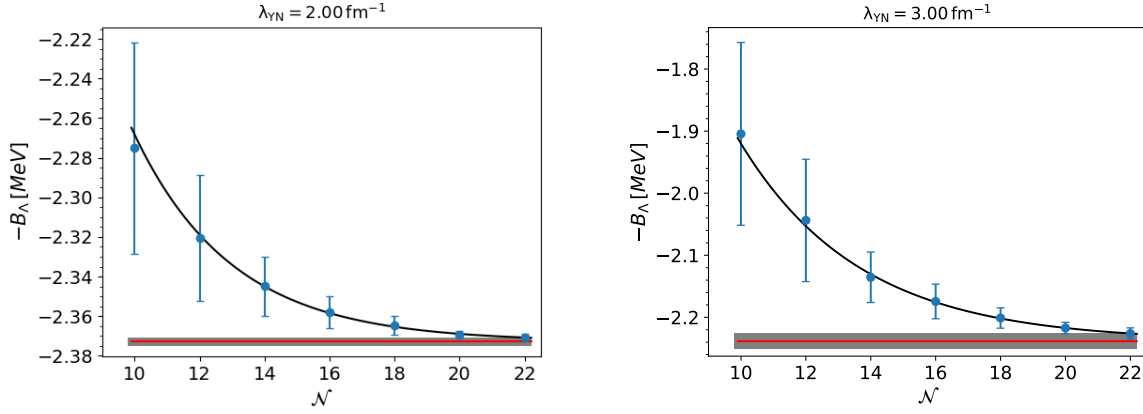


Figure 4.8: $B_\Lambda(^4_\Lambda \text{He}, 1^+)$ as a function of model space size $\mathcal{N}$. The same description as in Fig. 4.2.

state $^4_\Lambda \text{He}(0^+)$. We therefore expect that the variations of $B_\Lambda(^4_\Lambda \text{He}, 1^+)$ can be effectively removed once the nuclear core $^3\text{He}$ is properly described. Finally, we display in Fig. 4.11 the probability of finding $\Sigma$ particles $P_\Sigma$ in the wavefunction of the $^4_\Lambda \text{He}(1^+)$ state. In general, this quantity is very similar to that of the ground-state wavefunction. It is also less sensitive to the NN potentials but strongly decreased by the SRG-YN evolution.

## 4.2.3 $^5_\Lambda \text{He}(\frac{1}{2}^+, 0)$

$^5_\Lambda \text{He}$ is known as one of the best experimentally studied hypernuclei with more than 1000 events reported. Still its abnormally small separation energy $B_\Lambda(^5_\Lambda \text{He}) = 3.12 \pm 0.02$ MeV [6] was a puzzle for hypernuclear physics for decades. Any YN interaction models that reproduce binding energies
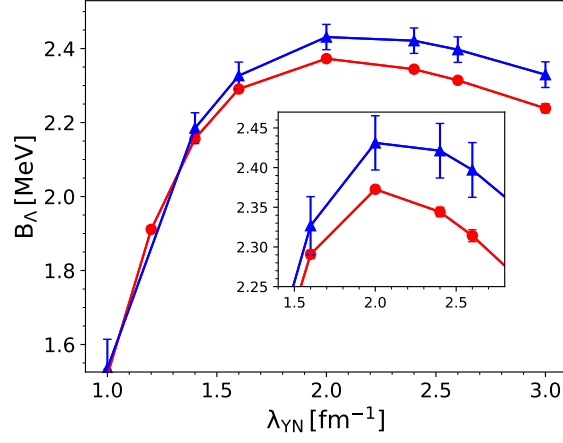
Figure 4.9: $\Lambda$-separation energy in $^4_\Lambda$He($1^+$) as a function of the SRG YN flow parameter $\lambda_{YN}$. The calculations are based on the YN NLO19(600) potential in combination with the Idaho-N$^3$LO(500) that is evolved to two flow parameters $\lambda_{NN} = 1.6$ fm$^{-1}$(red circles) and $\lambda_{NN} = 2.4$ fm$^{-1}$(blue triangles). The error bars show numerical uncertainties.



Figure 4.10: $\Lambda$-separation energy in $^4_\Lambda$He($1^+$) with respect to the $^3$He binding energies. Same description as in Fig. 4.5. The YN potential is evolved to a flow parameter of $\lambda_{YN} = 2.0$ fm$^{-1}$.

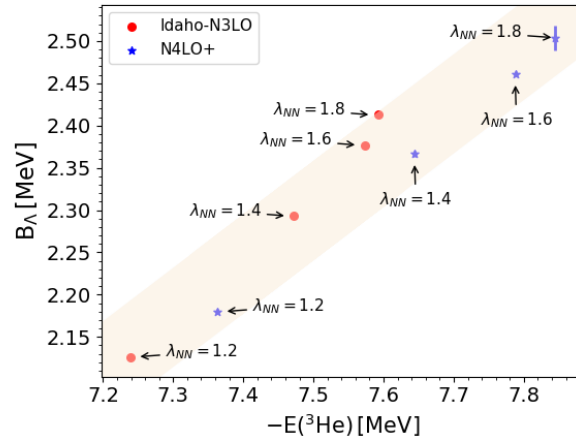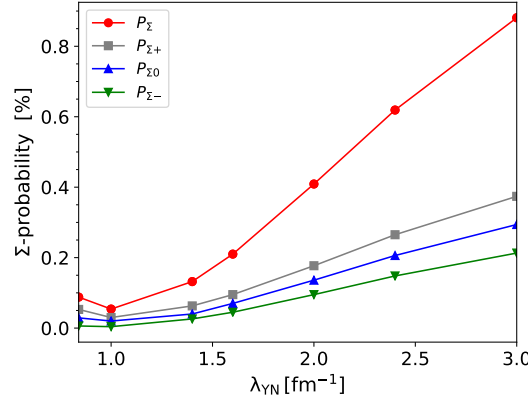Figure 4.11: Probabilities of finding a $\Sigma^+$ (grey squares), $\Sigma^0$ (blue up triangles) and $\Sigma^-$ (green down triangles) in $^4_\Lambda$He($1^+$) as functions of the SRG YN flow parameter $\lambda_{YN}$. Red circles are the total $\Sigma$ probability, $P_\Sigma = P_{\Sigma^+} + P_{\Sigma^-} + P_{\Sigma^0}$. Same description of the interactions employed as in Fig. 4.6(b).

of the $A = 3, 4$ hypernuclear systems would substantially overbind $^5_\Lambda$He [117]. It has been recently pointed out that it is the strong suppression of $\Lambda - \Sigma$ conversion in $^5_\Lambda$He that weakens the long-ranged parts of the YN interactions leading to significantly less binding energy [118, 119]. An interesting question, we want to address here, is how the SRG evolution then affects the $\Lambda$-separation energy as well as the $\Sigma$-suppression in $^5_\Lambda$He compared to the two states of the s-shell $^4_\Lambda$He hypernucleus.

First of all, due to the compactness of the nuclear core $^4$He, calculations for $^5_\Lambda$He converge much faster with respect to model space and HO frequencies $\omega$ than in the case of $^4_\Lambda$He. This is clearly exemplified in Fig. 4.12 where the dependences of the binding (left plot) and $\Lambda$ removal (right plot) energies on $\omega$ and $\mathcal{N}$ are shown, respectively. Undoubtedly, these calculations exhibit a nearly perfect convergence pattern already for model space sizes up to $\mathcal{N}_{max} = 14$ even at a rather high SRG-YN evolution parameter of $\lambda_{YN} = 2.6$ fm$^{-1}$. With that restriction on the largest model space sizes, the total number of basis states for $A = 5$ system is just slightly larger than the one for the ground state of $^4_\Lambda$He, (see Table 3.1). Consequently, binding energy calculations for $^5_\Lambda$He are almost as cheap as that for the $^4_\Lambda$He($0^+$) state. In Fig. 4.13, we study the effect of two NN interactions, the Idaho-N$^3$LO(500) (red circles) and chiral SMS N$^4$LO+(450) (blue triangles), on the binding (left figure) and $\Lambda$-separation (right figure) energies of $^5_\Lambda$He for a very wide range of YN flow parameters: $0.836 \leq \lambda_{YN} \leq 3.0$ fm$^{-1}$. To speed up the convergence, the two NN potentials are also evolved to a flow variable of $\lambda_{NN} = 1.6$ fm$^{-1}$. Evidently, the impact of these two NN models on $E(^5_\Lambda$He) is very substantial with the largest discrepancy of order of 2 MeV. On the contrary, the discrepancies in $B(^5_\Lambda$He) are considerably smaller (of order of 200 keV at $\lambda_{YN} = 2.0$ fm$^{-1}$ but are negligible for lower values of $\lambda_{YN}$). Additionally, Fig. 4.13 also clearly illustrates the pronounced influence of SRG-YN evolutions on the $\Lambda$-separation energy. The system is substantially overbound for almost all $\lambda_{YN}$ flow parameters. The strong overbiding of $^5_\Lambda$He has been also obtained by Wirth *et al.* in their calculations using the chiral YN potential at LO [41].

We further examine impact of the SRG-NN evolutions on $B_\Lambda(^5_\Lambda$He) in Fig. 4.14. Here, the $\Lambda$ removal energies are computed using the Idaho-N$^3$LO(500) (red circles) and SMS N$^4$LO+(450) (blue asterisks) that are evolved to several flow parameters $\lambda_{NN}$. We show the results for two YN
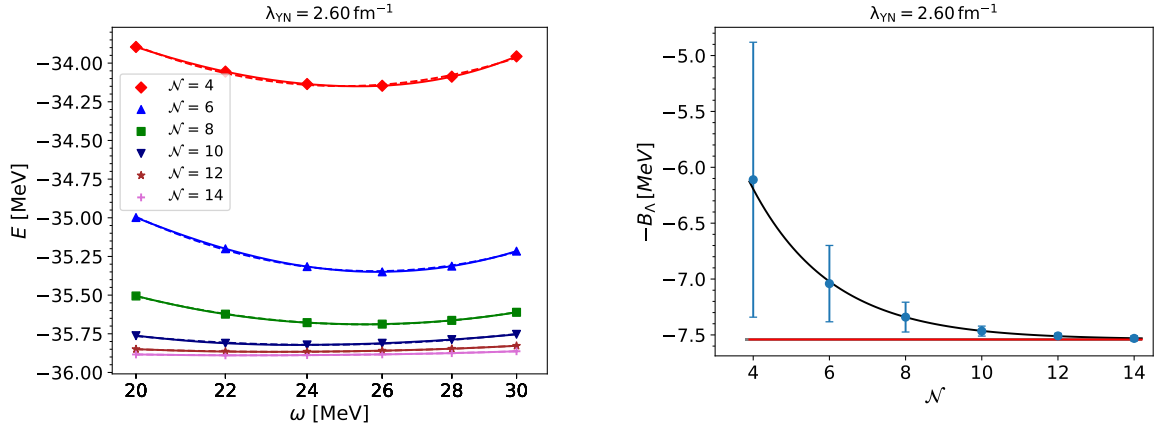
Figure 4.12: Binding energy (left figure) and $\Lambda$-separation energy (right figure) in $^5_\Lambda$He as functions of HO frequency $\omega$ (left figure) and model space size $\mathcal{N}$ (right figure), repsectively. The same descriptions of lines, symbols and interactions used as in Figs. 4.1 and 4.2.
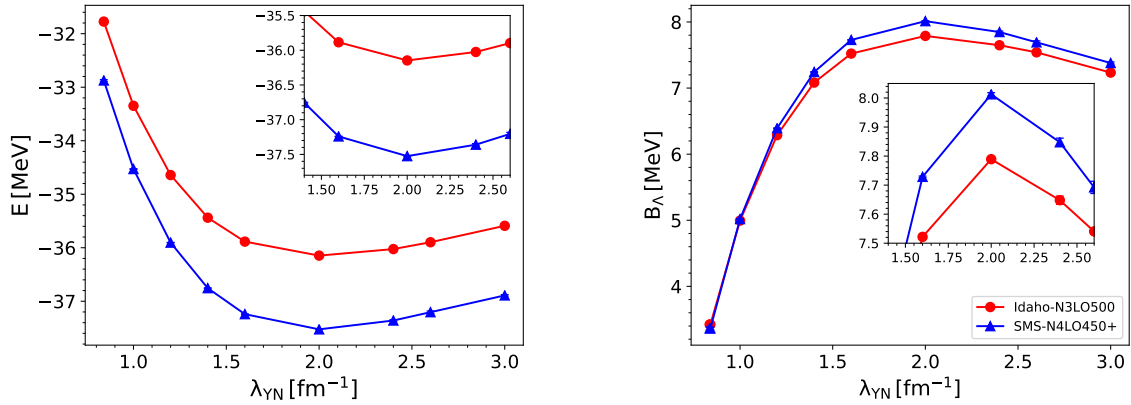


Figure 4.13: Binding energy (left figure) and $\Lambda$-separation energy (right figure) in $^5_\Lambda$He as functions of the SRG YN flow parameter $\lambda_{YN}$. The calculations are based on the YN NLO19(600) potential and two chiral NN interactions: the Idaho-N$^3$LO(500) (red circles) and the chiral-SMS N$^4$LO+(450). Both NN potentials are evolved to an SRG parameter of $\lambda_{NN} = 1.6$ fm$^{-1}$.

evolution variables: a low value of $\lambda_{YN} = 1.00$ fm$^{-1}$ (left figure) and a larger cutoff of $\lambda_{YN} = 2.0$ fm$^{-1}$ (right figure) for which the impact is expected to be most pronounced as already indicated by the right figure in Fig. 4.13. Clearly, at $\lambda_{YN} = 2.0$ fm$^{-1}$, the variation of $B_\Lambda$ stemming from the SRG evolution of individual NN interaction model is roughly 600 keV while the overall discrepancy between the two evolved NN potentials can be as twice as large. As we expected, such variation becomes insignificant at lower cutoff, $\lambda_{YN} = 1.0$ fm$^{-1}$. One can also quickly notice that, for both $\lambda_{YN}$ cutoffs, the widths of the linear fitting band (light colored band) are quite large, about 200 keV, as compared to that of the $A = 4$ systems. However, taken the considerable overbing of $^5_\Lambda$He (of order of 8 MeV), the relative width (roughly 25%) is approximately the same as for the two states of $^4_\Lambda$He.
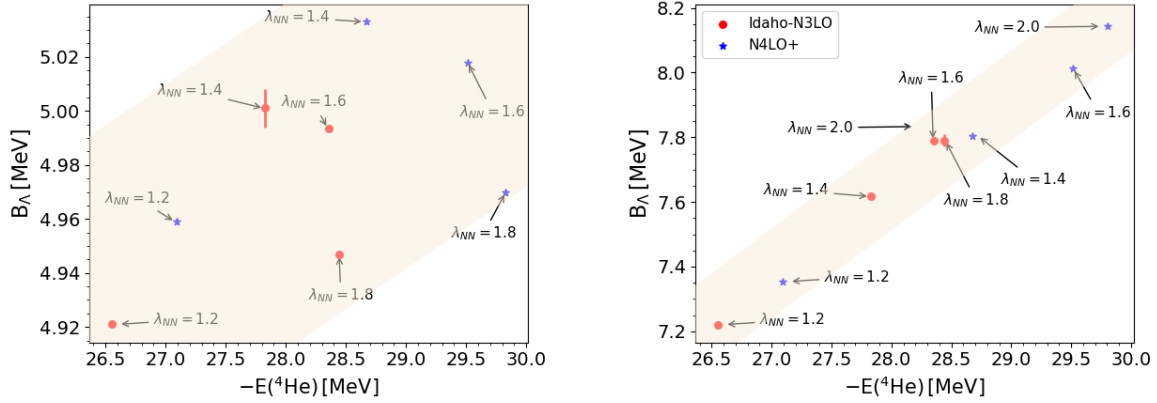
Figure 4.14: $\Lambda$-separation energy in $^5_\Lambda$He with respect to the $^4$He binding energies. Same description as in Fig. 4.5. The YN potential is evolved to two flow parameters of $\lambda_{YN} = 1.0$ fm$^{-1}$ (left) and $\lambda_{YN} = 2.0$ fm$^{-1}$ (right). Note the different scales for the y-axis in left and right figures.

Finally, Fig. 4.15 displays probabilities of finding $\Sigma$ particles $P_\Sigma$ in the ground-state wavefunction of $^5_\Lambda$He computed with the flow parameter $\lambda_{YN}$ ranging from 0.836 fm$^{-1}$ to 3.0 fm$^{-1}$ and the Idaho-N$^3$LO(5OO) potential that is evolved to an SRG parameter of $\lambda_{NN} = 1.6$ fm$^{-1}$. We note that, the $\Sigma$-probabilities calculated using the SMS N$^4$LO+(45O) are very similar to Fig. 4.15. Since the nuclear core $^4$He is predominantly (more than 98%) in its ground state with zero isospin, the hyperons $\Sigma^+, \Sigma^0$ and $\Sigma^-$ appear in the $^5_\Lambda$He$(\frac{1}{2}, 0)$ state with almost the same probabilities (which are why hardly distinguishable in Fig. 4.15). Surprisingly, at high SRG-YN cutoffs, the $\Sigma$-probability $P_\Sigma(^5_\Lambda$He$)$ is quite large, for example $P_\Sigma(^5_\Lambda$He$) = 1.3\%$ at $\lambda_{YN} = 3.0$ fm$^{-1}$, which is much larger than $P_\Sigma(^4_\Lambda$He$, 0^+) = 0.86\%$ at the same cutoff. Comparing Fig. 4.15 with Figs. 4.6(b) and 4.11 one can notice that $P_\Sigma(^5_\Lambda$He$)$ is suppressed by the SRG evolution somewhat faster than the $\Sigma$-probabilities in the doublet $^4_\Lambda$He$(0^+, 1^+)$. Furthermore, at SRG parameters below the value of $\lambda_{YN} = 1.2$ fm$^{-1}$ the probability of finding $\Sigma$ in $^5_\Lambda$He becomes negligible (less than 0.1%).

## 4.2.4 $^6_\Lambda$Li$(1^-, \frac{1}{2})$

We now investigate more complex p-shell hypernuclei. The smallest p-shell hypernuclei are the isospin mirror pair $^6_\Lambda$Li and $^6_\Lambda$He. While the $^6_\Lambda$Li hypernucleus is particle-unstable against proton emission ($^6_\Lambda$Li $\to$ $^5_\Lambda$He + p), the ground state of $^6_\Lambda$He is found experimentally bound by 0.17 MeV below the $^5_\Lambda$He + n threshold [73]. Nevertheless, the J-NCSM calculations for both of systems show a similar convergence behavior. Our results also show that, both $^6_\Lambda$Li and $^6_\Lambda$He hypernuclei are somewhat less bound than the s-shell hypernucleus $^5_\Lambda$He. Since these two systems are quite similar, we will focus mainly on the lowest state $(1^-, \frac{1}{2})$ of $^6_\Lambda$Li, which dominantly composes of a core nucleus $^5$Li in its lowest energy resonance state $(\frac{3}{2}^-, \frac{1}{2})$ (with more than 96%) and a $\Lambda$ hyperon in an s-orbital. Here, the resonance energies $E_{rs}(^5$Li$)$ and $E_\Lambda(^6_\Lambda$Li$)$ are normally measured from their particle breakup thresholds $^4$He +p and $^4$He + p +$\Lambda$, respectively, e.g. $E_\Lambda(^6_\Lambda$Li$) = E(^4$He$) - E(^6_\Lambda$Li$)$. The numerical $\Lambda$-separation energy $B_\Lambda(^6_\Lambda$Li$)$ can be then calculated as the difference between $E_{rs}(^5$Li$)$ and $E_\Lambda(^6_\Lambda$Li$)$, as considered in [73]. However, for the particle-unstable $^6_\Lambda$Li hypernucleus the
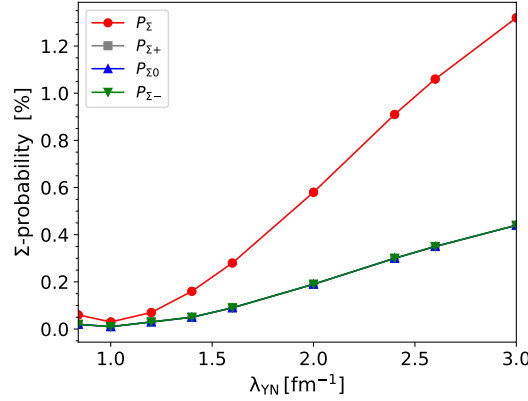
Figure 4.15: Probabilities of finding a $\Sigma^+$ (grey squares), $\Sigma^0$ (blue up triangles) and $\Sigma^-$ (green down triangles) in $^5_\Lambda$He as functions of the SRG YN flow parameter $\lambda_{YN}$. Red circles are the total $\Sigma$ probability, $P_\Sigma = P_{\Sigma^+} + P_{\Sigma^-} + P_{\Sigma^0} = 3P_{\Sigma^+}$. Same description of the employed interactions as in Fig. 4.6.
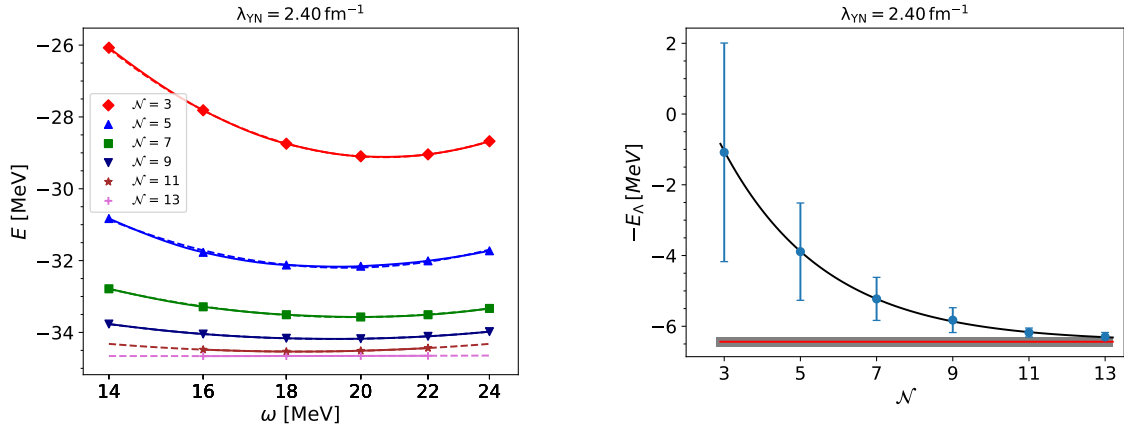


Figure 4.16: $B_\Lambda(^6_\Lambda\text{Li}, 1^- \frac{1}{2})$ as a function of model space size $\mathcal{N}$. The same description of lines and symbols as in Fig. 4.2.

resonance energy $E_\Lambda(^6_\Lambda\text{Li})$ itself will be more meaningful than the considered $\Lambda$-separation energy.

When switching to p-shell hypernuclei, the numbers of basis and intermediate states grow dramatically, as illustrated in Table 3.1. In order to make the energy calculations for the $A = 6$ systems, we truncate the basis size with $\mathcal{N}_{max} = 13$. Our calculations with model spaces up to $\mathcal{N} = 13$ exhibit a reasonable converged pattern for small values of the SRG-NN flow parameter. Fig. 4.16 together with the red curve in Fig. 4.17 demonstrably exemplify the well-converged results for the SRG-NN cutoff of $\lambda_{NN} = 1.6$ fm$^{-1}$. However, the numerical uncertainties grow rather quickly when the flow variable increases to $\lambda_{NN} = 2.0$ fm$^{-1}$ as it is clearly seen from the the blue curve in Fig. 4.17. The error bars now become too large, so no useful information can be deduced. We therefore refrain from investigating the effects of NN interactions on $E_\Lambda(^6_\Lambda\text{Li})$, but expect the
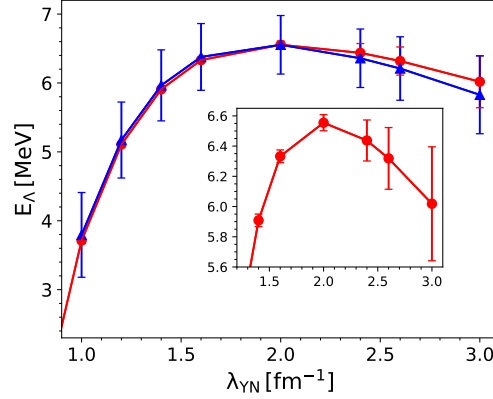
Figure 4.17: $E_\Lambda$ in $^6_\Lambda$Li($1^-$) as a function of the SRG YN flow parameter $\lambda_{YN}$. The calculations are based on the YN NLO19(600) potential in combination with the Idaho-N$^3$LO(500) evolved to two flow parameters of $\lambda_{NN} = 1.6$ fm$^{-1}$(red circles) and $\lambda_{NN} = 2.0$ fm$^{-1}$(blue triangles). The inset is to make the error bars for $\lambda_{NN} = 1.6$ fm$^{-1}$ more visible.

dependence is very similar to that of $^5_\Lambda$He.

## 4.2.5 $^7_\Lambda$Li($\frac{1}{2}^+$, 0)

We now turn to one of the most interesting p-shell hypernuclei, the $^7_\Lambda$Li system. This is an important system with many experimentally observed particle-stable states even when the corresponding nuclear core states are unbound. Thereby, many interesting properties of hypernuclei, e.g the glue-like role of a $\Lambda$ hyperon or skin structures can be demonstrated [73–75]. We will start with the ground state $^7_\Lambda$Li($\frac{1}{2}^+$, 0). As it has been demonstrated for the $A = 4 − 6$ systems, the numbers of basis states grow exponentially with increasing the particle number. The energy calculations hence become more and more expensive and eventually reach the limit of the computational resources. At that point, it is extremely crucial to seek some means of restrictions in order to somewhat reduce those basis states that are unimportant to the energy calculations, and thereby, facilitate calculations with very large model spaces. Fortunately, when carefully study the wavefunctions of the $A = 4 − 6$ hypernuclei, we observe that they predominantly compose of the nuclear cores in their lowest energy states and a hyperon in an s-shell. In other words, the basis functions with the lowest-lying core states then contribute dominantly to the final binding energies of these systems. We expect a very similar situation for the ground state of $^7_\Lambda$Li.

In Table 4.2, we present the probabilities of finding the $A = 6$ nuclear cores in different states determined by the total angular momentum $J_{core}$ together with the isospin $T_{core}$. Evidently, the largest contributions (more than 99.8%) to the ground state wavefunction are from basis states which are constructed from those nuclear core states with $J_{core} \leq J_{core}^{max} = 3$. Among those dominant nuclear core states, the ground state of $^6$Li ($J_{core} = 1, T_{core} = 0$) alone accounts for more than 99.2% and 98.2% for $\lambda_{YN} = 0.836$ and 1.6 fm$^{-1}$, respectively. The remaining contributions from other states with higher nuclear-core total angular momenta, $J_{core} > 3$, are insignificant, less than 0.2%. This observation is indeed in accordance with the results for the s-shell hypernuclei as well as with general expectation. Very often in many-body calculations such as the shell-model or cluster-model,

| $J_{core}$ | $\lambda_{YN} = 0.836$ fm$^{-1}$ | | $\lambda_{YN} = 1.6$ fm$^{-1}$ | |
|:---:|:---:|:---:|:---:|:---:|
| | $T_{core} = 0$ | $T_{core} = 1$ | $T_{core} = 0$ | $T_{core} = 1$ |
| 0 | 0.0152 | 0.037 | 0.0625 | 0.0325 |
| 1 | 99.2356 | 0.1146 | 98.277 | 0.1869 |
| 2 | 0.2266 | 0.0512 | 0.6692 | 0.1274 |
| 3 | 0.3143 | 0.0037 | 0.6293 | 0.0103 |
| 4 | 0.0013 | 0.0004 | 0.002 | 0.0016 |
| 5 | 0.0001 | 0.0000 | 0.0008 | 0.0000 |

Table 4.2: Probabilities (in percentage) of finding the A=6 nuclear core states with definite quantum numbers $(J_{core}, T_{core})$ in the ground state of $^{7}_{\Lambda}$Li$(\frac{1}{2}^{+}, 0)$ for model space up to $\mathcal{N} = 10$. Calculations were based on the chiral SMS N$^4$LO+(450) for the NN potential that is evolved to $\lambda_{NN} = 1.6$ fm$^{-1}$, in combination with the YN NLO13(700) for two flow parameters of $\lambda_{YN} = 0.836$ and 1.6 fm$^{-1}$.

| $J_{core}^{max}$ | $\lambda_{YN} = 0.836$ fm$^{-1}$ | $\lambda_{YN} = 1.60$ fm$^{-1}$ |
|:---:|:---:|:---:|
| 2 | -38.1824 | -43.9467 |
| 3 | -38.2560 | -44.1985 |
| 4 | -38.2570 | -44.2031 |
| 5 | -38.2571 | -44.2039 |
| 8 | -38.2571 | -44.2040 |

Table 4.3: Binding energy E($^{7}_{\Lambda}$Li, $\mathcal{N} = 10$) for different values of $J_{core}^{max}$. NN and YN potentials are the same as in Table 4.2. Energies are given in MeV.

one constraints the quantum numbers of the nuclear cores to that of the two lowest states, namely $J_{core} \leq 1$ and $T_{core} = 0$ [120].

In order to elaborate the convergence of $E(^{7}_{\Lambda}$Li$, \frac{1}{2}^{+})$ with respect to $J_{core}$, we perform calculations with various sets of basis states that are constructed based on different restrictions on the maximal value of the total angular momentum of the core, $J_{core}^{max}$. The results for model space up to $\mathcal{N} = 10$ and two YN flow parameters of $\lambda_{YN} = 0.836$ and 1.6 fm$^{-1}$ are tabulated in Table 4.3. One sees that, increasing $J_{core}^{max}$ from 3 to 8 changes the actual binding energies by only several keV, e.g., about 5 (1) keV for $\lambda_{YN} = 1.6\,(0.836)$ fm$^{-1}$, which is much smaller than the numerical accuracy we aim at. Therefore, restricting $J_{core}^{max} = 3$ should be sufficient to obtain accurate ground-state binding energies for $^{7}_{\Lambda}$Li. This, in turn, can greatly facilitate the basis states generation as well as the energy calculations. To illustrate for the last statement, we show in Tab. 4.4 the dimensions of the basis and

| $J_{core}^{max}$ | $\lvert \, \bullet\!-\!\bullet \, \rangle$ | $\lvert \, \bullet\!\!\perp\!\bullet \, \rangle$ | Gb/task |
|:---:|:---:|:---:|:---:|
| 2 | 161.847 | 2.622.437 | 5.8 |
| 3 | 182.488 | 2.970.265 | 8.9 |
| 4 | 187.825 | 3.064.627 | 9.8 |
| 8 | 188.638 | 3.080.633 | 15.5 |

Table 4.4: Total numbers of the basis states (second column), the intermediate states (third column) and memory usage per node (last column) for model space up to $\mathcal{N} = 10$ and different $J_{core}^{max}$.

intermediate states together with the memory usage[1] per node for several values of $J_{core}^{max}$.

Now, taking into account the restriction of $J_{core}^{max} = 3$, we are able to generate the basis sets for the ground-state energy calculations of the $^{7}_{\Lambda}$Li with model space up to $\mathcal{N}_{max} = 12$. The dimensionality of these bases are given in Table 3.1. Still, with the model-space truncation of $\mathcal{N}_{max} = 12$, the basis sizes have become tremendously large and hence the energy calculations for this model space are very expensive. In order to save some computational resources, one then needs to choose the useful range of HO frequencies $\omega$ for $\mathcal{N}_{max}$ with great consideration. Fortunately, this $\omega$-range can be obtained from an educated guess based on the $\omega$-dependence of the energy curve for the ($\mathcal{N}_{max} - 2$) model space, $E_{\mathcal{N}_{max}-2,\omega}$. In addition, because the $\omega$-dependence of the $E_{\mathcal{N}_{max},\omega}$ curve is quite flat, it requires only three or four points in order to obtain a good $\omega$-fit with the fitting function in Eq. (4.1). This strategy is applied, for example, to the energy curve $E_{\mathcal{N}=12,\omega}$ shown in the left plot of Fig. 4.18. Here, the right figure illustrates the extrapolation of the binding energy to infinite model space. Evidently, with the truncation of $\mathcal{N}_{max} = 12$, we obtain well-converged ground-state binding energies for the hypernucleus $^{7}_{\Lambda}$Li as well as for the parent nucleus $^{6}$Li. Figs. 4.19 demonstrate the convergence of $B_{\Lambda}(^{7}_{\Lambda}\text{Li}, \frac{1}{2}^{+} 0)$ with regard to model space $\mathcal{N}$ for several flow parameters $\lambda_{YN}$. Interestingly, for all the flow parameters $\lambda_{YN}$ considered, the $\Lambda$-separation energy converges significantly faster than the individual binding energies of the hypernucleus and of the corresponding core nucleus. It is therefore reasonable to employ a linear fitting function instead of the exponential form as in Eq. (4.2) for the extrapolation in model space. It can also be observed from Fig. 4.19 that with $\lambda_{YN}$ in a range of $1.0 \leq \lambda_{YN} \leq 2.0$ fm$^{-1}$, one obtains the best-converged separation energy. Surprisingly, the energy calculation with $\lambda_{YN} = 0.82$ fm$^{-1}$ converges somewhat more slowly as compared to the calculation with $\lambda_{YN} = 1.0$ fm$^{-1}$. This probably also relates to the observation that the $\Sigma$-probability reaches its minimum at the cutoff $\lambda_{YN} = 1.0$ fm$^{-1}$ and slightly increases as the YN potential being evolved further.

The excellent convergence of $B_{\Lambda}$ in $^{7}_{\Lambda}$Li($\frac{1}{2}^{+}$, 0) allows for a comprehensive study of the influences of SRG-YN and SRG-NN evolutions on this quantity. The results are presented in Figs. 4.20 and 4.21, respectively. The variation of $B_{\Lambda}(^{7}_{\Lambda}\text{Li}, \frac{1}{2}^{+})$ due to the SRG-YN evolution is rather substantial, about

---

[1] Note that the reduction in the memory usage per node will be much more significant when applying the $J_{core}^{max} = 3$ to the largest model space, namely $\mathcal{N}_{max} = 12$.
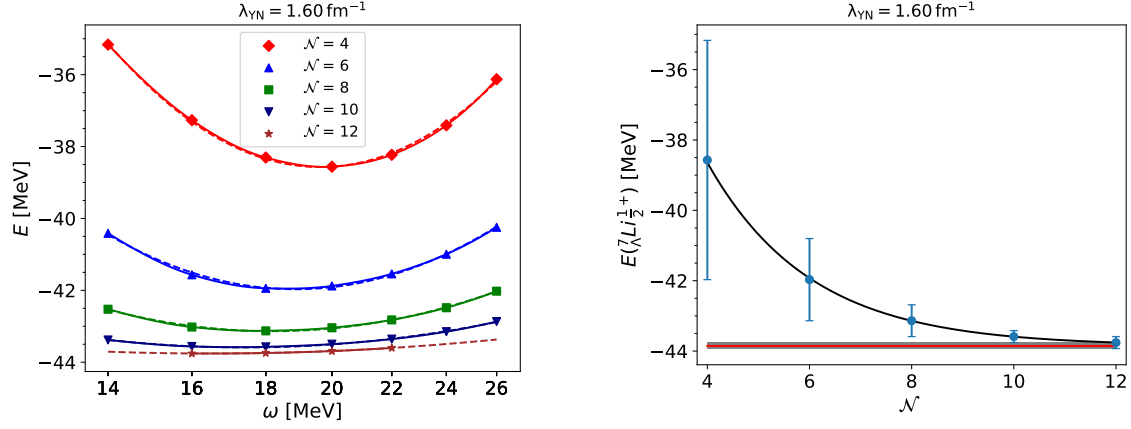
Figure 4.18: Extrapolations of the binding energy $E(^{7}_{\Lambda}\mathrm{Li}, \frac{1}{2}^{+} 0)$ in HO-$\omega$ (left figure) and $\mathcal{N}$ (right figure) spaces. Same descriptions of lines, symbols and employed interactions as in Figs. 4.1 and 4.2.
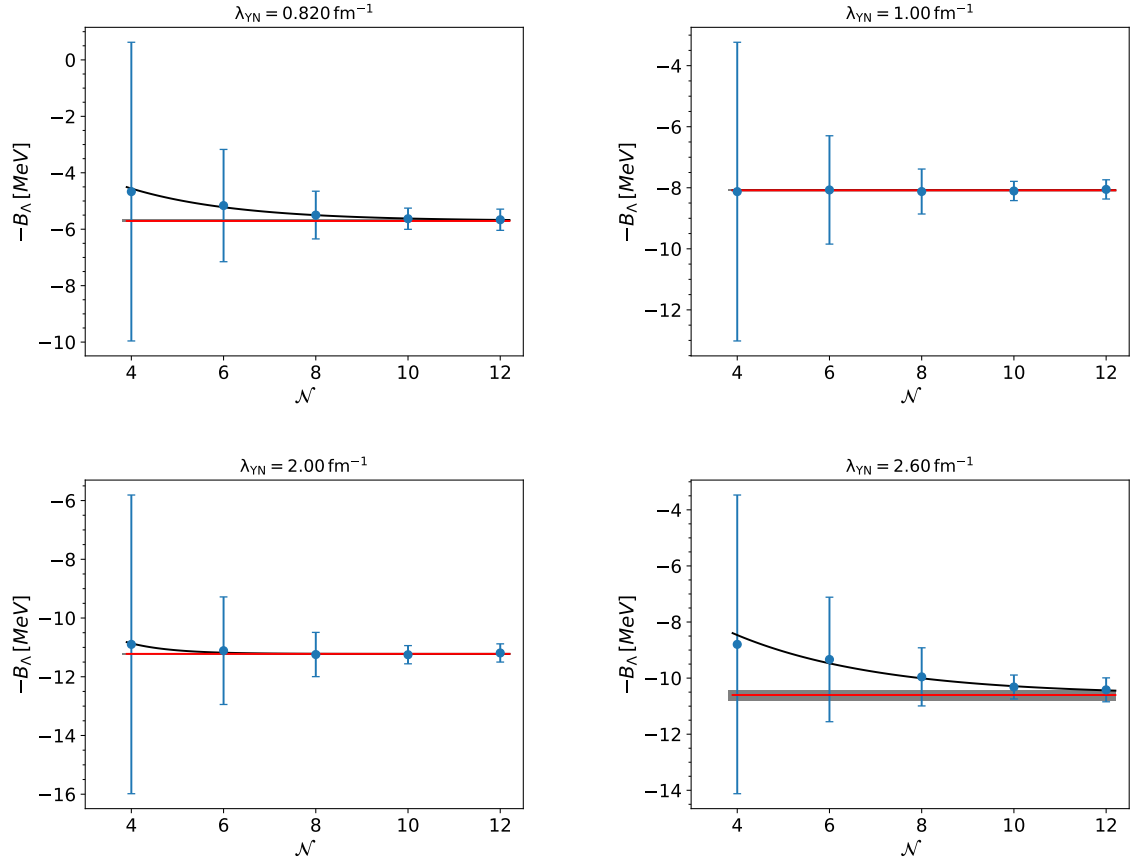


Figure 4.19: $B_{\Lambda}(^{7}_{\Lambda}\mathrm{Li}, \frac{1}{2}^{+} 0)$ as a function of model space size $\mathcal{N}$. The same description of lines and symbols and the employed interactions as in Fig. 4.2.
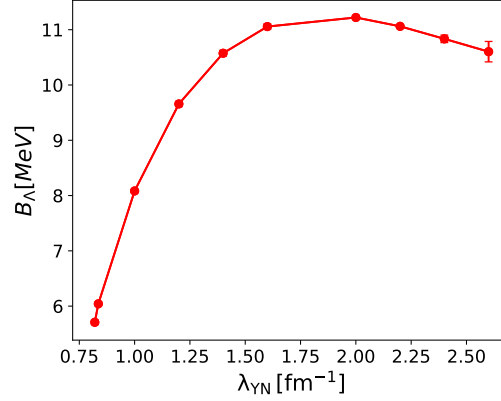
Figure 4.20: $B_\Lambda(^{7}_{\Lambda}\text{Li}, \frac{1}{2}^{+} 0)$ as a function of $\lambda_{YN}$. The calculations are based on the YN NLO19(600) potential in combination with the Idaho-N$^3$LO(500) evolved to a flow parameter of $\lambda_{NN} = 1.6$ fm$^{-1}$.

6 MeV, in comparison with a change of 4.5 MeV in $B_\Lambda(^{5}_{\Lambda}\text{He})$ for the same range of $\lambda_{YN}$, see also Fig. 4.13. Similarly, the effect of the SRG-NN evolution on $B_\Lambda(^{7}_{\Lambda}\text{Li}, \frac{1}{2}^{+})$ for a SRG-YN flow parameter of $\lambda_{YN} = 2.0$ fm$^{-1}$ is also pronounced, causing the overall variation of about 0.8 MeV in $B_\Lambda(^{7}_{\Lambda}\text{Li}, \frac{1}{2}^{+})$ for individual NN interaction, which is almost twice as large as the one in $B_\Lambda(^{5}_{\Lambda}\text{He})$. Also, the relative variation (relative width of the linear fitting band shown in Fig. 4.21) is also somewhat larger, about 40% in comparison with 25% for the s-shell hypernuclei. We should remark that the nuclear-core binding energy calculations converge visibly faster for the N$^4$LO+(450) than for the Idaho-N$^3$LO(500). If one leaves the result for the Idaho-N$^3$LO(500) at the SRG cutoff of $\lambda_{NN} = 1.8$ fm$^{-1}$ aside, the relative variation of $B_\Lambda(^{7}_{\Lambda}\text{Li}, \frac{1}{2}^{+})$ is much smaller, about 25%, which is the same as for the s-shell. Furthermore, at lower values of $\lambda_{YN}$ ($\lambda_{YN} \leq 1$ fm$^{-1}$) the discrepancies stemming from different NN forces is also small, of order of 0.2 MeV.

## 4.2.6 $^{7}_{\Lambda}\text{Li}(\frac{3}{2}^{+}, 0)$

We have experienced an exponential increase in the basis sizes for the ground state of $^{7}_{\Lambda}\text{Li}$. The situation is even much severer for the first excited state. Hence, in order to extend the calculations to large model space, we need to employ a similar restriction for the maximal total angular momentum of the core $J_{core}^{max}$, like for the ground state. It is natural to expect that the $J_{max}^{max}$ for the $(\frac{3}{2}^{+}, 0)$ state can be different from that for the $(\frac{1}{2}^{+}, 0)$ state. To determine the $J_{core}^{max}(\frac{3}{2}^{+})$ we shall investigate the convergence of $E(^{7}_{\Lambda}\text{Li}, \frac{3}{2}^{+})$ with respect to $J_{core}^{max}$ using model spaces up to $\mathcal{N} = 10$. In Tab. 4.2, we present the probabilities of finding $A = 6$ nuclear cores with definite angular momentum $J_{core}$ and isospin $T_{core}$ in the wavefunction of $^{7}_{\Lambda}\text{Li}(\frac{3}{2}^{+})$. Clearly, there is more than 99.4% that the $A = 6$ nuclear cores reside in their lowest states with the total angular momentum $J_{core} \leq 2$. Nevertheless, when checking the convergence of $E(^{7}_{\Lambda}\text{Li}(\frac{3}{2}^{+}, \mathcal{N} = 10)$, we observe that those states with $J_{core} = 3, 4$ still contribute visibly to the binding energy as shown in Tab. 4.6. Meanwhile, changing $J_{core}^{max}$ from
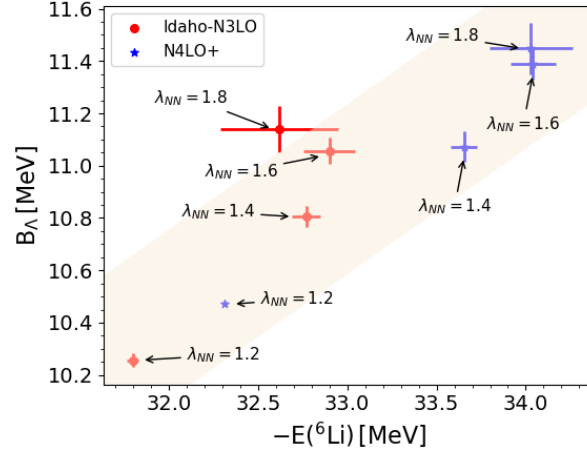
Figure 4.21: $B_\Lambda(^7_\Lambda\text{Li}, \frac{1}{2}^+ 0)$ with respect to the $^6$Li core binding energies. Same description as in Fig. 4.5. The YN potential is evolved to an evolution parameter of $\lambda_{YN} = 2.0$ fm$^{-1}$.

| $J_{core}$ | $\lambda_{YN} = 0.836$ fm$^{-1}$ | | $\lambda_{YN} = 1.6$ fm$^{-1}$ | |
| | $T_{core} = 0$ | $T_{core} = 1$ | $T_{core} = 0$ | $T_{core} = 1$ |
|---|---|---|---|---|
| 0 | 0.0136 | 0.0103 | 0.0935 | 0.0113 |
| 1 | 99.4128 | 0.0766 | 98.1598 | 0.1584 |
| 2 | 0.1988 | 0.094 | 0.8504 | 0.1328 |
| 3 | 0.186 | 0.0044 | 0.5468 | 0.0356 |
| 4 | 0.0017 | 0.0006 | 0.0018 | 0.0074 |
| 5 | 0.0000 | 0.0000 | 0.0008 | 0.0004 |

Table 4.5: Probabilities (in percentage) of finding A=6 nuclear core states with definite quantum numbers $(J_{core}, T_{core})$ in first excited state $^7_\Lambda\text{Li}(\frac{3}{2}^+, 0)$ for model space up to $\mathcal{N} = 10$.

| $J_{max}^{core}$ | $\lambda_{YN} = 0.836$ | $\lambda_{YN} = 1.60$ |
|---|---|---|
| 2 | -38.1422 | -43.5061 |
| 3 | -38.2032 | -43.5218 |
| 4 | -38.2046 | -43.7969 |
| 5 | -38.2049 | -43.7984 |
| 6 | -38.2049 | -43.7986 |

Table 4.6: Binding energy $E(^{7}_{\Lambda}\text{Li}\frac{3}{2}^{+}, \mathcal{N} = 10)$ for different values of $J_{core}^{max}$. NN and YN potentials are the same as in Table 4.2. Energies are given in MeV.
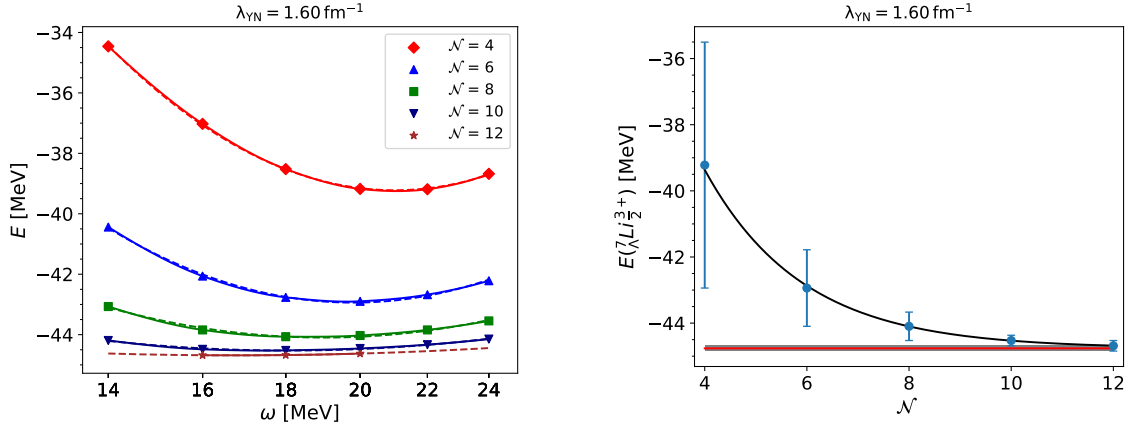


Figure 4.22: Binding energy in $^{7}_{\Lambda}\text{Li}(\frac{3}{2}^{+}, 0)$ as a function of model space size $\mathcal{N}$. The same description of lines and symbols as in Figs. 4.1 and 4.2. The calculations are based on SMS N$^4$LO+(450) evolved to a flow parameter of $\lambda_{NN} = 1.6$ fm$^{-1}$ and the YN NLO19(600) potential with an evolution variable of $\lambda_{YN} = 1.6$ fm$^{-1}$.

4 to 6 only lowers the binding energy binding roughly by 1.5 keV. Hence, for the first excited state of $^{7}_{\Lambda}\text{Li}$, we apply the truncation $J_{core}^{max} = 4$ for the maximal value of angular momentum of the cores. Although we expect that the excited state more slowly converges with regard to the model space $\mathcal{N}$ than the ground state does, like in the case of $^{4}_{\Lambda}\text{He}$, our calculations show that the two states converged practically with the same speed. This can be seen by comparing Figs. 4.18 and 4.22 or Figs. 4.18 and 4.23. It is noted that the first-excited state energy calculations are however slightly more expensive. Also, Figs. 4.22 and 4.23 clearly demonstrate the well-converged results for $^{7}_{\Lambda}\text{Li}(\frac{3}{2}^{+})$.
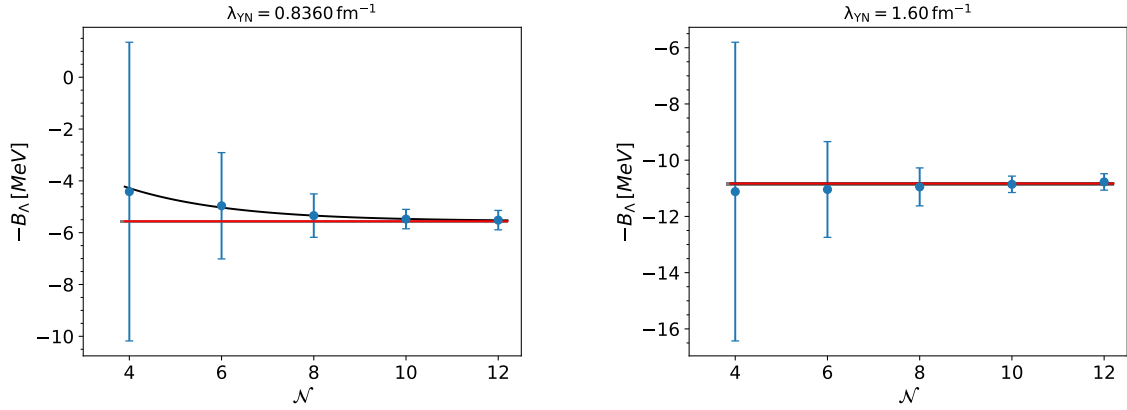
Figure 4.23: Separation energy in $^7_\Lambda\mathrm{Li}(\frac{3}{2}^+, 0)$ as a function of model space size $\mathcal{N}$. The calculations are based on SMS N$^4$LO+(450) evolved to a flow parameter of $\lambda_{NN} = 1.6$ fm$^{-1}$ and the YN NLO19(600) potential evolved to two values $\lambda_{YN} = 0.836$ (left) and 1.6 fm$^{-1}$ (right) .

We refrain from discussing the effects of the SRG-YN and SRG-NN evolutions on $B_\Lambda(^7_\Lambda\mathrm{Li}, \frac{3}{2}^+)$ but confirm that they are practically very similar to those in the ground state and move on to investigate the energy spectrum of $^7_\Lambda\mathrm{Li}$.

# 4.3 Energy spectrum of $^7_\Lambda\mathrm{Li}$

Energy spectra play an important role in hypernuclear physics. The level splittings of hypernuclei (in particular of the light $p$-shell hypernuclei such as $^7_\Lambda\mathrm{Li}$) provide valuable information on the spin-dependence parts of the YN interaction [12, 121]. The former has been intensively investigated in numerous theoretical works using the shell-model or cluster methods in combination with some effective potentials [12, 77, 121, 122], and also recently within the IT-NCSM employing the chiral YN interaction at LO [41, 88]. In this subsection, we focus on the level structure of $^7_\Lambda\mathrm{Li}$ calculated with the YN NLO19 potential. The impact of different chiral potentials on the level splitting will be thoroughly discussed in Section 4.6.

Unlike the $\Lambda$-separation energies, the excitation energies $E_{ex}$, deduced from the energies of the emitted $\gamma$-rays, are known with much higher accuracy. Likewise, these energies can also be accurately computed within the J-NCSM approach. Indeed, when investigating the excitation energies $E_{ex}(^7_\Lambda\mathrm{Li})$, we observe that they are much more stable with respect to the model space $\mathcal{N}$ than the individual binding energies of the corresponding states. We exemplify this with the first excitation energies, $E_{ex}(\frac{3}{2}^+)$, calculated with model space sizes up to $\mathcal{N} = 12$ and for two flow parameters of $\lambda_{YN} = 0.836$ and 1.6 fm$^{-1}$. The results are shown visually in Fig. 4.24 and also tabulated in Table 4.7. One sees that, for both values of $\lambda_{YN}$, $E_{ex}(\frac{3}{2}^+)$ practically converges within 10 keV already with model space up to $\mathcal{N} = 10$, meanwhile the individual binding energies still change by an order of 150 keV. Hence, for the other higher-lying energy levels[2], namely $\frac{5}{2}^+$ and

---

[2] Given that the experimental value of $E_{ex}(\frac{3}{2}^+)$ is rather small and measured with high very accuracy, $E_{ex}(\frac{3}{2}^+) = 691.7 \pm 0.6 \pm 1.0$ keV [123], we aim for the numerical uncertainty of less than 10 keV for the first excitation energy. In order to reach that level of accuracy, calculations with model space sizes up to $\mathcal{N}_{max} = 12$ are necessary.
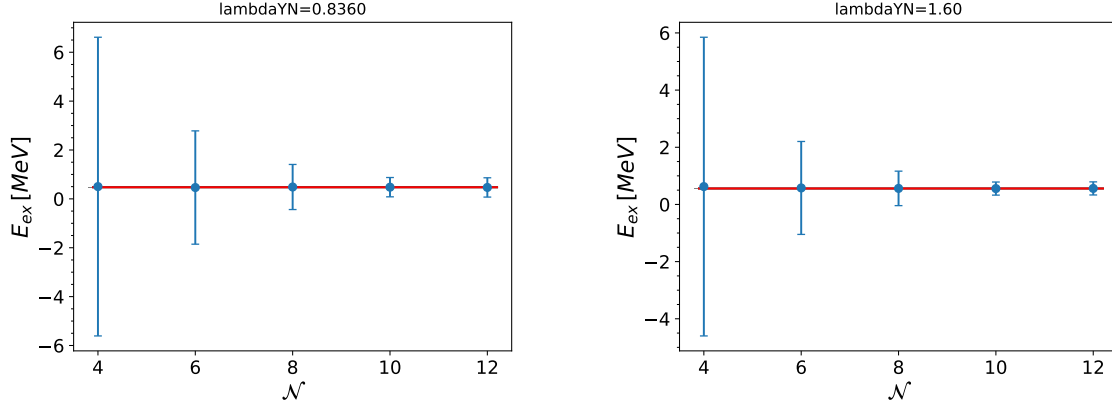
Figure 4.24: First excitation energy in $^{7}_{\Lambda}$Li as a function of model space size $\mathcal{N}$. Same description of lines, symbols and the employed NN and YN interactions as in Fig. 4.23.

| | $\lambda_{YN} = 0.836$ fm$^{-1}$ | | | $\lambda_{YN} = 1.6$ fm$^{-1}$ | | |
|---|---|---|---|---|---|---|
| $\mathcal{N}$ | $E(\frac{1}{2}^{+})$ | $E(\frac{3}{2}^{+})$ | $E_{\mathrm{ex}}$ | $E(\frac{1}{2}^{+})$ | $E(\frac{3}{2}^{+})$ | $E_{\mathrm{ex}}$ |
| 4 | -33.021 | -32.519 | 0.502 | -39.846 | -39.221 | 0.625 |
| 6 | -37.323 | -36.859 | 0.464 | -43.516 | -42.939 | 0.577 |
| 8 | -38.973 | -38.488 | 0.486 | -44.658 | -44.096 | 0.562 |
| 10 | -39.622 | -39.144 | 0.478 | -45.081 | -44.526 | 0.555 |
| 12 | -39.896 | -39.428 | 0.468 | -45.246 | -44.685 | 0.561 |

Table 4.7: Binding energies of the ground and first excited states, and the first excitation energy in $^{7}_{\Lambda}$Li. Same NN and YN potentials as in Fig. 4.23. Energies are given in MeV.

$\frac{7}{2}^{+}$ with isospin $T = 0$ and $\frac{1}{2}^{+}$ with isospin $T = 1$, it would be sufficient to truncate model-space size with $\mathcal{N}_{\mathrm{max}} = 10$. By doing so, we could save a considerable amount of computational resources while still obtain a well-converged (with the accuracy of several tens keV) energy spectrum of $^{7}_{\Lambda}$Li.

Fig. 4.25 displays the level splittings of $^{7}_{\Lambda}$Li computed using the SMS N$^{4}$LO+(450) evolved to an SRG cutoff of $\lambda_{NN} = 1.6$ fm$^{-1}$ in combination with the YN NLO19(600) for a flow parameter of $\lambda_{YN} = 0.82$ fm$^{-1}$. It is noted that, at this specific $\lambda_{YN}$ flow parameter, the experimental $\Lambda$-separation energies of both $^{5}_{\Lambda}$He and $^{7}_{\Lambda}$Li$(\frac{1}{2}^{+}, 0)$ are well-reproduced, for detailed discussion we refer to Section 4.4. Here, the energy levels are represented by bands with different colours. The width of each band indicates the numerical uncertainty which is hardly visible in all cases. The spectrum of the $^{6}$Li core is also shown together with its experimental levels. One sees that the presence of a $\Lambda$ hyperon causes the splitting of each energy level (with $J > 0$) of the core into a doublet. The splitting within a doublet is governed mainly by the strengths of the spin-spin, tensor and hyperon-spin-dependent spin-orbit YN interaction while the doublet spacing follows the excitations
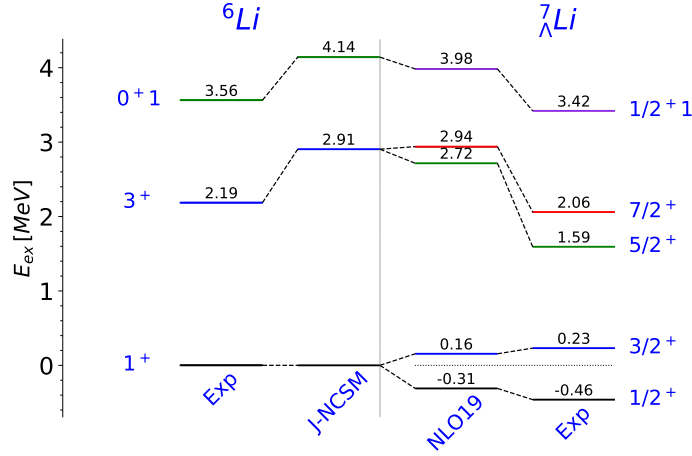
Figure 4.25: Energy spectra of $^{7}_{\Lambda}$Li and $^{6}$Li. Calculations are based on the chiral SMS N$^4$LO+(450) with $\lambda_{NN} = 1.6$ fm$^{-1}$ and the YN NLO19(600) with $\lambda_{YN} = 0.82$ fm$^{-1}$. The experimental values are taken from [8, 11, 126].

of the $^{6}$Li core and are affected by the nucleon-spin-dependent spin-orbit YN interaction [121]. Overall, our calculations overestimate the excitation energies of $^{6}$Li because of the missing of 3N forces. The latter also results in overestimations of the doublet spacings in $^{7}_{\Lambda}$Li. For the discussion, the relative positions of the $^{6}$Li($3^{+}$) state and the $\frac{5}{2}^{+}$ and $\frac{7}{2}^{+}$ states in $^{7}_{\Lambda}$Li are therefore more relevant. It is then instructive to plot individual energy levels in $^{7}_{\Lambda}$Li with respect to the centroid energy of the ground state $\bar{E}_{gs}$, which has been done for $^{7}_{\Lambda}$Li shown in Fig. 4.25. Generally, the centroid energy of a doublet is defined as [121, 124]

$$\bar{E}(J_N) = \frac{J_N + 1}{2J_N + 1} E_+ + \frac{J_N}{2J_N + 1} E_-, \qquad (4.6)$$

where $J_N$ is the angular momentum of the nuclear-core state and $E_{\pm}$ are the excitation energies of the $J_N \pm \frac{1}{2}$ states of the doublet. Hence, the ground-state centroid of $^{7}_{\Lambda}$Li is simply given by $\bar{E}_{gs} = \bar{E}(1^{+}) = \frac{2}{3}E_{ex}(\frac{3}{2}^{+})$, which then serves as zero energy by construction (indicated by the horizontal dotted line in Fig. 4.25). Evidently, the doublet splittings obtained from our calculations are comparable to the experimental measurements. We do not study the impact of different NN interactions here but expect very minor effects of various two- and three-body forces on the doublet splittings [121, 124, 125]. Additionally, shell-model studies shown that if there is a unique nuclear core state related to the doublet splitting, then the centroid energy in Eq. (4.6) is independent of the spin-spin, spin-orbit and tensor YN interactions [121]. In Section 4.6 we will study the effect of different chiral YN interactions on the energy spectrum of $^{7}_{\Lambda}$Li. One will see there that the shell-model result is indeed also observed in our J-NCSM calculations.

# 4.4 Correlations of Λ-separation energies

In Section 4.2, we have observed astonishingly similar behaviors of the Λ-separation energies of all investigated hypenuclei with respect to the running SRG-YN flow parameter $\lambda_{YN}$. This probably hints at some intriguing correlations between the Λ-separation energies of these systems. In order to quantitatively study these correlations, we compute $B_\Lambda$ of every two hypernuclei for the same range of $\lambda_{YN}$ evolution parameters, then plot them against each other. As mentioned earlier, $^5_\Lambda$He is so far the best experimentally-studied hypernucleus and also our J-NCSM results for this hypernucleus are well-converged. We therefore use $^5_\Lambda$He as a benchmark system and plot $B_\Lambda(^5_\Lambda$He) against the separation energies of other hypernuclear systems ($A = 3 - 7$). For that, we choose the Idaho-N$^3$LO(500) evolved to an SRG-NN cutoff of $\lambda_{NN} = 1.6$ fm$^{-1}$ for the NN interaction in combination with the YN NLO19 potential for a $\Lambda_Y = 600$ MeV. It is important to stress that similar results are observed for the SMS N$^4$LO+(450) and other YN interactions, see also Section 4.5.2.

We first look at the correlation between the Λ removal energies of the $^5_\Lambda$He hypernucleus and of the hypertriton. Note that, the hypertriton separation energies are computed within the Faddeev-Yakubovky approach. The correlation plot is shown in panel (a) of Fig. 4.26. Each symbol represents the numerical $B_\Lambda$ of the two systems calculated for the same $\lambda_{YN}$, which also include the estimated uncertainties that are small in most of the cases. The straight line is obtained from a linear fit to the results, imitating the Tjon line between the binding energies of $^4$He and $^3$He [127, 128]. We observe a perfectly linear correlation between $B_\Lambda(^3_\Lambda$H) and $B_\Lambda(^5_\Lambda$He) for the flow parameters up to $\lambda_{YN} = 2.0$ fm$^{-1}$ and a slight deviation from the straight line as $\lambda_{YN}$ further increases. Interestingly, the Tjon line goes through the experimental Λ-separation energies of the two systems at $\lambda_{YN} = 0.836$ fm$^{-1}$. We will refer to as the SRG-YN value that gives the correct $B_\Lambda(^5_\Lambda$He) a magic SRG-YN cutoff, $\lambda^m_{YN}$. Obviously, the specific value of $\lambda^m_{YN}$ may vary for different YN interactions or different regulators.

The correlation plots for the ground and excited states of $^4_\Lambda$He/$^4_\Lambda$H are displayed in panels (b) and (c), respectively. While there is a strictly linear correlation between the separation energies $B_\Lambda(^4_\Lambda$He/$^4_\Lambda$H, $1^+$) and $B_\Lambda(^5_\Lambda$He), the correlation line for $B_\Lambda(^4_\Lambda$He/$^4_\Lambda$H, $0^+$) and $B_\Lambda(^5_\Lambda$He) exhibits a small loop to the right for large values of the SRG-YN cutoff, $\lambda_{YN} \geq 2.4$ fm$^{-1}$, similar to the Tjon line for $B_\Lambda(^3_\Lambda$H) and $B_\Lambda(^5_\Lambda$He). Again, this slight deviation from linearity is of order of three-body chiral force contributions, which will be discussed more detail in Section 4.5.2. From panels (b) and (c), one also easily observes practically identical results for the isospin mirrors $^4_\Lambda$He and $^4_\Lambda$H. This is because there is no CSB terms in the employed version of the chiral YN potential. In addition, the CSB effect arising from the Coulomb point interactions is minor [129, 130]. It is interesting to point out that, at the magic cutoff, $\lambda^m_{YN} = 0.836$ fm$^{-1}$, the experimental value of $B_\Lambda(^4_\Lambda$He, $1^+$) is exactly reproduced while the ground state is somewhat underbound. Furthermore, at this magic cutoff, our J-NCSM results for the spin doublet of $^4_\Lambda$He, $B_{\Lambda,\text{NCSM}}(0^+(1^+)) = 1.57(0.97)$ MeV, are surprisingly close to the those obtained within the exact Faddeev-Yakubovsky method using the non-SRG evolved bare YN interactions, $^4_\Lambda$He, $B_{\Lambda,\text{FY}}(0^+(1^+)) = 1.46(1.06)$ MeV. The small discrepancies between two results can be traced back to the possible contributions from chiral 3BF.

Similarly, almost perfectly linear correlations are also found between $B_\Lambda(^5_\Lambda$He) and the ground-state resonance energies $E_\Lambda$ of the p-shell $^6_\Lambda$He and $^6_\Lambda$Li hypernuclei, panel(d), as well as the Λ-separation energies $B_\Lambda$ of the ground and first excited states in $^7_\Lambda$Li, panels (e) and (f), respectively. Let us remind that the resonance energies $E_\Lambda(^6_\Lambda$Li/$^6_\Lambda$He) are computed as the difference between the hypernuclear binding energies $E(^6_\Lambda$Li/$^6_\Lambda$He) and the binding energy $E(^4$He). In panel (d) one notices a pronounced difference in the binding energies $E_\Lambda$ of $^6_\Lambda$He and $^6_\Lambda$Li (about 1.08 MeV), which simply results from different contributions of the Coulomb interactions of the two nuclear cores $^5$He and

$^5$Li. We remark that the YN NLO19(600) potential with the magic cutoff of $\lambda_{YN}^m = 0.836$ fm$^{-1}$ underbinds the $^6_\Lambda$He/$^6_\Lambda$Li systems while slightly overbinds the first excited state in $^7_\Lambda$Li. The obtained $\Lambda$-separation energy for the ground state, $B_\Lambda(^7_\Lambda\text{Li}, \frac{1}{2}^+) = 5.59 \pm 0.01$ MeV, is however in very good agreement with the measurement from emulsion experiments, $B_{\Lambda,\text{emul}}(^7_\Lambda\text{Li}, \frac{1}{2}^+) = 5.58 \pm 0.03$ MeV [131]. It should however be noted that counter experiments however reported a somewhat larger value for $^7_\Lambda\text{Li}(\frac{1}{2}^+, 0)$, namely $B_{\Lambda,\text{coun}}(^7_\Lambda\text{Li}, \frac{1}{2}^+) = 5.85 \pm 0.13 \pm 0.1$ MeV [132].

We have demonstrated the strikingly linear correlations between the $\Lambda$-separation energies of different hypernucler systems. It will be important to study the same correlation using different YN bare interactions in order to check whether this favorable agreement is a universal feature or a signature of of the interaction chosen. Nevertheless, our interesting finding for the chiral forces with SRG evolution may suggest that the missing SRG-induced three-body forces may possibly depend on one adjustable parameter [3]. If this the case, one can try to minimize the effects of these omitted forces by tuning the SRG-YN flow parameters $\lambda_{YN}$ to the magic cutoff for which a particular hypernuclues, for example $^5_\Lambda$He, is properly described. This magic cutoff $\lambda_{YN}^m$ then can serve as a good starting point for hypernuclear calculations requiring SRG-YN evolutions which, in turn, may provide a good opportunity to study hypernuclear structures as well as the YN interaction models in a less expensive but realistic approach. A possible application of this will be considered in Section 4.6.

---

[3] The effects of SRG-induced higher-body forces on $B_\Lambda$ are expected to be insignificant [87]
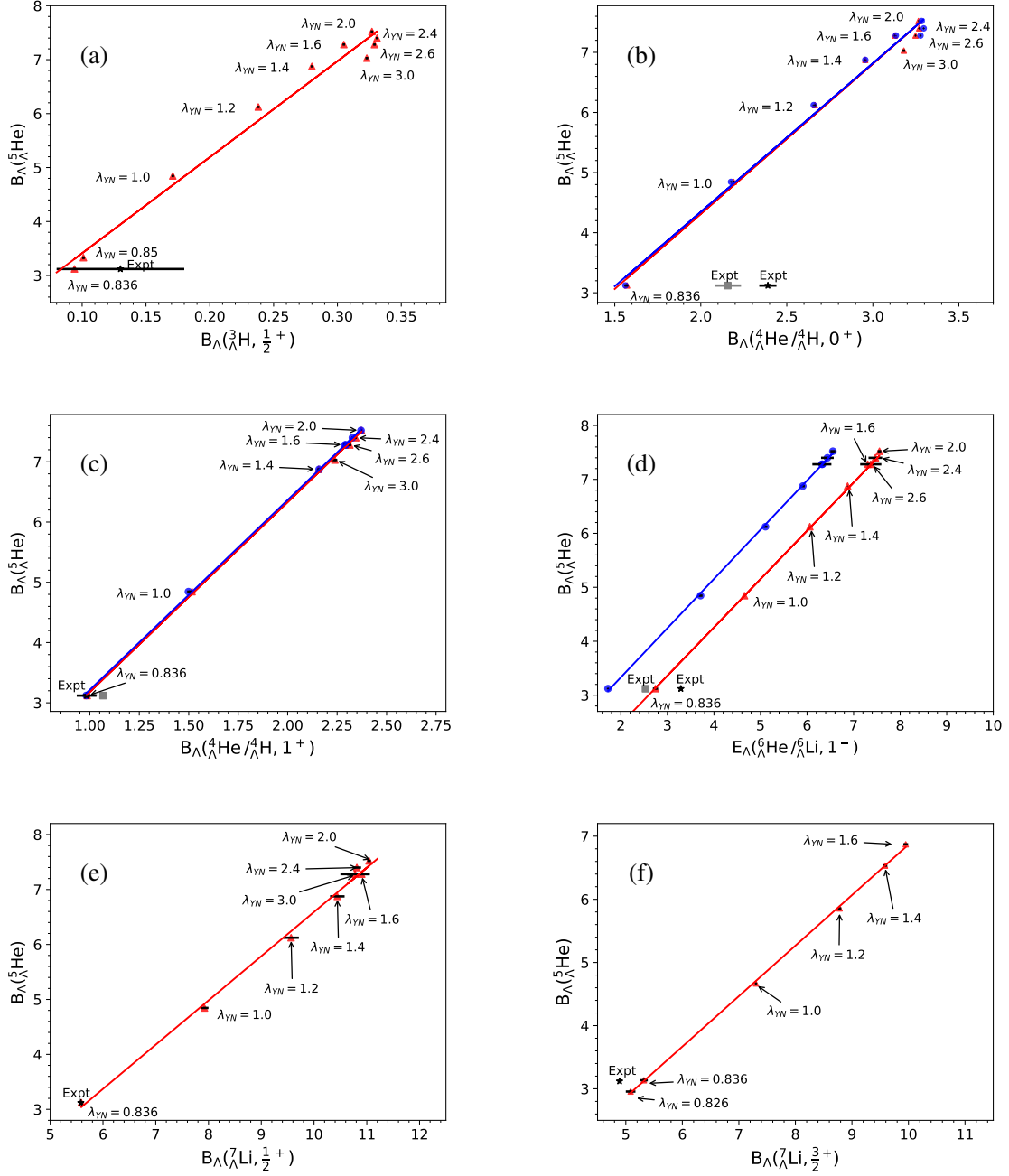
Figure 4.26: Correlations of Λ-separation energies for a wide range of flow parameters $\lambda_{YN}$ of $^5_\Lambda$He and (a) $^3_\Lambda$H, (b) the $0^+$ state of $^4_\Lambda$He (red) and $^4_\Lambda$H (blue), (c) the $1^+$ state of $^4_\Lambda$He (red) and $^4_\Lambda$H (blue), (d) $^6_\Lambda$He (red) and $^6_\Lambda$Li (blue), (e) $^7_\Lambda$Li($\frac{1}{2}^+$, 0) and (f) $^7_\Lambda$Li($\frac{3}{2}^+$, 0). The error bars represent numerical uncertainties which are small in most of the cases. The experimental Λ-separation energy for $^5_\Lambda$He is from [6]. The results for other systems are taken from: (a) [6], (b)-(c) [123] for $^4_\Lambda$He (black asterisk) and $^4_\Lambda$H (grey square), (d) [73] for $^6_\Lambda$He (black asterisk) and $^6_\Lambda$Li (grey square), (e) [6] (emulsion experiments) and (f) [133].

## 4.5 Effects of the YN NLO13 and NLO19 on light hypernuclei

Section 4.2 has been devoted to study the impact of various NN chiral interaction models and SRG evolutions on the $\Lambda$-separation energies $B_\Lambda$ employing the YN NLO19 for a regulator of $\Lambda_Y = 600$ MeV. It is also of importance to comprehensively investigate the predictions of different YN chiral interactions, which will be the main subject of this section. For that purpose it is sufficient to choose a specific NN potential that can accurately describe NN scattering data and provide accurate predictions for nuclear structure calculations. We shall employ the SMS N$^4$LO+(450) potential, and evolve it to a flow parameter of $\lambda_{NN} = 1.6$ fm$^{-1}$ in order to speed up the convergence.

In contrast to very sophisticated and accurate NN interactions (up to fifth order in chiral expansion), YN chiral potentials are still at a rather primitive level (up to second order in chiral expansion) due to the scarcity of YN experimental data. The leading order (LO) interaction has been successfully derived by Polinder *et al.* [45] and recently extended by Haidenbauer *et al.* to next-to-leading order (NLO) [46, 47]. As mentioned in Section 1.1, at LO there are five unknown LECs that are fitted entirely to the sparse set of 36 YN data. At that order, one can not expect that the YN potential describe all the available YN data perfectly and give reliable predictions for other hypernuclear systems. Indeed, the LO YN interaction does not nicely reproduce the energy dependence of the $\Lambda p$ total cross section at low energy, leads to a somewhat large total $\chi^2$ ($\chi^2_{LO} \approx 28.3$ as compared to $\chi^2_{NLO} \approx 16$ obtained with NLO ) and also rather strong dependence of the two-body observables on the regulator cutoffs [45]. On the other hand, the NLO interactions describe the YN data comparably to the so-far most realistic meson-based YN models and also exhibit much lesser regulator-dependence. It is therefore advisable to utilize the more advanced NLO versions for hypernuclear calculations.

The YN NLO interactions recently come in two realizations, the NLO13 [46] and NLO19 [47], both with several momentum-space regulators of $\Lambda_Y = 500 - 650$ MeV. General speaking, the two NLO forces are completely equivalent in terms of describing two-body YN observables, furthermore, by construction, they reproduce the experimental binding energy of $^3_\Lambda$H within its uncertainty (of order of 50 keV). However, the NLO19 leads to somewhat weaker $\Lambda - \Sigma$ transitions (in particular in the $^3S_1$ partial-wave channel) which are believed to be closely related to the strength of chiral YNN forces [47, 87]. The latter is expected to manifest itself in the predictions of observables (e.g. separation energies) for $A \geq 4$ hypernuclei and in nuclear matter. Indeed, it is found that the NLO19 potential is more attractive in the medium than the NLO13 [47]. Also, in [47] the authors have thoroughly investigated possible impacts of the NLO13 and NLO19 potentials on the A=4 hypernucleus using the Faddeev-Yakubovsky method. Nevertheless, here we also provide our results for the spin-doublet states of $^4_\Lambda$He for benchmarking and extend the study further to $A = 5, 7$ hypernuclei. We will first carefully investigate the impacts of the two YN interactions on the $\Lambda$-separation energies and $\Sigma$-probabilities of the $A = 4 - 7$ systems. We then show the linear correlations between these separation energies which then allow us to quantitatively study the effects of these potentials on the energy spectrum of $^7_\Lambda$Li.

### 4.5.1 $\Lambda$-separation energies

The separation energies $B_\Lambda$ of the ground- and first-excited states of $A = 4 - 7$ hypernuclei computed utilizing the two NLO potentials with various regulators $\Lambda_Y = 500 - 650$ MeV are presented in Fig. 4.27. Both interactions are evolved to the same range of SRG-YN flow parameters, $0.8 \leq \lambda_{YN} \leq 3.0$ fm$^{-1}$. For $^7_\Lambda$Li, the calculations have been only performed up to $\lambda_{YN} \leq 1.6$ fm$^{-1}$ in

order save some computational resources. Overall, the dependence of $B_\Lambda$ on the chiral regulator $\Lambda_Y$ is somewhat stronger for the NLO19 than for the NLO13 potential. This, however, does not relate to any physical reason but simply reflects the fact that in the NLO19 realization one has less freedom to absorb the regulator sensitivity into the LECs. Moreover there are noticeable differences between the $\Lambda$-separation energies obtained with the two interactions, which apparently exceed the $\Lambda_Y$-dependence. For all states except $^4_\Lambda$He($0^+$), see panels (b-e), one observes a general tendency toward larger $B_\Lambda$ predicted by the NLO19 than those predicted by the NLO13. In other words, the interaction with weaker $\Lambda - \Sigma$ conversion potential generally leads to larger $\Lambda$-separation energies. That trend is however not clear for the ground state of $^4_\Lambda$He, see panel (a). We note that similar regulator-dependence and interaction-model sensitivity have been observed for the Faddeev-Yakubovsky results for $A = 3, 4$ hypernuclei computing with the bare YN interactions [47]. There the authors also give a persuasive explanation for the potentially larger-separation energies obtained with the NLO19. It turns out that the dispersive effect arising when the $\Lambda N$ interaction takes place in the medium (more precisely in the presence of other spectators) leads to a less attractive effective interaction. The latter is evidently proportional to the $\Lambda - \Sigma$ conversion which implies that the interaction with stronger $\Lambda - \Sigma$ conversion (i.e. the NLO13) then becomes less attractive in the medium. Nevertheless, the pronounced variations of $B_\Lambda$ predicted by the two interaction models are the strikingly evidence of the possible contribution 3BFs to the $\Lambda$ separation energy. These variations (of order of 300 and 700 keV for the $0^+$ and $1^+$ states in $^4_\Lambda$He, respectively [47]) will be definitely removed once proper chiral YNN forces are taken into account.

Furthermore, the strong sensitivity of the $\Lambda$-separation energies of $^4_\Lambda$He($1^+$) and $^5_\Lambda$He on the $\Lambda - \Sigma$ transition potential can also be understood using a simple approximation for the effective spin-dependent $\Lambda N$ potential in s-shell hypernuclei, which can be written as [134, 135]

$$
\begin{aligned}
^3_\Lambda\text{H} : \quad & \tilde{V}_{\Lambda N} \approx \frac{3}{4} V^s_{\Lambda N} + \frac{1}{4} V^t_{\Lambda N} \\[2mm]
^4_\Lambda\text{He}(0^+) : \quad & \tilde{V}_{\Lambda N} \approx \frac{1}{2} V^s_{\Lambda N} + \frac{1}{2} V^t_{\Lambda N} \\[2mm]
^4_\Lambda\text{He}(1^+) : \quad & \tilde{V}_{\Lambda N} \approx \frac{1}{6} V^s_{\Lambda N} + \frac{5}{6} V^t_{\Lambda N} \\[2mm]
^5_\Lambda\text{He} : \quad & \tilde{V}_{\Lambda N} \approx \frac{1}{4} V^s_{\Lambda N} + \frac{3}{4} V^t_{\Lambda N},
\end{aligned}
\tag{4.7}
$$

where $V^s_{\Lambda N}$ and $V^t_{\Lambda N}$ are the single- and triplet two-body potentials, respectively. It follows clearly from Eq. (4.7) that the two states, $^4_\Lambda$He($1^+$) and $^5_\Lambda$He, are dominated by the spin-triplet $\Lambda N$ interaction, which is, as already mentioned, strongly influenced by the $\Lambda - \Sigma$ conversion. From panels(b)-(e) of Fig. 4.27, one can also quickly notice that the two interactions, NLO13 and NLO19, affect $B_\Lambda$ of the two states $^7_\Lambda$Li($\frac{1}{2}^+$, $\frac{3}{2}^+$) in a similar way as for $^4_\Lambda$He($1^+$) and $^5_\Lambda$He. Hence, it is likely that the spin-triplet interaction also predominantly contributes to the two lowest-lying states in $^7_\Lambda$Li.

It is also interesting to study the probability of finding a $\Sigma$ particle $P_\Sigma$ in the hypernuclear wavefunctions obtained with the two NLO potentials. The results displayed in panel(a) of Fig. 4.28 clearly indicate a noticeable dependence of $P_\Sigma(^4_\Lambda\text{He}, 0^+)$ on the chiral cutoff $\Lambda_Y$. However, such regulator dependence becomes somewhat less visible for all other states (panels (b-e)). Moreover, the variation of $P_\Sigma(^4_\Lambda\text{He}, 0^+)$ due to the two NLO potentials is most significant as compared to other states. This is exactly opposite to what have been observed for the separation energies. Overall, the

tendency toward larger $P_\Sigma$ predicted by the NLO13 is somewhat blurred by the regulator-dependence of the $\Sigma$-probabilities. Finally, while there is a visible difference between the $\Sigma$-probabilities of the s-shell spin-doublet states (in particular for the predictions of the NLO13), the p-shell doublet $P_\Sigma(^7_\Lambda\text{Li}, \frac{1}{2}^+)$ and $P_\Sigma(^7_\Lambda\text{Li}, \frac{3}{2}^+)$ are quite similar for both interactions. As for a final conclusion, one sees that the $\Lambda$-separation energies and $\Sigma$-probabilities are somehow correlated. However, we do not observe an one-to-one connection between the two quantities.
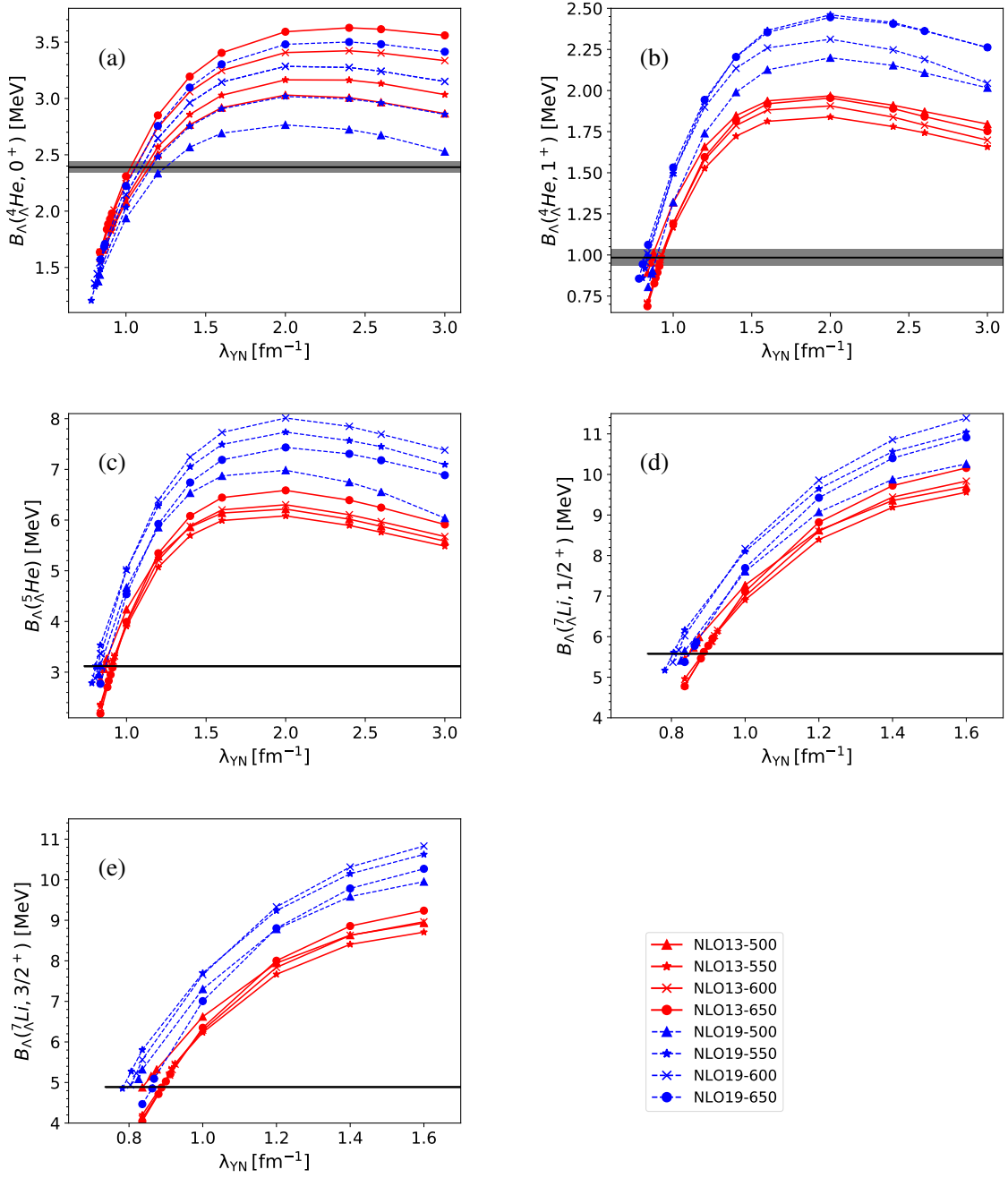
Figure 4.27: $\Lambda$-separation energies $\lambda_{YN}$, (a) $^4_\Lambda$He(0$^+$), (b) $^4_\Lambda$He(1$^+$), (c) $^5_\Lambda$He($\frac{1}{2}^+$), (d) $^7_\Lambda$Li(1/2$^+$), (e) $^7_\Lambda$Li(3/2$^+$) as functions of SRG-YN flow parameter $\lambda_{YN}$. Black lines with grey bands represent experimental $B_\Lambda$ and the uncertainties, respectively. Calculations are based on the chiral SMS N$^4$LO+(450) with the SRG-NN evolution parameter of $\lambda_{NN} = 1.6$ fm$^{-1}$ in combination with the YN-NLO13 (red solid lines) and YN-NLO19 (dashed blue lines) for four regulators, $\Lambda_Y = 500$ (triangles), 550 (stars), 600 (crosses) and 650 (circles) MeV.
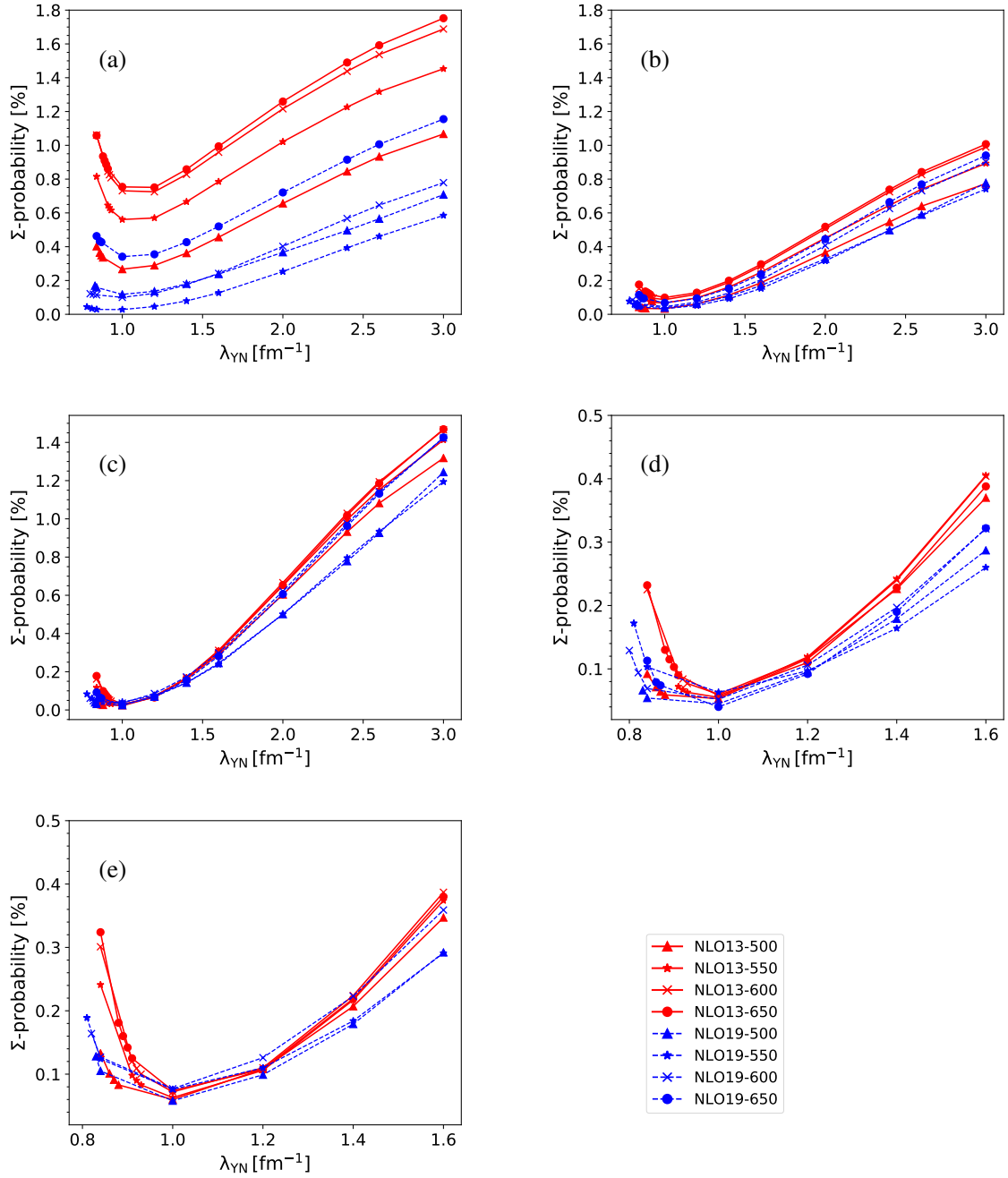
Figure 4.28: Probabilities of finding $\Sigma$ particles in the wavefunctions of: (a) $^4_\Lambda$He($0^+$), (b) $^4_\Lambda$He($1^+$), (c) $^5_\Lambda$He($\frac{1}{2}^+$), (d) $^7_\Lambda$Li($1/2^+$), (e) $^7_\Lambda$Li($3/2^+$) as functions of SRG-YN flow parameter $\lambda_{YN}$. Same NN potential, symbols and lines as in Fig. 4.27.

## 4.5.2 Correlation of $B_\Lambda$ for two chiral NLO interactions

We also investigate the correlations between $B_\Lambda(^5_\Lambda$He$)$ and the separation energies of the ground- and first-excited states in the $^4_\Lambda$He and $^7_\Lambda$Li hypernuclei employing both NLO interactions with
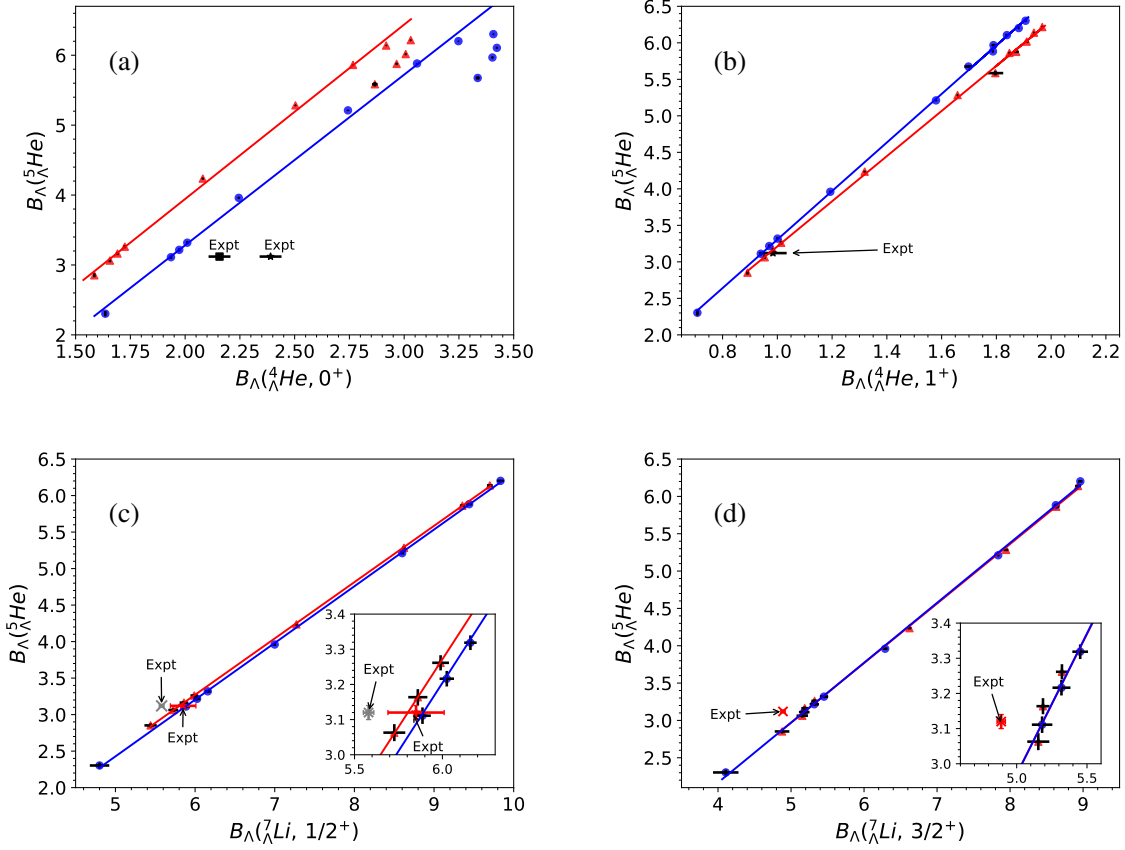
Figure 4.29: Correlations of $\Lambda$-separation energies for a wide range of SRG-YN flow parameters $\lambda_{YN}$ of $^5_\Lambda$He and (a) $^4_\Lambda$He($0^+$), (b) $^4_\Lambda$He($1^+$), (c) $^7_\Lambda$Li($\frac{1}{2}^+$, 0) and (f) $^7_\Lambda$Li($\frac{3}{2}^+$, 0). The experimental results are from [6, 123, 132, 133, 137]. Calculations are based on the SMS N$^4$LO+(450) evolved to a flow parameter of $\lambda_{YN} = 1.6$ fm$^{-1}$ and the YN NLO13 with two regulators of $\Lambda_Y = 500$ MeV (red triangles) and $\Lambda_Y = 600$ MeV (blue circles).

four different regulators of $\Lambda_Y = 500 - 650$ MeV. We confirm the strong correlations as reported in Section 4.4 when utilizing the NN Idaho-N$^3$LO(450) interaction combined with the NLO19 YN potential for a cutoff of $\Lambda_Y = 600$ MeV. For completeness, let us illustrate in Fig. 4.29 such correlations with the NLO13 potential for two regulators: $\Lambda_Y = 500$ MeV (red triangles) and $\Lambda_Y = 600$ MeV (blue circles). Evidently, one observes nearly perfect linear correlations for the excited state $^4_\Lambda$He($1^+$) and the two states $^7_\Lambda$Li($\frac{1}{2}^+, \frac{3}{2}^+$). The correlation between $B_\Lambda(^5_\Lambda$He) and $B_\Lambda(^4_\Lambda$He, $0^+$) follows a straight line for low SRG-YN values of $\lambda_{YN} \leq 2.0$ fm$^{-1}$ and exhibit a small loop to the right for higher flow parameters, which is quite similar to panel(b) in Fig. 4.26. It can be further estimated that the slight deviation from the straight line in the case of $^4_\Lambda$He($0^+$) is actually of the order of the 3BFs (about 200-300 keV for $^4_\Lambda$He($0^+$) [47, 136]). Furthermore, at the magic SRG-YN cutoff $\lambda^m_{YN}$, where the $\Lambda$-separation energy of $^5_\Lambda$He is correctly reproduced, the computed values for $^3_\Lambda$H, $^4_\Lambda$He($1^+$) and $^7_\Lambda$Li($\frac{1}{2}^+$) are in perfect agreement with the experiments as shown in Table 4.8. We also provide the magic cutoffs for each individual YN interaction and regulator in

| YN ($\Lambda_Y$) | $\lambda_{YN}^m$ | $B_\Lambda(^3_\Lambda\text{H})$ | $B_\Lambda(^4_\Lambda\text{He}, 0^+)$ | $B_\Lambda(^4_\Lambda\text{He}, 1^+)$ | $B_\Lambda(^5_\Lambda\text{He})$ | $B_\Lambda(^7_\Lambda\text{Li})$ |
|---|---|---|---|---|---|---|
| NLO19(500) | 0.836 | 0.07 | 1.44 | 1.01 | 3.13(2) | 5.64(7) |
| NLO19(550) | 0.806 | 0.07 | 1.33 | 0.94 | 3.12(2) | 5.61(6) |
| NLO19(600) | 0.820 | 0.08 | 1.44 | 0.92 | 3.10(4) | 5.67(6) |
| NLO19(650) | 0.868 | 0.11 | 1.71 | 0.91 | 3.14(2) | 5.86(5) |
| NLO13(500) | 0.868 | 0.11 | 1.69 | 0.98 | 3.16(2) | 5.86(5) |
| NLO13(550) | 0.910 | 0.12 | 1.83 | 0.93 | 3.12(2) | 5.87(5) |
| NLO13(600) | 0.910 | 0.13 | 1.94 | 0.94 | 3.11(2) | 5.89(5) |
| NLO13(650) | 0.912 | 0.13 | 1.98 | 0.93 | 3.14(2) | 5.96(5) |
| experiment | – | 0.13(5) [6] | 2.39(3) [137] | 0.98(3) [123] | 3.12(2) [137] | 5.58(3) [6] |
| | | | | | | 5.85(13)(10) [132] |

Table 4.8: Separation energies of $^3_\Lambda$H, $^4_\Lambda$He, $^5_\Lambda$He and $^7_\Lambda$Li calculated using the NLO13-19 interactions with different regulators, SRG evolved such that the $B_\Lambda(^5_\Lambda\text{He})$ is well reproduced. The values for $^3_\Lambda$H are obtained by solving the Faddeev Yakubovsky equations. The corresponding SRG parameter $\lambda_{YN}^m$ is given in fm$^{-1}$ and energies are in MeV. Table is taken from [136].

the second column Table 4.8. It turns out that the separation energies $B_\Lambda$ for the $A = 3, 4$ systems calculated at the magic cutoffs are also well in line with the results obtained using the non-SRG evolved (bare) YN potentials (see Table 4.9) when one takes into account the possible contributions of 3BFs. As discussed in Section 4.4, this interesting result indicates that, by tuning the SRG flow parameter to the magic cutoffs, we may have minimized the effects of the SRG-induced 3BFs bringing the evolved potentials close to the bare ones.

# 4.6  Implications of an increased $B_\Lambda(^3_\Lambda\text{H})$

$^3_\Lambda$H is the lightest observed hypernucleus that plays an essential role in hypernuclear physics like the deuteron for ordinary nuclear physics. Indeed, $B_\Lambda(^3_\Lambda\text{H})$ is commonly exploited as an important constraint (that enters through the singlet $a_s$ and triplet $a_t$ scattering lengths) in addition with the sparse YN data in order to develop realistic YN interactions. It is reasonable to expect that the effect of 3BFs contributed to the $\Lambda$-separation energy is smallest for $^3_\Lambda$H, which makes the hypertriton a perfect candidate for benchmarking YN interaction models. Hence, accurate measurement of

| YN interaction($\Lambda_Y$) | $B_\Lambda({}^3_\Lambda H))$ | $B_\Lambda({}^4_\Lambda He, 0^+)$ | $B_\Lambda({}^4_\Lambda He, 1^+)$ | $\Delta E_\Lambda({}^4_\Lambda He)$ |
|---|---|---|---|---|
| NLO19(500) | 0.10 | 1.64 | 1.23 | 0.42 |
| NLO19(550) | 0.09 | 1.54 | 1.24 | 0.30 |
| NLO19(600) | 0.09 | 1.46 | 1.06 | 0.41 |
| NLO19(650) | 0.10 | 1.53 | 0.92 | 0.61 |
| NLO13(500) | 0.14 | 1.71 | 0.79 | 0.92 |
| NLO13(550) | 0.10 | 1.50 | 0.59 | 0.92 |
| NLO13(600) | 0.09 | 1.48 | 0.58 | 0.90 |
| NLO13(650) | 0.09 | 1.49 | 0.62 | 0.88 |

Table 4.9: Faddeev-Yakubovsky results for the $\Lambda$-separation energies of ${}^3_\Lambda H$ and ${}^4_\Lambda He$ calculated using the non-SRG evolved bare NLO13 and NLO19 interactions for various regulators. Table is taken from [136].

$B_\Lambda({}^3_\Lambda H)$ is of importance. So far, the hypertriton separation energy is commonly accepted as $B_\Lambda({}^3_\Lambda H) = 0.13 \pm 0.05$ MeV, which is obtained by averaging the widely varying results of different emulsion measurements [137]. We note that this value of $B_\Lambda({}^3_\Lambda H)$ is used when constructing the NLO13 and NLO19 interactions. Recent measurements from the STAR collaboration however suggest a significantly larger $\Lambda$-separation energy, namely $B_\Lambda({}^3_\Lambda H) = 0.41 \pm 0.12$ MeV [138]. In addition, some recent hypertriton lifetime measurements that yield $\tau_{{}^3_\Lambda H}$ well below that value of free $\Lambda$ [139, 140] may be considered as an indication of a stronger hypertrition binding energy [141]. From theoretical aspect, these new results however raise several important questions: what can be the possible impact of an increasing hypertriton separation energy to observables in other hypernuclei like $B_\Lambda$ or the energy spectra? Do the changes of $B_\Lambda$ or spectra support or rule out the new measurements? It is the aim of this section to throughly address those questions.

Let us first discuss possible modifications to the NLO interactions following the increase in $B_\Lambda({}^3_\Lambda H)$. We shall take the NLO19 as our starting point. It is well known that the hypertriton binding energy is much more sensitive to the strength of $\Lambda N$ interactions in the spin-singlet channel than in the spin-triplet one, see Eq. (4.7). This is often implemented via the constraint that the spin-singlet scattering length $a_s$ is noticeably larger than the spin-triplet one $a_t$ ($|a_s| \geq |a_t|$). Therefore, in order to achieve the much larger binding energy of $B_\Lambda({}^3_\Lambda H)$ while still maintain a perfect description of the available $\Lambda N$ data, one will need to to significantly increase $|a_s|$, and at the same time reduce the triplet scattering $|a_t|$. It turns out that, the overall excellent description of $\Sigma N$ data can also be preserved when one loosens the strict self-imposed SU(3) symmetry for the contact interactions in the $\Lambda N$ and $\Sigma N$ forces [46, 47, 136]. Taking into account all the just mentioned considerations, we derived three possible modifications to the NLO19, labelled as Fit A, Fit B and Fit C, with the increased singlet scattering length of 4.0, 4.5 and 5.0 fm, respectively. These newly fitted interactions are almost phase equivalent to the NLO13 and NLO19 but lead to much stronger hypertriton binding energies toward the STAR measurements with the Fit B predicting the exact value [136].

We are now in a position to study the impact of the Fit A-C interactions on the ${}^4_\Lambda He$ and ${}^7_\Lambda Li$ hypernuclei by comparing their predictions with those predicted by the NLO13 and NLO19 and the experimental values as well. In order to obtain meaningful comparison, it is important to minimize

| YN ($\Lambda_Y$) | $\lambda_{YN}^m$ | $B_\Lambda(^3_\Lambda\mathrm{H})$ | $B_\Lambda(^4_\Lambda\mathrm{He}, 0^+)$ | $B_\Lambda(^4_\Lambda\mathrm{He}, 1^+)$ | $B_\Lambda(^5_\Lambda\mathrm{He})$ | $B_\Lambda(^7_\Lambda\mathrm{Li})$ |
|---|---|---|---|---|---|---|
| Fit A (500) | 0.849 | 0.23 | 1.75 | 0.95 | 3.11(2) | |
| Fit A (550) | 0.832 | 0.24 | 1.70 | 0.83 | 3.12(2) | |
| Fit A (600) | 0.836 | 0.27 | 1.84 | 0.80 | 3.14(2) | 6.09(4) |
| Fit A (650) | 0.890 | 0.33 | 2.17 | 0.75 | 3.10(2) | |
| Fit B (500) | 0.872 | 0.31 | 1.84 | 0.87 | 3.11(2) | |
| Fit B (550) | 0.836 | 0.32 | 1.82 | 0.78 | 3.12(2) | |
| Fit B (600) | 0.843 | 0.36 | 1.97 | 0.75 | 3.13(2) | 6.20(3) |
| Fit B (650) | 0.910 | 0.42 | 2.31 | 0.70 | 3.14(2) | |
| Fit C (500) | 0.880 | 0.39 | 1.97 | 0.83 | 3.14(2) | |
| Fit C (550) | 0.843 | 0.40 | 1.94 | 0.75 | 3.14(2) | |
| Fit C (600) | 0.843 | 0.46 | 2.12 | 0.69 | 3.11(2) | 6.31(3) |
| Fit C (650) | 0.913 | 0.51 | 2.41 | 0.65 | 3.11(2) | |
| experiment | – | 0.13(5) [6] | 2.39(3) [137] | 0.98(3) [123] | 3.12(2) [137] | 5.58(3) [6] |
| | | | | | | 5.85(13)(10) [132] |

Table 4.10: Separation energies of $^3_\Lambda\mathrm{H}$, $^4_\Lambda\mathrm{He}$, $^5_\Lambda\mathrm{He}$ and $^7_\Lambda\mathrm{Li}$ calculated using the Fit A-C interactions with different regulators, SRG evolved such that the $B_\Lambda(^5_\Lambda\mathrm{He})$ is well reproduced. The values for $^3_\Lambda\mathrm{H}$ are obtained by solving the Faddeev-Yakubovsky equations. The corresponding SRG parameter $\lambda_{YN}^m$ is given in fm$^{-1}$ and energies are in MeV. The table is taken from [136].

the possible effects of the SRG-induced 3BFs. As we have demonstrated in Sections 4.4 and 4.5, the $\Lambda$-separation energies for different flow parameters are strongly correlated. Also, they are particularly close to the values for the original bare interactions once the $^5_\Lambda\mathrm{He}$ system is properly described (i.e. at the magic SRG cutoffs $\lambda_{YN}^m$). That feature is independent of the chosen NN and YN interactions. It is therefore instructive to compare the predictions of different YN interactions, namely the NLO13, NLO19 and Fit A-C for their magic SRG cutoffs. These special SRG cutoffs and the corresponding separation energies of the $A = 3 - 7$ systems for the two NLO13 and NLO19 potentials have been tabulated in Table 4.8. The results for the Fit A-C are also provided in Table 4.10. Since it is observed that the regulator dependence for the new fits follows the same trend of the initial NLO19 in the $A = 4, 5$ systems, we calculate $B_\Lambda(^7_\Lambda\mathrm{Li})$ for the modified interactions for
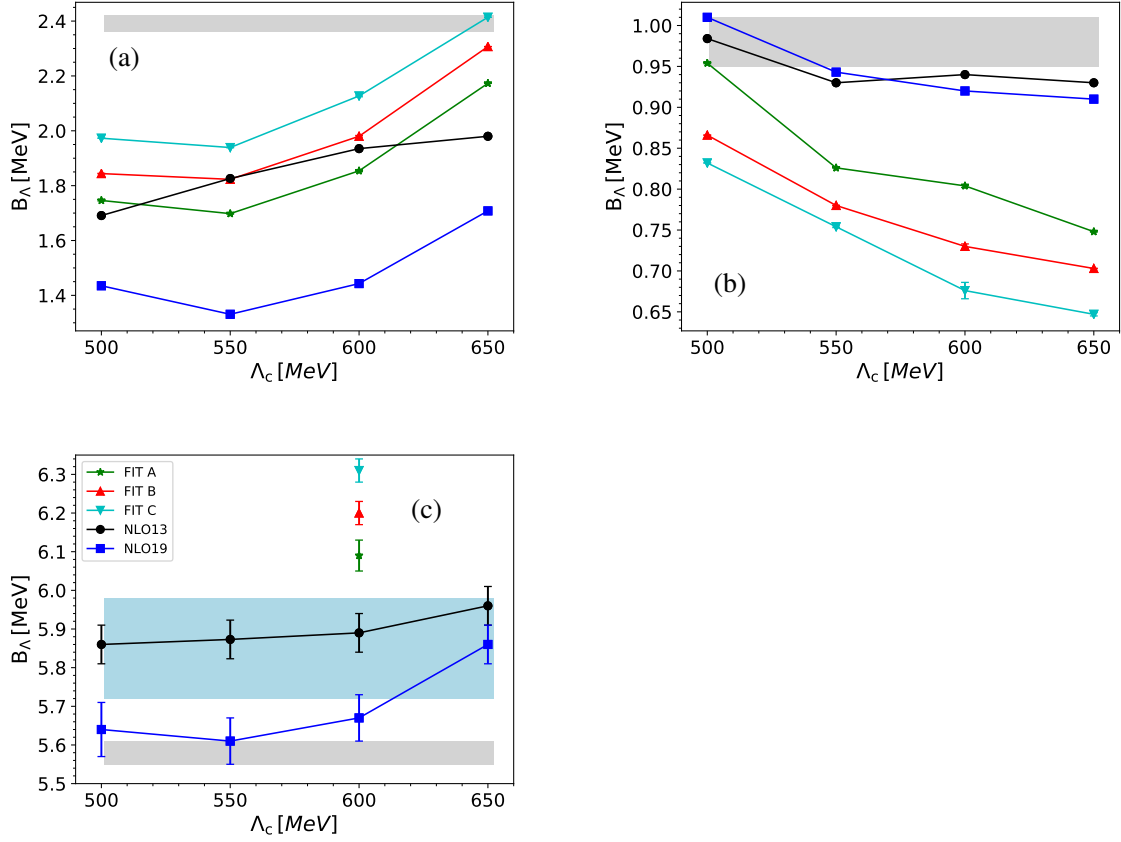
Figure 4.30: Separation energies of: (a) $^4_\Lambda He(0^+)$, (b) $^4_\Lambda He(1^+)$, (c) $^7_\Lambda Li(1/2^+)$, as a function of regulator $\Lambda_Y$. Calculations are based on the NLO13 (blue squares), NLO19 (black circles), Fit C (cyan down triangles), Fit B (red up triangles) and Fit C (grey stars) that are evolved to the magic flow parameter. The bands indicate the experimental value with the uncertainty. In figure (c) the grey and blue bands are results from the emulsion and counter experiments, respectively.

only one regulator in order to save a substantial amount of computational resources.

For a better visualization, we also plot the $\Lambda$-separation energies tabulated in Tables 4.8 and 4.10 for each $^4_\Lambda He(0^+)$, $^4_\Lambda He(1^+)$ and $^7_\Lambda Li(\frac{1}{2}^+)$ as a function of $\Lambda_Y$ regulators as shown in panels (a)-(c) of Fig. 4.30, respectively. Interestingly, the predictions of the NLO13 and NLO19 are quite similar to each other. This holds especially for the $^4_\Lambda He(1^+)$ state, see e.g. the blue and black lines in panel (b). Overall the regulator dependence is sizable in all the systems. It amounts to 200 keV in the $A = 4$ systems and approximately 300 keV for the $^7_\Lambda Li(\frac{1}{2}^+)$ state, indicating at rather significant contributions of the missing chiral 3BFs. We also observe noticeable changes in the separation energies for the two spin states of $^4_\Lambda He(0^+, 1^+)$ when changing from the NLO19 to Fit A-C. The results for the $0^+$ state increase and become much more closer to the experimental value. $\Lambda$-separation energy of $^4_\Lambda He(1^+)$, on the other hand, decreases with the Fit C predicting the smallest separation energies. This is not a surprise. As has been discussed for Eq. (4.7), the $1^+$ state is
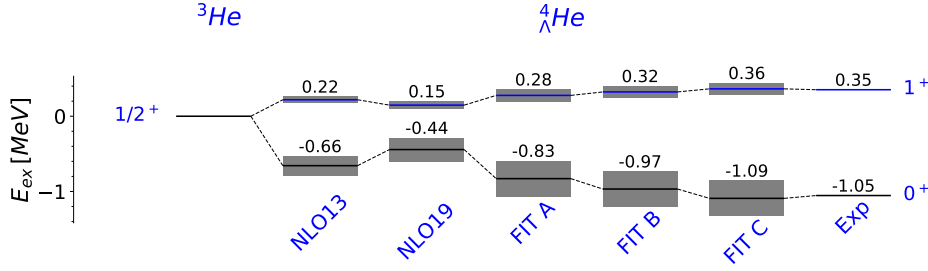
Figure 4.31: Energy spectrum of $^{4}_{\Lambda}$He. Calculations are based on chiral SMS N$^4$LO+(450) with $\lambda_{NN}$ = 1.6 fm$^{-1}$ and the YN NLO13, NLO19 interactions and FIT A-C for a wide range of chiral cutoffs $\Lambda_Y$ = 500 − 650 MeV. The experimental values are taken from [8, 123].

predominantly driven by the spin triplet $\Lambda N$ potentials and the corresponding scattering length $|a_t|$ is reduced for interactions from Fit C, B, A compared to the NLO19. Remarkably, the changes in the $\Lambda$-separation energies of the $0^+$ and $1^+$ states, caused by the new fits, leads to a significant improvement of the predictions of the level splitting $\Delta E$ between these two spin states. This is undoubtedly illustrated in Fig. 4.31. One sees that the new interactions indeed increase the splitting toward the experimental value of $\Delta E(exp)$ = 1.4 MeV [123], in particular Fit C that practically gives the correct value. On the contrary, the splittings of the order of $\Delta E$ = 0.88 and 0.59 MeV predicted by the NLO13 and NLO19 potentials, respectively, are considerably smaller than $\Delta E(exp)$. The pronounced discrepancy between $\Delta E$(NLO13) and $\Delta E$(NLO19) again stress the importance of the 3BFs to this observable. As a conclusion, the large splitting $\Delta E(exp)$ between the two $^{4}_{\Lambda}$He($0^+$) and $^{4}_{\Lambda}$He($1^+$) states is somewhat in favor of an increase of the singlet scattering length.

It is quite opposite to the predictions for the ground state of $^{7}_{\Lambda}$Li as shown in panel (c) of Fig. 4.30. Here, the $\Lambda$-separation energies predicted by the NLO13 and NLO19 are in fair agreement with the experiments. It should, however, be stressed again that there is a sizeable discrepancy between the emulsion- and counter-experiments as indicated by the grey and blue bands in panel (c), respectively. The predictions of the Fit A to C are somewhat larger than both experimental values for $B_\Lambda(^{7}_{\Lambda}$Li, $\frac{1}{2}^+)$. Nevertheless, the changes in $B_\Lambda(^{7}_{\Lambda}$Li, $\frac{1}{2}^+)$ are of the order of the 3BF contributions (about 300 keV) estimated from the regulator dependence.

It is also interesting to compare the predictions of these interactions for the $^{7}_{\Lambda}$Li spectrum. The results are displayed in Fig. 4.32 with the energy levels of $^{7}_{\Lambda}$Li positioned with respect to the centroid energy of the ground state as discussed in Fig. 4.25. Interestingly, by doing so, we observe that the energy level $(\frac{1}{2}^+, 1)$ (that is now identical with its relative centroid energy $\Delta\bar{E}(0^+)$ = $\bar{E}(0^+) - \bar{E}_{gs}$ = 3.95) is practically insensitive to the YN interactions employed, confirming the shell-model results obtained by Gal *et al.* in [121]. A slight variation (of about 50 keV) in our calculations is probably due to the contributions from the admixtures of the excited core states. Similarly, the relative centroid energy of the second doublet $\frac{5}{2}^+ - \frac{7}{2}^+$ is also almost constant, positioned at $\Delta\bar{E}(3^+)$ = $\bar{E}(3^+) - \bar{E}_{gs}$ = 2.83 MeV (see red dotted line). The insensitivity of $\Delta\bar{E}(3^+)$
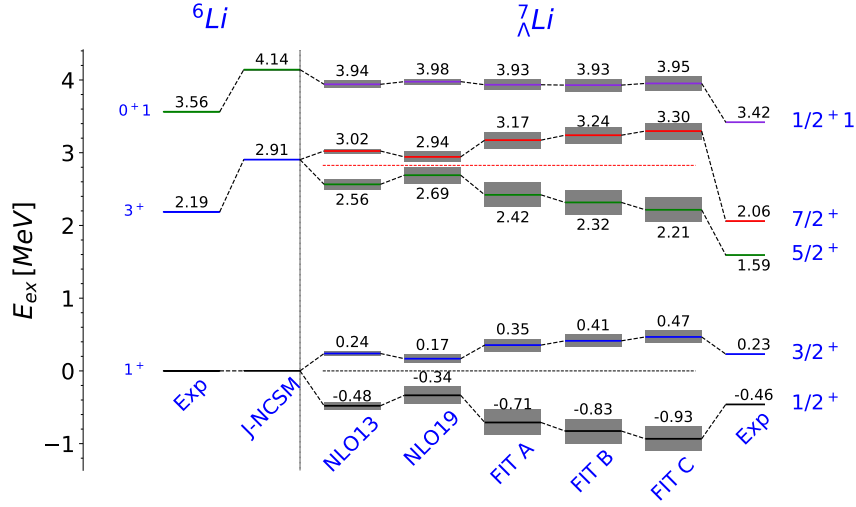
Figure 4.32: Energy spectra of $^7_\Lambda$Li and $^6$Li. Same NN and YN interactions as in ]. Calculations are based on chiral SMS N$^4$LO+(450) with $\lambda_{NN} = 1.6$ fm$^{-1}$ and the YN NLO13, NLO19 and Fit A-C interactions for a range of regulator $\Lambda_Y = 500 - 650$ MeV regulator. The experimental values are taken from [8, 11, 126].

and $\Delta\bar{E}(0^+)$ to the chosen YN interaction indicates the similarity of the overall strength of all employed potentials. Moreover, the main differences among these NLO YN potentials should arise mostly from their spin dependence. As a result, one finds that the doublet levels shift relative to the centroid energies and depend strongly on the interactions employed. Finally, the grey bands in Fig. 4.32 represent the dependence of the results on the chiral regulator $\Lambda_Y$, which are rather sizable for most of the energy levels. This possibly indicates a large influence of chiral 3BFs on the levels. Also, the NLO13 and NLO19 lead to slightly different predictions further reinforcing that 3BFs are non-negligible for the excitation energies. Let us further stress that the $P$-wave interactions of all considered NLO forces are by construction identical and small. We found that neglecting $P$- and higher partial waves in the interactions changes the energies only marginally, well within our regulator dependence.

In general all of the considered interactions qualitatively reproduce the $^7_\Lambda$Li spectrum. Quantitatively, however, none of the interactions is able to describe the experiment. For example, we find that the predicted $5/2^+$ state of $^7_\Lambda$Li is located above the $3^+$ state of $^6$Li whereas the ordering is opposite for the experimental values. While the two potentials NLO13 and NLO19 predicts the correct splittings of the two lowest doublets, the new fits A to C, however, further increase the splittings bringing them away from the experimental values. Nevertheless the deviations are minor when taking into account the possible contributions from 3BFs. In any case, the result show that changes of singlet scattering length (and consequently the hypertriton binding energies) indeed affect the spectra of p-shell hypernuclei. However, the changes are moderate and, therefore, the separation energy and spectrum remains qualitatively consistent with experiment for the new fits.

| | YN-NLO13 | YN-NLO19 | Exp |
|---|---|---|---|
| | $\lambda_{YN}^m = 0.904$ fm$^{-1}$ | $\lambda_{YN}^m = 0.87$ fm$^{-1}$ | |
| $^7_\Lambda$Li$^*$ | 5.45 ± 0.10 | 5.38 ± 0.09 | 5.26 ± 0.03 |
| $^7_\Lambda$Be | 5.44 ± 0.09 | 5.38 ± 0.08 | 5.16 ± 0.08 |
| $^7_\Lambda$He | 5.37 ± 0.09 | 5.30 ± 0.09 | 5.55 ± 0.1 ± 0.11 |

Table 4.11: Λ-separation energies of the A=7 isotriplet calculated with the NLO13 and NLO19 potentials for a regulator of 700 MeV in combination with the chiral SMS N$^4$LO+(450) evolved to an SRG cutoff of $\lambda_{NN} = 1.6$ fm$^{-1}$. The NLO13 and NLO19 are also evolved to their magic cutoffs of, at which $^5_\Lambda$He is properly described. The experiment values are from [133, 137, 144]. All energies are given in MeV.

## 4.7  A=7 isotriplet and CSB splittings

It has been demonstrated in Fig. 4.26 that without CSB terms included in the YN interactions, the CSB splittings of the $A = 4$ hypernuclei ($^4_\Lambda$He and $^4_\Lambda$H) are almost invisible. Let us also remind that the s-shell CSB effect arising from the Coulomb interaction and different masses within the isospin multiplet of nucleons and $\Sigma$'s are tiny [129, 130]. However, these calculations are an important baseline for starting investigations of CSB in hypernuclei (see works by Gazda [142] and Nogga [130] for recent progresses). Obviously, such investigations need to be carried out into the p-shell hypernuclei. Undoubtedly, the $A = 7$ isotriplet hypernuclei, $^7_\Lambda$He($\frac{1}{2}^+$, 1), $^7_\Lambda$Li$^*$($\frac{1}{2}^+$, 1) and $^7_\Lambda$Be($\frac{1}{2}^+$, 1) will be the most perfect candidates to start such a study. These systems are both experimentally and theoretically very interesting. Generally, hypernuclear binding energies are measured with rather large uncertainties, the situation is even worse for p-shell hypernuclei in particular $^7_\Lambda$He with only 16 events from emulsion experiments being reported so far [143]. Recently, the separation energy $B_\Lambda(^7_\Lambda$He) has been measured at JLab but with an uncomfortably large uncertainty, $B_\Lambda(^7_\Lambda$He)= 5.55 ± 0.1 ± 0.11 MeV [144] in comparison with that for $^7_\Lambda$Li$^*$: $B_\Lambda(^7_\Lambda$Li$^*$)= 5.26 ± 0.03 MeV [133, 137] and $^7_\Lambda$Be: $B_\Lambda(^7_\Lambda$Be)= 5.16 ± 0.08 MeV [137]. Theoretically, the Λ-separation energies $B_\Lambda$ of these isotriplets together with their energy level splittings can serve as key elements for studying the spin-dependence YN interactions [7, 8] as well as the origin of CSB splitting in combination with the CSB observed in the s-shell hypernuclei [113]. This motivates us to also study these isotriplets within the NCSM approach. With regard to the convergence of resonance states, we should stress that although the ground state of $^6$Be($0^+$, 1) is not a particle-stable state (decaying through the channel $^6$Be $\rightarrow^4$He $+p + p$), nevertheless it exhibits a very narrow resonance with the width of $\Gamma = 92 \pm 6$ keV [126]. We can therefore still obtain well-converged results for the ground states of the core $^6$Be and of the $^7_\Lambda$Be hypernucleus within the J-NCSM approach for model space size up to $\mathcal{N} = 10$.

Overall, we observe again the strong dependence of the Λ-separation energies for the $A = 7$ isotriplet on the regulator and on the SRG evolution, like for the other states of $^7_\Lambda$Li. There are also strong correlations between the $B_\Lambda$ of the multiplet and that of the $^5_\Lambda$He, as exemplified in Fig. 4.33 for the NLO13 potential. Furthermore, at the magic SRG cutoffs, the results predicted by the NLO13 and NLO19 are quite similar to each other and also comparable to the experiments. We provide in Table 4.11 the Λ-separation energies computed with the two potentials for a regulator of $\Lambda_Y = 700$
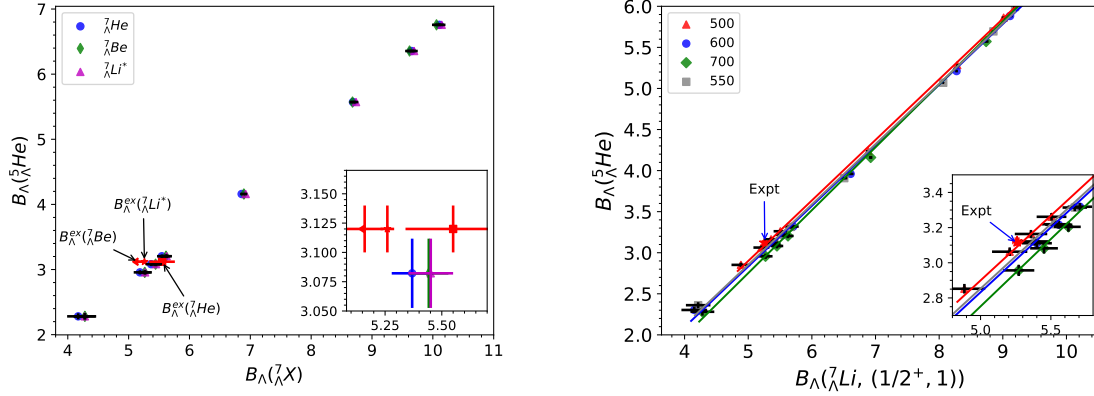
Figure 4.33: Correlations of $\Lambda$-separation energies for a wide range of flow parameters $\Lambda_Y$ of $^5_\Lambda$He and (a) $B_\Lambda(^7_\Lambda X)$, where X=He, Li$^*$ and Be using the NLO13(700) interaction, (b) $B_\Lambda(^7_\Lambda Li^*)$ using the NLO13 for several regulators of $\Lambda_Y = 500 - 700$ MeV. Same NN interaction as in Table 4.11.

MeV as an illustration. One sees that within the numerical uncertainties, the separation energies of the A=7 multiplet are actually the same. We also remark that our estimated errors are, however, rather large, of the same size as of the CSB estimated by Gal, $\Delta B_\Lambda(^7_\Lambda Be, ^7_\Lambda Li^*) = -17$ keV [113] or deduced from the experimental $\Lambda$-separation energies, e.g. $\Delta B_\Lambda^{exp}(^7_\Lambda Be, ^7_\Lambda Li^*) = -100 \pm 90$ keV [133, 137]. It is therefore more meaningfull to extract the CSB splittings of the multiplet from the separation energies calculated for a specific model space size (for example, the largest one i.e. $\mathcal{N} = 10$) instead of using the final extrapolated $B_\Lambda$. Before extracting CSB, let us first study the binding energies $E_{hyp}$ of the triplet for the largest model space $\mathcal{N} = 10$ in some details. To clarify the importance of different contributions to the binding (separation) energies, it is instructive to decompose $E_{hyp}$ into the kinetic energy $T$, strong NN potential $V_{NN}^{nucl}$, strong YN potential $V_{YN}^{nucl}$ and Coulomb interactions between a proton-proton (pp) pair $V_{NN}^C$ and between a YN pair $V_{YN}^C$. Note that similar decompositions have also been considered by Nogga when studied the CSB effects of the s-shell hypernuclei [145]. The decomposition for $^7_\Lambda Li^*$ using the NLO13(700) potential evolved to several SRG flow parameters is tabulated in Table 4.12. Similar tables are also obtained for the other two hypernuclei of the isotriplet which we refrain from showing here since they exhibit very similar trends to that of $^7_\Lambda Li^*$.

Overall, the NN Coulomb interaction is small (about 1.9 MeV) and almost independent of the evolution. The similar interaction (between a proton and a $\Sigma$) $V_{YN}^C$ is much smaller, of order of several keV only, and it is attractive in $^7_\Lambda Li^*$ and $^7_\Lambda He$ but becomes repulsive in $^7_\Lambda Be$ due to the difference between $\Sigma^+$- and $\Sigma^-$-probabilities in each system. In addition, at low SRG parameters ($\lambda_{YN} \leq 3.0$ fm$^{-1}$), the $\Lambda N - \Lambda N$ interaction, $V_\Lambda^{nucl}$, dominantly contributes to the total YN potential, $V_{YN}^{nucl}$, as compared to the contributions from the $\Lambda N - \Sigma N$ and $\Sigma N - \Sigma N$ interactions, $V_{\Lambda\Sigma}^{nucl}$ and $V_\Sigma^{nucl}$, respectively. However, at higher SRG cutoffs, the two potentials $V_\Lambda^{nucl}$ and $V_{\Lambda\Sigma}^{nucl}$ are practically of the same size. The $V_\Sigma^{nucl}$ potential is in general small (about several hundreds keV at most) but changes sign during the SRG evolution. Interestingly, we observe noticeable growths in $V_\Sigma^{nucl}$ and

| $\lambda_{\text{YN}}$ | $T$ | $V_{NN}^{C}$ | $V_{YN}^{C}$ | $V_{NN}^{nucl}$ | $V_{YN}^{nucl}$ | $V_{\Lambda}^{nucl}$ | $V_{\Lambda\Sigma}^{nucl}$ | $V_{\Sigma}^{nucl}$ | $E_{hyp}$ |
| --- | --- | --- | --- | --- | --- | --- | --- | --- | --- |
| [fm$^{-1}$] | [MeV] | [MeV] | [keV] | [MeV] | [MeV] | [MeV] | [MeV] | [MeV] | [MeV] |
| 0.836 | 89.851 | 1.841 | -2 | -113.903 | -11.767 | -10.277 | -1.122 | -0.370 | -33.981 |
| 1.0 | 93.944 | 1.871 | -1 | -116.880 | -15.415 | -14.861 | -0.482 | -0.072 | -36.480 |
| 1.6 | 101.315 | 1.917 | -1 | -120.827 | -22.012 | -20.560 | -1.374 | -0.080 | -39.608 |
| 2.0 | 102.399 | 1.920 | -1 | -120.938 | -23.053 | -20.167 | -2.824 | -0.063 | -39.672 |
| 2.6 | 101.392 | 1.901 | -2 | -119.647 | -22.109 | -17.062 | -4.894 | 0.065 | -38.457 |
| 3.0 | 99.604 | 1.895 | -2 | -118.300 | -20.205 | -14.200 | -6.192 | 0.186 | -37.007 |
| 4.0 | 93.765 | 1.857 | -2 | -114.901 | -13.218 | -7.337 | -6.288 | 0.405 | -32.499 |

Table 4.12: Difference contributions to the binding energy in $^{7}_{\Lambda}\text{Li}^{*}$ for model space $\mathcal{N} = 10$. The calculations are based on the SMS N$^4$LO+(450) with an SRG cutoff of $\lambda_{NN} = 1.6$ fm$^{-1}$ and the YN NLO13(700) evolved to several $\lambda_{YN}$ flow parameters.

$V_{\Lambda\Sigma}^{nucl}$ when evolving from the flow parameter of $\lambda_{YN} = 1.0$ to $\lambda_{YN} = 0.836$ fm$^{-1}$. Note that this is also consistent with the slight increase in $P_{\Sigma}$ that was observed before. During the evolution, the kinetic energy $T$ and the strong NN interaction $V_{NN}^{nucl}$ also vary, but their effects largely cancel each other. As a result, the change in the total binding energy $E_{hyp}$ is mainly driven by the dependence of the $V_{Y}^{nucl}$ on the evolution parameter.

Analogously, the nuclear-core binding energies can also be decomposed into the kinetic energy $T(core)$, strong NN potential $V_{NN}^{nucl}(core)$, and Coulomb interactions between a proton-proton (pp) pair $V_{NN}^{C}(core)$. Now, based on the decompositions of the hypernuclear and nuclear-core binding energies, we can compute the CSB, $\Delta_{CSB}$, between every two components of the multiplet, saying $^{7}_{\Lambda}\text{He}$ and $^{7}_{\Lambda}\text{Li}^{*}$ as follows

$$
\begin{aligned}
\Delta_{CSB}(^{7}_{\Lambda}\text{He}, {}^{7}_{\Lambda}\text{Li}^{*}) &= B_{\Lambda}(^{7}_{\Lambda}\text{He}) - B_{\Lambda}(^{7}_{\Lambda}\text{Li}^{*}) \\
&= (E(^{6}\text{He}) - E(^{6}\text{Li}^{*})) - (E(^{7}_{\Lambda}\text{He}) - E(^{7}_{\Lambda}\text{Li}^{*})) \\
&= (T(^{6}\text{He}) - T(^{6}\text{Li}^{*})) - (T(^{7}_{\Lambda}\text{He}) - T(^{7}_{\Lambda}\text{Li}^{*})) \\
&\quad + (V_{NN}^{nucl}(^{6}\text{He}) - V_{NN}^{nucl}(^{6}\text{Li}^{*})) - (V_{NN}^{nucl}(^{7}_{\Lambda}\text{He}) - V_{NN}^{nucl}(^{7}_{\Lambda}\text{Li}^{*})) \\
&\quad + (V_{NN}^{C}(^{6}\text{He}) - V_{NN}^{C}(^{6}\text{Li}^{*})) - (V_{NN}^{C}(^{7}_{\Lambda}\text{He}) - V_{NN}^{C}(^{7}_{\Lambda}\text{Li}^{*})) \\
&\quad - (V_{YN}^{nucl}(^{7}_{\Lambda}\text{He}) - V_{YN}^{nucl}(^{7}_{\Lambda}\text{Li}^{*})) \\
&\quad - (V_{YN}^{C}(^{7}_{\Lambda}\text{He}) - V_{YN}^{C}(^{7}_{\Lambda}\text{Li}^{*})) \\
&\equiv \Delta_{T}^{\text{CSB}} + \Delta_{V_{NN,nucl}}^{\text{CSB}} + \Delta_{V_{NN,C}}^{\text{CSB}} + \Delta_{V_{YN,nucl}}^{\text{CSB}} + \Delta_{V_{YN,C}}^{\text{CSB}}.
\end{aligned}
\tag{4.8}
$$

We further estimate perturbatively the individual CSB contributions in Eq. (4.8), employing the two wavefunctions $^{7}_{\Lambda}\text{Li}^{*}$ and $^{6}\text{Li}^{*}$. At this exploratory stage, let us stick with specific NN and YN

| | $\lambda_{YN}$ | $\delta_\Sigma$ | $\Delta_T^{CSB}$ | $\Delta_{NN,nucl}^{CSB}$ | $\Delta_{NN,C}^{CSB}$ | $\Delta_{YN,nucl}^{CSB}$ | $\Delta_{YN,C}^{CSB}$ | $\Delta_{CSB}$ | $\Delta_{CSB}^{exact}$ |
|---|---|---|---|---|---|---|---|---|---|
| | [fm$^{-1}$] | [%] | [keV] | [keV] | [keV] | [keV] | [keV] | [keV] | [keV] |
| | 0.836 | -0.34 | -16.8 | -2.0 | 15.0 | -52.1 | 1.0 | -54.9 | -53.3 |
| | 1.0 | -0.14 | -6.8 | -8.0 | 34.0 | -24.4 | -0.0 | -5.2 | -5.4 |
| $^7_\Lambda$He$-^7_\Lambda$Li$^*$ | 1.60 | -0.18 | -9.8 | -13.0 | 58.0 | -16.7 | 1.0 | 19.5 | 19.4 |
| | 2.0 | -0.26 | -12.8 | -13.0 | 59.0 | -14.1 | 2.0 | 21.1 | 19.9 |
| | 2.6 | -0.36 | -19.8 | -12.0 | 53.0 | -9.8 | 2.0 | 13.4 | 14.3 |
| | 3.0 | -0.41 | -21.8 | -10.0 | 46.0 | -7.7 | 3.0 | 9.5 | 8.5 |
| | 4.0 | -0.41 | -21.8 | -7.0 | 26.0 | -4.4 | 2.0 | -5.2 | -9.7 |
| $^7_\Lambda$He$-^7_\Lambda$Li$^*$ [146] | | | | | | | | | 20(230) |
| | 0.836 | 0.35 | 16.7 | -5.0 | -19.0 | 21.5 | -5 | 9.2 | 8.0 |
| | 1.0 | 0.15 | 7.7 | -12.0 | -49.0 | 19.8 | -2.0 | -35.5 | -37.1 |
| $^7_\Lambda$Be$-^7_\Lambda$Li$^*$ | 1.6 | 0.21 | 8.7 | -20.0 | -83.0 | 16.3 | -3.0 | -81.0 | -81.1 |
| | 2.0 | 0.29 | 13.7 | -21.0 | -83.0 | 13.8 | -4.0 | -80.5 | -82.4 |
| | 2.6 | 0.41 | 17.7 | -19.0 | -74.0 | 9.8 | -6.0 | -71.5 | -71.8 |
| | 3.0 | 0.47 | 21.7 | -16.0 | -64.0 | 7.5 | -7.0 | -57.8 | -59.6 |
| | 4.0 | 0.46 | 20.7 | -11.0 | -35.0 | 4.5 | -6.0 | -26.8 | -34.0 |
| $^7_\Lambda$Be$-^7_\Lambda$Li$^*$ [113] | | 0.12 | 3.0 | | -70.0 | 50.0 | | | -17.0 |
| $^7_\Lambda$Be$-^7_\Lambda$Li$^*$ [137] | | | | | | | | | $-100(90)$ |

Table 4.13: Perturbative calculation of the CSB splitting in the A=7 isotriplet for model space $\mathcal{N} = 10$. Same NN and YN potentials as in Table 4.12. The second columns is the difference between probabilities of finding $\Sigma^+$ and $\Sigma^-$ for $^7_\Lambda$He and $^7_\Lambda$Be. Note that in Gal calculations [113] (second last row), 0.12 % is the total $\Sigma$ probability but not the difference between $P_{\Sigma^+}$ and $P_{\Sigma^-}$. This extremely small $\Sigma$-admixture leads to a negligibly weak $\Delta_T^{CSB}$ contribution. The negative 70 keV contribution attributed to the Coulomb forces is in fact a net effect of the nuclear-core Coulomb energy modification $\Delta_{NN,C}^{CSB}$ and the $\Sigma p$ Coulomb interaction $\Delta_{YN,nucl}^{CSB}$.

interactions, namely the SMS N$^4$LO+(450) for the NN interaction evolved to an SRG parameter of $\lambda_{NN} = 1.6$ fm$^{-1}$ and the NLO13(700) interaction. The YN potential is also SRG evolved to a range of flow parameters, $0.836 \leq \lambda_{YN} \leq 4.0$ fm$^{-1}$. The influence of the interaction models on the results will be investigated in future. Table 4.13 displays various contributions to the perturbative $\Delta_{CSB}$ and the exact CSB $\Delta_{CSB}^{exact}$ splittings (the last two columns) between every two members of the isotriplet. Clearly, our perturbative estimations of $\Delta_{CSB}$ agree perfectly (within less than 5 keV) with the full calculations. This accuracy is definitely sufficient for our purpose of studying the origin of p-shell CSB splittings.

It apparently sticks out from Table 4.13 that our estimated CSB for $^7_\Lambda$Be -$^7_\Lambda$Li$^*$ actually agrees both in sign and magnitude with the experimental value. It is, however, difficult to compare the CSB results for $^7_\Lambda$He$-^7_\Lambda$Li$^*$ with the experiments. Our computed values even change sign with respect to the flow parameters while experimental estimation, $\Delta_{exp} = 20 \pm 230$ keV, comes with a large uncertainty. Nevertheless, it can be seen that the overall CSB for the pair $^7_\Lambda$Be$-^7_\Lambda$Li$^*$ is insignificantly small. In general, one can read off that the $\Delta_{\text{CSB}}$ splitting in A=7 isotriplet is fairly small, and driven predominantly by the NN Coulomb modification $\Delta^{\text{CSB}}_{NN,C}$. The latter is mostly a result of the contraction of nuclear cores induced by a hyperon, therefore, strongly influenced by the SRG-YN evolutions as it can be seen from the table. The contributions due to the NN and YN interactions and the $\Sigma^+/\Sigma^-$ mass differences, $\Delta^{\text{CSB}}_{NN,nucl}$, $\Delta^{\text{CSB}}_{YN,nucl}$ and $\Delta^{\text{CSB}}_T$, respectively, are of the same order of magnitude. However these contributions largely cancel each other in $^7_\Lambda$Be$-^7_\Lambda$Li$^*$ leaving a sole contribution from $\Delta^{\text{CSB}}_{NN,C}$. As a result, the $\Delta_{CSB}$ between the two members, $^7_\Lambda$Be and $^7_\Lambda$Li$^*$, about 80 keV at the SRG cutoff of $\lambda_{YN} = 1.6$ fm$^{-1}$, is much larger than that between $^7_\Lambda$He and $^7_\Lambda$Li$^*$ at the same cutoff. In the second column in Tab. 4.13 we also listed the difference between the $\Sigma^\pm$-probabilities, $\delta_\Sigma = P_{\Sigma^+} - P_{\Sigma^-}$, for $^7_\Lambda$He and $^7_\Lambda$Be. It is further noticed that the kinetic contribution $\Delta^{\text{CSB}}_T$ has the same sign as the CSB splitting due to $\Sigma^+$ and $\Sigma^-$ rest mass difference, which is given by [145]

$$\Delta T^{\text{CSB}}_{M_R} = \delta_\Sigma (m_{\Sigma^-} - m_{\Sigma^+}), \qquad m_{\Sigma^-} - m_{\Sigma^+} = 8.1 \text{ MeV}.$$

However, its size is noticeably smaller, $\Delta^{\text{CSB}}_T \approx \frac{2}{3}\Delta T^{\text{CSB}}_{M_R}$ at most. Additionally, we observe a strong influence the of SRG-YN evolution on $\Delta^{\text{CSB}}_{YN,nucl}$, the value of which however vanishes as the YN potential being less and less evolved. This is not a surprise. Let us remind that there is no explicit CSB terms in the employed version of the YN interaction model. The only source of the $\Delta^{\text{CSB}}_{YN,nucl}$ is then the physical masses of nucleons and $\Sigma$'s that were used in the generator of the flow equation Eq. (2.5). Furthermore, the CSB effect induced by the YN Coulomb interactions, $\Delta^{\text{CSB}}_{YN,C}$, is rather small but stable, its size is of order of 6 keV in $^7_\Lambda$Be -$^7_\Lambda$Li$^*$.

Let us finally summarize that, without explicit CSB terms in YN interactions, our results for CSB in the A=7 isotriplet are rather small but in a good agreement with the experimental values, and they are are dominantly given by the Coulomb NN interaction. In order to verify the sufficiency of studying CSB splittings for the largest model space $\mathcal{N}_{max} = 10$, we additionally show the CSB splitting calculated with the model space size $\mathcal{N} = 8$ in Table 4.14. Comparing the two tables, one notices that all the different contributions to CSB except $\Delta^{\text{CSB}}_{NN,C}$ converge very quickly (within several keV at most). The slight discrepancies of about 7 keV for $\Delta_{\text{CSB}}(^7_\Lambda$He $-^7_\Lambda$ Li) and 15 keV for $\Delta_{\text{CSB}}(^7_\Lambda$Be $-^7_\Lambda$ Li) between the two model space sizes, occurring at large flow parameters, are primarily due to the slow convergence of $\Delta^{\text{CSB}}_{NN,C}$. We therefore conclude that the model space $\mathcal{N} = 10$ is sufficient to understand the essence of CSB in the A=7 isotriplet.

| | $\lambda_{YN}$ | $\delta_\Sigma$ | $\Delta_T^{CSB}$ | $\Delta_{NN,nucl}^{CSB}$ | $\Delta_{NN,C}^{CSB}$ | $\Delta_{YN,nucl}^{CSB}$ | $\Delta_{YN,C}^{CSB}$ | $\Delta_{CSB}$ | $\Delta_{CSB}^{exact}$ |
| | [fm$^{-1}$] | [%] | [keV] | [keV] | [keV] | [keV] | [keV] | [keV] | [keV] |
|---|---|---|---|---|---|---|---|---|---|
| | 0.836 | -0.38 | -18.3 | 0.0 | 9.0 | -58.0 | 1.0 | -66.3 | -64.2 |
| | 1.0 | -0.14 | -7.3 | -6.0 | 27.0 | -25.5 | -0.0 | -11.8 | -12.0 |
| | 1.6 | -0.18 | -8.3 | -11.0 | 48.0 | -17.0 | 1.0 | 12.7 | 11.7 |
| $^7_\Lambda$He$-^7_\Lambda$Li$^*$ | 2.0 | -0.25 | -12.3 | -11.0 | 49.0 | -13.9 | 1.0 | 12.8 | 12.2 |
| | 2.6 | -0.35 | -17.3 | -9.0 | 41.0 | -9.4 | 2.0 | 7.3 | 7.0 |
| | 3.0 | -0.40 | -20.3 | -8.0 | 34.0 | -7.2 | 2.0 | 0.5 | 1.3 |
| | 4.0 | -0.41 | -20.3 | -3.0 | 14.0 | -4.3 | 2.0 | -11.6 | -11.4 |
| | 0.836 | 0.39 | 18.4 | -2.0 | -10.0 | 23.6 | -5.0 | 25.0 | 23.3 |
| | 1.0 | 0.16 | 7.4 | -9.0 | -38.0 | 20.6 | -2.0 | -21.0 | -22.9 |
| | 1.6 | 0.21 | 9.4 | -17.0 | -69.0 | 16.5 | -3.0 | -63.1 | -64.5 |
| $^7_\Lambda$Be$-^7_\Lambda$Li$^*$ | 2.0 | 0.29 | 13.4 | -18.0 | -68.0 | 13.8 | -4.0 | -62.8 | -65.2 |
| | 2.6 | 0.39 | 18.4 | -15.0 | -58.0 | 9.4 | -6.0 | -51.2 | -52.6 |
| | 3.0 | 0.45 | 19.4 | -13.0 | -46.0 | 7.2 | -6.0 | -38.4 | -39.2 |
| | 4.0 | 0.46 | 20.4 | -5.0 | -20.0 | 4.3 | -7.0 | -7.3 | -8.0 |

Table 4.14: Perturbative calculation of the CSB splitting in the A=7 isotriplet for model space $\mathcal{N}=8$. The second columns is the difference between probabilities of finding $\Sigma^+$ and $\Sigma^-$ for $^7_\Lambda$He and $^7_\Lambda$Be. Calculations based on the same interactions as in Table 4.12.

## 4.8 RMS radii and correlations in hypernuclei

When diagonalizing the Hamiltonian Eq. (3.1), one obtains both the binding energies and the corresponding wavefunctions. The former provides precious information about how strong the interactions among the constituent particles are. The latter is necessary in order to understand the dynamics of the systems as well as to compute many other important quantities such as quadrupole moments, electromagnetic transitions and so on. Our primary goal in this section is to explore the spatial distributions of a hyperon and a nucleon in hypernuclei exploiting the hypernuclear wavefunctions calculated in the previous sections. That is to say, we are interested in the density distribution functions (one-body density) and the correlations within YN and NN pairs (two-body density). We define the density distribution of a hyperon ($\Lambda$, $\Sigma$) or a nucleon ($n$, $p$), labelled as the $A$-th particle, in momentum-space as follows

$$\mathcal{D}_A(p) = \langle\Psi|\delta(p - p_A)P_A|\Psi\rangle, \tag{4.9}$$

where the $\delta$ function fixes the magnitude of the particle momentum $p_A$ to $p$ and the isospin projection operator $P_A$ is to single out the particle A-th with isospin $t$ and the third component $m_t$

$$P_A = |tm_t\rangle_{AA}\langle tm_t|. \tag{4.10}$$

The distribution functions $\mathcal{D}_A(p)$ Eq. (4.9) are subjected to the following normalization conditions

$$\int_0^\infty \mathcal{D}_n(p)dp + \int_0^\infty \mathcal{D}_p(p)dp = 1 \quad \text{and} \quad \int_0^\infty \mathcal{D}_\Lambda(p)dp + \int_0^\infty \mathcal{D}_\Sigma(p)dp = 1. \tag{4.11}$$

Similarly, the momentum-space correlation functions $C_{NN/YN}$, which determine the probability of finding a pair $NN/YN$ with relative momentum $p$, together with their normalization conditions read

$$
\begin{aligned}
C_{NN}(p) &= \langle\Psi|\delta(p - p_{NN})|\Psi\rangle, & \int_0^\infty C_{NN}dp &= 1, \\
C_{YN}(p) &= \langle\Psi|\delta(p - p_{YN})P_{\tau_Y}|\Psi\rangle, & \int_0^\infty C_{\Lambda N}(p)dp + \int_0^\infty C_{\Sigma N}(p)dp &= 1.
\end{aligned}
\tag{4.12}
$$

One can analogously define the distribution and correlation functions in configuration space. The evaluations of $\mathcal{D}_A$ and $C_{NN/YN}$ with respect to the Jacobi bases are considered in Appendix B. We have experienced that the two chiral interactions, NLO13 and NLO19, together with the SRG evolution have strong influence on the separation energies and the $\Sigma$-probability as well. It motivates us to examine whether the two interactions and the SRG evolution have similar impacts on the distributions Eqs. (4.9) and (4.12) in Section 4.8.1.

Furthermore, based on the distributions $\mathcal{D}_A$ and $C_{NN/YN}$, one can easily compute the RMS point-particle radii and the relative distance of a pair $NN$ or $YN$, for instance

$$\bar{r}_{n/p}^2 \equiv \langle r_{n/p}^2 \rangle = \frac{\int_0^\infty \mathcal{D}_{n/p}(r)r^2 dr}{\int_0^\infty \mathcal{D}_{n/p}(r)dr}, \qquad \bar{r}_{NN}^2 \equiv \langle r_{NN}^2 \rangle = \frac{\int_0^\infty C_{NN}(r)r^2 dr}{\int_0^\infty C_{NN}(r)dr}. \tag{4.13}$$

Similar expressions can be written for $\bar{r}_{\Lambda N}$, $\bar{r}_{\Sigma N}$, $\bar{r}_\Lambda$ and $\bar{r}_\Sigma$. Note that in Eq. (4.13) we have employed the the bare operator $r^2$ rather than an SRG-evolved one. Therefore, results for RMS and radii will certainly be SRG-dependent. Nevertheless, for typical long-ranged operators like $r^2$, we expect a rather mild effect of the SRG evolution [147]. The sensitivities of these quantities to the YN chiral interactions and their SRG evolutions are thoroughly studied in Sections 4.8.3 to 4.8.5. In the following, we shall employ the SMS N$^4$LO+(450) evolved to an SRG parameter of $\lambda_{NN} = 1.6$ fm$^{-1}$ for the NN interaction in all the calculations.

## 4.8.1  Distribution and correlation functions in hypernuclei

We now investigate the effect of the NLO13 and NLO19, and their SRG evolutions on the one- and two-body densities for the ground states of $A = 4 − 7$ hypernuclei. We show explicitly results for a chiral cutoff of $\Lambda_Y = 650$ MeV and two SRG flow parameters of $\lambda_{YN} = 0.836$ and $2.6$ fm$^{-1}$. Since the potentials are derived in momentum space, it is natural to compare the distributions (correlations) also in momentum space. We start with the momentum-space correlations. Such correlations of a YN and NN pairs computed for the ground-state wavefunctions of $^4_\Lambda$He, $^5_\Lambda$He and $^7_\Lambda$Li are illustrated in Fig. 4.34. Overall, the $NN$ correlation functions $C_{NN}$ (dashed lines) are smooth and have a very similar shape in all systems. The maximum of the $NN$ correlations is close to that of the $C_{\Sigma N}$, which positions around $p = 0.4$ fm$^{-1}$ for $^4_\Lambda$He and shifts to $p = 0.55$ fm$^{-1}$ for $^5_\Lambda$He and $^7_\Lambda$Li. It can also be observed that both YN interactions and the SRG evolutions have very little influence on

(a) $^4_\Lambda$He, $\lambda_{YN} = 0.836$ fm$^{-1}$.

(b) $^4_\Lambda$He, $\lambda_{YN} = 2.6$ fm$^{-1}$.

(c) $^5_\Lambda$He, $\lambda_{YN} = 0.836$ fm$^{-1}$.

(d) $^5_\Lambda$He, $\lambda_{YN} = 2.6$ fm$^{-1}$.

(e) $^7_\Lambda$Li, $\lambda_{YN} = 0.836$ fm$^{-1}$.

(f) $^7_\Lambda$Li, $\lambda_{YN} = 2.6$ fm$^{-1}$.
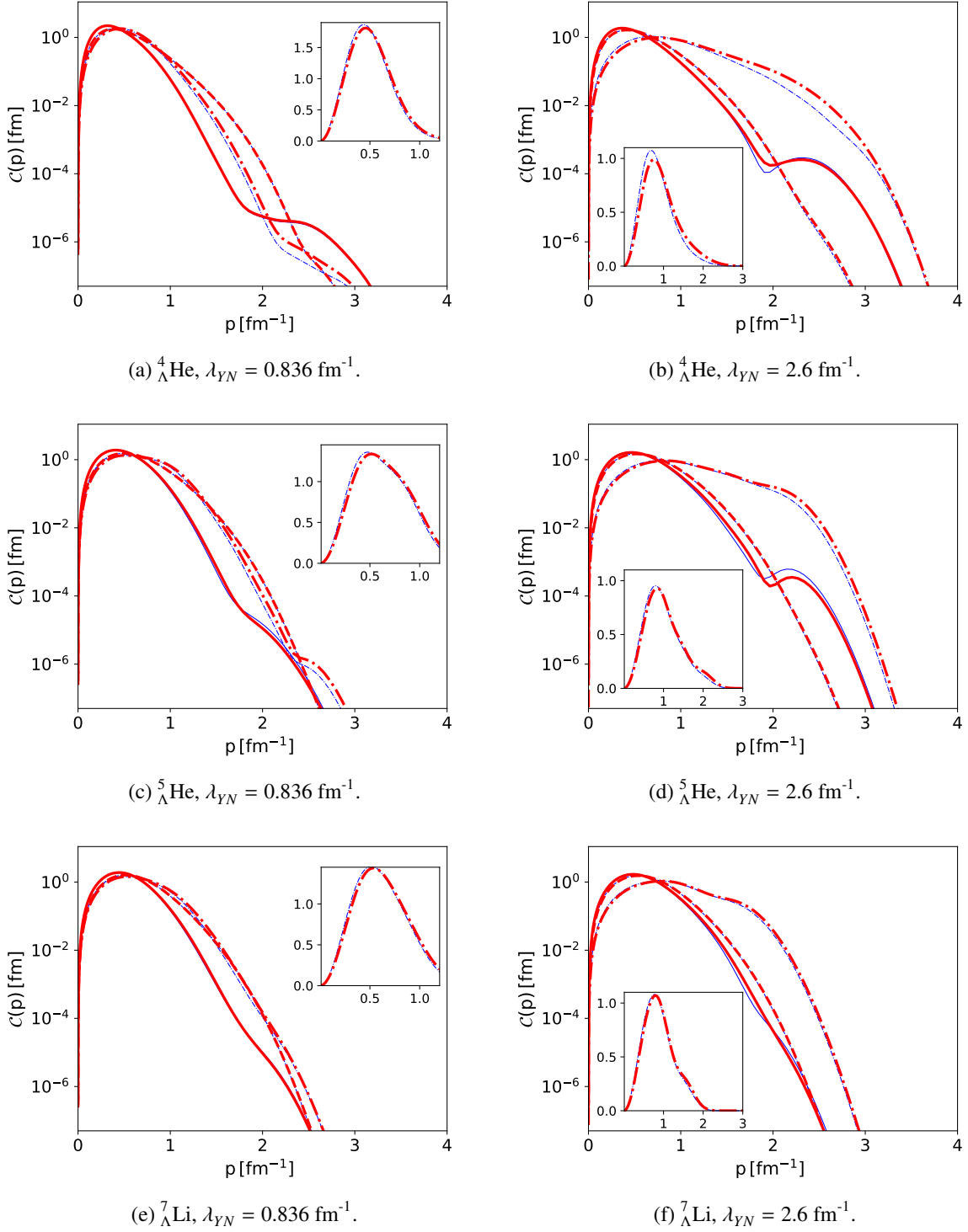
Figure 4.34: Momentum-space correlation functions of the $\Lambda N$ (solid line), $\Sigma N$ (dash-dotted line) and NN (dashed line) pairs in the ground states of $^4_\Lambda$He, $^5_\Lambda$He and $^7_\Lambda$Li. The calculations were performed with the SMS N$^4$LO+(450) for an SRG-NN cutoff of $\lambda_{NN} = 1.6$ fm$^{-1}$ in combination with the two YN potentials NLO13(650) (thin blue lines) and NLO19(650) (thick red lines) potentials evolved to two flow parameters of $\lambda_{YN} = 0.836$ fm$^{-1}$ (left) and 2.6 fm$^{-1}$ (right). The correlation functions are normalized to $\int C_{YN/NN}(p)dp = 1$ for better a comparison. The inset shows the $C_{\Sigma N}$ function on a linear scale.

| | $\lambda_{YN} = 0.836$ fm$^{-1}$ | | $\lambda_{YN} = 2.6$ fm$^{-1}$ | |
|---|---|---|---|---|
| | NLO13 | NLO19 | NLO13 | NLO19 |
| $^4_\Lambda$He($0^+$) | 1.676(3) | 1.571(3) | 3.615(4) | 3.842(4) |
| $^5_\Lambda$He($\frac{1}{2}^+$) | 2.27(4) | 2.77(3) | 6.29(2) | 7.18(1) |
| $^7_\Lambda$Li($\frac{1}{2}^+$) | 4.78(12) | 5.38(7) | | 10.53(15) |

Table 4.15: Separation energies of the ground states of the s- and p-shell hypernuclei calculated using the SMS N$^4$LO+(450) with an evolution parameter of $\lambda_{NN} = 1.6$ fm$^{-1}$ in combination with the NLO13 and NLO19 interactions for a regulator of $\Lambda_Y = 650$ MeV and two flow parameters of $\lambda_{YN} = 0.836$ and 2.6 fm$^{-1}$. Energies are given in MeV.

the NN correlations. Indeed, over the entire momentum range, the $C_{NN}(p)$ functions, obtained using the NLO13 and NLO19 potentials for the two $\lambda_{YN}$ cutoffs, are hardly distinguishable. On the contrary, the *YN* correlations exhibit a rather strong SRG-dependence in particular the $C_{\Sigma N}$ functions (dash-dotted line). For all investigated systems, the $\Sigma N$-correlations become considerably narrow for a low SRG-YN cutoff of $\lambda_{YN} = 0.836$ fm$^{-1}$ (left figures) as compared to the same functions for $\lambda_{YN} = 2.6$ fm$^{-1}$ (right figures). There are also some deviations between the $C_{YN}$ correlations calculated with the two chiral potentials. The small deviations at low momenta (see also the inset plots) can probably be traced back to the difference in the separation energies, see Table 4.15, which are obviously more enhanced for the higher SRG cutoff. At high momenta, the discrepancy in the $\Lambda N$-correlations is negligible, whereas that in $C_{\Sigma N}$ remains quite visible for the s-shell hypernuclei, but again becomes negligibly small for $^7_\Lambda$Li. It also clearly sticks out that the $\Lambda N$-correlations for the s- and p-shell hypernuclei have quite different shapes. There is a dip structure in the $C_{\Lambda N}(^4_\Lambda$He$)$ and $C_{\Lambda N}(^5_\Lambda$He$)$ functions around $p = 1.8$ fm$^{-1}$. This dip structure is strongly amplified as the cutoff $\lambda_{YN}$ increases from 0.836 fm$^{-1}$ to 2.6 fm$^{-1}$, as easily noticed in the first four plots in Fig. 4.34. It, however, disappears in $C_{\Lambda N}(^7_\Lambda$Li$)$ which exhibits a smooth behavior over the whole momentum range. This is possibly related to different contributions of the *P*-waves to the ground-state wavefunctions. The hypernuclear wavefunctions of $^4_\Lambda$He and $^5_\Lambda$He are apparently dominated by the *S*-waves (at low momenta), while the ground state of $^7_\Lambda$Li may also get significant contributions from higher-momentum partial waves (dominantly the *P*-waves). When these *P*-waves contributions are strong enough they may fill up the dip structure that presence due to the short-range repulsion in the *S*-waves.

We now turn to study the configuration space correlations in hypernucei. Although these functions are not yet experimentally observable, they are still of great interest since they can provide qualitatively information about the contractions of nuclear cores due to the presence of a hyperon. Experimentally, the nuclear core contraction can be deduced from the reduction of the electric quadrupole transition probabilities $B(E2)$ which scale with the fourth order of the nuclear size [75, 133]. To the aim of exploring the dynamic change of the nuclear cores, we present in Fig. 4.35 the

(a) $^4_\Lambda$He, $\lambda_{YN} = 0.836$ fm$^{-1}$.

(b) $^4_\Lambda$He, $\lambda_{YN} = 2.6$ fm$^{-1}$.

(c) $^5_\Lambda$He, $\lambda_{YN} = 0.836$ fm$^{-1}$.

(d) $^5_\Lambda$He, $\lambda_{YN} = 2.6$ fm$^{-1}$.

(e) $^7_\Lambda$Li, $\lambda_{YN} = 0.836$ fm$^{-1}$.

(f) $^7_\Lambda$Li, $\lambda_{YN} = 2.6$ fm$^{-1}$.
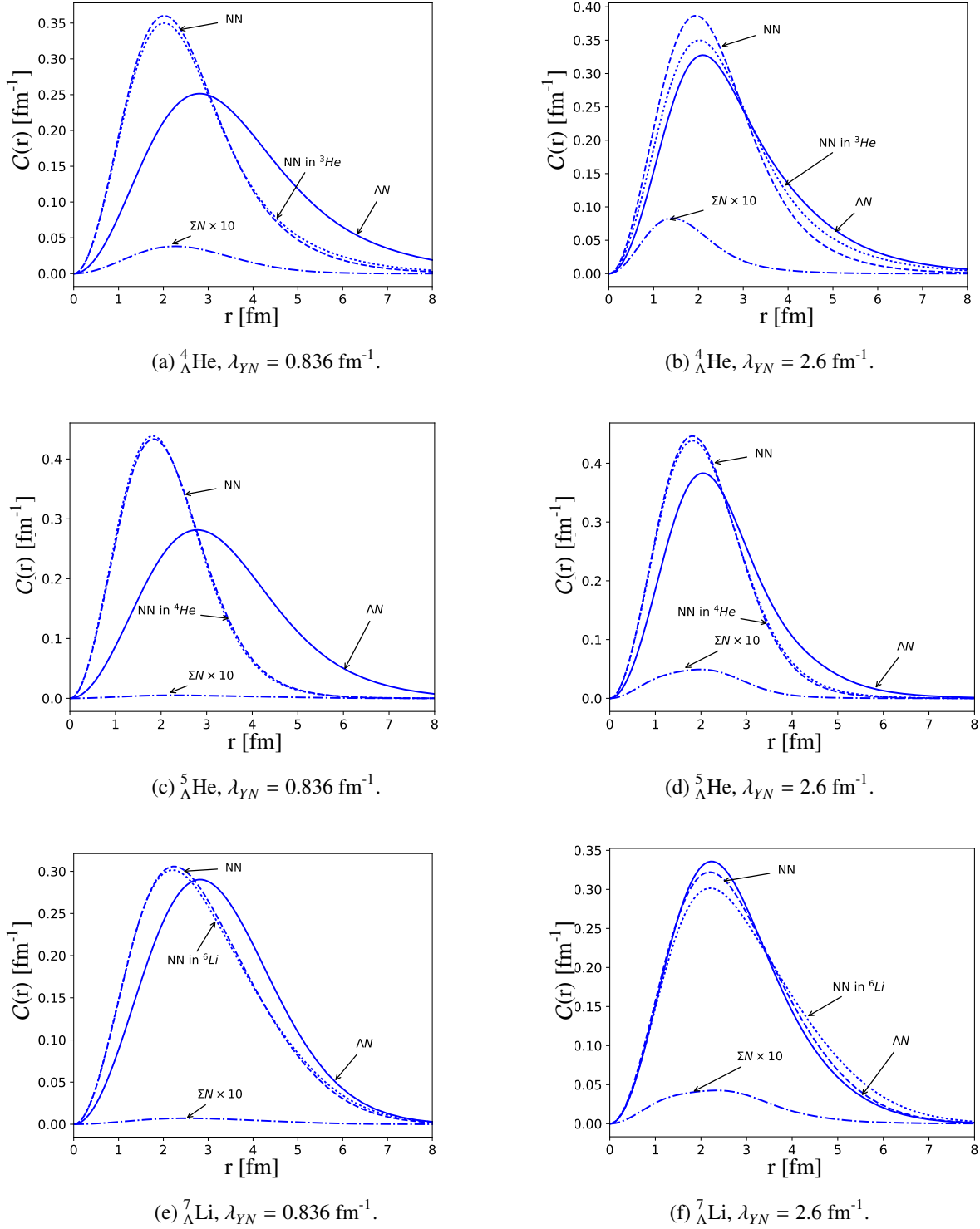
Figure 4.35: Configuration space $\Lambda N$, $\Sigma N$ and $NN$ correlation functions in $A = 4 - 7$ hypernuclei together with the $NN$ correlation of the nuclear core. The calculations are based on the SMS N$^4$LO+(450) with an SRG-NN cutoff of $\lambda_{NN} = 1.6$ fm$^{-1}$ in combination with the NLO13(650) potential for two flow parameters of $\lambda_{YN} = 0.836$ fm$^{-1}$ (left) and $\lambda_{YN} = 2.6$ fm$^{-1}$ (right). The functions are normalized to $\int C_{\Lambda N}(r)dr + \int C_{\Sigma N}(r)dr = 1$ and $\int C_{NN}(r)dr = 1$. The $C_{\Sigma N}$ correlation was multiplied by a factor of 10 to make it visible.

r-space *NN*, Λ*N* and Σ*N*correlation functions for the s- and p-shell hypernuclei together with the *NN* correlation for the parent nucleus.

The calculations are based on the NLO13 potential for a regulator of $\Lambda_Y = 650$ MeV and two flow parameters of $\lambda_{YN} = 0.836$ and 2.6 fm$^{-1}$. We refrain from showing the results for NLO19(650) since they are quite similar to the NLO13(650) results. Here, we use the linear scale and normalize the functions to

$$\int C_{\Lambda N}(r)dr + \int C_{\Sigma N}(r)dr = 1 \quad \text{and} \quad \int C_{NN}(r)dr = 1, \tag{4.14}$$

since we are more interested in the actual form of the correlations which in turn can visually provide information about the relative distance between a pair of particles. It is quickly noticed that the *NN* correlations in all hypernuclear systems exhibit a very similar shape as that of $C_{NN}$ for the parent nucleus, indicating that the contraction of the core occurring along the relative *NN* distance is small. This indeed agrees with the observation by Hiyama *et al.* [74] who found that the nuclear-core contraction occurs primarily between the two centers of mass of an *NN* pair and the remaining nucleons whereas the change in the relative distance of an *NN* pair is minor. Furthermore, the Σ*N* correlations (dash-dotted lines) are of the shortest range with the positions of the maxima located closely to those of the NN correlations (as we have seen for the momentum-space correlations). Moreover, for the s-shell hypernuclei, the Λ*N* correlation functions (solid lines) are longer-ranged and flatter than the $C_{NN}$ for both values of $\lambda_{YN}$. It is, however, not always observed for the Λ*N* correlation in $^7_\Lambda$Li. For high $\lambda_{YN}$ cutoffs, e.g. $\lambda_{YN} = 2.6$ fm$^{-1}$ (see bottom right plot), $C_{\Lambda N}(^7_\Lambda\text{Li})$ is even of somewhat larger extent than $C_{NN}(^7_\Lambda\text{Li})$. That is not very surprising. Generally, one can expect that the *NN* correlations are of shorter range than $C_{\Lambda N}$ since the strength of *NN* interactions is significantly stronger compared to that of YN potentials, which is indeed true for the s-shell hyprernuclei independent of the SRG evolutions (see also Tables 4.16 and 4.19). However, this no longer holds for $^7_\Lambda$Li at high SRG cutoffs ($\lambda_{YN} \geq 1.60$ fm$^{-1}$ see also Table 4.21) because the SRG evolutions then strongly overbind $^7_\Lambda$Li so that the Λ-separation energies, e.g. $B_\Lambda(^7_\Lambda\text{Li}) = 10.16$ MeV at $\lambda_{YN} = 1.6$ fm$^{-1}$, significantly exceed the nuclear separation energy of the core, $B_N(^6\text{Li}) = 5.33$ MeV [148].

In the next step, we study the impact of YN interactions on the momentum distributions of a Λ, Σ hyperon and a nucleon. We use the logarithmic scale and normalize the distribution functions to

$$\int \mathcal{D}_{\Lambda/\Sigma/N}(p)dp = 1. \tag{4.15}$$

In Fig. 4.36, we present the $\mathcal{D}_\Lambda(p)$ (solid lines) and $\mathcal{D}_\Sigma(p)$ (dash-dotted lines) distributions for the ground states of the $A = 4 - 7$ hypernuclei. The calculations are based on the NLO13 (thin blue lines) and NLO19 (red thick lines) interactions for $\Lambda_Y = 650$ MeV and two SRG cutoffs, $\lambda_{YN} = 0.836$ fm$^{-1}$ (left) and $\lambda_{YN} = 2.6$ fm$^{-1}$ (right). We do not show the nuclear distribution $\mathcal{D}_N(p)$ explicitly but report that their dependence on the YN models and on the SRG evolution are very mild like for the *NN* correlations. As expected, the Σ distributions show somewhat stronger dependence on the interaction models than the Λ distribution functions do. Indeed, the discrepancy between $\mathcal{D}_\Sigma(p)$ computing with the NLO13 and NLO19 is noticeable over the whole momentum range (see also the insets) and for all three hypernuclei whereas that in $\mathcal{D}_\Lambda(p)$ is only visible for $^5_\Lambda$He and $^7_\Lambda$Li at moderate momenta, $1.5 \leq p \leq 2.5$ fm$^{-1}$. Likewise, the SRG evolution seems to also strongly affect

(a) $^4_\Lambda$He, $\lambda_{YN} = 0.836$ fm$^{-1}$.

(b) $^4_\Lambda$He, $\lambda_{YN} = 2.6$ fm$^{-1}$.

(c) $^5_\Lambda$He, $\lambda_{YN} = 0.836$ fm$^{-1}$.

(d) $^5_\Lambda$He, $\lambda_{YN} = 2.6$ fm$^{-1}$.

(e) $^7_\Lambda$Li, $\lambda_{YN} = 0.836$ fm$^{-1}$.

(f) $^7_\Lambda$Li, $\lambda_{YN} = 2.6$ fm$^{-1}$.
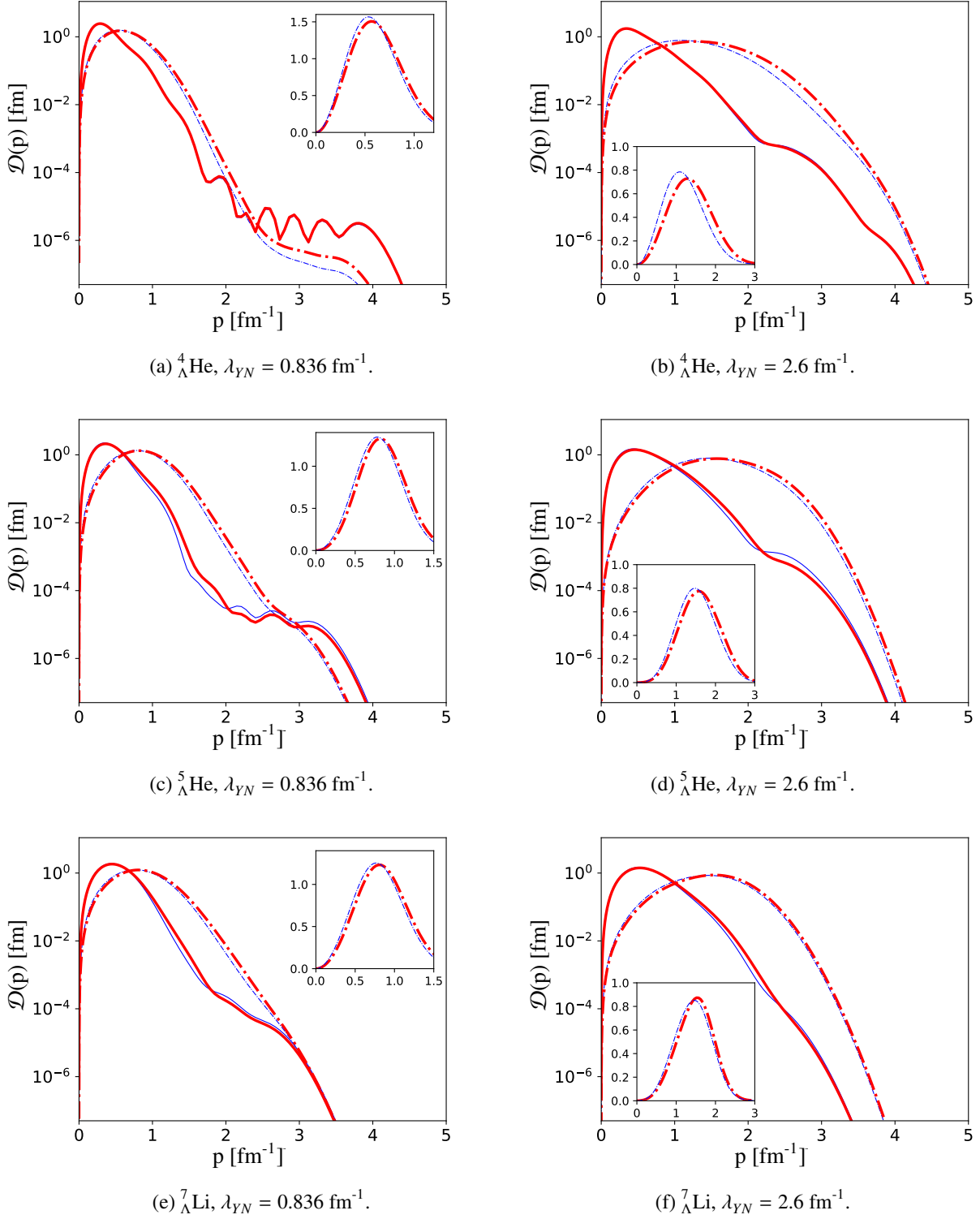
Figure 4.36: Momentum distribution functions $\mathcal{D}_\Lambda$ (solid line) and $\mathcal{D}_\Sigma$ (dash-dotted) line hyperon for the ground states of $A = 4 - 7$ hypernuclei. The calculations were performed with the SMS N$^4$LO+(450) for an SRG-NN cutoff of $\lambda_{NN} = 1.6$ fm$^{-1}$ in combination with the two YN potentials NLO13(650) (thin blue lines) and NLO19(650) (thick red lines) potentials evolved to two flow parameters of $\lambda_{YN} = 0.836$ fm$^{-1}$ (left) and 2.6 fm$^{-1}$ (right). The functions normalized to $\int \mathcal{D}_{\Lambda/\Sigma}(p)dp = 1$ for a better comparison. The insets show $\mathcal{D}_\Sigma$ on a linear scale.

both low- and high-momentum components of $\mathcal{D}_\Sigma(p)$. At the SRG cutoff of $\lambda_{YN} = 2.6$ fm$^{-1}$, the $\Sigma$-distribution functions for $^5_\Lambda$He and $^7_\Lambda$Li have exhibit a peak around $p = 1.6$ fm$^{-1}$ and $\mathcal{D}_\Sigma(^4_\Lambda$He$)$ is maximal at $p = 1.3$ fm$^{-1}$. At a lower SRG parameter of $\lambda_{YN} = 0.836$ fm$^{-1}$, we observe a shift of the $\Sigma$-distribution peaks to much lower momentum, around $p = 0.6$ fm$^{-1}$ for all three hypernuclei. It is quite different for the $\Lambda$ distribution whose low-momentum components are less influenced by the evolution. One can easily notice a stable peak of the $\Lambda$ distributions, around $p = 0.4$ fm$^{-1}$, for both values of $\lambda_{YN}$.

## 4.8.2  Extracting RMS distance and radii

In the previous section, we have discussed some interesting features of the one- and two-body correlation functions as well as their YN-model and SRG-evolution dependence. Let us now employ these functions to compute the RMS distances and point-particle radii in hypernuclei. Obviously, these quantities must be dependent on the HO frequency $\omega$ and model space $\mathcal{N}$. Because of the long-ranged operator $r^2$, the behavior of the radii and distances with respect to $\omega$ is expected to substantially differ from that of the energy. This is clearly illustrated in Fig. 4.37 where the $\omega$-dependence of $\Lambda$, $\Sigma$, p/n radii and their relative distances together with the binding energy for the $^4_\Lambda$He$(0^+)$ state are shown. For all model spaces $\mathcal{N}$, the radii and distance steadily decrease as $\omega$ grows, in contrast to an approximately parabolic $\omega$-dependence of the energy. Nevertheless, the slope of the radii (distances) curves becomes flatter with increasing model space. Moreover, in most of the cases, one can find the optimal frequency, $\omega^{opt}_{rad}$, at which the $\omega$-dependence curves of different $\mathcal{N}$ intersect or at least stay most closely to each other. In addition, around the intersection point $\omega^{opt}_{rad}$, the radii (distances) curves are practically flat for sufficiently large model space $\mathcal{N}$. This is very similar to the behavior of the point-proton radii in ordinary nuclei computed using the NCSM approach [81, 93], see also our results for the radii and binding energy of the $^3$He core in Fig. 4.38. We note that similar patterns are observed for the RMS radii and distances in $^5_\Lambda$He and $^7_\Lambda$Li. Additionally, it turns out that in conventional nuclei, $\omega^{opt}_{rad}$ is often rather close to the optimal frequency, $\omega^{opt}_E$, that gives the lowest binding energy (calculated with the largest model space $\mathcal{N}_{max}$). This $\omega^{opt}_E$ is often used in order to extract the final results for the proton or neutron radii [93]. Unfortunately, this is no longer the case for radii and distances calculated using the hypernuclear wavefunctions. We do not observe a similar relation between the minima of the energy curves, $\omega^{opt}_E$, and the intersection point of all radii (distances) curves, $\omega^{opt}_{rad}$. Nevertheless, it appears that around the crossing point $\omega^{opt}_{rad}$, the dependence of radii and distances on $\omega$ frequency and model space $\mathcal{N}$ are smallest. We can therefore use the values for radii and distances around $\omega^{opt}_{rad}$ for extracting the final model-independent results. Here, we also follow the two-step extrapolating procedure as done for the binding energy in Section 4.1 but with some modifications for the fitting functions. Based on the above observations, it is expected that linear fitting functions for radii (distances) will be more appropriate than the parabolic and exponential forms (Eqs. (4.1) and (4.2)) used for the energy extrapolation. Hence, in the first step of minimizing the $\omega$ dependence, we employ a straight line to fit those values of radii (or distances) around the intersection point $\omega^{opt}_{rad}$ (we take usually two to three points to each sides). This $\omega$-fitting procedure is performed separately for each model space $\mathcal{N}$. Note that, we do not enforce the same optimal $\omega$ ranges for all model space sizes. Here, the standard uncertainty is assigned for each $\omega$-fitting radius (distance). The $\omega$-fitting line (dashed line)
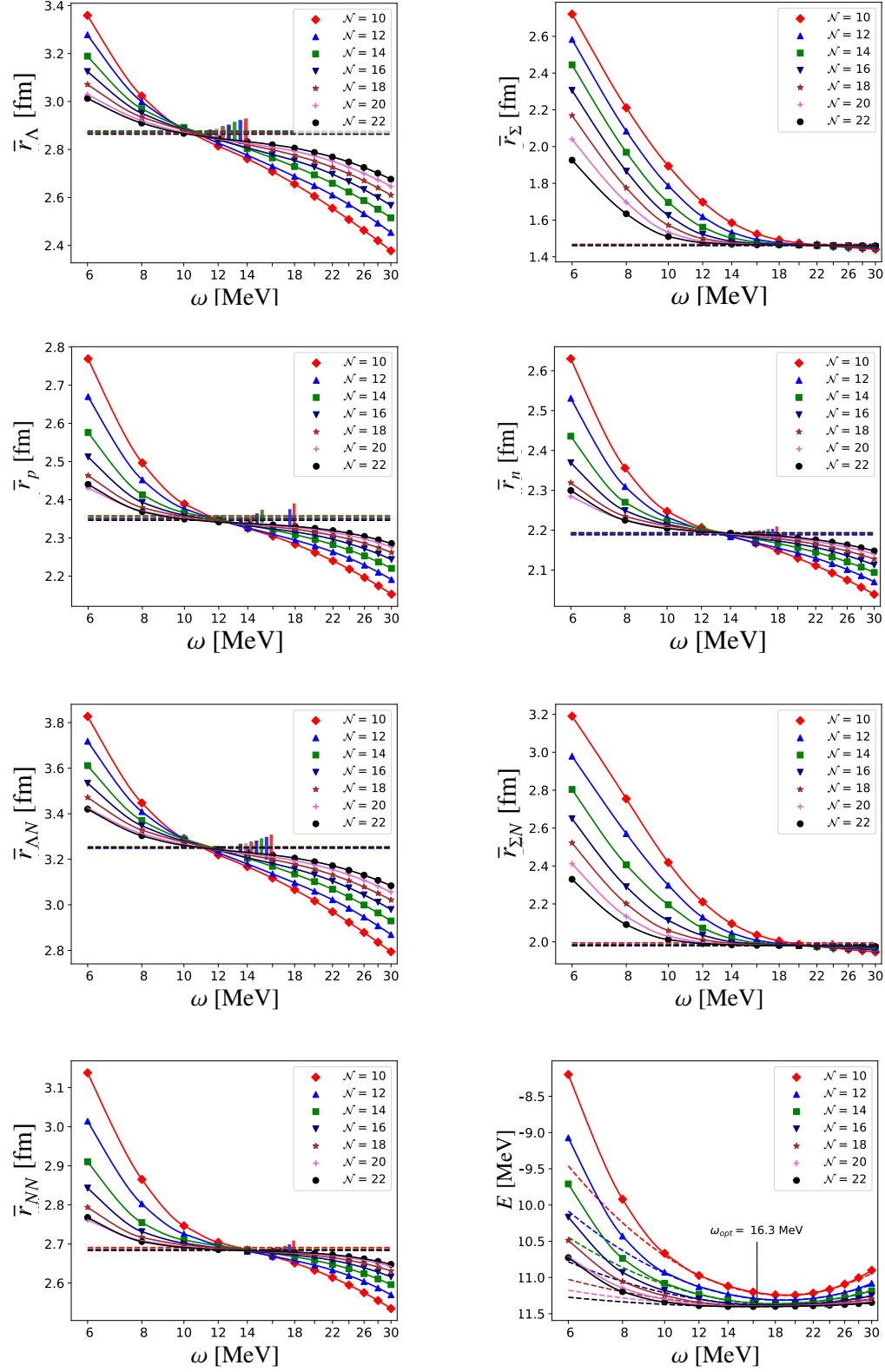
Figure 4.37: $\omega$-dependence of particle radii and distances for different model space in $^{4}_{\Lambda}\mathrm{He}(0^+)$. Calculations are performed using the SMS N$^4$LO+(450) potential for an SRG cutoff of $\lambda_{NN} = 1.6$ fm$^{-1}$ in combination with the NLO13 for $\Lambda_Y = 650$ MeV and a flow parameter of $\lambda_{\mathrm{YN}} = 2.6$ fm$^{-1}$. Solid lines are used to guide the eyes, dashed lines are obtained from the fitting and the vertical bars indicate the estimated uncertainty.
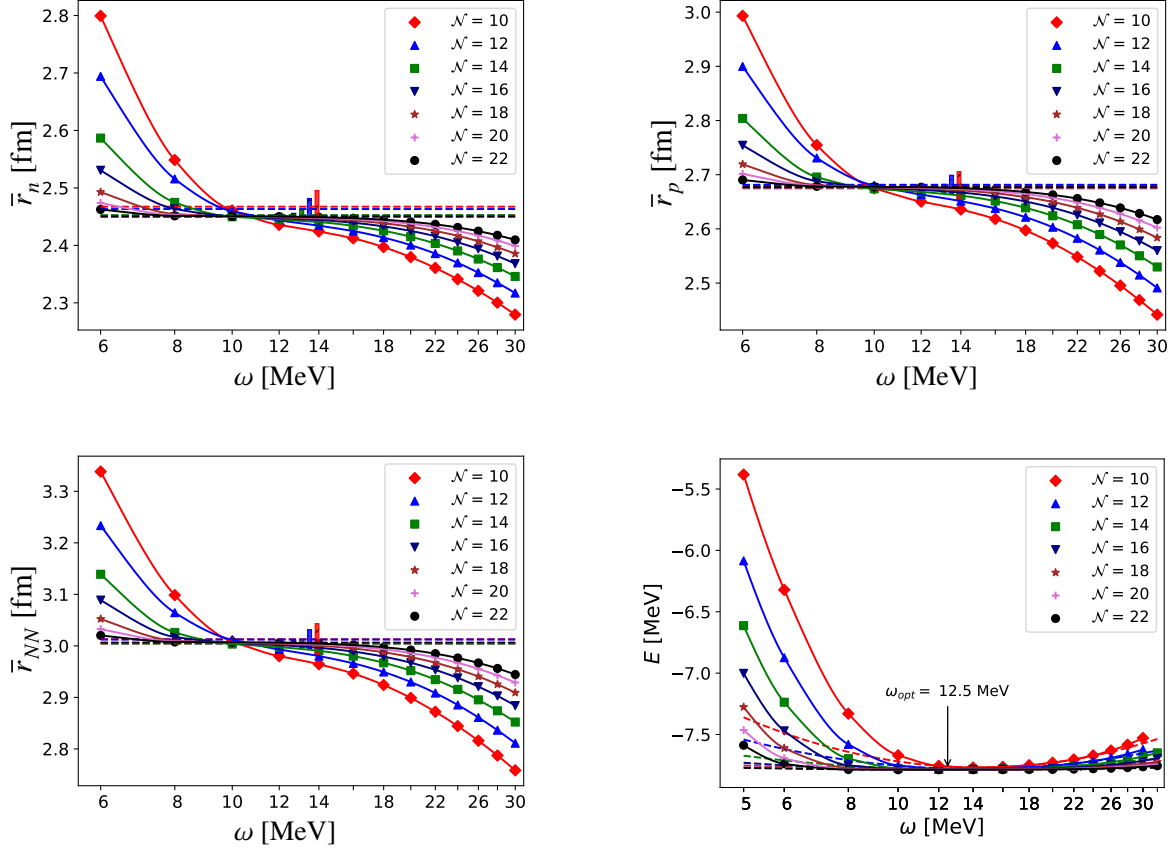
Figure 4.38: $\omega$-dependence of proton and neutron radii, RMS distance and energy in $^3$He. Same description of the NN interaction and lines as in Fig. 4.37.

and its uncertainty (vertical bar) for each model space $\mathcal{N}$ are also shown in Fig. 4.37 or the right plot in Fig. 4.39.

### 4.8.3  $^4_\Lambda$He($0^+$)

We now apply the just described procedure to extract radii and distances in $^4_\Lambda$He($0^+$) and study the effect of the NLO13(650) and NLO19(650) together with the SRG evolutions on these quantities. We will first focus on the SRG dependence and present results for the NLO13 interactions in some details. The converged results for the two interactions and wide a range of flow parameters will be finally tabulated in tables.

In Fig. 4.40, we illustrate the $\omega$-dependence of $\bar{r}_\Lambda$ and its convergence with respect to model spaces for a range of $\lambda_{YN}$. In general, most of the $\omega$-dependence curves for different $\mathcal{N}$ cross at very similar $\omega_{rad}^{opt}$, especially when the SRG cutoffs are high ($\lambda_{YN} > 1.0$ fm$^{-1}$). For these values of $\lambda_{YN}$, we observe a perfect convergence pattern for the $\Lambda$ radius in model spaces. With decreasing $\lambda_{YN}$, the crossing point , $\omega_{rad}^{opt}$ shifts to smaller values, for instance $\omega_{rad}^{opt} = 9$ MeV for $\lambda_{YN} = 2.0$ fm$^{-1}$
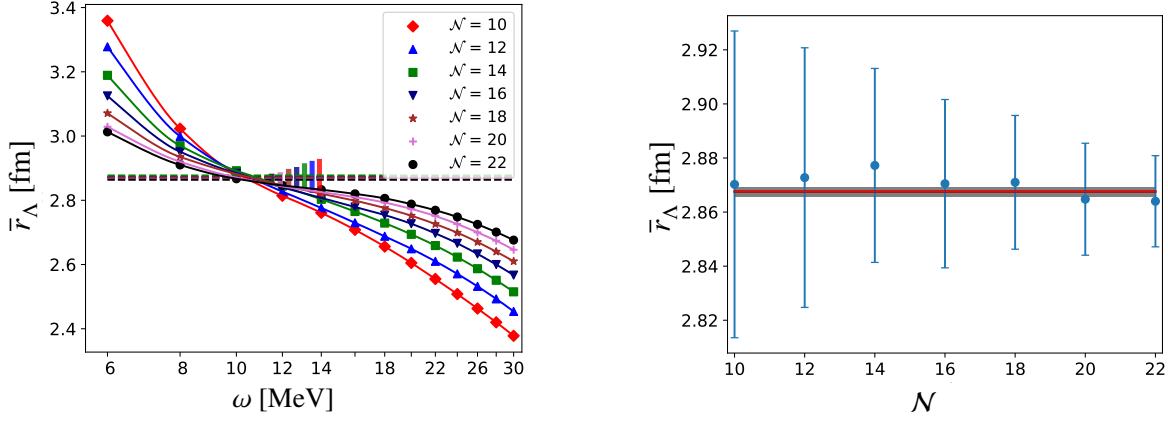
Figure 4.39: Extraction of $\Lambda$ radius with respect to $\omega$ (left figure) and model spaces $\mathcal{N}$ (right figure) in $^4_\Lambda$He($0^+$). Same description of interactions as in Fig. 4.37.

and $\omega_{rad}^{opt} = 5$ MeV for $\lambda_{YN} = 0.836$ fm$^{-1}$, which is even further away from the optimal $\omega$ for the energies, $\omega_E^{opt} \approx 16$ MeV. For low values of $\lambda_{YN}$, especially $\lambda_{YN} = 0.836$ fm$^{-1}$, the $\mathcal{N}_{max} = 22$ curve somehow deviates from the rest, which makes it rather difficult to obtain the converged results, see the last row in Fig. 4.40. The slow convergence of $\bar{r}_\Lambda$ for $\lambda_{YN} \leq 1.0$ fm$^{-1}$ is likely a consequence of long-ranged tails of the wavefunctions that are not well-described by the HO bases. As our results for separation energies in Section 4.2 have shown, over the considered range of $\lambda_{YN}$ ($0.836 \leq \lambda_{YN} \leq 3.00$ fm$^{-1}$) lower SRG cutoffs lead to smaller separation energies. The latter will result in even longer-range wavefunctions since the tails of the wavefunctions are proportional to $\exp(-\sqrt{2\mu B_\Lambda} r)/r$, with $\mu$ and $B_\Lambda$ being the reduced mass of a nucleon and a $\Lambda$ hyperon, and the $\Lambda$-separation energy, respectively. Due to this long-tail behavior, $\mathcal{D}_\Lambda(r)$ should behave like $\exp(-\sqrt{2\mu B_\Lambda} r)$ at large distances. Assuming that the short- and intermediate-distance behaviors of the J-NCSM based $\Lambda$ distribution are well converged, we therefore attempt to fit an exponential function of the form $A \exp(-2\sqrt{2\mu E} r)$ to the distribution $\mathcal{D}_\Lambda(r)$ (obtained from our calculations for each $\omega$ and $\mathcal{N}$) over a certain range determined by two parameters, $r_1$ and $r_2$,

$$\mathcal{D}_\Lambda(r) = A \exp(-2\sqrt{2\mu B_\Lambda} r) \qquad r_1 \leq r \leq r_2 \qquad (4.16)$$

The "repaired" distribution $\mathcal{D}_\Lambda^r(r)$ is then taken as

$$\mathcal{D}_\Lambda^r(r) = \begin{cases} \mathcal{D}_\Lambda(r) & r \leq r_2 \\ A \exp(-2\sqrt{2\mu B_\Lambda} r) & r_2 < r \end{cases} \qquad (4.17)$$

Here, the fitting parameters $r_1$ and $r_2$ are at first an educated guess but they must be carefully adjusted such that in this range the exponential form Eq. (4.16) exactly describes the calculated distribution $\mathcal{D}_\Lambda(r)$ and there is a smooth transition from $\mathcal{D}_\Lambda(r)$ to $\mathcal{D}_\Lambda^r(r)$. These criteria for choosing an appropriate fitting interval ($r_1$, $r_2$) for the distribution computed for $\mathcal{N} = 10$ and $\omega = 10$ are exemplified in Fig. 4.41.

Figure 4.40: $\omega$- and $\mathcal{N}$-dependence of $\Lambda$ radius in $^{4}_{\Lambda}\mathrm{He}(0^{+})$ computed using the NLO13 for a regulator of $\Lambda_Y = 650$ MeV and several flow parameters, $\lambda_{YN} = 2.0\,1.6$ and $0.836$ fm$^{-1}$. Same descriptions of the employed NN interaction and lines as in Fig. 4.37.
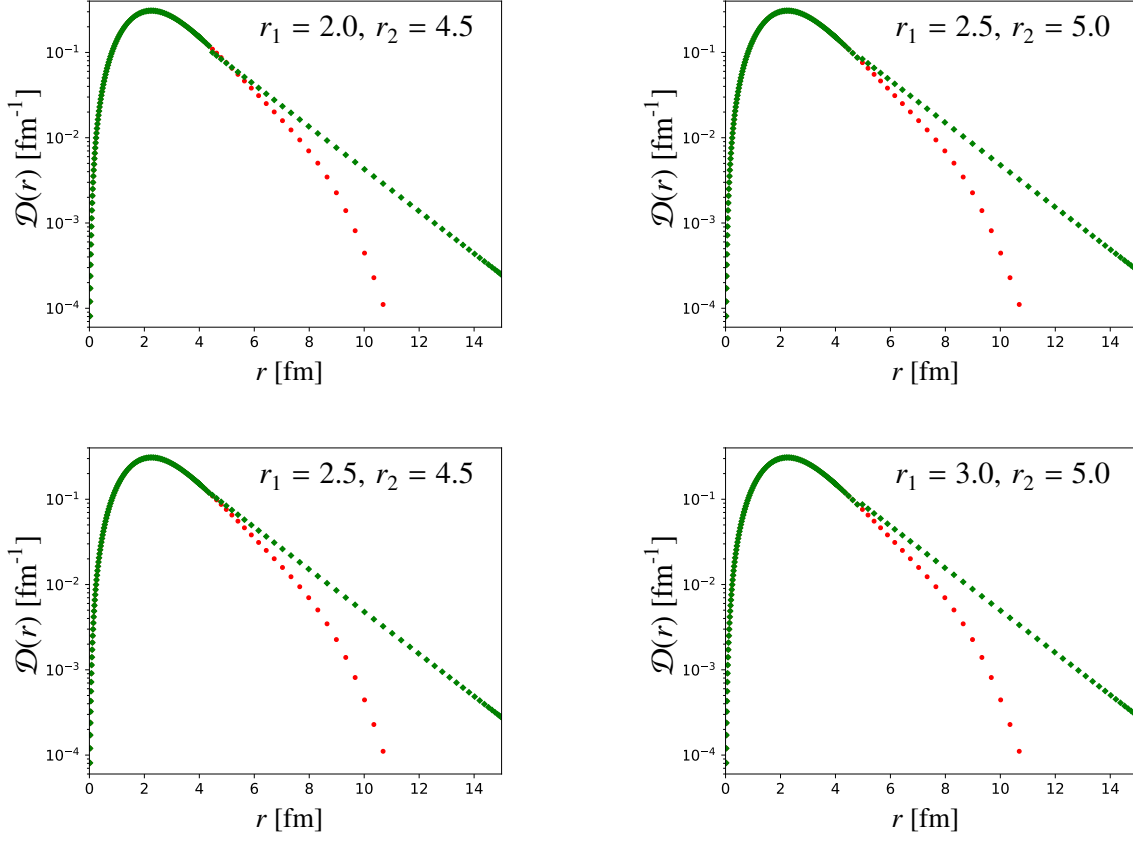
Figure 4.41: Repaired distributions $\mathcal{D}^r_\Lambda(r)$ (blue squares) using different fitting ranges $(r_1, r_2)$. The original distribution $\mathcal{D}_\Lambda(r)$ (red circles ) was calculated using the wavefunction for $^4_\Lambda\text{He}(0^+)$ with $\mathcal{N} = 10$, $\omega = 10$ and $\lambda_{YN} = 0.912$ fm$^{-1}$.
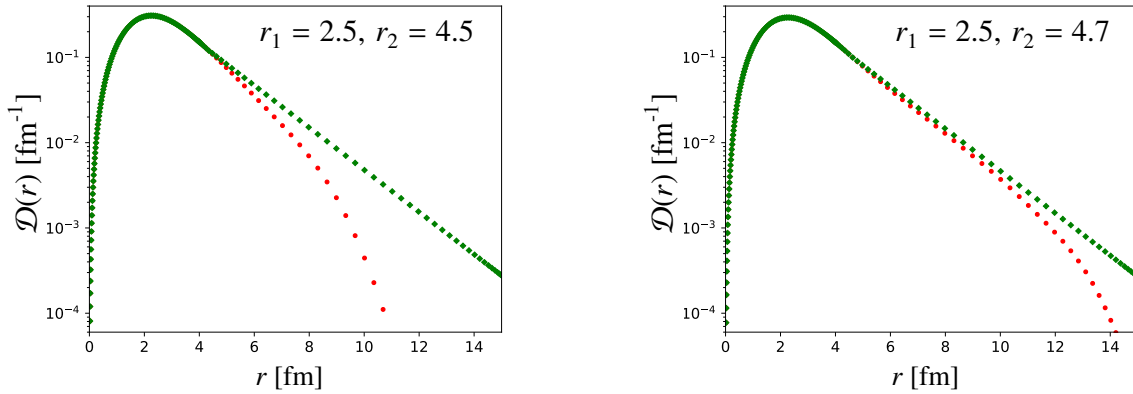


Figure 4.42: Repaired distributions $\mathcal{D}^r_\Lambda(r)$ (blue squares) for two model space $\mathcal{N} = 10$ (left) and $\mathcal{N} = 22$ (right). The original distributions $\mathcal{D}_\Lambda(r)$ (red circles ) were calculated using the wavefunctions for $^4_\Lambda\text{He}(0^+)$ with same model spaces $\mathcal{N}$ and $\omega = 10$ MeV, $\lambda_{YN} = 0.912$ fm$^{-1}$.

We see that, for our specific example, $r_1 = 2.5$ fm and $r_2 = 4.5$ fm are the most suitable choice, and a wrong choice of $r_1$ or $r_2$ could result in a pronounced step in the repaired distribution $\mathcal{D}_\Lambda^r(r)$. It should be stressed that, in general, generally each HO $\omega$ and model space $\mathcal{N}$ may require different fitting ranges. Furthermore, as $\mathcal{N}$ increases the fitting interval $r_1, r_2$ shifts to larger values and the discrepancy between the long-ranged part of the original distribution and that of the corrected one becomes smaller. This is clearly seen in Fig. 4.42 where we compare the repaired functions $\mathcal{D}_\Lambda(r)$ for two model spaces up to $\mathcal{N} = 10$ (left) and $\mathcal{N} = 22$ (right).

Once the repaired distribution $\mathcal{D}_\Lambda^r(r)$ is found, one can easily utilize the definition Eq. (4.13) to recalculate the $\Lambda$ radius. We have performed the long-tail correction to the distributions $\mathcal{D}_\Lambda(r)$ for two cutoffs, $\lambda_{YN} = 0.912$ fm$^{-1}$ and $\lambda_{YN} = 0.836$ fm$^{-1}$. As an example, we present in Fig. 4.43 the comparison between the $\Lambda$ radii computed with the two distributions: the original function $\mathcal{D}_\Lambda(r)$ and the corrected one $\mathcal{D}_\Lambda^r(r)$. One sees that the long-ranged correction has not only flattened out the $\omega$-dependence of $\bar{r}_\Lambda$ but also shifted the crossing point $\omega_{rad}^{opt}$ of different $\omega$-dependence curves to the



Figure 4.43: $\omega$- and $\mathcal{N}$-dependence of $\Lambda$ radius in $^4_\Lambda$He($0^+$) based on the NLO13 for a regulator of $\Lambda_Y = 650$ MeV and an SRG flow parameter of $\lambda_{YN} = 0.836$ fm$^{-1}$ before and after repairing the long-ranged tail of the wavefunction. Same descriptions of the NN interaction and lines as in Fig. 4.37. Note the different scales for $\bar{r}_\Lambda$ in the upper and lower figures.

right. As a result, the convergence of $\bar{r}_\Lambda$ with respect to $\mathcal{N}$ has been substantially improved (see right figures).

We have clearly demonstrated that, for low cutoffs $\lambda_{YN}$, the long-ranged wavefunction correction significantly improves the convergence of the $\Lambda$ radius with respect to the model spaces. So, what happens if we also apply the similar long-ranged correction to the tail of the wavefunctions computed for larger values of $\lambda_{YN}$, where the $\Lambda$ radii already exhibit a nicely convergenced pattern in model spaces. Do the radii obtained with and without the long-tail repairing in these cases differ noticeably? To answer for these questions, let us compare the $\omega$-dependence and model-space convergence of $r_\Lambda$ extracted with and without repairing for a flow parameter of $\lambda_{YN} = 1.6$ fm$^{-1}$. The results are shown in Fig. 4.44. One immediately notices that the long-tail correction to the wavefunctions again flattens out the $\omega$ dependence and hence somewhat speeds up the convergence with respect to $\mathcal{N}$ (right figures). Nevertheless, the two converged radii obtained with and without correction are in very good agreement, 2.93 and 2.933 fm, respectively. It is therefore not necessarily to apply the
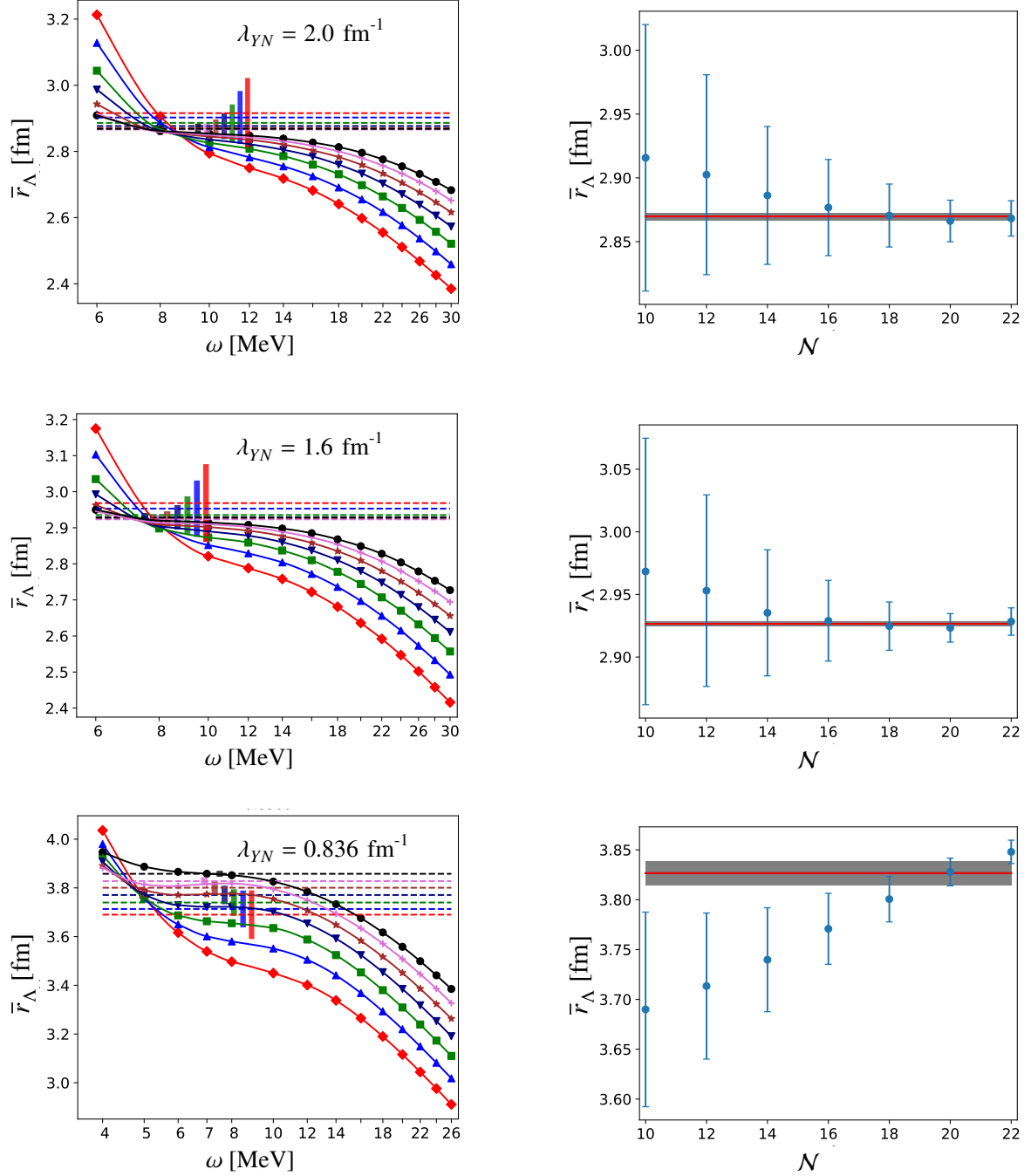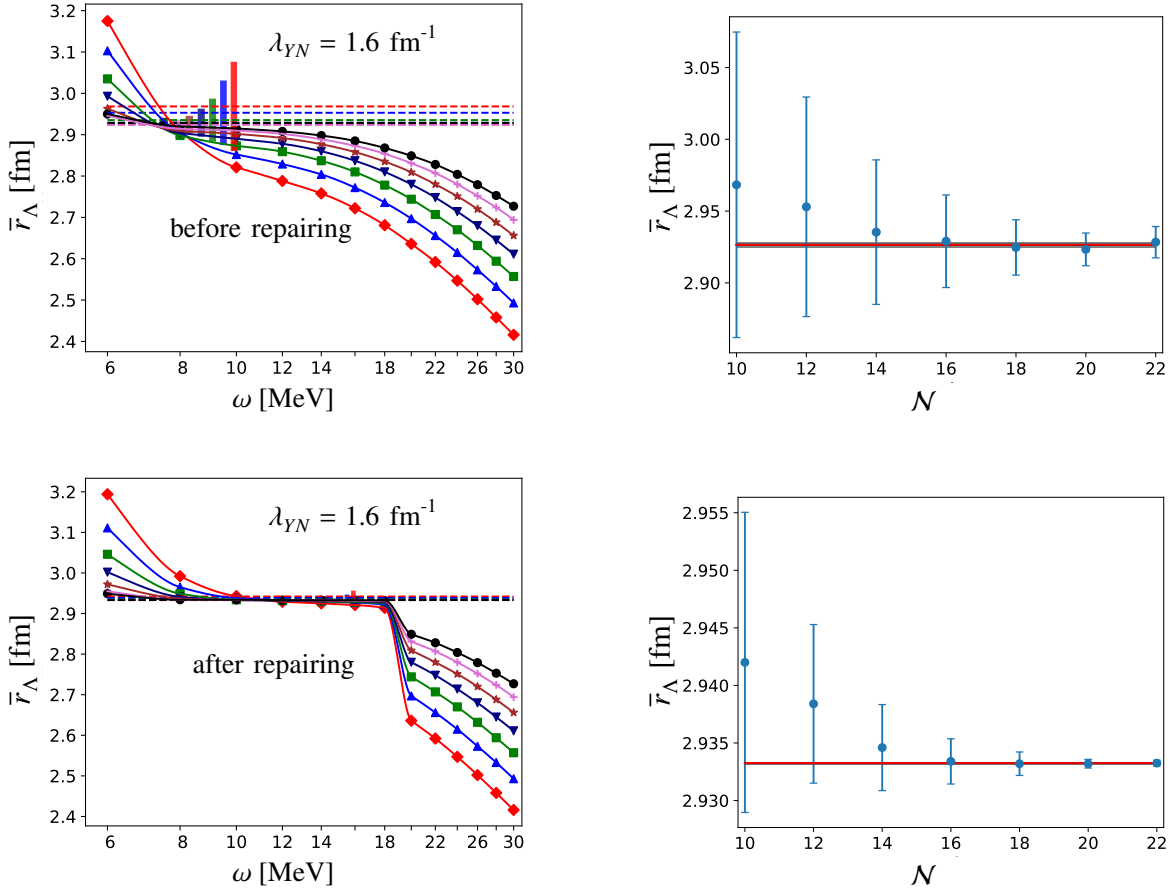


Figure 4.44: $\omega$- and $\mathcal{N}$-dependence of $\Lambda$ radius in $^4_\Lambda$He($0^+$) based on the NLO13 for a regulator of $\Lambda_Y = 650$ MeV and an SRG flow parameter of $\lambda_{YN} = 1.6$ fm$^{-1}$ before and after repairing the long-ranged tail of the wavefunction for $6 \leq \omega \leq 18$ MeV. The tail of the wavefunction for $\omega \geq 20$ is not repaired since they do not contribute to the averaging. Same descriptions of the NN interaction and lines as in Fig. 4.37.

long-ranged correction to the wavefunctions when the radii already exhibit good convergence.

For completeness, let us quickly present the $\omega$-dependence of $\Sigma$ and proton radii in the $^{4}_{\Lambda}$He($0^{+}$) state and their convergence with respect to model spaces $\mathcal{N}$. We refrain from showing the results for neutron radii and distances since they exhibit quite similar behaviors are those of proton and $\Lambda(\Sigma)$ radii, as already seen in Fig. 4.37. The results for $\bar{r}_{\Sigma}$ for two SRG cutoffs of $\lambda_{YN} = 1.6$ fm$^{-1}$ and 0.836 fm$^{-1}$ are shown in Fig. 4.45. It is interesting to observe that for all values of $\lambda_{YN}$ considered, all the curves of different space sizes $\mathcal{N}$ intersect at the same points. Like in the case of $\Lambda$ radius, the crossing points $\omega^{opt}_{rad}$ also shift to the left as $\lambda_{YN}$ decreases. Moreover, for $\omega \geq \omega_{inter}$ most of all the $\omega$-dependence curves become approximately flat, indicating a perfect convergence already with respect to the HO frequency $\omega$. This is also apparently reflected in the model-space convergence plots on the right of Fig. 4.45. The beautiful convergence pattern of $\bar{r}_{\Sigma}$ evidently manifests the short-range nature of the $\Sigma$ radius, which can also be clearly seen from the distribution plots in configuration space.
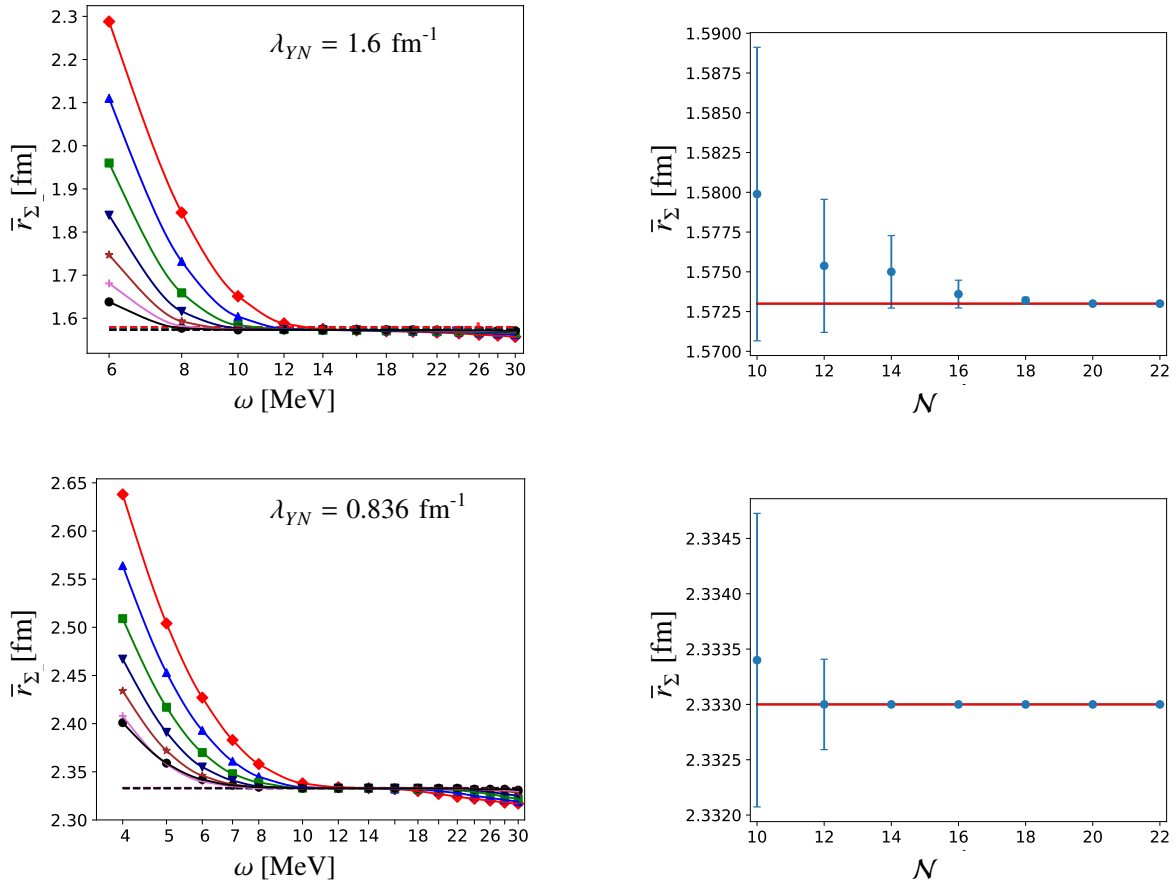


Figure 4.45: $\omega$- and $\mathcal{N}$-dependence of $\Sigma$ radius in $^{4}_{\Lambda}$He($0^{+}$) computed using the NLO13 for a regulator of $\Lambda_{Y} = 650$ MeV and two flow parameters of $\lambda_{YN} = 1.6$ fm$^{-1}$ (upper figures) and $\lambda_{YN} = 0.836$ fm$^{-1}$ (lower figures). Same descriptions of the employed NN interaction and lines as in Fig. 4.37.

The similar results for $\bar{r}_p$ are displayed in Fig. 4.46. It sticks out that the $\omega$-dependence is rather insensitive to SRG-YN cutoffs and it closely resembles the behavior of proton radius in the corresponding nuclear core $^3$He, as shown in Fig. 4.38. Overall, the $\omega$-dependence of the proton radii for different $\mathcal{N}$ is not as steep as those of $\Lambda$, as expected from the lesser extent of $\bar{r}_p$ in comparison with $\bar{r}_\Lambda$. This can also be manifestly seen from our converged results for $\bar{r}_\Lambda$ and $\bar{r}_p$ listed in Tab. 4.16. Here, we also tabulate the extracted $\Sigma$ and neutron radii together with their RMS distances calculated employing the NLO13 for a regulator of $\Lambda_Y = 650$ MeV and a wide range of $\lambda_{YN}$. It should be pointed out that the particle radii tabulated in the tables are measured from the C.M. of the hypernucleus, while those values in the plots, for convenience are measured with respect to the C.M. of the remaining particles. The two radii are related by a simple factor determined by the total number of particles and their masses.
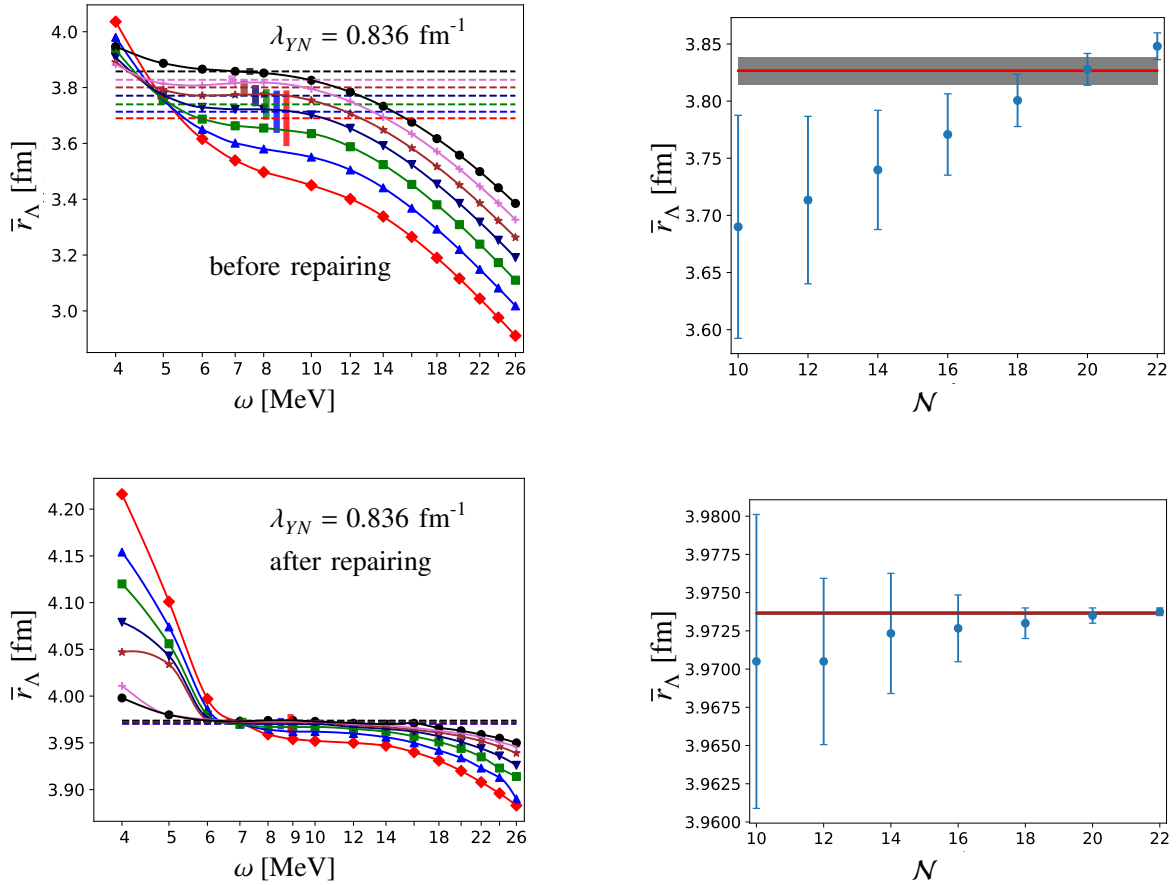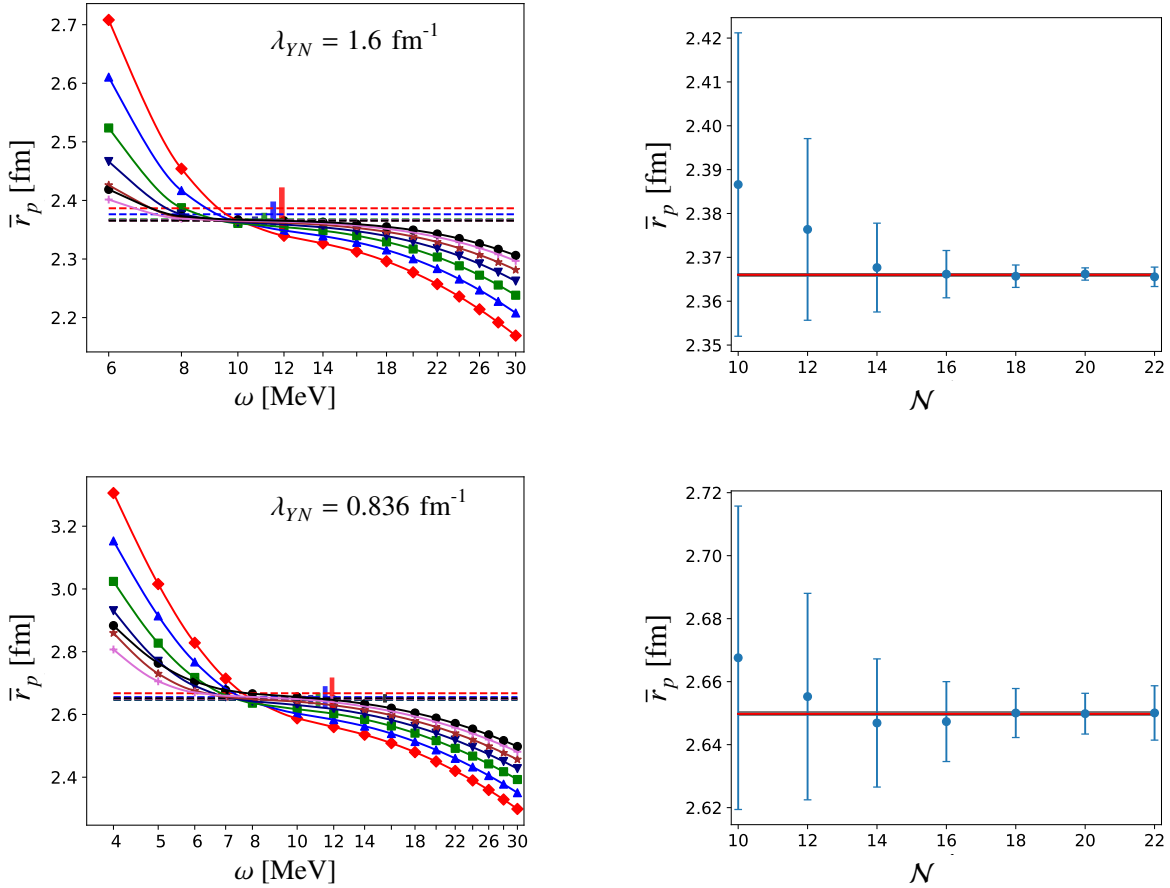


Figure 4.46: $\omega$- and $\mathcal{N}$-dependence of proton radius in $^4_\Lambda$He($0^+$) based on the NLO13 for a regulator of $\Lambda_Y = 650$ MeV and two flow parameters of $\lambda_{YN} = 1.6$ (upper figures) and 0.836 fm$^{-1}$ (lower figures). Same descriptions of the employed NN interaction and lines as in Fig. 4.37

| $\lambda_{YN}$ | $\bar{r}_\Lambda$ | $\bar{r}_\Sigma$ | $\bar{r}_{\Lambda N}$ | $\bar{r}_{\Sigma N}$ | $\bar{r}_n$ | $\bar{r}_p$ | $\bar{r}_{NN}$ | $P_\Sigma$ | $B_\Lambda$ |
|---|---|---|---|---|---|---|---|---|---|
| [fm$^{-1}$] | [fm] | [fm] | [fm] | [fm] | [fm] | [fm] | [fm] | [%] | [MeV] |
| 0.836 | 2.84 | 1.639 | 4.171 | 2.835 | 1.909 | 2.018 | 2.891 | 1.07 | 1.636 |
| 0.912 | 2.644 | 1.505 | 3.954 | 2.641 | 1.855 | 1.968 | 2.853 | 0.94 | 1.928 |
| 1.00 | 2.442 | 1.397 | 3.801 | 2.486 | 1.810 | 1.925 | 2.820 | 0.76 | 2.309 |
| 1.60 | 2.101 | 1.105 | 3.317 | 2.075 | 1.692 | 1.801 | 2.705 | 0.99 | 3.405 |
| 2.00 | 2.056 | 1.052 | 3.261 | 2.007 | 1.675 | 1.782 | 2.688 | 1.26 | 3.592 |
| 2.60 | 2.054 | 1.028 | 3.251 | 1.980 | 1.670 | 1.788 | 2.684 | 1.58 | 3.615 |
| 3.00 | 2.055 | 1.023 | 3.266 | 1.978 | 1.671 | 1.783 | 2.687 | 1.74 | 3.560 |

Table 4.16: RMS point $\Lambda, \Sigma, n$ and $p$ radii and RMS distances of an $YN$, $NN$ pair in $^4_\Lambda$He($0^+$) calculated using the SMS N$^4$LO+(450) for an SRG parameter of $\lambda_{NN}$ = 1.6 fm$^{-1}$ and the NLO13(650) for a range of $\lambda_{YN}$. Particle radii are measured from the C.M. of the hypernucleus. The RMS radii of two nucleons, point proton and neutron in $^3$He are 2.984, 1.770 and 1.627 fm, respectively. The experimental value for the point-proton radius in $^3$He is $\bar{r}_{p,exp}$($^3$He) = 1.776 fm [149, 150].

| $\lambda_{YN}$ | $\bar{r}_\Lambda$ | $\bar{r}_{\Sigma^-}$ | $\bar{r}_{\Sigma^+}$ | $\bar{r}_{\Sigma^0}$ | $\bar{r}_n$ | $\bar{r}_p$ |
|---|---|---|---|---|---|---|
| [fm$^{-1}$] | [fm] | [fm] | [fm] | [fm] | [fm] | [fm] |
| 0.836 | 2.836 | 2.160 | 1.677 | 1.647 | 1.935 | 2.046 |
| 0.912 | 2.627 | 1.930 | 1.513 | 1.511 | 1.871 | 1.984 |
| 1.00 | 2.468 | 1.734 | 1.403 | 1.404 | 1.822 | 1.935 |
| 1.60 | 2.106 | 1.451 | 1.109 | 1.111 | 1.699 | 1.810 |
| 2.00 | 2.059 | 1.286 | 1.054 | 1.057 | 1.680 | 1.793 |
| 2.60 | 2.052 | 1.138 | 1.027 | 1.029 | 1.676 | 1.790 |
| 3.00 | 2.063 | 1.085 | 1.022 | 1.023 | 1.679 | 1.794 |

Table 4.17: Faddeev-Yakubovsky calculations of $\Lambda, \Sigma$ and nucleon radii in $^4_\Lambda$He($0^+$) [145]. The same interactions as in Table 4.16.

In order to verify the correctness of the extraction procedure employed for RMS radii and distances, we benchmark our results with those obtained from the Faddeev-Yakubovsky calculations [145], see Tab. 4.17. Apparently, the $\Sigma$, proton and neutron radii calculated by two different approaches agree perfectly for all values of $\lambda_{YN}$. Without any correction to the wavefunctions, our converged $\Lambda$ radius $\bar{r}_\Lambda$ is also in a good agreement with the Faddeev results for flow parameters $\lambda_{YN} \geq 1.0$ fm$^{-1}$. At lower SRG cutoffs, the long-ranged correction to the wavefunctions is undoubtedly necesssary. Strikingly, after the corrections, our $\Lambda$ radii for $\lambda_{YN} \leq 1$ fm$^{-1}$ converged exactly to the Faddeev-Yakubovsky results.

So far, we have presented results for particle radii and distances calculated with the NLO13

| $\lambda_{YN}$ | $\bar{r}_\Lambda$ | $\bar{r}_\Sigma$ | $\bar{r}_{\Lambda N}$ | $\bar{r}_{\Sigma N}$ | $\bar{r}_n$ | $\bar{r}_p$ | $\bar{r}_{NN}$ | $P_\Sigma$ | $B_\Lambda$ |
| [fm$^{-1}$] | [fm] | [fm] | [fm] | [fm] | [fm] | [fm] | [fm] | [%] | [MeV] |
|---|---|---|---|---|---|---|---|---|---|
| 0.836 | 2.879 | 1.588 | 4.21(7) | 2.762 | 1.919 | 2.027 | 2.886 | 0.47 | 1.571 |
| 0.868 | 2.786 | 1.519 | 4.08(5) | 2.663 | 1.893 | 2.004 | 2.868 | 0.43 | 1.708 |
| 1.00 | 2.46(2) | 1.344 | 3.79(2) | 2.415 | 1.815 | 1.926 | 2.822 | 0.34 | 2.223 |
| 1.60 | 2.103 | 1.098 | 3.333 | 2.071 | 1.697 | 1.806 | 2.710 | 0.50 | 3.303 |
| 2.00 | 2.069 | 1.062 | 3.279 | 2.028 | 1.682 | 1.791 | 2.694 | 0.72 | 3.480 |
| 2.60 | 2.072 | 1.047 | 3.274 | 2.017 | 1.677 | 1.790 | 2.693 | 1.00 | 3.482 |
| 3.00 | 2.072 | 1.043 | 3.288 | 2.016 | 1.679 | 1.790 | 2.696 | 1.15 | 3.415 |

Table 4.18: RMS point $\Lambda, \Sigma, n$ and $p$ radii and RMS distances of an *YN* and *NN* pair in $^4_\Lambda\text{He}(0^+)$ calculated using the SMS N$^4$LO+(450) for an SRG parameter of $\lambda_{NN} = 1.6$ fm$^{-1}$ and the NLO19 for a regulator of $\Lambda_Y = 650$ MeV.

interaction. We confirm that very similar convergence behaviors are found for the RMS radii and distances computed using the NLO19 potential. We shall skip the detail of these calculations but provide the final converged results for this interaction in Table 4.18. Comparing Tables 4.16 and 4.18, one can quickly notice that all RMS radii and distances obtained with the two YN interactions are quite similar to each other. The discrepancies due to the YN-interaction models are considerably smaller than the variations induced by the SRG evolutions. Nevertheless, the SRG dependence of the RMS distances and radii in $^4_\Lambda\text{He}(0^+)$ are somewhat small when compared to the strong variations of $B_\Lambda(^4_\Lambda\text{He})$ and $P_\Sigma(^4_\Lambda\text{He})$ due to the evolutions, see for examples the last two columns in Tables 4.16 and 4.18 or Section 4.2. Our observations again reassert the conclusion in [147] that renormalization of the interactions has minor effect on the long-ranged operators such as radii. Furthermore, as we have seen from the distribution and correlation functions, the $\Sigma$ resides nearest to the nuclear core whereas the $\Lambda$ exhibits the largest extent, even well outside the core, $\bar{r}_\Lambda > \bar{r}_p > \bar{r}_\Sigma$. Likewise, the $\Lambda$N correlation $\bar{r}_{\Lambda N}$ is evidently longer-range than the $\bar{r}_{NN}$. Finally, when comparing the RMS distance of a NN pair in the nuclear core $^3$He, $\bar{r}_{NN}(^3\text{He}) = 2.984$ fm, with the one for $^4_\Lambda$He we notice a slight contraction of the core, i.e. about 3 % for $\lambda_{YN} = 0.836$ fm$^{-1}$ and approximately 10% for $\lambda_{YN} = 2.6$ fm$^{-1}$. Interestingly, our J-NCSM result for the point-proton radius in $^3$He, $\bar{r}_p(^3\text{He}) = 1.77$ fm is in perfect agreement with the experimental value of $\bar{r}_{p,exp}(^3\text{He}) = 1.776$ fm [149, 150].

## 4.8.4 $^5_\Lambda$He

We have throughly studied the convergence of particle radii and relative distances with respect to the HO $\omega$ and model space $\mathcal{N}$ in $^4_\Lambda\text{He}(0^+)$ in the previous section. Similar convergence patterns are observed for these quantities in the ground states of $^5_\Lambda$He and $^7_\Lambda$Li. Moreover, their $\Lambda$ radius even converges somewhat faster than $\bar{r}_\Lambda(^4_\Lambda\text{He}, 0^+)$. Therefore, we shall skip the convergence study but provide the final converged results here. The RMS radii and distances in $^5_\Lambda$He computed using the two interactions, NLO13 and NLO19 for $\Lambda_Y = 650$ MeV and a wide range of SRG flow parameters

| $\lambda_{YN}$ | $\bar{r}_\Lambda$ | $\bar{r}_\Sigma$ | $\bar{r}_{\Lambda N}$ | $\bar{r}_{\Sigma N}$ | $\bar{r}_p$ | $\bar{r}_{NN}$ | $P_\Sigma$ |
|---|---|---|---|---|---|---|---|
| [fm$^{-1}$] | [fm] | [fm] | [fm] | [fm] | [fm] | [fm] | [%] |
| 0.836 | 2.553 | 2.021 | 3.69(2) | 3.232 | 1.628 | 2.361 | 0.17 |
| 0.912 | 2.334 | 1.857 | 3.48(1) | 3.018 | 1.593 | 2.344 | 0.10 |
| 1.00 | 2.186 | 1.924 | 3.206 | 3.085 | 1.563 | 2.328 | 0.03 |
| 1.60 | 1.820 | 1.503 | 2.742 | 2.539 | 1.498 | 2.284 | 0.30 |
| 2.00 | 1.799 | 1.359 | 2.721 | 2.351 | 1.495 | 2.283 | 0.65 |
| 2.60 | 1.869 | 1.267 | 2.79(1) | 2.231 | 1.502 | 2.291 | 1.16 |
| 3.00 | 1.97(2) | 1.244 | 2.792 | 2.200 | 1.512 | 2.298 | 1.41 |

Table 4.19: RMS point $\Lambda, \Sigma$ and $p$ radii and RMS distances of an $YN$, $NN$ pair in $^5_\Lambda$He calculated using the SMS N$^4$LO+(450) for an SRG parameter of $\lambda_{NN} = 1.6$ fm$^{-1}$ and the NLO13 for a regulator of $\Lambda_Y = 650$ MeV. Particle radii are measured measured from the C.M. of the hypernucleus. The RMS radii of two nucleons and a point nucleon in $^4$He are 1.432 and 2.338 fm, respectively. The experimental value for the point-proton radius in $^4$He is $\bar{r}_{p,exp} = 1.462$ fm [151, 152].

| $\lambda_{YN}$ | $\bar{r}_\Lambda$ | $\bar{r}_\Sigma$ | $\bar{r}_{\Lambda N}$ | $\bar{r}_{\Sigma N}$ | $\bar{r}_p$ | $\bar{r}_{NN}$ | $P_\Sigma$ |
|---|---|---|---|---|---|---|---|
| [fm$^{-1}$] | [fm] | [fm] | [fm] | [fm] | [fm] | [fm] | [%] |
| 0.836 | 2.473 | 2.061 | 3.487 | 3.246 | 1.603 | 2.352 | 0.10 |
| 0.868 | 2.335 | 1.991 | 3.367 | 3.162 | 1.588 | 2.343 | 0.06 |
| 1.00 | 2.077 | 2.002 | 3.050 | 3.169 | 1.546 | 2.317 | 0.03 |
| 1.60 | 1.742 | 1.452 | 2.653 | 2.465 | 1.481 | 2.266 | 0.30 |
| 2.00 | 1.719 | 1.317 | 2.624 | 2.288 | 1.475 | 2.262 | 0.61 |
| 2.60 | 1.766 | 1.229 | 2.675 | 2.172 | 1.481 | 2.269 | 1.11 |
| 3.00 | 1.83(1) | 1.205 | 2.742 | 2.142 | 1.493 | 2.276 | 1.36 |

Table 4.20: RMS point $\Lambda, \Sigma$ and $p$ radii and RMS distances of an $YN$, $NN$ pair in $^5_\Lambda$He calculated using the SMS N$^4$LO+(450) for an SRG parameter of $\lambda_{NN} = 1.6$ fm$^{-1}$ and the NLO19 for a regulator of $\Lambda_Y = 650$ MeV. Particle radii are measured from the C.M. of the hypernucleus.

are tabulated in Tables 4.19 and 4.20, respectively. Overall, the $\Lambda$ and $\Sigma$ radii as well as their relative distance to a nucleon exhibit a slight dependence on the YN-nteraction models but are more strongly influenced by the SRG evolution, like in $^4_\Lambda$He. However, neither the interactions nor the evolution have noticeable effects on the proton radius or the relative distance of an NN pair in $^5_\Lambda$He. Furthermore, the NN distance of about $\bar{r}_{NN}(^5_\Lambda$He$) = 2.3$ fm is practically close to the value of $\bar{r}_{NN}(^4$He$) = 2.33$ fm for the $^4$He($0^+$) state, reinforcing that contraction of the $^4$He core due to the presence of a $\Lambda$ hyperon is insignificant. Also, the J-NCSM prediction for the point nucleon radius

| $\lambda_{YN}$ | $\bar{r}_\Lambda$ | $\bar{r}_\Sigma$ | $\bar{r}_{\Lambda N}$ | $\bar{r}_{\Sigma N}$ | $\bar{r}_p$ | $\bar{r}_{NN}$ | $P_\Sigma$ |
|------|------|------|---------|--------|-------|-------|------|
| [fm$^{-1}$] | [fm] | [fm] | [fm] | [fm] | [fm] | [fm] | [%] |
| 0.836 | 2.495 | 2.084 | 3.65(1) | 3.379 | 2.143 | 3.244 | 0.23 |
| 0.912 | 2.35(1) | 1.973 | 3.47(1) | 3.251 | 2.119 | 3.213 | 0.13 |
| 1.00 | 2.147 | 2.123 | 3.329 | 3.328 | 2.098 | 3.187 | 0.06 |
| 1.60 | 1.886 | 1.680 | 2.965 | 2.859 | 2.000 | 3.047 | 0.39 |
| 2.00 | 1.863 | 1.531 | 2.956 | 2.723 | 1.998 | 3.044 | 0.77 |
| 2.60 | 1.945 | 1.447 | 3.042 | 2.619 | 2.009 | 3.059 | 1.29 |

Table 4.21: RMS point $\Lambda, \Sigma$ and $p$ radii and RMS distances of an $YN$, $NN$ pair in the ground state of $^7_\Lambda$Li calculated using the SMS N$^4$LO+(450) for an SRG parameter of $\lambda_{NN} = 1.6$ fm$^{-1}$ and the YN NLO13(650) for a range of $\lambda_{YN}$. Particle radii are measured from the C.M. of the hypernucleus. The RMS radii of two nucleons and a point nucleon in $^6$Li are 2.08 and 3.21 fm, respectively. The experimental value for the point-proton radius in $^6$Li is $\bar{r}_{p,exp} = 2.45$ fm [150].

in $^4$He, $\bar{r}_N(^4\mathrm{He}) = 1.432$ fm agrees nicely with the empirical result of $\bar{r}_{N,exp} = 1.462$ fm [151, 152].

## 4.8.5 $^7_\Lambda$Li($\frac{1}{2}^+$, 0)

Similarly, results for RMS radii and distances for the ground state of $^7_\Lambda$Li calculated with the NLO13 and NLO19 are also provided in Tables 4.21 and 4.22, respectively. Again, the two interactions have negligible effects on all of these quantities whereas the SRG evolution shows slight influences on the $\Lambda$ and $\Sigma$ radii and their relative distance to a nucleon. Comparing the RMS distance of two nucleons in the hypernucleus, $\bar{r}_{NN}(^7_\Lambda\mathrm{Li})$ (second-last column), with the computed value for the core nucleus, $\bar{r}_{NN}(^6\mathrm{Li}) = 3.21$ fm, we observe a slight contraction of the nuclear core for high flow parameters, e.g. about 5% for $\lambda_{YN} = 2.0$ fm$^{-1}$, but practically no change in the $^6$Li dynamic structure for $\lambda_{YN} \leq 1.0$ fm$^{-1}$. As already pointed out in Section 4.8.1, the $\Lambda$ radius $\bar{r}_\Lambda(^7_\Lambda\mathrm{Li})$ is of somewhat larger extent than $\bar{r}_N(^7_\Lambda\mathrm{Li})$ for the SRG cutoffs $\lambda_{YN} \geq 1.6$ fm$^{-1}$. We remark that our computed point-proton radius in $^6$Li, $r_p(^6\mathrm{Li}) = 2.08$ fm is somewhat smaller than the empirical value of $\bar{r}_{p,exp} = 2.45$ fm.

In conclusion, our results have undoubtedly exemplified that density distributions can be accurately obtained from the J-NCSM calculations of hypernuclei up to the p-shell. Before turning to $S = -2$ hypernuclei, we note that a comparison to densities calculated with other approaches such as DFT (density functional theory) [153, 154] calculations will be very interesting. It turns out that in order to achieve a quantitative comparison, the C.M. motion present in the DFT results must be properly corrected for. The effect of the C.M. motion is minor when applying the DFT to heavy systems like $^{208}_\Lambda$Pb. However, it apparently becomes visible for very light hypernuclei such as $^7_\Lambda$Li where a possible connection between J-NCSM and DFT results can be achieved. Once such connection is established, the results from J-NCSM calculations may be employed as a benchmark for tuning the parameters that determine the effective potentials for the DFT calculations. That is to say, one may

| $\lambda_{YN}$ | $\bar{r}_\Lambda$ | $\bar{r}_\Sigma$ | $\bar{r}_{\Lambda N}$ | $\bar{r}_{\Sigma N}$ | $\bar{r}_p$ | $\bar{r}_{NN}$ | $P_\Sigma$ |
|---|---|---|---|---|---|---|---|
| [fm$^{-1}$] | [fm] | [fm] | [fm] | [fm] | [fm] | [fm] | [%] |
| 0.836 | 2.439 | 2.14(1) | 3.576 | 3.403 | 2.131 | 3.230 | 0.122 |
| 0.868 | 2.40(1) | 2.066 | 3.47(1) | 3.336 | 2.120 | 3.215 | 0.07 |
| 1.00 | 2.10(1) | 2.165 | 3.28(1) | 3.425 | 2.088 | 3.174 | 0.04 |
| 1.60 | 1.809 | 1.592 | 2.918 | 2.787 | 1.990 | 3.033 | 0.33 |
| 2.00 | 1.800 | 1.483 | 2.906 | 2.598 | 1.986 | 3.029 | 0.65 |
| 2.60 | 1.852 | 1.413 | 2.987 | 2.516 | 1.997 | 3.043 | 1.09 |

Table 4.22: RMS point $\Lambda, \Sigma$ and $p$ radii and RMS distances of an *YN*, *NN* pair in $^7_\Lambda$Li($\frac{1}{2}^+$, 0) calculated using the SMS N$^4$LO+(450) for an SRG parameter of $\lambda_{NN} = 1.6$ fm$^{-1}$ and the YN NLO19(650) for a range of $\lambda_{YN}$. Particle radii are measured from the C.M. of the hypernucleus.

indirectly apply the predictions of $\chi$EFT to the mean field calculations.

# Part II

# Double Strangeness Hypernuclei

# Jacobi NCSM for $S = -2$ systems

Given the situation that YN scattering data is extremely scarce, hypernuclear experiments together with reliable many-body calculations for $S = -1$ systems are nowadays the indispensable tools even for studying the basic properties of YN interactions and the important links to the non-strange $S = 0$ sector. Ultimately, one wishes to understand the underlying interactions that govern systems with different strangeness and to establish the fundamental connections between ordinary nuclei and all multi-strangeness systems. Being able to accurately describe double-strangeness hypernucei and make reliable predictions to guide experiments will be an inevitable step toward our ultimate goal. Observable $\Lambda\Lambda$ hypernuclei, in particular the best-known $^{6}_{\Lambda\Lambda}$He, are expected to provide invaluable information to constrain realistic YY interactions, taken into account the practically complete lack of direct YY scattering data.

We have demonstrated in Chapter 4 that the J-NCSM method is versatile and capable of accurately computing properties of hypernuclei up to the p-shell. It is therefore natural to extend the approach to $S = -2$ systems. In this chapter, we briefly discuss the generalization of the $S = -1$ J-NCSM approach (as explained in Chapter 3) in order to describe double-$\Lambda$ hypernuclei. The application of the method to the double-$\Lambda$ s-shell hypernuclei, $^{4}_{\Lambda\Lambda}$H, $^{5}_{\Lambda\Lambda}$He and $^{6}_{\Lambda\Lambda}$He, will be discussed in Chapter 6.

## 5.1 Jacobi basis for double-$\Lambda$ hypernuclei

Adding a second $\Lambda$ hyperon to single-strangeness systems not only dramatically increases the basis sizes but also complicates the numerical realization in many other ways. All particle conversions that involve a $\Xi$ hyperon, for instance $\Lambda\Lambda \leftrightarrow \Xi N$, $\Sigma\Sigma \leftrightarrow \Xi N$ or $\Lambda\Sigma \leftrightarrow \Xi N$ change the total number of nucleons in the system by one. The latter must be explicitly taken into account for the many-body Hamiltonian as well as the corresponding basis states including obeying the Pauli principle. Furthermore, particle conversions in both $S = -1$ and $S = -2$ sectors can also lead to couplings between states of identical and non-identical hyperons, for which one should pay special attention when evaluating the Hamiltonian matrix elements. We will come back to this in Sections 5.2 and 5.3. Let us first start with the construction of the many-body basis states. For convenience, we split the basis functions into two orthogonal sets: one set that involves two singly strange hyperons referred to as $|\psi\rangle_{Y_1Y_2}$, and the other that contains a doubly strange $\Xi$ hyperon denoted as $|\psi\rangle_{\Xi}$. The former are constructed by coupling the completely antisymmetrized states of $(A - 2)$ nucleons, $|\alpha_{(A-2)N}\rangle$, to the

states describing a system of two hyperons, $|Y_1 Y_2\rangle$

$$
\begin{aligned}
|\psi\rangle_{Y_1 Y_2} &\equiv |\alpha^{*(Y_1 Y_2)}\rangle = |\alpha_{(A-2)N}\rangle \otimes |Y_1 Y_2\rangle \\
&= |\mathcal{N} JT, \alpha_{(A-2)N}\, \alpha_{Y_1 Y_2}\, n_\lambda \lambda; \\
&\qquad (((l_{Y_1 Y_2}(s_{Y_1} s_{Y_2}) S_{Y_1 Y_2}) J_{Y_1 Y_2}(\lambda J_{A-2}) I_\lambda) J, ((t_{Y_1} t_{Y_2}) T_{Y_1 Y_2} T_{A-2}) T\rangle \\
&\equiv \Big| \;\overset{Y_1}{\underset{Y_2}{\vdots}}\!\!-\!\!\bullet\Big\rangle,
\end{aligned}
\tag{5.1}
$$

with $Y_1, Y_2 = \Lambda, \Sigma$ and $Y_1 \leq Y_2$. The latter inequality $Y_1 \leq Y_2$ expresses the fact that we only distinguish the $|\Lambda\Lambda\rangle$, $|\Lambda\Sigma\rangle$ and $|\Sigma\Sigma\rangle$ states but do not explicitly consider the $|\Sigma\Lambda\rangle$ state. Here, we have adopted the same notations as those used in Eq. (3.16). For example, the symbol $\alpha_{(A-2)N}$ stands for all quantum numbers characterizing the antisymmetrized states of $A - 2$ nucleons: the total number of oscillator quanta $\mathcal{N}_{A-2}$, total angular momentum $J_{A-2}$, isospin $T_{A-2}$ and state index $\zeta_{A-2}$ as well. Similarly, $\alpha_{Y_1 Y_2}$ stands for all quantum numbers describing the subcluster of two hyperons $Y_1$ and $Y_2$: the total number of oscillator energy $\mathcal{N}_{Y_1 Y_2}$, total angular momentum $J_{Y_1 Y_2}$, isospin $T_{Y_1 Y_2}$ and the state index $\zeta_{Y_1 Y_2}$. Finally, the HO energy number $n_\lambda$ together with the orbital angular $\lambda$ describe the relative motion of the $(A-2)$N core with respect to the C.M. of the $Y_1 Y_2$ subcluster. The orders, in which these quantum numbers are coupled, are explicitly shown after the semicolon. Note that, when the two hyperons $Y_1$ and $Y_2$ are identical, only the antisymmetrized states of $|Y_1 Y_2\rangle$, i.e. those states with the quantum numbers satisfying the condition $(-1)^{T_{Y_1 Y_2} - t_{Y_1} - t_{Y_2}} (-1)^{S_{Y_1 Y_2} - s_{Y_1} - s_{Y_2}} (-1)^{l_{Y_1 Y_2}} = -1$, are taken into account.

Analogously, the basis functions $|\psi\rangle_\Xi$ are obtained when one combines the antisymmetrized states of an $(A - 1)$-nucleon system, $|\alpha_{(A-1)N}\rangle$, with the HO states, $|\Xi\rangle$, describing the relative motion of a $\Xi$ hyperon with respect to the C.M. of the (A-1)N subcluster

$$
\begin{aligned}
|\psi\rangle_\Xi &\equiv |\alpha^{*(\Xi)}\rangle = |\alpha_{(A-1)N}\rangle \otimes |\Xi\rangle \\
&= |\mathcal{N} JT, \alpha_{(A-1)N}\, n_\Xi\, I_\Xi\, t_\Xi; \; (J_{A-1}(l_\Xi s_\Xi) I_\Xi) J, (T_{A-1}\, t_\Xi) T\rangle \\
&\equiv \Big|\bullet\!\!-\!\!\overset{\Xi}{\bullet}\;\Big\rangle.
\end{aligned}
\tag{5.2}
$$

The notation used in Eq. (5.2) follow exactly as the one of Eq. (3.2). Thus, $\alpha_{(A-1)N}$ denotes a set of quantum numbers describing an antisymmetrized state of $A - 1$ nucleons: the total oscillator energy number $\mathcal{N}_{A-1}$, total angular momentum $J_{A-1}$, isospin $T_{A-1}$ and state index $\zeta_{A-1}$. Likewise, the relative motion of a $\Xi$ hyperon is labeled by the HO energy number $n_\Xi$, the orbital angular momentum $l_\Xi$ and spin $s_\Xi = \frac{1}{2}$ which combine together to form the total angular momentum $I_\Xi$ as well as the isospin $t_\Xi = \frac{1}{2}$. Finally, the last lines in Eqs. (5.1) and (5.2) show the graphical representations of the states.

Having defined the basis states, we can now expand the $S = -2$ hypernuclear wavefunction $|\Psi(\pi, J, T)\rangle$,

$$
\big|\Psi(\pi JT)\big\rangle = \sum_{\alpha^{*(Y_1 Y_2)}} C_{\alpha^{*(Y_1 Y_2)}} \big|\alpha^{*(Y_1 Y_2)}(\mathcal{N} JT)\big\rangle + \sum_{\alpha^{*\Xi}} C_{\alpha^{*\Xi}} \big|\alpha^{*(\Xi)}(\mathcal{N} JT)\big\rangle,
\tag{5.3}
$$

where the expansion coefficients are obtained when diagonalizing the $A$-body Hamiltonians in the

bases Eqs. (5.1) and (5.2). In order to facilitate numerical calculations we also apply a restriction to the largest possible value of the model space size $\mathcal{N}$, i.e. $\mathcal{N} = \mathcal{N}_{A-2} + 2n_\lambda + l_\lambda + \mathcal{N}_{Y_1 Y_2} = \mathcal{N}_{A-1} + l_\Xi + 2n_\Xi \leq \mathcal{N}_{max}$, like for $S = -1$ systems. Of course, by doing so, the calculated binding energies will be $\mathcal{N}_{max}$- and $\omega$-dependent. For extracting the converged results, we shall follow exactly the two-step extrapolation procedure (see Section 4.1) that has been intensively employed for all single-$\Lambda$ hypernuclear calculations present in Chapter 6.

So far, we have not yet mentioned the explicit form of the many-body Hamiltonian. Nevertheless, with the expansion Eq. (5.3), one can straightforwardly express the $A$-body Hamiltonian matrix elements as follows

$$
\begin{aligned}
\langle \Psi(\pi JT) | H | \Psi(\pi JT) \rangle = & \sum_{\substack{\alpha^{*(Y_1 Y_2)} \\ \alpha'^{*(Y_1 Y_2)}}} C_{\alpha^{*(Y_1 Y_2)}} C_{\alpha'^{*(Y_1 Y_2)}} \langle \alpha^{*(Y_1 Y_2)} | H | \alpha'^{*(Y_1 Y_2)} \rangle \\
& + \sum_{\alpha^{*(\Xi)}, \alpha'^{*(\Xi)}} C_{\alpha^{*(\Xi)}} C_{\alpha'^{*(\Xi)}} \langle \alpha^{*(\Xi)} | H | \alpha'^{*(\Xi)} \rangle \\
& + 2 \sum_{\substack{\alpha^{*(Y_1 Y_2)} \\ \alpha'^{*(\Xi)}}} C_{\alpha^{*(Y_1 Y_2)}} C_{\alpha'^{*(\Xi)}} \langle \alpha^{*(Y_1 Y_2)} | H | \alpha'^{*(\Xi)} \rangle .
\end{aligned}
\tag{5.4}
$$

The last line in Eq. (5.4) is obtained exploiting the Hermiticity of the Hamiltonian. It should be clear from Eq. (5.4) that the part of the Hamiltonian that only involves a doubly strange hyperon $\Xi$ does not contribute to the matrix element $\langle \alpha^{*(Y_1 Y_2)} | H | \alpha'^{*(Y_1 Y_2)} \rangle$ (in the first line). Similarly, the matrix element $\langle \alpha^{*(\Xi)} | H | \alpha'^{*(\Xi)} \rangle$ does not receive contribution from the part of the Hamiltonian that contains two singly strange hyperons $Y_1$ and $Y_2$, while the last term is nonzero only for the transition potential in the $S = -2$ channels. Therefore, in order to write down the explicit form of the doubly strange $A$-body Hamiltonian, we distinguish three Hamiltonians, $H_{Y_1 Y_2}$, $H_\Xi$ and $H_{Y_1 Y_2 - \Xi N}^{S=-2}$ that can contribute to the matrix elements in the first, second and third lines in Eq. (5.4), respectively. Intuitively, the first Hamiltonian $H_{Y_1 Y_2}$ corresponds to a system consisting of $A - 2$ nucleons and two singly strange hyperons $Y_1$ and $Y_2$. In this case, the $A$-body Hamiltonian $H_{Y_1 Y_2}$ can be expressed as

$$
\begin{aligned}
H_{Y_1 Y_2} = & H_{Y_1 Y_2}^{S=0} + H_{Y_1 Y_2}^{S=-1} + H_{Y_1 Y_2}^{S=-2} \\
= & \sum_{i<j=1}^{A-2} \left( \frac{2p_{ij}^2}{M(t_{Y_1}, t_{Y_2})} + V_{ij}^{s=0} \right) \\
& + \sum_{i=1}^{A-2} \left( \frac{m_N + m(t_{Y_1})}{M(t_{Y_1}, t_{Y_2})} \frac{p_{iY_1}^2}{2\mu_{iY_1}} + V_{iY_1}^{s=-1} + \frac{m_N + m(t_{Y_2})}{M(t_{Y_1}, t_{Y_2})} \frac{p_{iY_2}^2}{2\mu_{iY_2}} + V_{iY_2}^{s=-1} \right) \\
& + \frac{m_{t_{Y_1}} + m_{t_{Y_2}}}{M(t_{Y_1}, t_{Y2})} \frac{p_{Y_1 Y_2}^2}{2\mu_{Y_1 Y_2}} + V_{Y_1 Y_2}^{s=-2} + (m(t_{Y_1}) + m(t_{Y_2}) - 2m_\Lambda) + \cdots ,
\end{aligned}
\tag{5.5}
$$

with $Y_1, Y_2 = \Lambda, \Sigma$ and $Y_1 \leq Y_2$. Here, $m(t_{Y_1}), m(t_{Y_2})$ and $m_N$ are the $Y_1, Y_2$ hyperon and nucleon rest masses, respectively. And $M(t_{Y_1}, t_{Y_2})$ is the total mass of the system $M(t_{Y_1}, t_{Y_2}) = m(t_{Y_1}) + m(t_{Y_2}) + (A-2)m_N$ while $\mu_{iY_1}$ and $\mu_{Y_1 Y_2}$ denote the hyperon-nucleon and hyperon-hyperon reduced masses, respectively. We neglect the mass difference within the nucleon and hyperon isospin multiplets. The

last term in Eq. (5.5) accounts for the difference in the rest masses of $Y_1, Y_2$ hyperons and two $\Lambda$ hyperons. Likewise, the second Hamiltonian, $H_\Xi$ (involving a $\Xi$ hyperon) is for a system composing of a $\Xi$ hyperon and $A − 1$ nucleons. Hence,

$$
\begin{aligned}
H_\Xi &= H_\Xi^{S=0} + H_\Xi^{S=-2} \\
&= \sum_{i<j=1}^{A-1} \Big(\frac{2p_{ij}^2}{M(\Xi)} + V_{ij}^{s=0}\Big) \\
&\quad + \sum_{i=1}^{A-1} \Big(\frac{m_N + m_\Xi}{M(\Xi)} \frac{p_{\Xi i}^2}{2\mu_{\Xi i}} + V_{\Xi i}^{s=-2}\Big) + (m_\Xi + m_N - 2m_\Lambda) + \cdots,
\end{aligned}
\tag{5.6}
$$

where $m_\Xi$ is the $\Xi$ hyperon rest mass and $\mu_{i\Xi}$ is the reduced mass of a $\Xi$ and a nucleon. The total mass of the system is given by $M(\Xi) = m_\Xi + (A − 1)m_N$. The ellipses in Eqs. (5.5) and (5.6) stand for those higher-body forces that are omitted. Clearly, the transition Hamiltonian $H_{Y_1Y_2-\Xi N}^{S=-2}$ is simply given by

$$
H_{Y_1Y_2-\Xi N}^{S=-2} = \sum_{i=1}^{A-1} V_{Y_1Y_2-\Xi i}^{s=-2}.
\tag{5.7}
$$

## 5.2 Evaluation of the $S = −2$ Hamiltonian matrix elements

Now, taking into account the explicit forms of the $A$-body Hamiltonian Eqs. (5.5) to (5.7), all contributions to the matrix element $\langle\Psi(\pi JT)|H|\Psi(\pi JT)\rangle$ can be split into three groups involving non-strange , single-strange and double-strange parts of the Hamiltonian

$$
\begin{aligned}
\langle\Psi(\pi JT)|H|\Psi(\pi JT)\rangle = &\langle\Psi(\pi JT)|H^{S=0}|\Psi(\pi JT)\rangle \\
&+ \langle\Psi(\pi JT)|H^{S=-1}|\Psi(\pi JT)\rangle \\
&+ \langle\Psi(\pi JT)|H^{S=-2}|\Psi(\pi JT)\rangle.
\end{aligned}
\tag{5.8}
$$

The non-strange Hamiltonian matrix element is further expanded as

$$
\begin{aligned}
\langle\Psi(\pi JT)|H^{S=0}|\Psi(\pi JT)\rangle = &\sum_{\substack{\alpha^{*(Y_1Y_2)} \\ \alpha'^{*(Y_1Y_2)}}} C_{\alpha^{*(Y_1Y_2)}} C_{\alpha'^{*(Y_1Y_2)}} \langle\alpha^{*(Y_1Y_2)}|H_{Y_1Y_2}^{S=0}|\alpha'^{*(Y_1Y_2)}\rangle \\
&+ \sum_{\alpha^{*(\Xi)},\alpha'^{*(\Xi)}} C_{\alpha^{*(\Xi)}} C_{\alpha'^{*(\Xi)}} \langle\alpha^{*(\Xi)}|H_\Xi^{S=0}|\alpha'^{*(\Xi)}\rangle.
\end{aligned}
\tag{5.9}
$$

The evaluation of Eq. (5.9) can be performed analogously as shown for the $S = −1$ systems in Section 3.2.1, and it also does not involve any new transition coefficients. Furthermore, the combinatorial factors that relate the $A$-body matrix elements $\langle\alpha^{*(Y_1Y_2)}|H_{Y_1Y_2}^{S=0}|\alpha'^{*(Y_1Y_2)}\rangle$ and $\langle\alpha^{*(\Xi)}|H_\Xi^{S=0}|\alpha'^{*(\Xi)}\rangle$ to the two-nucleon matrix elements in the two-body sector are given by the binomial coefficients of $\binom{A_{nucl}}{2} = A_{nucl}(A_{nucl} − 1)/2$ with $A_{nucl} = A − 2$ and $A_{nucl} = A − 1$, respectively, being the number of

nucleons in the system, see Eqs. (A.33) and (A.42). The matrix elements of the double-strange part $H^{S=-2}$ of the Hamiltonian

$$
\begin{aligned}
\langle \Psi(\pi JT) | H^{S=-2} | \Psi(\pi JT) \rangle = &\sum_{\substack{\alpha^{*(Y_1 Y_2)} \\ \alpha'^{*(Y_1 Y_2)}}} C_{\alpha^{*(Y_1 Y_2)}} C_{\alpha'^{*(Y_1 Y_2)}} \langle \alpha^{*(Y_1 Y_2)} | H_{Y_1 Y_2}^{S=-2} | \alpha'^{*(Y_1 Y_2)} \rangle \\
&+ 2 \sum_{\substack{\alpha^{*(Y_1 Y_2)} \\ \alpha'^{*(\Xi)}}} C_{\alpha^{*(Y_1 Y_2)}} C_{\alpha'^{*(\Xi)}} \langle \alpha^{*(Y_1 Y_2)} | H_{Y_1 Y_2 - \Xi N}^{S=-2} | \alpha'^{*(\Xi)} \rangle \\
&+ \sum_{\alpha^{*(\Xi)}, \alpha'^{*(\Xi)}} C_{\alpha^{*(\Xi)}} C_{\alpha'^{*(\Xi)}} \langle \alpha^{*(\Xi)} | H_\Xi^{S=-2} | \alpha'^{*(\Xi)} \rangle,
\end{aligned}
\tag{5.10}
$$

can be evaluated likewise. Here, in order to calculate the last two terms in Eq. (5.10), one needs to expand the states $|\alpha^{*(\Xi)}\rangle$ in another set of the intermediate states $|\alpha^{*(\Xi N)}\rangle$ that explicitly single out a $\Xi N$ pair,

$$
|\alpha^{*(\Xi)}\rangle = \sum_{\alpha^{*(\Xi N)}} \langle \alpha^{*(\Xi)} | \alpha^{*(\Xi N)} \rangle |\alpha^{*(\Xi N)}\rangle,
\tag{5.11}
$$

where the transition coefficients $\langle \alpha^{*(\Xi)} | \alpha^{*(\Xi N)} \rangle$ can be computed straightforwardly exploiting the same expression as in Eq. (3.21). One can also quickly show that the last term $\langle \alpha^{*(\Xi)} | H_\Xi^{S=-2} | \alpha'^{*(\Xi)} \rangle$ is connected with the matrix elements of the two-body $\Xi N$ Hamiltonian in the basis $|\Xi N\rangle$ by a combinatorial factor of $A - 1$. The factor that relates $\langle \alpha^{*(Y_1 Y_2)} | H_{Y_1 Y_2 - \Xi N}^{S=-2} | \alpha'^{*(\Xi)} \rangle$ to the two-body transition potentials $V_{Y_1 Y_2 - \Xi N}$ is, however, not obvious because of possible couplings between identical and non-identical two-body states, for instances $\Sigma\Sigma - \Xi N$ or $\Lambda\Lambda - \Xi N$. We have systematically shown in Appendix A that, in this case, the corresponding combinatorial factor is given by $\sqrt{A-1}$ (see also Table A.2).

## 5.3 Separation of an *YN* pair

Let us now discuss the evaluation of the second term in Eq. (5.8) that involves the single strange part of the Hamiltonian in Eq. (5.5)

$$
\langle \Psi(\pi JT) | H^{S=-1} | \Psi(\pi JT) \rangle = \sum_{\substack{\alpha^{*(Y_1 Y_2)} \\ \alpha'^{*(Y_1 Y_2)}}} C_{\alpha^{*(Y_1 Y_2)}} C_{\alpha'^{*(Y_1 Y_2)}} \langle \alpha^{*(Y_1 Y_2)} | H_{Y_1 Y_2}^{S=-1} | \alpha'^{*(Y_1 Y_2)} \rangle,
\tag{5.12}
$$

in some details since it requires to calculate new sets of transition coefficients. In order to further evaluate the matrix elements $\langle \alpha^{*(Y_1 Y_2)} | H_{Y_1 Y_2}^{S=-1} | \alpha'^{*(Y_1 Y_2)} \rangle$, one needs to employ other sets of intermediate states that explicitly separate out a YN pair . Since each hyperon, $Y_1$ and $Y_2$, can be involved in the interaction with a nucleon independently (as clearly seen from the expression for $H_{Y_1 Y_2}^{S=-1}$ in Eq. (5.5)), it is instructive to employ two different intermediate sets, $|(\alpha^{*(Y_1 N)})^{*(Y_2)}\rangle$ and $|(\alpha^{*(Y_2 N)})^{*(Y_1)}\rangle$. The first set, $|(\alpha^{*(Y_1 N)})^{*(Y_2)}\rangle$, is needed when computing the matrix elements of the first two terms of $H_{Y_1 Y_2}^{S=-1}$ where $Y_1$ is the active hyperon while $Y_2$ plays the role of a spectator. Similarly, the second set is useful for the two remaining terms of the $H_{Y_1 Y_2}^{S=-1}$ Hamiltonian where the roles of $Y_1$ and $Y_2$

hyperons have been interchanged ($Y_2$ is now the active particle). The construction of these bases is straightforward. For example, the first set can be formed by combining the hyperon states $|Y_2\rangle$, depending on the Jacobi coordinate of the $Y_2$ hyperon relative with the C.M. of the $((A-3)N + Y_1 N)$ subsystem, with the $|\alpha^{*(Y_1 N)}\rangle$ states constructed in Eq. (3.16). Thus,

$$
\begin{aligned}
|(\alpha^{*(Y_1 N)})^{*(Y_2)}\rangle &= |\alpha^{*(Y_1 N)}\rangle \otimes |Y_2\rangle \\
&= |\mathcal{N}JT, \alpha^{*(Y_1 N)}_{A-1}\tilde{n}_{Y_2}\tilde{I}_{Y_2}\tilde{t}_{Y_2}; (J^{*(Y_1 N)}_{A-1}(\tilde{l}_{Y_2} s_{Y_2})\tilde{I}_{Y_2})J, (T^{*(Y_1 N)}_{A-1}\tilde{t}_{Y_2})T\rangle \\
&\equiv \Big| \; \overset{Y_1}{\underset{Y_2}{\rule{0pt}{0pt}}} \Big\rangle,
\end{aligned}
\tag{5.13}
$$

and, similarly

$$
\begin{aligned}
|(\alpha^{*(Y_2 N)})^{*(Y_1)}\rangle &= |\alpha^{*(Y_2 N)}\rangle \otimes |Y_1\rangle \\
&= |\mathcal{N}JT, \alpha^{*(Y_2 N)}_{A-1}\tilde{n}_{Y_1}\tilde{I}_{Y_1}\tilde{t}_{Y_1}; (J^{*(Y_2 N)}_{A-1}(\tilde{l}_{Y_1} s_{Y_1})\tilde{I}_{Y_1})J, (T^{*(Y_2 N)}_{A-1}\tilde{t}_{Y_1})T\rangle \\
&\equiv \Big| \; \overset{Y_2}{\underset{Y_1}{\rule{0pt}{0pt}}} \Big\rangle.
\end{aligned}
\tag{5.14}
$$

It is obvious that the two sets Eqs. (5.13) and (5.14) are orthogonal to each other when the two $Y_1$ and $Y_2$ hyperons are distinguishable. Furthermore, each of the intermediate sets is complete with respect to the basis states $|\alpha^{*(Y_1 Y_2)}\rangle$, which in turn allows for the following expansions

$$
|\alpha^{*(Y_1 Y_2)}\rangle = \sum_{(\alpha^{*(Y_1 N)})^{*(Y_2)}} \langle(\alpha^{*(Y_1 N)})^{*(Y_2)}|\alpha^{*(Y_1 Y_2)}\rangle \, |(\alpha^{*(Y_1 N)})^{*(Y_2)}\rangle,
\tag{5.15}
$$

and,

$$
|\alpha^{*(Y_1 Y_2)}\rangle = \sum_{(\alpha^{*(Y_2 N)})^{*(Y_1)}} \langle(\alpha^{*(Y_2 N)})^{*(Y_1)}|\alpha^{*(Y_1 Y_2)}\rangle \, |(\alpha^{*(Y_2 N)})^{*(Y_1)}\rangle.
\tag{5.16}
$$

Clearly, when $Y_1$ and $Y_2$ are identical, the two sets of intermediate states are the same, and there is no need to distinguish the two expansions in Eqs. (5.15) and (5.16). In any cases, the expansion coefficients in Eqs. (5.15) and (5.16) are very similar to each other and can be calculated in the same way. In the following, we shall focus on the transition coefficients of the first expansion. For calculating this overlap, $\langle(\alpha^{*(Y_1 N)})^{*(Y_2)}|\alpha^{*(Y_1 Y_2)}\rangle$, one will need to exploit another set of auxiliary states $|(\alpha^{*(Y_1)})^{*(Y_2)}\rangle$ which are obtained by coupling the hyperon states $|Y_2\rangle$ to the basis states of the $((A-2)N + Y_1)$ system, $|\alpha^{*(Y_1)}\rangle_{A-1}$, defined in Eq. (3.2)

$$
\begin{aligned}
|(\alpha^{*(Y_1)})^{*(Y_2)}\rangle &= |\alpha^{*(Y_1)}\rangle_{A-1} \otimes |Y_2\rangle \\
&= |\mathcal{N}JT, \alpha^{*(Y_1)}_{A-1}n_{Y_2}I_{Y_2}t_{Y_2}; (J^{*(Y_1)}_{A-1}(l_{Y_2} s_{Y_2})I_{Y_2})J, (T^{*(Y_1)}_{A-1}t_{Y_2})T\rangle \\
&= |\mathcal{N}JT, \mathcal{N}'_{A-2}, n_{Y_1}I_{Y_1}t_{Y_1}n_{Y_2}I_{Y_2}t_{Y_2}; ((J'_{(A-2)N}(l_{Y_1} s_{Y_1})I_{Y_1})J^{*(Y_1)}_{A-1}(l_{Y_2} s_{Y_2})I_{Y_2})J, \\
&\qquad ((T'_{(A-2)N}t_{Y_1})T^{*(Y_1)}_{A-1}t_{Y_2})T\rangle \\
&\equiv \Big| \; \overset{Y_1}{\underset{Y_2}{\rule{0pt}{0pt}}} \Big\rangle.
\end{aligned}
\tag{5.17}
$$

The third line in Eq. (5.17) is to illustrate how the quantum number of the three subclusters: (A-2) nucleons, $Y_1$ and $Y_2$ hyperons are combined to form the auxiliary states with the quantum numbers $\mathcal{N}, J$ and $T$ (the state indexes are again dropped out). Now, exploiting the completeness of the auxiliary states $|(\alpha^{*(Y_1)})^{*(Y_2)}\rangle$, the transition coefficient in Eq. (5.15) becomes

$$\langle(\alpha^{*(Y_1 N)})^{*(Y_2)}|\alpha^{*(Y_1 Y_2)}\rangle = \langle(\alpha^{*(Y_1 N)})^{*(Y_2)}|(\alpha^{*(Y_1)})^{*(Y_2)}\rangle\langle(\alpha^{*(Y_1)})^{*(Y_2)}|\alpha^{*(Y_1 Y_2)}\rangle$$

$$\equiv \left\langle \;\vcenter{\hbox{(diagram)}}\; \Big| \;\vcenter{\hbox{(diagram)}}\;\right\rangle\left\langle\;\vcenter{\hbox{(diagram)}}\;\Big|\;\vcenter{\hbox{(diagram)}}\;\right\rangle \tag{5.18}$$

$$= \delta_{Y_2 Y_2}\left\langle\;\vcenter{\hbox{(diagram)}}\;\Big|\;\vcenter{\hbox{(diagram)}}\;\right\rangle_{(A-1)}\left\langle\;\vcenter{\hbox{(diagram)}}\;\Big|\;\vcenter{\hbox{(diagram)}}\;\right\rangle,$$

where a summation over the states $|(\alpha^{*(Y_1)})^{*(Y_2)}\rangle$ is implied. One quickly sees that the first overlap $\langle(\alpha^{*(Y_1 N)})^{*(Y_2)}|(\alpha^{*(Y_1)})^{*(Y_2)}\rangle$ in Eq. (5.18) is essentially given by the transition coefficient given by Eq. (3.21) for a system consisting of $(A-2)$ nucleons and the $Y_1$ hyperon whereas the second transition $\langle(\alpha^{*(Y_1)})^{*(Y_2)}|\alpha^{*(Y_1 Y_2)}\rangle$ can be straightforwardly deduced from Eq. (3.24). One obtains,

$$\langle(\alpha^{*(Y_1)})^{*(Y_2)}|\alpha^{*(Y_1 Y_2)}\rangle = \delta_{T'_{A-2}T_{A-2}}\delta_{J'_{A-2}J_{A-2}}\delta_{\mathcal{N}'_{A-2}\mathcal{N}_{A-2}}\delta_{\zeta'_{A-2}\zeta_{A-2}}$$

$$\times \hat{I}_{Y_1}\hat{I}_{Y_2}\hat{J}_{Y_1 Y_2}\hat{S}_{Y_1 Y_2}\hat{T}_{Y_1 Y_2}\hat{I}_\lambda \hat{J}^{*(Y_1)}_{A-1}\hat{T}^{*(Y_1)}_{A-1}$$

$$\times (-1)^{3J_{A-2}+2T_{A-2}+T_{Y_1 Y_2}+S_{Y_1 Y_2}+\lambda+t_{Y_1}+l_{Y_1}+t_{Y_2}+l_{Y_2}+I_{Y_1}+1}$$

$$\times \sum_{S_{A-1}=J_{A-2}+s_N}(-1)^{S_{A-1}}\hat{S}^2_{A-1}\begin{Bmatrix} J_{A-2} & s_{Y_1} & S_{A-1} \\ l_{Y_1} & J^{*(Y_1)}_{A-1} & I_{Y_1}\end{Bmatrix}$$

$$\times \sum_{\substack{L=l_{Y_1}+l_{Y_2} \\ S=S_{A-1}+s_{Y_2}}}\hat{L}^2\hat{S}^2\begin{Bmatrix} l_{Y_1} & S_{A-1} & J^{*(Y_1)}_{A-1} \\ l_{Y_2} & s_{Y_2} & I_{Y_2} \\ L & S & J \end{Bmatrix}\begin{Bmatrix} l_{Y_1 Y_2} & S_{Y_1 Y_2} & J_{Y_1 Y_2} \\ \lambda & J_{A-2} & I_\lambda \\ L & S & J \end{Bmatrix} \tag{5.19}$$

$$\times \langle n_{Y_1} l_{Y_1} n_{Y_2} l_{Y_2} : L | n_{Y_1 Y_2} l_{Y_1 Y_2} n_\lambda \lambda : L\rangle_d$$

$$\times \begin{Bmatrix} s_{Y_2} & s_{Y_1} & S_{Y_1 Y_2} \\ J_{A-2} & S & S_{A-1}\end{Bmatrix}\begin{Bmatrix} t_{Y_2} & t_{Y_1} & T_{Y_1 Y_2} \\ T_{A-2} & T & T^{*(Y_1)}_{A-1}\end{Bmatrix},$$

with

$$d = \frac{(A-2)m_N m(t_{Y_2})}{m(t_{Y_1})((A-2)m_N + m(t_{Y_1}) + m(t_{Y_2}))}.$$

Finally, the summation over the $|(\alpha^{*(Y_1)})^{*(Y_2)}\rangle$ states can be carried out very efficiently using the Fox's matrix multiplication Algorithm 1 as explained in Section 3.3.1. The transition coefficients for the second expansion Eq. (5.16) are computed analogously.

Now, employing the expansions Eqs. (5.15) and (5.16), the matrix element $\langle\alpha^{*(Y_1 Y_2)}|H^{S=-1}_{Y_1 Y_2}|\alpha'^{*(Y_1 Y_2)}\rangle$

in Eq. (5.12) can be decomposed into,

$$\langle\alpha^{*(Y_1Y_2)}|H^{S=-1}_{Y_1Y_2}|\alpha'^{*(Y_1Y_2)}\rangle = \langle\alpha^{*(Y_1Y_2)}|H^{S=-1}_{Y_1Y_2}|\alpha'^{*(Y_1Y_2)}\rangle_{Y_2} + \langle\alpha^{*(Y_1Y_2)}|H^{S=-1}_{Y_1Y_2}|\alpha'^{*(Y_1Y_2)}\rangle_{Y_1}. \quad (5.20)$$

The subscript in each term on the right-hand side of Eq. (5.20) specifies the spectator hyperon. The first contribution is given by

$$\langle\alpha^{*(Y_1Y_2)}|H^{S=-1}_{Y_1Y_2}|\alpha'^{*(Y_1Y_2)}\rangle_{Y_2} = \langle\bullet\!\!-\!\!\!\!\phantom{|}\;|\;\phantom{|}\!\!-\!\!\bullet\rangle\langle\bullet\!\!-\!\!\!\!\phantom{|}\;|H^{S=-1}_{Y_1Y_2}|\;\phantom{|}\!\!-\!\!\bullet\rangle\langle\bullet\!\!-\!\!\!\!\phantom{|}\;|\;\phantom{|}\!\!-\!\!\bullet\rangle$$

$$(5.21)$$

$$= \langle\bullet\!\!-\!\!\!\!\phantom{|}\;|\;\phantom{|}\!\!-\!\!\bullet\rangle\delta_{Y_2Y'_2}\langle\bullet\!\!-\!\!\!\!\phantom{|}\;|H^{S=-1}_{Y_1Y_2}|\;\phantom{|}\!\!-\!\!\bullet\rangle\langle\bullet\!\!-\!\!\!\!\phantom{|}\;|\;\phantom{|}\!\!-\!\!\bullet\rangle.$$

Similarly, the second contribution $\langle\alpha^{*(Y_1Y_2)}|H^{S=-1}_{Y_1Y_2}|\alpha'^{*(Y_1Y_2)}\rangle_{Y_1}$ can be deduced from Eq. (5.21) by interchanging the roles of $Y_1$ and $Y_2$ hyperons for the intermediate states,

$$\langle\alpha^{*(Y_1Y_2)}|H^{S=-1}_{Y_1Y_2}|\alpha'^{*(Y_1Y_2)}\rangle_{Y_1} = \langle\bullet\!\!-\!\!\!\!\phantom{|}\;|\;\phantom{|}\!\!-\!\!\bullet\rangle\delta_{Y_1Y'_1}\langle\bullet\!\!-\!\!\!\!\phantom{|}\;|H^{S=-1}_{Y_1Y_2}|\;\phantom{|}\!\!-\!\!\bullet\rangle\langle\bullet\!\!-\!\!\!\!\phantom{|}\;|\;\phantom{|}\!\!-\!\!\bullet\rangle. \quad (5.22)$$

Although Eqs. (5.21) and (5.22) are very similar to Eq. (3.27), the presence of a hyperon spectator $Y_2(Y_1)$ makes it rather complicated to properly determine the corresponding combinatorial factors that relate the many-body matrix elements $\delta_{Y_2Y'_2}\langle\bullet\!\!-\!\!\!\!\phantom{|}\;|H^{S=-1}_{Y_1Y_2}|\;\phantom{|}\!\!-\!\!\bullet\rangle$ $(\delta_{Y_1Y'_1}\langle\bullet\!\!-\!\!\!\!\phantom{|}\;|H^{S=-1}_{Y_1Y_2}|\;\phantom{|}\!\!-\!\!\bullet\rangle)$ to the YN Hamiltonian matrix elements in the two-body sector. These combinatorial factors are listed in Table A.1. In Appendix A one can also find the detail of the derivation. As it is shown in Table A.1 the factors generally depend not only on the total number of nucleons but also the two hyperons $Y_1$ and $Y_2$ in the intermediate states.

# Results for $\Lambda\Lambda$ $s$-shell hypernuclei

In this chapter, we are going to report our first results for the doubly strange s-shell hypernuclei, $^{4}_{\Lambda\Lambda}\text{H}(1^{+}, 0)$, $^{5}_{\Lambda\Lambda}\text{He}(\frac{1}{2}^{+}, \frac{1}{2})$ and $^{6}_{\Lambda\Lambda}\text{He}(0^{+}, 0)$. To zeroth approximation, these systems can be regarded as a $\Lambda\Lambda$ pair in the $^{1}S_{0}$ state being attached to the corresponding core-nuclei in their ground states. While the quantum numbers of $^{5}_{\Lambda\Lambda}\text{He}$, $(J^{+}, T) = (\frac{1}{2}^{+}, \frac{1}{2})$, are obvious, those for the $^{4}_{\Lambda\Lambda}\text{H}$ hypernucleus are chosen according to our observations that the state with $(J^{+}, T) = (1^{+}, 0)$ is the lowest-lying level and the only possible bound state of $^{4}_{\Lambda\Lambda}\text{H}$ [155].

For all calculations present here, we employ the SMS N$^4$LO+(450) potential with an SRG flow parameter of $\lambda_{NN} = 1.6$ fm$^{-1}$ for describing NN interactions, and the NLO19 potential with a regulator of $\Lambda_Y = 650$ MeV and an SRG cutoff of $\lambda_{YN} = 0.868$ fm$^{-1}$ for the YN interactions. We remark that the chosen NN and YN potentials successfully predict the empirical $\Lambda$ separation energies for $^{3}_{\Lambda}\text{H}$, $^{4}_{\Lambda}\text{He}(1^{+})$ and $^{5}_{\Lambda}\text{He}$ but slightly underbind $^{4}_{\Lambda}\text{He}(0^{+})$ (see also Section 4.2). To describe the two-body interactions in the $S = -2$ sector, we utilize the YY chiral interactions at LO [61] and NLO [48, 156] for a cutoff of $\Lambda_{YY} = 600$ MeV. It is our primary focus here to study the impact of these two chiral potentials on the double-$\Lambda$ s-shell hypernuclei. Ultimately, we expect that results from such a study may provide meaningful constraints for constructing realistic YY interaction models. Before discussing the detailed results, let us give a brief overview of the LO and NLO interactions.

As we have mentioned in the introduction, using strict SU(3) flavour symmetry one can determine most of the LECs needed in the $S = -2$ sector at LO and NLO via a fit to the pertinent NN and YN data. Still, there are two LECs (one at each expansion order) in the isospin zero $^{1}S_{0}$ channel, $C^{1}$'s, that are only present in the double strangeness sector and remain undetermined. These two contact terms $C^{1}$'s must be constrained by the extremely sparse and uncertain YY data (i.e. a total cross section for $\Xi^{-}p - \Lambda\Lambda$ [63] and the upper limits of elastic and inelastic $\Xi^{-}p$ cross sections [62]). Such poor empirical data do not allow for quantitative but rather approximate determinations of the two unknown coupling $C^{1}$'s . One, for example, varies $C^{1}$'s within reasonable ranges around the natural value $(4\pi/f_{\pi}^{2})$ for the LO partial-wave projected contact term and then compares the computed scattering cross sections with the experimentally available data. Nevertheless, it turns out that reasonable choices for $C^{1}$'s can be made and the YY cross sections predicted by the two chiral models are compatible to each other and also fairly consistent with the sparse experimental constraints. The LO model, however, yields somewhat larger $\Lambda\Lambda$ scattering length than the values predicted by the meson exchange or quarks models and also exhibits rather strong

regulator dependence. The NLO is somewhat more preferable when describing nuclear matter, especially in its newer version [156]. The latter yields a moderately attractive $\Xi$ single-particle potential, $U_\Xi$, which is very similar to the prediction of the meson-based potentials, and importantly, well in line with recent experimental evidence of the existence of $\Xi N$ systems [157].

It should also be pointed out that the previous version of NLO [48] and the current fit [156] differ essentially by the in-medium $\Xi$ properties. We further observe that the two fits yield very similar binding energies for the double-$\Lambda$ s-shell hypernuclei. This possibly indicates that the in-medium properties of the interactions have little influences on the few-body observables like the binding energies. In the following, we therefore present results for the LO and the new fit of the NLO interactions for a chiral cutoff of $\Lambda_{YY} = 600$ MeV. In order to speed up the convergence, both YY potentials are also evolved to a wide range of the SRG flow parameters, namely $1.4 \leq \lambda_{YY} \leq 3.0$ fm$^{-1}$.

# 6.1 $_{\Lambda\Lambda}^{6}$He$(0^+, 0)$

The $_{\Lambda\Lambda}^{6}$He hypernucleus is so far the lightest double-$\Lambda$ system being unambiguously determined. Since the observation in the Nagara event, its $\Lambda\Lambda$-separation energy $B_{\Lambda\Lambda}(_{\Lambda\Lambda}^{6}\text{He})$, defined as $B_{\Lambda\Lambda}(_{\Lambda\Lambda}^{6}\text{He}) = E(^4\text{He}) - E(_{\Lambda\Lambda}^{6}\text{He})$, has been intensively exploited as a crucial constraint for many realistic YY interaction models, such as the meson-based Nijmegen ESC04 [158] or the quark model of Fujiwara [59], as well as for constructing effective potentials that are then employed in many-body calculations like the Gaussian expansion method [159, 160] or the cluster Faddeev-Yakubovsky approach [161, 162]. The recent re-examination of the Nagara event that yields slightly smaller $\Lambda\Lambda$ separation energy of $B_{\Lambda\Lambda}(_{\Lambda\Lambda}^{6}\text{He}) = 6.91 \pm 0.16$ MeV [17] (compared to the initial extracted value of $B_{\Lambda\Lambda}(_{\Lambda\Lambda}^{6}\text{He}) = 7.25 \pm 0.19$ [16]) may change the theoretical predictions for potentially observable bound states of other s-shell $\Lambda\Lambda$ hypernuclei [163], see also the discussion in Section 6.3. Let us further emphasize that the information about $B_{\Lambda\Lambda}(_{\Lambda\Lambda}^{6}\text{He})$ has not been directly utilized in order to constrain the LECs appearing in the chiral LO and NLO potentials. It is therefore of enormous interest to explore the $_{\Lambda\Lambda}^{6}$He hypernucleus using these two chiral interactions to confirm or disprove their consistency with $\Lambda\Lambda$ hypernuclei binding energies.

As mentioned in Chapter 5, in order to eliminate the model-dependence of the computed binding energies, we shall follow the same extrapolation procedure as explained in Section 4.1. The $\omega$- and $\mathcal{N}$-space extrapolations for $E(_{\Lambda\Lambda}^{6}\text{He})$ are illustrated in Figs. 6.1(a) and 6.1(b), respectively. For the illustrative purpose, we only present results for the LO potential with an SRG flow parameter of $\lambda_{YY} = 2.4$ fm$^{-1}$ but stress that the convergence trend does not depend on the chosen interaction nor on the specific value of $\lambda_{YY}$. One quickly sees that the behavior of $E(_{\Lambda\Lambda}^{6}\text{He})$ with respect to $\omega$ and $\mathcal{N}$ are very similar to that of the binding energy of the parent $_{\Lambda}^{5}$He hypernucleus as shown in Fig. 4.12. Furthermore, Fig. 6.1(b) also clearly demonstrates a nice convergence pattern of the binding energy $E(_{\Lambda\Lambda}^{6}\text{He})$ computed for model spaces up to $\mathcal{N}_{max} = 14$. Likewise, the $\Lambda\Lambda$-separation energy $B_{\Lambda\Lambda}(_{\Lambda\Lambda}^{6}\text{He})$, displayed in Fig. 6.1(c), is also well-converged for $\mathcal{N}_{max} = 14$ (practically with the same speed as that of $E(_{\Lambda\Lambda}^{6}\text{He})$). We note that for single-$\Lambda$ hypernuclei, the separation energy $B_\Lambda$ converges somewhat faster than the individual binding energies. Similar to $B_{\Lambda\Lambda}$ for $S = -1$ systems, here the $\Lambda\Lambda$-separation energy is also more interesting than the binding energy itself. The two removal energies, $B_{\Lambda\Lambda}$ and $B_\Lambda$, together may shed light onto many interesting effects. Indeed,

(a) $E(^{6}_{\Lambda\Lambda}He)$ as a function of $\omega$

(b) $E(^{6}_{\Lambda\Lambda}He)$ as a function of $\mathcal{N}$

(c) $B_{\Lambda\Lambda}(^{6}_{\Lambda\Lambda}He)$ as a function of $\mathcal{N}$

(d) $\Delta B_{\Lambda\Lambda}(^{6}_{\Lambda\Lambda}He)$ as a function of $\mathcal{N}$
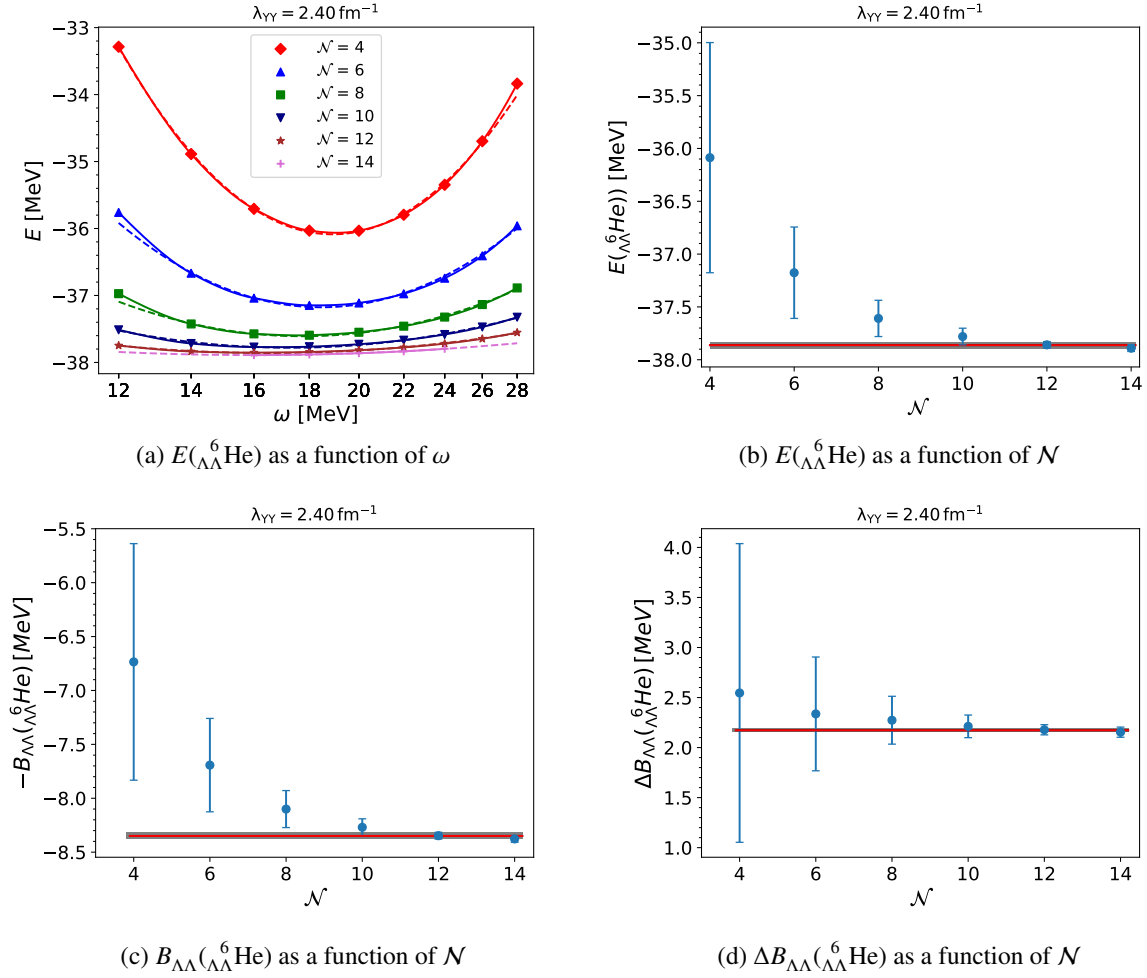
Figure 6.1: Binding energy $E$, $\Lambda\Lambda$-separation energy $B_{\Lambda\Lambda}$ and separation-energy difference $\Delta B_{\Lambda\Lambda}$ for $^{6}_{\Lambda\Lambda}He$ computed using the YY LO(600) interaction that is SRG evolved to a flow parameter of $\lambda_{YY} = 2.4$ fm$^{-1}$. The SMS N$^4$LO+(450) with $\lambda_{NN} = 1.6$ fm$^{-1}$ and YN NLO19(650) with $\lambda_{YN} = 0.868$ fm$^{-1}$ are employed for the NN and YN interactions.
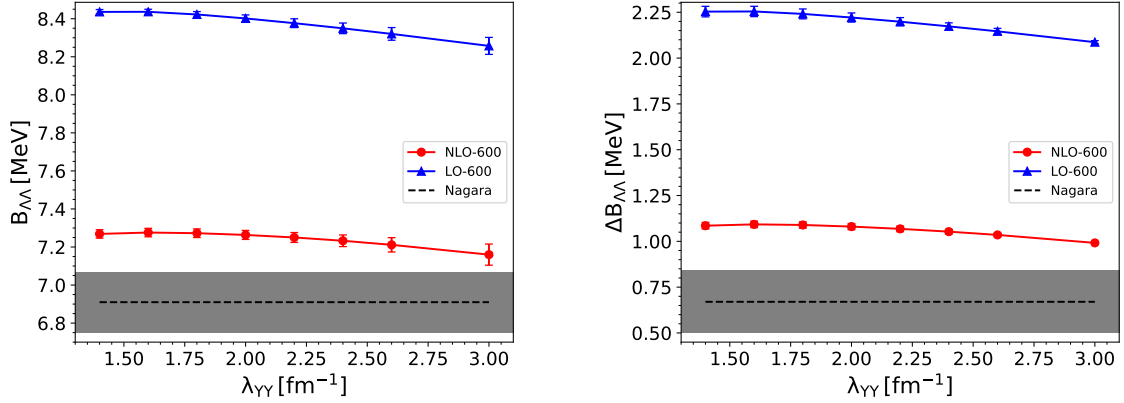
Figure 6.2: $B_{\Lambda\Lambda}(^{6}_{\Lambda\Lambda}\text{He})$ (left) and $\Delta B_{\Lambda\Lambda}(^{6}_{\Lambda\Lambda}\text{He})$ (right) as functions of flow parameter $\lambda_{YY}$. Calculations are based on the YY LO(600) (blue triangles) and NLO(00) (red circles). The dashed line with grey band represents the experimental value and its uncertainty. Same NN and YN interactions as in Fig. 6.1.

the value of the difference,

$$\Delta B_{\Lambda\Lambda}(^{A}_{\Lambda\Lambda}\text{X}) = B_{\Lambda\Lambda}(^{A}_{\Lambda\Lambda}\text{X}) - 2B_{\Lambda}(^{A-1}_{\Lambda}\text{X}), \qquad (6.1)$$

contain information not only about the strength of ΛΛ interaction but also the spin-dependent part of the Λ-core interaction, the dynamical changes in the core-nucleus structure as well as the polarization (screening) effects. In the case of $^{6}_{\Lambda\Lambda}\text{He}$, the spin-dependent part of the Λ-core interaction vanishes due to the zero spin of the core nucleus $^{4}\text{He}$, hence the difference

$$\Delta B_{\Lambda\Lambda}(^{6}_{\Lambda\Lambda}\text{He}) = B_{\Lambda\Lambda}(^{6}_{\Lambda\Lambda}\text{He}) - 2B_{\Lambda}(^{5}_{\Lambda}\text{He}),$$

will reflect the net contributions of the ΛΛ interactions, the $^{4}\text{He}$ core-distortion[1] and the screening effects. In Fig. 6.1(d), we exemplify the model-space extrapolation for $\Delta B_{\Lambda\Lambda}(^{6}_{\Lambda\Lambda}\text{He})$. Interestingly, $\Delta B_{\Lambda\Lambda}$ converges with respect to $\mathcal{N}$ noticeably faster than both ΛΛ-separation and the binding energies.

Being able to accurately extract $B_{\Lambda\Lambda}(^{6}_{\Lambda\Lambda}\text{He})$ and $\Delta B_{\Lambda\Lambda}(^{6}_{\Lambda\Lambda}\text{He})$, we are in a position to study the impacts of the two chiral interactions on these quantities. The converged results for $B_{\Lambda\Lambda}$ and $\Delta B_{\Lambda\Lambda}$, calculated with a wide range of the SRG flow parameter $\lambda_{YY}$, are presented in the left and right figures of Fig. 6.2, respectively. Evidently, the LO potential (blue triangles) predicts too much strength for the hyperon-hyperon interactions (larger than 2 MeV), which, as a consequence, leads to a somewhat large overbinding (by about 1.4 MeV) in $^{6}_{\Lambda\Lambda}\text{He}$. Meanwhile, the NLO potential predicts moderately attractive YY interactions with $\Delta B_{\Lambda\Lambda} \approx 1.1$ MeV, that is only slightly larger than the empirical value of $\Delta B_{\Lambda\Lambda}^{exp} = 0.67 \pm 0.17$ MeV [17]. As a result the, ΛΛ-separation energy obtained

---

[1]  Our preliminary results for the RMS distances of an NN pair and point-nucleon radii in $^{6}_{\Lambda\Lambda}\text{He}$, $^{5}_{\Lambda}\text{He}$ and $^{4}\text{He}$ are very similar to each other which implies that the distortions of the $^{4}\text{He}$ core are small. However, we also note that Hiyama *et al.* in their study for $A = 7 - 10$ double-strangeness systems using the Gaussian-basis coupled cluster method found that the dynamical changes in the nuclear core structures are significant [164]. Further study is necessary in order to clarify the discrepancy.

| $\lambda_{YN}$ | NLO(600) | | | LO(600) | | |
|---|---|---|---|---|---|---|
| fm$^{-1}$ | $P_{\Lambda\Sigma}$ | $P_{\Sigma\Sigma}$ | $P_{\Xi}$ | $P_{\Lambda\Sigma}$ | $P_{\Sigma\Sigma}$ | $P_{\Xi}$ |
| 1.4 | 0.13 | 0.11 | 0.02 | 0.17 | 0.04 | 0.5 |
| 2.0 | 0.13 | 0.11 | 0.07 | 0.17 | 0.05 | 0.84 |
| 3.0 | 0.12 | 0.13 | 0.12 | 0.18 | 0.08 | 1.08 |

Table 6.1: Probabilities (in percentage) of finding single and double $\Sigma$, and a $\Xi$ hyperons in the ground-state wavefunction of $_{\Lambda\Lambda}^{6}$He. Note that the corresponding $P_{\Sigma}$ in the wavefunction of the parent hypernucleus is $P_{\Sigma(_{\Lambda}^{5}He)} = 0.07\%$.

with the NLO stays very close to the experiment.

It is also exciting to notice that both $B_{\Lambda\Lambda}(_{\Lambda\Lambda}^{6}He)$ and $\Delta B_{\Lambda\Lambda}(_{\Lambda\Lambda}^{6}He)$ exhibit very weak dependence on the SRG cutoff $\lambda_{YY}$, of order of 100 keV only, that is at least one order of magnitude smaller than the variation of, say, $B_{\Lambda}(_{\Lambda}^{5}He)$ with respect to the SRG YN flow parameter $\lambda_{YN}$, see also Fig. 4.13. The insensitivity of the $\Lambda\Lambda$-separation energy on the SRG evolution probably indicates that the SRG-induced (and possibly the chiral) YYN forces are negligibly small. This, again supports the common believe that the $\Lambda\Lambda$ interaction strength is also relatively weak.

Finally, we think that it is also interesting to compare the probabilities of finding one $\Sigma$ ($P_{\Lambda\Sigma}$) or two $\Sigma$ ($P_{\Sigma\Sigma}$), and a $\Xi$ ($P_{\Xi}$) hyperons in the ground-state wavefunction of $_{\Lambda\Lambda}^{6}$He obtained for the two chiral potentials. Such probabilities for several cutoffs $\lambda_{YY}$ are summarised in Table 6.1. Overall, the $P_{\Lambda\Sigma}$ and $P_{\Sigma\Sigma}$ probabilities are fairly small, but rather stable with respect to the SRG evolution. Also, their dependence on the two interaction models is practically negligible. We remark that the probability of finding a $\Sigma$ in $_{\Lambda}^{5}$He for the same NN and a YN interactions is also very small, $P_{\Sigma(_{\Lambda}^{5}He)} = 0.07\%$. In contrast, $P_{\Xi}$ is more sensitive to the evolution and also strongly influenced by the interactions. Surprisingly, the NLO potential, that yields a more attractive $\Xi$-nuclear interaction [156], predicts considerably smaller $\Xi$ probability (less than 0.2 % for $\lambda_{YY} = 3.0$ fm$^{-1}$) compared to the value of $P_{\Xi} = 1.1\%$ obtained for the LO at the same $\lambda_{YY}$ cutoff. This again reflects the observation in the $S = -1$ sector that there is no one-to-one connection between the probabilities of finding a hyperon particle ($\Sigma$, $\Xi$) and the interaction strength.

## 6.2 $_{\Lambda\Lambda}^{5}$He$(\frac{1}{2}^{+}, \frac{1}{2})$

The next system, we want to investigate is the $_{\Lambda\Lambda}^{5}$He hypernucleus. Although the existence of $_{\Lambda\Lambda}^{5}$He has not been experimentally confirmed yet, most of the many-body calculations employing effective potentials that reproduce the separation energy $B_{\Lambda\Lambda}(_{\Lambda\Lambda}^{6}He)$ predict a particle-stable bound state of $_{\Lambda\Lambda}^{5}$He [159, 163, 165, 166]. However, there are visible discrepancies among the values of $B_{\Lambda\Lambda}(_{\Lambda\Lambda}^{5}He)$ predicted by different numerical approaches and different interaction models. Additionally, it is also found, using the Faddeev-Yakubovsky cluster approach, that there is an almost linear correlation between the calculated values of $B_{\Lambda\Lambda}$ for the $_{\Lambda\Lambda}^{5}$He ($_{\Lambda\Lambda}^{5}$H) and $_{\Lambda\Lambda}^{6}$He hypernuclei [166]. It will be very interesting to see whether one observes a similar correlation for chiral interactions. At this

(a) $E(^5_{\Lambda\Lambda}\text{He})$ as a function of $\omega$

(b) $E(^5_{\Lambda\Lambda}\text{He})$ as a function of $\mathcal{N}$

(c) $B_{\Lambda\Lambda}(^5_{\Lambda\Lambda}\text{He})$ as a function of $\mathcal{N}$

(d) $\Delta B_{\Lambda\Lambda}(^5_{\Lambda\Lambda}\text{He})$ as a function of $\mathcal{N}$
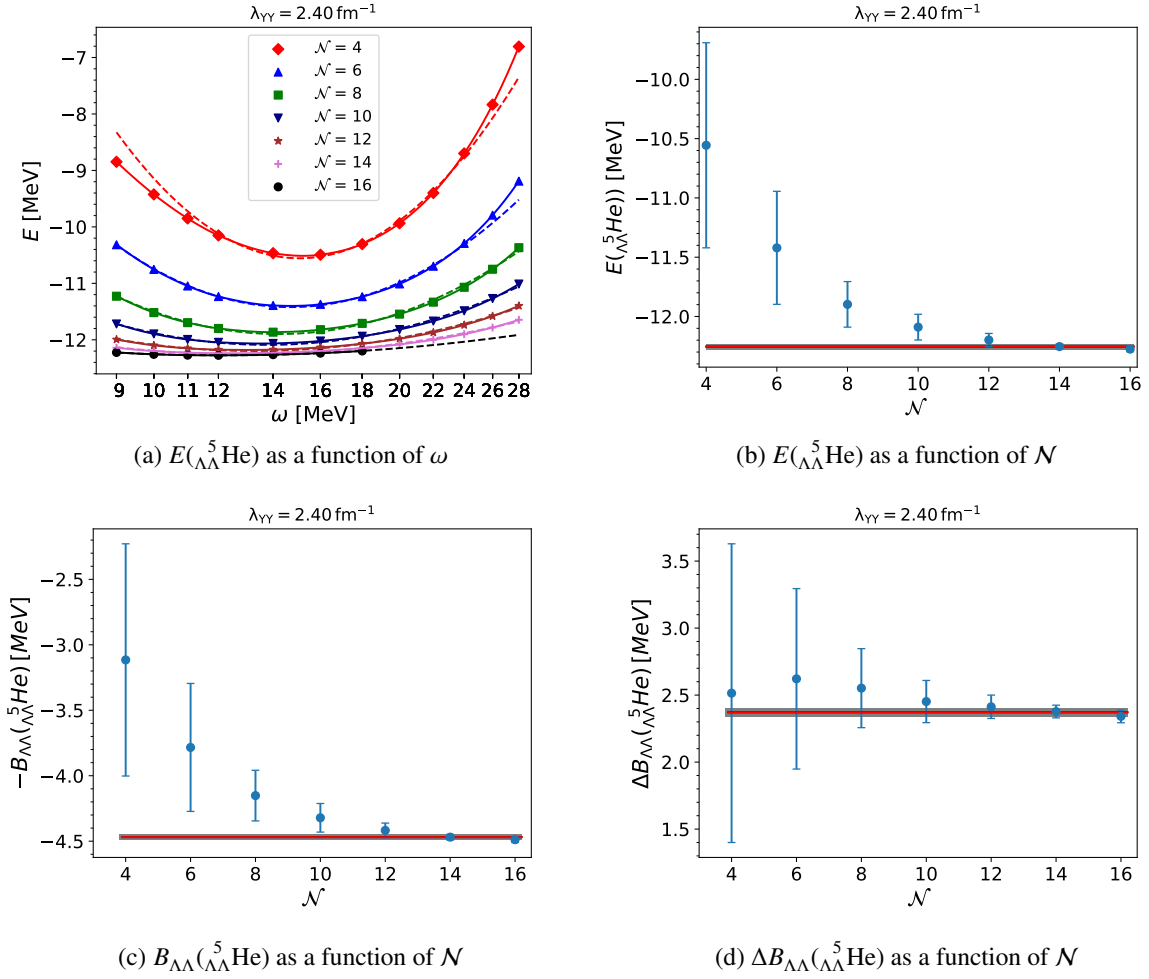
Figure 6.3: Binding energy $E$, ΛΛ separation energy $B_{\Lambda\Lambda}$ and separation-energy difference $\Delta B_{\Lambda\Lambda}$ for $^5_{\Lambda\Lambda}\text{He}$ computed using the YY LO(600) interaction that is SRG evolved to a flow parameter of $\lambda_{YY} = 2.4$ fm$^{-1}$. Same NN and YN interactions as in Fig. 6.1.

exploratory stage, we need to postpone this question to a future study and focus on the different effects of the LO and NLO potentials on $B_{\Lambda\Lambda}(^5_{\Lambda\Lambda}\text{He})$ instead.

The $\omega$- and $\mathcal{N}$-extrapolation of the binding energy $E$, ΛΛ-separation energy $B_{\Lambda\Lambda}$ and the separation-energy difference $\Delta B_{\Lambda\Lambda}$ of $^5_{\Lambda\Lambda}\text{He}$ are illustrated in Fig. 6.3. The calculations are also based on the LO potentials with a flow parameter of $\lambda_{YY} = 2.4$ fm$^{-1}$ and for all model spaces up to $\mathcal{N}_{max} = 16$. It is noted that in case of $^4_{\Lambda}\text{He}$, the calculations were performed for model spaces up to $\mathcal{N}_{max}(^4_{\Lambda}\text{He}) = 22$ in order to achieve a good convergence. Calculations with such large model spaces are currently not feasible for $^5_{\Lambda\Lambda}\text{He}$ because of memory constraints. Nonetheless, our illustrative results in Figs. 6.3(b) to 6.3(d) clearly indicate that well-converged results are achieved for this double-Λ hypernucleus already for model spaces up to $\mathcal{N}_{max} = 16$. Moreover, the employed extrapolation procedure from Section 4.1 also allows for a reliable estimate of the truncation uncertainty.

Figure 6.4: $B_{\Lambda\Lambda}(_{\Lambda\Lambda}^{5}\text{He})$ (left) and $\Delta B_{\Lambda\Lambda}(_{\Lambda\Lambda}^{5}\text{He})$ (right) as functions of flow parameter $\lambda_{YY}$. Calculations are based on the YY LO(600) (blue triangles) and NLO(600) (red circles). Same NN and YN interactions as in Fig. 6.1.

Let us further remark that when calculating the difference

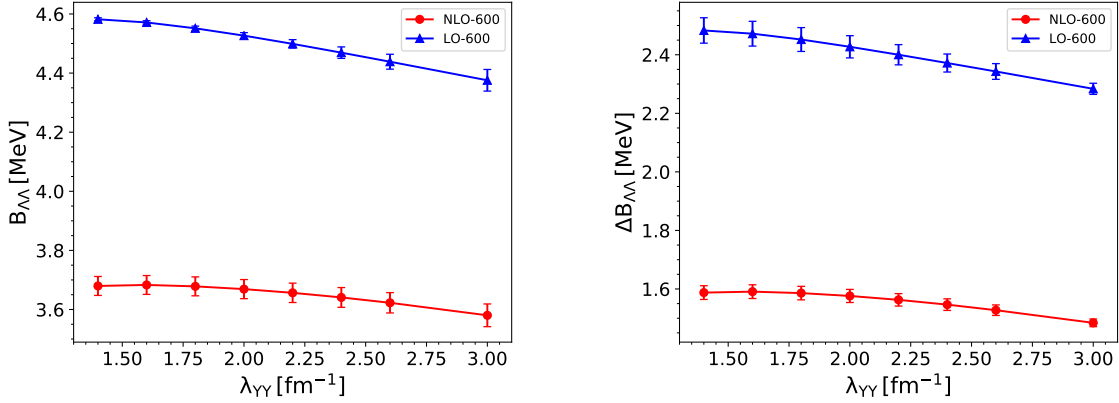$$\Delta B_{\Lambda\Lambda}(_{\Lambda\Lambda}^{5}\text{He}) = B_{\Lambda\Lambda}(_{\Lambda\Lambda}^{5}\text{He}) - 2B_{\Lambda}(_{\Lambda}^{4}\text{He}) \tag{6.2}$$

we do not simply assign the ground-state $\Lambda$-separation energy $B_{\Lambda}(_{\Lambda}^{4}\text{He}, 0^{+})$ to $B_{\Lambda}(_{\Lambda}^{4}\text{He})$ but rather the spin-averaged value $\overline{B}_{\Lambda}(_{\Lambda}^{4}\text{He})$ of the ground-state doublet [164]

$$\overline{B}_{\Lambda}(_{\Lambda}^{4}\text{He}) = \frac{1}{4}B_{\Lambda}(_{\Lambda}^{4}\text{He}, 0^{+}) + \frac{3}{4}B_{\Lambda}(_{\Lambda}^{4}\text{He}, 1^{+}). \tag{6.3}$$

By replacing $B_{\Lambda}(_{\Lambda}^{4}\text{He})$ in Eq. (6.2) with $\overline{B}_{\Lambda}(_{\Lambda}^{4}\text{He})$, the computed quantity $\Delta B_{\Lambda\Lambda}(_{\Lambda\Lambda}^{5}\text{He})$ then is free from the spin-dependenct effect of the $\Lambda$-core interactions, and therefore, can be used as a measure of the $\Lambda\Lambda$ interaction strength, provided that the nuclear contraction and screening effects are small.

Having achieved well-converged results for the particle-stable $_{\Lambda\Lambda}^{5}\text{He}$ hypernucleus, we can now study the predictions of the LO and NLO potentials for this $S = -2$ system. The results for $B_{\Lambda\Lambda}(_{\Lambda\Lambda}^{5}\text{He})$ and $\Delta B_{\Lambda\Lambda}(_{\Lambda\Lambda}^{5}\text{He})$ calculated for the two interactions and a wide range of flow parameter, $1.4 \leq \lambda_{YY} \leq 3.0$ fm$^{-1}$, are shown in the left and right figures of Fig. 6.4, respectively.

Overall, we observe very weak dependence of these two quantities on the SRG flow parameter as seen for $_{\Lambda\Lambda}^{6}\text{He}$, reinforcing the insignificance of the SRG-induced YYN forces. Here, again the LO interaction predicts a larger $\Lambda\Lambda$-separation energy and a stronger $\Lambda\Lambda$ interaction strength than the NLO does. It is further noticed that the separation-energy difference $\Delta B_{\Lambda\Lambda}$ computed for $_{\Lambda\Lambda}^{5}\text{He}$, e.g. $\Delta B_{\Lambda\Lambda}(_{\Lambda\Lambda}^{5}\text{He}, \text{NLO}) = 1.6$ MeV, is slightly larger than the corresponding one for $_{\Lambda\Lambda}^{6}\text{He}$, $\Delta B_{\Lambda\Lambda}(_{\Lambda\Lambda}^{6}\text{He}, \text{NLO}) = 1.12$ MeV (see also Fig. 6.2). The main deviations must come from the nuclear-core distortion and polarisation effects as mentioned earlier. An elaborate study is necessary in order to clarify the roles of these different contributions to $\Delta B_{\Lambda\Lambda}$ which in turn will enable an accurate estimation of the actual strength of the $\Lambda\Lambda$ interaction.

To finalize this section, we also provide the probabilities of finding a $\Sigma$ ($P_{\Lambda\Sigma}$), double $\Sigma$ ($P_{\Sigma\Sigma}$) and a $\Xi$ ($P_{\Xi}$) in the $_{\Lambda\Lambda}^{5}\text{He}$ ground-state wavefunction in Table 6.2 and compare results for the LO

| $\lambda_{YN}$ | NLO(600) | | | LO(600) | | |
|:---:|:---:|:---:|:---:|:---:|:---:|:---:|
| fm$^{-1}$ | $P_{\Lambda\Sigma}$ | $P_{\Sigma\Sigma}$ | $P_{\Xi}$ | $P_{\Lambda\Sigma}$ | $P_{\Sigma\Sigma}$ | $P_{\Xi}$ |
| 1.4 | 0.61 | 0.07 | 0.4 | 0.53 | 0.02 | 1.25 |
| 2.0 | 0.6 | 0.08 | 0.38 | 0.51 | 0.03 | 1.36 |
| 3.0 | 0.57 | 0.08 | 0.23 | 0.51 | 0.05 | 1.35 |

Table 6.2: Probabilities (in percentage) of finding a $\Sigma$ ($P_{\Lambda\Sigma}$), double $\Sigma$ ($P_{\Sigma\Sigma}$) and a $\Xi$ ($P_{\Xi}$) hyperons in $_{\Lambda\Lambda}^{5}$He, $P_{\Sigma}(_{\Lambda}^{4}$He$) = 0.43$

and NLO interactions for several SRG cutoffs, $\lambda_{YY} = 1.4, 2.0$ and $3.0$ fm$^{-1}$. Apparently, all the probabilities, including also $P_{\Xi}$ are less sensitive to the flow parameter. The two interactions seem to have little impact on the $\Sigma$-probabilities ($P_{\Lambda\Sigma}$ and $P_{\Sigma\Sigma}$) while they again strongly influence the $\Xi$-probability. Like in the $_{\Lambda\Lambda}^{6}$He system, here, the LO potential yields considerably larger $\Xi$-probability as compared to the value predicted by the NLO interaction. When comparing Tables 6.1 and 6.2, one immediately notices that the probabilities of finding $\Sigma$ or $\Xi$ hyperons in $_{\Lambda\Lambda}^{5}$He are much larger than the corresponding ones in $_{\Lambda\Lambda}^{6}$He. This is indeed consistent with the $\Sigma$-probabilities in ground-state wavefunctions of their parent hypernuclei (e.g. $P_{\Sigma}(_{\Lambda}^{4}$He$) = 0.43\%$ and $P_{\Sigma}(_{\Lambda}^{5}$He$) = 0.07\%$ for the same employed YN and NN interactions).

## 6.3 $_{\Lambda\Lambda}^{4}$H($1^{+}, 0$)

Our final exploratory *s*-shell hypernucleus is $_{\Lambda\Lambda}^{4}$H. This system has been subject to many interesting theoretical and experimental studies. It turns out that theoretical predictions of the stability of $_{\Lambda\Lambda}^{4}$H against the $_{\Lambda}^{3}$H + $\Lambda$ breakup is very sensitive to the interpretations of double-strangeness hypernuclear data in particular the $_{\Lambda\Lambda}^{6}$He hypernucleus [163]. Indeed, Nemura *et al.* [159] using the full-coupled channel stochastic variational method in combination with effective YY potentials that are fitted to reproduce the initially extracted value of $B_{\Lambda\Lambda}(_{\Lambda\Lambda}^{6}$He$) = 7.25 \pm 0.19$ MeV [16] observed a particle-stable but loosely bound state of $_{\Lambda\Lambda}^{4}$H (about 20 keV below the $_{\Lambda}^{3}$H + $\Lambda$ threshold). On the other hand, Filikhin *et al.* [161] found in their Faddeev-Yakubovsky calculations with YY potentials that yield the re-evaluated separation energy $B_{\Lambda\Lambda}(_{\Lambda\Lambda}^{6}$He$) = 6.79 \pm 0.91$ MeV that the $_{\Lambda\Lambda}^{4}$H system is not stable. Also, an observation of this hypernucleus was reported by an experiment at BNL [167], but, unfortunately this has been recently invalidated by a thorough reevaluation of the recorded events [168]. Nevertheless, the existence of a stable $_{\Lambda\Lambda}^{4}$H hypernucleus is not completely ruled out and the search for its experimental confirmation or rejection is still ongoing.

In view of the previous calculations, it seems unlikely that $_{\Lambda\Lambda}^{4}$H is bound for the NLO interaction. An interesting question we want to address here as a starting point is whether the chiral YY potentials at LO that overbinds $_{\Lambda\Lambda}^{6}$He (and possibly $_{\Lambda\Lambda}^{5}$He?) lead to a particle-stable state of $_{\Lambda\Lambda}^{4}$H against $\Lambda$ emission provided that the hypertriton is properly described? It is well-known that $B_{\Lambda}(_{\Lambda}^{3}$H$)$ is extremely small, and the NCSM calculations for very loosely bound systems converge slowly. Hence, in order to unambiguously answer that question, the converged binding energies of the parent

(a) $E(_{\Lambda\Lambda}^{4}H)$ as a function of $\omega$

(b) $E(_{\Lambda\Lambda}^{4}H)$ as a function of $\mathcal{N}$

(c) $E(_{\Lambda}^{3}H)$ as a function of $\mathcal{N}$

(d) $E(_{\Lambda\Lambda}^{4}H)$ as a function SRG flow parameter $\lambda_{YY}$
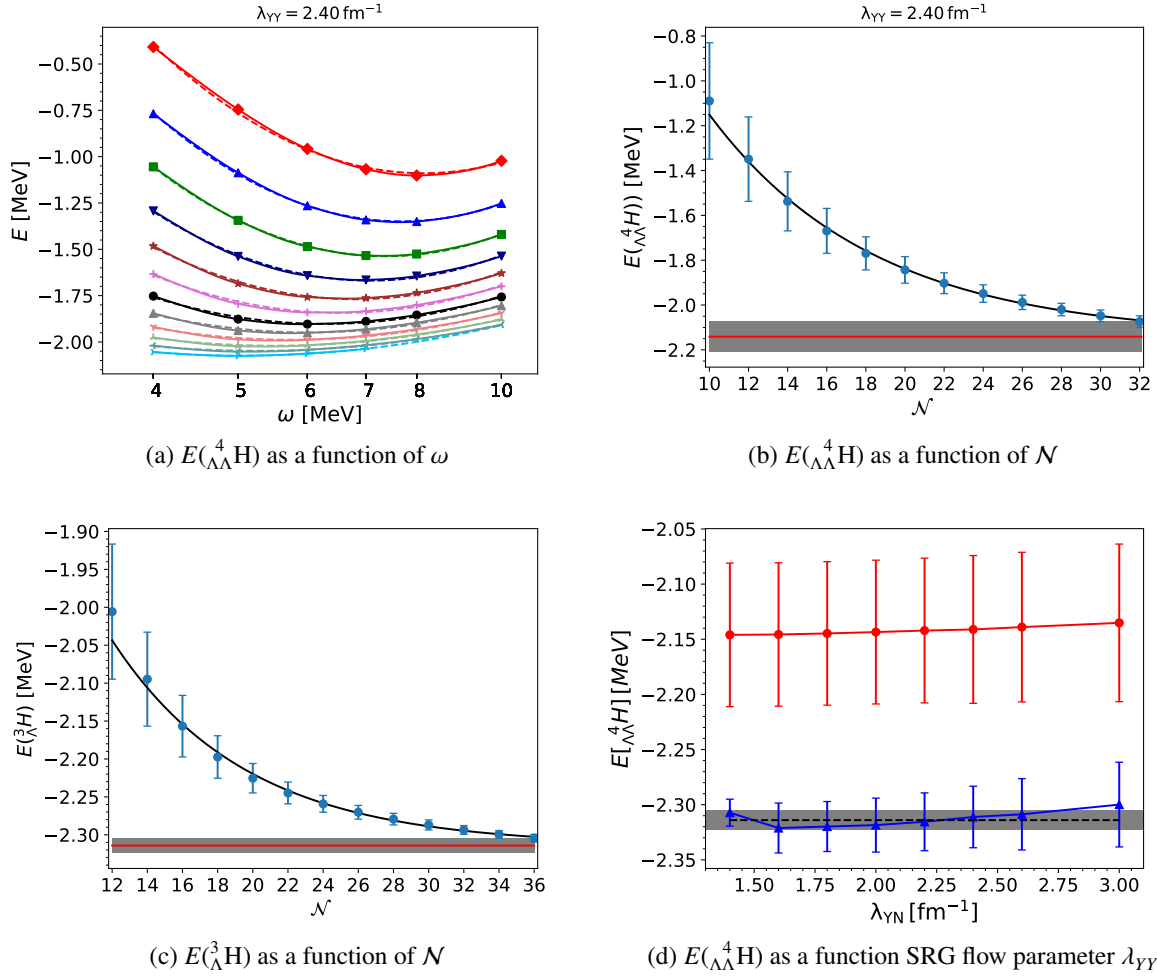
Figure 6.5: (a): Binding energies of $_{\Lambda\Lambda}^{4}He$ as functions of $\omega$ for model space $\mathcal{N} = 10 - 32$. Calculations are performed with the YY NLO(600) potential evolved to a flow parameter of $\lambda_{YY} = 2.4$ fm$^{-1}$. (b): model space extrapolation of $E(_{\Lambda\Lambda}^{4}H)$ with the same YY interaction as in (a). (c): model space extrapolation of $E(_{\Lambda}^{3}H)$. (d): Converged binding energy of $E(_{\Lambda\Lambda}^{4}H)$ as functions of flow parameter for the LO(600) (blue triangles) and NLO(600) (red circles) potentials. The dashed line with grey band is the calculated hypertriton binding energy and the theoretical uncertainty, respectively. Same NN and YN interactions as in Fig. 6.1

hypertriton and of $_{\Lambda\Lambda}^{4}H$ are crucial.

In Figs. 6.5(a) and 6.5(b), we illustrate the convergence of $E(_{\Lambda\Lambda}^{4}H)$ in $\omega$- and $\mathcal{N}$-space, respectively, using model space up sizes to $\mathcal{N}_{max} = 32$. The results are shown for for the NLO(600) potential with a flow parameter of $\lambda_{YY} = 2.4$ fm$^{-1}$. For a better comparison, the model-space extrapolation of the hypertrition binding energy computed with model space up to $\mathcal{N} = 36$ is also presented in Fig. 6.5(c). As we expected, due to the weak binding of hypertriton, the binding energy calculations for both hypernuclei, $_{\Lambda\Lambda}^{4}H$ and $_{\Lambda}^{3}H$ hypernuclei converge very slowly when using HO bases. It also clearly sticks out that the optimal HO frequencies $\omega$ for large model space sizes are around $\omega_{opt} \approx 6$ MeV which is much smaller than the value of $\omega_{opt} \approx 16$ MeV for the $A = 4, 5$ systems. This again reflects

the large spatial extent of the wavefunctions of $_{\Lambda\Lambda}^{4}$H and $_{\Lambda}^{3}$H . Nevertheless, one can still observe a slightly faster speed of convergence for $E(_{\Lambda\Lambda}^{4}$H) as compared to the one for $E(_{\Lambda}^{3}$H). Moreover, our extrapolated value of $E(_{\Lambda}^{3}$H) $= -2.314 \pm 0.009$ MeV (for model space up to $\mathcal{N} = 36$)[2] agrees within 20 keV with the Faddeev-Yakubovsky result $E_{FY}(_{\Lambda}^{3}$H) $= -2.333 \pm 0.002$ MeV [136]. We conclude that a model space truncation of $\mathcal{N}_{max} = 32$ for the energy calculations in $_{\Lambda\Lambda}^{4}$H should be sufficient in order to draw a definite conclusion about the stability of the system against $\Lambda$ emission.

The extrapolated binding energies $E(_{\Lambda\Lambda}^{4}$H) for the NLO (red circles) and LO (blue triangles) potentials evolved to a wide range of flow parameters are displayed in Fig. 6.5(d). Here, the dashed black line together with the grey band represent the calculated hypertriton binding energy and its estimated uncertainty. Calculations with the NLO potential seem to converge more slowly than those with the LO potential. Nonetheless, one can clearly see that both chiral interactions lead to an unbound $_{\Lambda\Lambda}^{4}$H system with respect to the hypertriton $_{\Lambda}^{3}$H, despite the fact that the LO considerably overbinds the $_{\Lambda\Lambda}^{6}$He hypernucleus. It should, however, be stressed that in order to draw a final conclusion, this first exploratory stage clearly needs to be confirmed by a more careful estimate of uncertainties that must include a wide range of NN, YN and YY interactions.

---

[2] For model space $\mathcal{N}_{max} = 32$, the extrapolated hypertriton binding energy is $E(_{\Lambda}^{3}$H) $= -2.293 \pm 0.02$ MeV.

# Summary and Conclusions

Hypernuclear experiments together with reliable *ab initio* many-body calculations are indispensable tools for understanding the fundamental baryon-baryon (BB) interactions beyond the ordinary nuclear sector. In this thesis, we advance the nuclear J-NCSM to calculate properties of hypernuclear systems with strangeness $S = -1$ and $S = -2$. The approach also allows for a systematic and rigorous study of the stringent connections between hypernuclear observables (such as the binding energies) and the underlying chiral YN and YY interactions.

The first part of the thesis is devoted to single-strangeness hypernuclei up to the p-shell. Since nuclear interactions generally depend on relative coordinates between particles, it is natural to express the many-body Hamiltonian in Jacobi coordinates where the C.M. degrees of freedom are trivially excluded. Accordingly, the many-body bases are constructed from HO functions depending also on relative Jacobi coordinates which, in turn, allow for a straightforward evaluation of the two-body (or higher-body) Hamiltonian matrix elements. However, the inclusion of the strangeness degree of freedom tremendously increases the dimensionality of the linear equations needed to be solved (which is also the biggest limitation of the approach for the nuclear sector). This demands the most efficient way of implementing the J-NCSM approach on high-performance parallel supercomputers that require shared memory parallelization on nodes using OpenMP as well as distributed memory parallelization between nodes using MPI. The flexibility of HO functions expressed in Jacobi coordinates enables us to compute the bases and the necessary transition coefficients beforehand and store them in the machine independent HDF5 format. The latter allows for the most practical parallel I/O using the HDF5 standard library but can also result in a bottleneck problem, therefore, requires special consideration. The details of the numerical challenges and special techniques to overcome these difficulties are elaborated in Chapter 3.

For practical purposes, we need to restrict basis sizes by applying a truncation on the largest model space, $\mathcal{N} \leq \mathcal{N}_{max}$. Consequently, the results from the NCSM calculations are $\omega$- and $\mathcal{N}_{max}$-dependent. We apply a two-step ($\omega$- and $\mathcal{N}$-space) extrapolation procedure explained in Section 4.1 in order to extract the converged results and to reliably estimate the numerical uncertainties. Overall, our numerical errors are smaller than the theoretical uncertainties caused by the regulator-dependence of the employed chiral interactions.

In order to speed up the convergence of the NCSM calculations, we prediagonalize the Hamiltonian via the Similarity Renormalization Group (SRG) transformations. Such transformations decouple the low- and high-momentum states resulting in much softer BB interactions, therefore,

improve the convergence rate. The evolutions of the chiral YN and potentials at LO and NLO during the SRG are also discussed in Chapter 2.

The SRG transformations unavoidably introduce higher-body terms even beyond the ones that are included in the initial (bare) Hamiltonian. Omitting these terms leads to the dependence of the separation (binding) energies on the SRG flow parameters. In Section 4.2, we therefore thoroughly investigate the impact of the chiral NN interactions as well as of the SRG evolutions on the separation energies $B_\Lambda$ of the $A = 4 - 7$ hypernuclei. We found that, at low values of SRG YN flow parameter, $\lambda_{YN} \leq 1.4$ fm$^{-1}$, the separation energies are less dependent on the SRG NN evolution as well as on the NN potentials employed. The dependence somewhat increases for higher $\lambda_{YN}$, of order of $0.3, 0.8$ and $1.2$ MeV for $^4_\Lambda$He, $^5_\Lambda$He and $^7_\Lambda$Li, respectively. However, the relative variations are still small, about 50 keV for the s-shell and roughly 300 keV for the p-shell hypernuclei. We conclude that the sensitivity of the $\Lambda$-separation energies on the nuclear interactions can be substantially reduced once the 3N forces are properly included. In Section 4.3, we also study the excitation energies of $^7_\Lambda$Li which are experimentally well known. Especially, the splittings of spin doublets will provide interesting constraints of the spin dependence of the YN interactions. The results from Sections 4.2 and 4.3 also indicate that the variations of $B_\Lambda$ due to the SRG YN evolution are pronounced, about 1 MeV for $^4_\Lambda$He but can be as large as 5 MeV for the $A = 5 - 7$ hypernuclei, implying the importance of the SRG-induced YNN forces. Additionally, the probabilities of finding a $\Sigma$ hyperon in the ground-state wavefunctions of these systems are also strongly influenced by the evolution. However, there is no simple one-to-one relation between the $\Sigma$-probabilities and the calculated $\Lambda$ separation energies.

Our study in Section 4.4 shows that there are almost perfectly linear correlations between the $\Lambda$ separation energies of the $A = 4 - 7$ hypernuclei calculated for a wide range of the SRG YN flow parameters. Interestingly, at the magic SRG cutoff $\lambda_{YN}^m$ that yields the empirical separation energy of $^5_\Lambda$He, the separation energies of $^3_\Lambda$H and $^4_\Lambda$He$(0^+, 1^+)$ are in good agreement with the results for the non-evolved (bare) YN interactions, while the one for $^7_\Lambda$Li is surprisingly close to the experimental value. This observation suggests that by tuning the SRG parameter such that the $^5_\Lambda$He hypernucleus is correctly predicted, one can effectively minimize the effects of the missing SRG-induced 3BFs. Thereby, the special flow parameter $\lambda_{YN}^m$ can be a good starting point for hypernuclear studies that require the SRG evolutions.

In Section 4.5, we study the predictions of the two almost phase-equivalent chiral interactions, NLO13 and NLO19. Although the two potentials describe the sparse YN scattering data equally well, the strength of the $\Lambda N$-$\Sigma N$ transition potential in NLO19 is somewhat weaker than in NLO13. We observe similarly interesting results for s- and light p-shell hypernuclei. It turns out that, in all systems considered except $^4_\Lambda$He$(0^+)$, the separation energies predicted by NLO19 are apparently larger than the values predicted by NLO13 which is opposite to the $\Sigma$ probabilities. We do not see such a clear tendency in the ground state of $^4_\Lambda$He. The large discrepancies between the predictions of the two phase-equivalent interactions can probably be traced back to the contributions of the three-body YNN chiral forces.

Section 4.6 demonstrates one of the possible applications of the intriguing linear correlations of $B_\Lambda$. There, we exploit the special SRG cutoffs $\lambda_{YN}^m$ to investigate the consequences of a more strongly bound hypertriton which has been indeed suggested by recent measurements from the STAR collaboration. We find that increasing the $^3_\Lambda$H binding energy leads to an improvement in the predictions for the ground-state separation energy as well as the doublet splitting in $^4_\Lambda$He. The $\Lambda$ separation energy in $^7_\Lambda$Li is also slightly increased further away from the experimental value and its energy spectrum is somewhat distorted. However, the changes are in general small compared to

possible effects of the chiral three-body forces contribution that we previously estimated based on the $B_\Lambda(^7_\Lambda \text{Li})$ results for the NLO13 and NLO19 potentials.

CSB splittings in the $A = 7$ isotriplet are discussed in Section 4.7. In the current study, we do not include any CSB terms in the YN interaction model. Our results for the CSB splittings between every two components of the triplet are small but agree with the values extracted from experiments both in sign and magnitude. We also notice that the splittings are predominantly driven by the NN Coulomb modifications arising from the contractions of the nuclear cores when a hyperon is added into the system. The individual contributions of the kinetic energy operator, the NN and YN interactions are also visible but come with opposite signs, therefore, largely cancel each other.

Based on the computed wavefunctions, we have further access to the spatial distributions of hyperons and nucleons in hypernuclei, and be able to extract the point-particle radii and their relative distance to each other. In Section 4.8.2, we also explain our approach to extract the model-independent radii and distances for the NCSM calculations is explained in. Generally, calculations using long-range operators like $r^2$ converge slowly within the NCSM. We demonstrate that by applying the long-range corrections to the tails of the wavefunctions, well-converged results for RMS radii and distances can be indeed attained. Our results also confirm that the SRG evolution has minor effect on the long-range operator $r^2$. Furthermore, the contraction of the nuclear core due to the presence of a hyperon is rather small.

The second part of the thesis is dedicated to double strangeness hypernuclei. Adding a second hyperon to single-$\Lambda$ hypernuclei complicates the numerical realization significantly. Particle conversions such as $YY - \Xi N$ can couple states with identical hyperons to states with non-identical ones. Therefore, special consideration is required in order to relate the many-body Hamiltonian matrix elements to the ones in the two-body sector. In addition, the total number of nucleons is no longer conserved. These issues are comprehensively addressed in Chapter 5 and Appendix A. We have generalized the J-NCSM formalism so that the extension to other multi-strangeness sectors is straightforward. In Chapter 6, we then apply the advanced J-NCSM approach to study the predictions of the chiral YY interactions at LO and NLO for the $\Lambda\Lambda$ s-shell hypernuclei. In order to speed up the energy calculations, the two interactions are also evolved via SRG. Unlike for the $S = -1$ systems, here, we only observe very small effect of the YY evolution on the $\Lambda\Lambda$-separation energies, implying the insignificance of the SRG-induced YYN force contributions. Furthermore, we find in Section 6.1 that the YY NLO potential predicts fairly well the empirical value of $^6_{\Lambda\Lambda}\text{He}$ while the LO one slightly overbinds the system. Both interactions also yield a particle-stable $^5_{\Lambda\Lambda}\text{He}$ hypernucleus as shown in Section 6.2. Finally, the $^4_{\Lambda\Lambda}\text{H}$ hypernucleus is investigated in Section 6.3. The LO and NLO interactions result in instability of $^4_{\Lambda\Lambda}\text{H}$ against a breakup to $^3_\Lambda\text{H} + \Lambda$ in this case. However, in order to draw a final conclusion, an elaborate study that involves a more careful estimate of uncertainties stemming from various NN, YN and YY interactions is definitely necessary. It will be also very interesting to study the predictions of the chiral YY interactions for other s-shell $\Lambda\Lambda$ systems such as $^4_{\Lambda\Lambda}\text{n}$ or $^4_{\Lambda\Lambda}\text{He}$, as well as the p-shell ones. Likewise, investigating the possible Tjon lines for $B_{\Lambda\Lambda}$ of different systems is also of importance.

The preparations for including three-body chiral and SRG-induced forces are in progress. With the three-body forces included, we will definitely have a better understanding of hypernuclei and be at a good position to predict quantities that have not been measured yet, as well as to unambiguously connect hypernuclear properties to that of the underlying YN and YY interactions. In the meantime, study the possible impacts of the $P$-waves YN interaction on the separation energies and especially on the energy spectrum of $^7_\Lambda\text{Li}$ will be extremely useful. Given the situation that the few available YN data consists practically only of total cross sections which are predominantly determined by the

strength of the $S$-wave interactions, it is currently not possible to uniquely determine the $P$-waves LECs present at NLO in the chiral expansion.

As a final conclusion, in this thesis, we have demonstrated that the J-NCSM approach is capable of calculating observable properties of light $p$-shell single- and double-strangeness hypernuclei. The necessary tools are now ready and hypernuclear properties can be used to improve the existing YN and YY interactions, and therefore, our understanding of the strong interaction involving strange quarks.

# The many-body Schrödinger equation in second quantization

Generally, baryon-baryon (BB) interactions in the strangeness $S = -2$ sector can lead to couplings between states with identical particles and those with non-identical particles, for example $\Lambda\Lambda \to \Sigma\Lambda$. Such transitions will make it difficult to determine the proper combinatorial factors of the free space two-body potentials embedded in the matrix elements of the many-body Hamiltonian in an $A$-body basis. In this appendix, we demonstrate that these factors can be systematically deduced by comparing the Schrödinger equation for a system of $A$ particles with the two-body Schrödinger equation, provided that these equations are derived in a consistent way. We show explicit examples for systems of three and four particles, and then generalize to the $A$-body problem.

In order to derive the general Schrödinger equation, it is convenient to work with the second quantization formalism. The many-body Hamiltonian then can generally be written as follows

$$
H = \sum_{k_1 k_1'} T_{k_1' k_1} a_{k_1'}^\dagger a_{k_1} + \frac{1}{2} \sum_{\substack{k_1 k_2 \\ k_1' k_2'}} V_{k_1' k_2', k_1 k_2} a_{k_1'}^\dagger a_{k_2'}^\dagger a_{k_2} a_{k_1},
\tag{A.1}
$$

where $k_i$ stands for a set of quantum numbers characterizing the particle state, i.e. momentum, spin, isospin as well as the particle kind $\lambda_i$. When it is necessary to separate particle kinds from other quantum numbers, we use $k_i = \tilde{k}_i \times \lambda_i$. Let us further assume that the potential matrix elements $V_{k_1' k_2', k_1 k_2}$ in Eq. (A.1) are antisymmetric under exchanges of two indices, i.e., $V_{k_1' k_2', k_1 k_2} = -V_{k_1' k_2', k_2 k_1} = -V_{k_2' k_1', k_1 k_2} = V_{k_2' k_1', k_2 k_1}$. Note that, we do not require any ordering for quantum numbers of the incoming particles $k_1$ and $k_2$ or of the outgoing pair $k_1'$ and $k_2'$ in Eq. (A.1).

## A.1 Two-body Schrödinger equation

We shall start with the derivation of the Schrödinger equation in the two-particle basis. For that, we define the ordered two-body antisymmetrized basis states as

$$
|\{p_1 p_2\}\rangle \equiv a_{p_1}^\dagger a_{p_2}^\dagger |0\rangle = \frac{1}{\sqrt{2}} (|p_1\rangle|p_2\rangle - |p_2\rangle|p_1\rangle),
\tag{A.2}
$$

with the right-hand side being the states in first quantization. Also, $p_1$ and $p_2$ stand for the sets of quantum numbers (momentum, spin, isospin and particle kind) describing particles 1 and 2. The completeness relation of the basis Eq. (A.2) reads

$$\sum_{p_1<p_2} |\{p_1p_2\}\rangle\langle\{p_1p_2\}| \equiv \sum_{\lambda_1<\lambda_2} \int d^3\tilde{p}_1 d^3\tilde{p}_2 |\{\lambda_1\tilde{p}_1\lambda_2\tilde{p}_2\}\rangle\langle\{\lambda_1\tilde{p}_1\lambda_2\tilde{p}_2\}| = \mathbb{1}, \tag{A.3}$$

where the inequality $p_1 < p_2$ is to account for the ordering of the basis states in Eq. (A.2). Note that by exploiting the antisymmetry of the basis states, the left hand side of Eq. (A.3) can also be rewritten as

$$\sum_{p_1<p_2} |\{p_1p_2\}\rangle\langle\{p_1p_2\}| = \frac{1}{2}\Big\{ \sum_{p_1<p_2} |\{p_1p_2\}\rangle\langle\{p_1p_2\}| + \sum_{p_1<p_2} |\{p_1p_2\}\rangle\langle\{p_1p_2\}|\Big\}$$

$$= \frac{1}{2}\Big\{ \sum_{p_1<p_2} |\{p_1p_2\}\rangle\langle\{p_1p_2\}| + \sum_{p_1>p_2} |\{p_2p_1\}\rangle\langle\{p_2p_1\}|\Big\} \tag{A.4}$$

$$= \frac{1}{2} \sum_{p_1,p_2} |\{p_1p_2\}\rangle\langle\{p_1p_2\}|.$$

Hence, the summation over the ordered particle kinds on the right hand side of Eq. (A.2) can be replaced by a normal summation over all particle kinds with a factor of $\frac{1}{2}$. When the two particle are identical, i.e. $\lambda_1 = \lambda_2$, the completeness relation then becomes,

$$\frac{1}{2} \int d^3\tilde{p}_1 d^3\tilde{p}_2 |\{\lambda_1\tilde{p}_1\lambda_1\tilde{p}_2\}\rangle\langle\{\lambda_1\tilde{p}_1\lambda_1\tilde{p}_2\}| = \mathbb{1}. \tag{A.5}$$

Note that the factor $\frac{1}{2}$ can also be absorbed into the definition of the states by rewriting Eq. (A.5) as

$$\int d^3\tilde{p}_1 d^3\tilde{p}_2 \frac{1}{\sqrt{2}}|\{\lambda_1\tilde{p}_1\lambda_1\tilde{p}_2\}\rangle\langle\{\lambda_1\tilde{p}_1\lambda_1\tilde{p}_2\}|\frac{1}{\sqrt{2}} = \mathbb{1}. \tag{A.6}$$

Now, using the anticommutator relations for the creation and annihilation operators, one easily evaluates the kinetic and potential operators in the basis Eq. (A.2)

$$\langle\{p_1'p_2'\}|T|\{p_1p_2\}\rangle = \delta_{p_1'p_1}T_{p_2'p_2} - \delta_{p_1'p_2}T_{p_2'p_1} + \delta_{p_2'p_2}T_{p_1'p_1} - \delta_{p_2'p_1}T_{p_1'p_2}$$

$$= \delta_{p_1'p_1}\delta_{p_2'p_2}t_{p_2'} - \delta_{p_1'p_2}\delta_{p_2'p_1}t_{p_2'} + \delta_{p_2'p_2}\delta_{p_1'p_1}t_{p_1'} - \delta_{p_2'p_1}\delta_{p_1'p_2}t_{p_1'}$$

$$\langle\{p_1'p_2'\}|V|\{p_1p_2\}\rangle = \frac{1}{2}(V_{p_1'p_2',p_1p_2} - V_{p_1'p_2',p_2p_1} - V_{p_2'p_1',p_1p_2} + V_{p_2'p_1',p_2p_1}) \tag{A.7}$$

$$= 2V_{p_1'p_2',p_1p_2}.$$

In the second line of Eq. (A.7), we have exploited the fact that the kinetic operator is diagonal in the momentum basis. The Schrödinger equation

$$H|\Psi\rangle = E|\Psi\rangle, \tag{A.8}$$

in the basis Eq. (A.2) then reads

$$\sum_{p_1 < p_2} \langle \{p'_1 p'_2\} | H | \{p_1 p_2\} \rangle \langle \{p_1 p_2\} | \Psi \rangle = E \underbrace{\langle \{p'_1 p'_2\} | \Psi \rangle}_{\equiv \Psi(p'_1 p'_2)}. \tag{A.9}$$

Here, it is sufficient to consider only those components of $\Psi(p'_1 p'_2)$ with $p'_1 < p'_2$. Since the basis states are antisymmetric, the other components of $\Psi(p'_1 p'_2)$ with $p'_1 < p'_2$ will differ from the ones with $p'_1 > p'_2$ only by a phase factor. When plugging Eq. (A.7) into Eq. (A.9), one arrives at a general Schrödinger equation in the two-body basis

$$t_{p'_1} \Psi(p'_1 p'_2) + t_{p'_2} \Psi(p'_1 p'_2) + \sum_{p_1 < p_2} 2 V_{p'_1 p'_2, p_1 p_2} \Psi(p_1 p_2) = E \Psi(p'_1 p'_2). \tag{A.10}$$

We notice that there is a factor of 2 in front of the potential matrix elements, which drops out for the case of the two-identical particle basis, i.e. $\lambda_1 = \lambda_2$. In that case, the equation Eq. (A.10) becomes

$$t_{p'_1} \Psi(p'_1 p'_2) + t_{p'_2} \Psi(p'_1 p'_2) + \sum_{p_1 p_2} V_{p'_1 p'_2, p_1 p_2} \Psi(p_1 p_2) = E \Psi(p'_1 p'_2). \tag{A.11}$$

To better understand the prefactors of the potential matrix elements present in Eqs. (A.10) and (A.11) we consider several explicit bases. In the first case, the basis includes two particle states, one with identical particles and one with distinguishable particles, for example $|\{\Lambda\Lambda\}\rangle$ and $|\{N\Xi\}\rangle$. then the completeness relation

$$\int d^3 \tilde{p}_1 d^3 \tilde{p}_2 |\{\Xi \tilde{p}_1 N \tilde{p}_2\}\rangle \langle \{\Xi \tilde{p}_1 N \tilde{p}_2\}| + \int d^3 \tilde{p}_1 d^3 \tilde{p}_2 \frac{1}{\sqrt{2}} |\{\Lambda \tilde{p}_1 \Lambda \tilde{p}_2\}\rangle \langle \{\Lambda \tilde{p}_1 \Lambda \tilde{p}_2\}| \frac{1}{\sqrt{2}} = \mathbb{1}, \quad (A.12)$$

leads to the following expression for the norm of the wavefunction

$$\langle \Psi | \Psi \rangle = \int d^3 \tilde{p}_1 d^3 \tilde{p}_2 |\Psi_{N\Xi}(\tilde{p}_1 \tilde{p}_2)|^2 + \int d^3 \tilde{p}_1 d^3 \tilde{p}_2 |\frac{1}{\sqrt{2}} \Psi_{\Lambda\Lambda}(\tilde{p}_1 \tilde{p}_2)|^2. \tag{A.13}$$

We absorb the $\frac{1}{\sqrt{2}}$ factor into the amplitude of states by introducing a new set of the wavefunction components,

$$\Phi_{\Lambda\Lambda}(\tilde{p}_1 \tilde{p}_2) = \frac{1}{\sqrt{2}} \Psi_{\Lambda\Lambda}(\tilde{p}_1 \tilde{p}_2) \qquad \text{and} \qquad \Phi_{N\Xi}(\tilde{p}_1 \tilde{p}_2) = \Psi_{N\Xi}(\tilde{p}_1 \tilde{p}_2), \tag{A.14}$$

so that the Schrödinger equation Eqs. (A.10) and (A.11) for the two new components now gets a symmetric form

$$\begin{pmatrix} 2t_\Lambda + V_{\Lambda\Lambda,\Lambda\Lambda} & \sqrt{2} V_{\Lambda\Lambda,N\Xi} \\ \sqrt{2} V_{N\Xi,\Lambda\Lambda} & t_\Xi + t_N + 2V_{N\Xi,N\Xi} \end{pmatrix} \begin{pmatrix} \Phi_{\Lambda\Lambda} \\ \Phi_{N\Xi} \end{pmatrix} = E \begin{pmatrix} \Phi_{\Lambda\Lambda} \\ \Phi_{N\Xi} \end{pmatrix}, \tag{A.15}$$

where, for readability, we have omitted the dependence on $\tilde{p}$ and $\tilde{p}'$. Similarly, for the basis consisting of four states $\{|\Lambda\Lambda\}\rangle$, $|\{\Sigma\Sigma\}\rangle$, $|\{\Lambda\Sigma\}\rangle$ and $|\{\Xi N\}\rangle$ one can intuitively define a new set of

wavefunction components,

$$\Phi_{\Lambda\Lambda} = \frac{1}{\sqrt{2}}\Psi_{\Lambda\Lambda}, \quad \Phi_{\Sigma\Sigma} = \frac{1}{\sqrt{2}}\Psi_{\Sigma\Sigma}, \quad \Phi_{\Lambda\Sigma} = \Psi_{\Lambda\Sigma} \quad \text{and} \quad \Phi_{N\Xi} = \Psi_{N\Xi}, \quad (A.16)$$

which lead to the following symmetric Schrödinger equation

$$H\begin{pmatrix} \Phi_{\Lambda\Lambda} \\ \Phi_{\Sigma\Sigma} \\ \Phi_{\Lambda\Sigma} \\ \Phi_{N\Xi} \end{pmatrix} = E\begin{pmatrix} \Phi_{\Lambda\Lambda} \\ \Phi_{\Sigma\Sigma} \\ \Phi_{\Lambda\Sigma} \\ \Phi_{N\Xi} \end{pmatrix}, \quad (A.17)$$

where

$$H = \begin{pmatrix} 2t_{\Lambda} + V_{\Lambda\Lambda,\Lambda\Lambda} & V_{\Lambda\Lambda,\Sigma\Sigma} & \sqrt{2}V_{\Lambda\Lambda,\Lambda\Sigma} & \sqrt{2}V_{\Lambda\Lambda,N\Xi} \\ V_{\Sigma\Sigma,\Lambda\Lambda} & 2t_{\Sigma} + V_{\Sigma\Sigma,\Sigma\Sigma} & \sqrt{2}V_{\Sigma\Sigma,\Lambda\Sigma} & \sqrt{2}V_{\Sigma\Sigma,N\Xi} \\ \sqrt{2}V_{\Lambda\Sigma,\Lambda\Lambda} & \sqrt{2}V_{\Lambda\Sigma,\Sigma\Sigma} & t_{\Lambda} + t_{\Sigma} + 2V_{\Lambda\Sigma,\Lambda\Sigma} & 2V_{\Lambda\Sigma,N\Xi} \\ \sqrt{2}V_{N\Xi,\Lambda\Lambda} & \sqrt{2}V_{N\Xi,\Sigma\Sigma} & 2V_{N\Xi,\Lambda\Sigma} & t_{\Xi} + t_{N} + 2V_{N\Xi,N\Xi} \end{pmatrix}. \quad (A.18)$$

One sees that there is a $\sqrt{2}$-factor for the transition between states of identical and of distinguishable particles, and a factor of 2 for the transition between states of nonidentical particles. It is important to mention that these factors are already included in the definition of the two-body potentials derived from the Chiral EFT [46] or phenomenological models [169]. We therefore denote these initial two-body potentials $V_{\lambda_1\lambda_2,\lambda'_1\lambda'_2}$ with an appropriate factor of $\sqrt{2}$ or 2 or 1 to be our new potential $\tilde{V}_{\lambda_1\lambda_2,\lambda'_1\lambda'_2}$. Expressing in terms of the new potentials $\tilde{V}$, the Hamiltonian Eq. (A.18) now has a more intuitive form

$$H = \begin{pmatrix} 2t_{\Lambda} + \tilde{V}_{\Lambda\Lambda,\Lambda\Lambda} & \tilde{V}_{\Lambda\Lambda,\Sigma\Sigma} & \tilde{V}_{\Lambda\Lambda,\Lambda\Sigma} & \tilde{V}_{\Lambda\Lambda,N\Xi} \\ \tilde{V}_{\Sigma\Sigma,\Lambda\Lambda} & 2t_{\Sigma} + \tilde{V}_{\Sigma\Sigma,\Sigma\Sigma} & \tilde{V}_{\Sigma\Sigma,\Lambda\Sigma} & \tilde{V}_{\Sigma\Sigma,N\Xi} \\ \tilde{V}_{\Lambda\Sigma,\Lambda\Lambda} & \tilde{V}_{\Lambda\Sigma,\Sigma\Sigma} & t_{\Lambda} + t_{\Sigma} + \tilde{V}_{\Lambda\Sigma,\Lambda\Sigma} & \tilde{V}_{\Lambda\Sigma,N\Xi} \\ \tilde{V}_{N\Xi,\Lambda\Lambda} & \tilde{V}_{N\Xi,\Sigma\Sigma} & \tilde{V}_{N\Xi,\Lambda\Sigma} & t_{\Xi} + t_{N} + \tilde{V}_{N\Xi,N\Xi} \end{pmatrix}. \quad (A.19)$$

In the next step we are going to derive a similar Schrödinger equation in the three-body basis. Then, by comparing the obtained equation with the one in two-body basis, we be will able to determine the corresponding combinatorial factors for the potentials in each strangeness sectors.

## A.2 Three-body Schrödinger equation

We define the ordered three-body basis states in second quantization and its completeness relations as

$$|\{p_1 p_2 p_3\}\rangle \equiv a^{\dagger}_{p_1} a^{\dagger}_{p_2} a^{\dagger}_{p_3}|0\rangle; \qquad \sum_{p_1 < p_2 < p_3} |\{p_1 p_2 p_3\}\rangle\langle\{p_1 p_2 p_3\}| = \mathbb{1}. \quad (A.20)$$

The kinetic and potential operators can also be easily evaluated employing the anticommutator relations for the annihilation and creation operators. One obtains

$$
\begin{aligned}
\langle\{p'_1 p'_2 p'_3\}|T|\{p_1 p_2 p_3\}\rangle = {} & T_{p'_1 p_1}\delta_{p'_2 p_2}\delta_{p'_3 p_3} - T_{p'_1 p_1}\delta_{p'_2 p_3}\delta_{p'_3 p_2} + T_{p'_1 p_2}\delta_{p'_2 p_3}\delta_{p'_3 p_1} \\
& - T_{p'_1 p_2}\delta_{p'_2 p_1}\delta_{p'_3 p_3} + T_{p'_1 p_3}\delta_{p'_2 p_1}\delta_{p'_3 p_2} - T_{p'_1 p_3}\delta_{p'_2 p_2}\delta_{p'_3 p_1} \\
& + T_{p'_2 p_1}\delta_{p'_1 p_3}\delta_{p'_3 p_2} - T_{p'_2 p_1}\delta_{p'_1 p_2}\delta_{p'_3 p_3} + T_{p'_2 p_2}\delta_{p'_1 p_1}\delta_{p'_3 p_3} \\
& - T_{p'_2 p_2}\delta_{p'_1 p_3}\delta_{p'_3 p_1} + T_{p'_2 p_3}\delta_{p'_3 p_1}\delta_{p'_1 p_2} - T_{p'_2 p_3}\delta_{p'_1 p_1}\delta_{p'_3 p_2} \\
& + T_{p'_3 p_1}\delta_{p'_1 p_2}\delta_{p'_2 p_3} - T_{p'_3 p_1}\delta_{p'_1 p_3}\delta_{p'_2 p_2} + T_{p'_3 p_2}\delta_{p'_1 p_3}\delta_{p'_2 p_1} \\
& - T_{p'_3 p_2}\delta_{p'_1 p_1}\delta_{p'_2 p_3} + T_{p'_3 p_3}\delta_{p'_1 p_1}\delta_{p'_2 p_2} - T_{p'_3 p_3}\delta_{p'_1 p_2}\delta_{p'_2 p_1},
\end{aligned}
\tag{A.21}
$$

and

$$
\begin{aligned}
\langle\{p'_1 p'_2 p'_3\}|V|\{p_1 p_2 p_3\}\rangle = 2\{ & V_{p'_2 p'_3, p_2 p_3}\delta_{p'_1 p_1} + V_{p'_2 p'_3, p_3 p_1}\delta_{p'_1 p_2} + V_{p'_2 p'_3, p_1 p_2}\delta_{p'_1 p_3} \\
& + V_{p'_3 p'_1, p_2 p_3}\delta_{p'_2 p_1} + V_{p'_3 p'_1, p_3 p_1}\delta_{p'_2 p_2} + V_{p'_3 p'_1, p_1 p_2}\delta_{p'_2 p_3} \\
& + V_{p'_1 p'_2, p_2 p_3}\delta_{p'_3 p_1} + V_{p'_1 p'_2, p_3 p_1}\delta_{p'_3 p_2} + V_{p'_1 p'_2, p_1 p_2}\delta_{p'_3 p_3} \}.
\end{aligned}
\tag{A.22}
$$

Now, projecting the Schrödinger equation Eq. (A.8) onto the state $|\{p'_1 p'_2 p'_3\}\rangle$ and then ultilizing the completeness relation in Eq. (A.20), one arrives at

$$
\begin{aligned}
\sum_{p_1 < p_2 < p_3} & \langle\{p'_1 p'_2 p'_3\}|T|\{p_1 p_2 p_3\}\rangle\langle\{p_1 p_2 p_3\}|\Psi\rangle \\
& + \sum_{p_1 < p_2 < p_3} \langle\{p'_1 p'_2 p'_3\}|V|\{p_1 p_2 p_3\}\rangle\langle\{p_1 p_2 p_3\}|\Psi\rangle = E \underbrace{\langle\{p'_1 p'_2 p'_3\}|\Psi\rangle}_{\equiv\Psi(p'_1 p'_2 p'_3)}.
\end{aligned}
\tag{A.23}
$$

Similar to the case of a two-body basis, here it is also sufficient to consider only those components of $\Psi(p'_1 p'_2 p'_3)$ with $p'_1 < p'_2 < p'_3$. With these conditions, only three of the kinetic terms in Eq. (A.21) survive, namely

$$
\sum_{p_1 < p_2 < p_3} \langle\{p'_1 p'_2 p'_3\}|T|\{p_1 p_2 p_3\}\rangle\langle\{p_1 p_2 p_3\}|\Psi\rangle = (t_{p'_1} + t_{p'_2} + t_{p'_3})\Psi(p'_1 p'_2 p'_3).
\tag{A.24}
$$

The contributions from the potential operator are a little bit more cumbersome, but can be deduced to a compact form by exploiting the antisymmetry properties under the exchange of two indices of

the potential as well as of the wavefunction. For examples the first three terms in Eq. (A.22) give

$$
\sum_{p_1<p_2<p_3} V_{p_2'p_3',p_2p_3}\delta_{p_1'p_1}\Psi(p_1p_2p_3) + V_{p_2'p_3',p_3p_1}\delta_{p_1'p_2}\Psi(p_1p_2p_3) + V_{p_2'p_3',p_1p_2}\delta_{p_1'p_3}\Psi(p_1p_2p_3)
$$
$$
\begin{aligned}
&= \sum_{p_1<p_2<p_3} V_{p_2'p_3',p_2p_3}\delta_{p_1'p_1}\Psi(p_1p_2p_3) + \sum_{p_2<p_1<p_3} V_{p_2'p_3',p_3p_2}\delta_{p_1'p_1}\Psi(p_2p_1p_3) \\
&\quad + \sum_{p_3<p_2<p_1} V_{p_2'p_3',p_3p_2}\delta_{p_1'p_1}\Psi(p_3p_2p_1) \\
&= \sum_{p_1<p_2<p_3} V_{p_2'p_3',p_2p_3}\delta_{p_1'p_1}\Psi(p_1p_2p_3) + \sum_{p_2<p_1<p_3} V_{p_2'p_3',p_2p_3}\delta_{p_1'p_1}\Psi(p_1p_2p_3)+ \\
&\quad + \sum_{p_2<p_3<p_1} V_{p_2'p_3',p_2p_3}\delta_{p_1'p_1}\Psi(p_1p_2p_3) \\
&= \sum_{p_1}\sum_{p_2<p_3} V_{p_2'p_3',p_2p_3}\delta_{p_1'p_1}\Psi(p_1p_2p_3) \\
&= \sum_{p_2<p_3} V_{p_2'p_3',p_2p_3}\Psi(p_1'p_2p_3).
\end{aligned}
\tag{A.25}
$$

Analogously, the next three terms in Eq. (A.22) yield

$$
\sum_{p_1<p_2<p_3} V_{p_3'p_1',p_2p_3}\delta_{p_2'p_1}\Psi(p_1p_2p_3) + V_{p_3'p_1',p_3p_1}\delta_{p_2'p_2}\Psi(p_1p_2p_3) + V_{p_3'p_1',p_1p_2}\delta_{p_2'p_3}\Psi(p_1p_2p_3)
$$
$$
= \sum_{p_1<p_3} V_{p_1'p_3',p_1p_3}\Psi(p_1p_2'p_3),
\tag{A.26}
$$

and, the three remaining terms finally give

$$
\sum_{p_1<p_2<p_3} V_{p_1'p_2',p_2p_3}\delta_{p_3'p_1}\Psi(p_1p_2p_3) + V_{p_1'p_2',p_3p_1}\delta_{p_3'p_2}\Psi(p_1p_2p_3) + V_{p_1'p_2',p_1p_2}\delta_{p_3'p_3}\Psi(p_1p_2p_3)
$$
$$
= \sum_{p_1<p_2} V_{p_1'p_2',p_1p_2}\Psi(p_1p_2p_3').
\tag{A.27}
$$

Taking into account Eqs. (A.24) to (A.27), the Schrödinger equation Eq. (A.23) in the three-body basis Eq. (A.20) now becomes

$$
\begin{aligned}
&(t_{p_1'} + t_{p_2'} + t_{p_3'})\Psi(p_1'p_2'p_3') + \sum_{p_1<p_2} 2V_{p_1'p_2',p_1p_2}\Psi(p_1p_2p_3') \\
&\quad + \sum_{p_1<p_3} 2V_{p_1'p_3',p_1p_3}\Psi(p_1p_2'p_3) + \sum_{p_2<p_3} 2V_{p_2'p_3',p_2p_3}\Psi(p_1'p_2p_3) = E\Psi(p_1'p_2'p_3'),
\end{aligned}
\tag{A.28}
$$

which, as one expected, differs from the Schrödinger equation in the two-body basis Eq. (A.10) by the kinetic energy of the third particle and the two-body interactions between particles 1-3 and 2-3. Again, the factor of 2 in front of the potential vanishes when the incoming particles are identical and the summations include all states $\tilde{p}_1, \tilde{p}_2$ etc. For illustration purposes, let us consider the equation Eq. (A.28) in an explicit basis consisting of four states, $|\{N\Lambda\Lambda\}\rangle$, $|\{N\Sigma\Sigma\}\rangle$, $|\{N\Lambda\Sigma\}\rangle$ and $|\{NN\Xi\}\rangle$.

The norm of the wavefunction in this four-state basis can be calculated as follows

$$\langle\Psi|\Psi\rangle = \int d^3\tilde{p}_1 d^3\tilde{p}_2 d^3\tilde{p}_3 |\frac{1}{\sqrt{2}}\Psi_{N\Lambda\Lambda}(\tilde{p}_1\tilde{p}_2\tilde{p}_3)|^2 + \int d^3\tilde{p}_1 d^3\tilde{p}_2 d^3\tilde{p}_3 |\frac{1}{\sqrt{2}}\Psi_{N\Sigma\Sigma}(\tilde{p}_1\tilde{p}_2\tilde{p}_3)|^2$$
$$+ \int d^3\tilde{p}_1 d^3\tilde{p}_2 d^3\tilde{p}_3 |\Psi_{N\Lambda\Sigma}(\tilde{p}_1\tilde{p}_2\tilde{p}_3)|^2 + \int d^3\tilde{p}_1 d^3\tilde{p}_2 |\frac{1}{\sqrt{2}}\Psi_{NN\Xi}(\tilde{p}_1\tilde{p}_2\tilde{p}_3)|^2. \tag{A.29}$$

Based on Eq. (A.29), we define the new wavefunction components

$$\Phi_{N\Lambda\Lambda} = \frac{1}{\sqrt{2}}\Psi_{N\Lambda\Lambda}, \quad \Phi_{N\Sigma\Sigma} = \frac{1}{\sqrt{2}}\Psi_{N\Sigma\Sigma}, \quad \Phi_{N\Lambda\Sigma} = \Psi_{N\Lambda\Sigma} \quad \text{and} \quad \Phi_{NN\Xi} = \frac{1}{\sqrt{2}}\Psi_{NN\Xi}. \tag{A.30}$$

The Schrödinger equation Eq. (A.28), applied to the wavefunction components in Eq. (A.30), has a symmetric form,

$$(T+V)\begin{pmatrix} \Phi_{N\Lambda\Lambda} \\ \Phi_{N\Sigma\Sigma} \\ \Phi_{N\Lambda\Sigma} \\ \Phi_{NN\Xi} \end{pmatrix} = E\begin{pmatrix} \Phi_{N\Lambda\Lambda} \\ \Phi_{N\Sigma\Sigma} \\ \Phi_{N\Lambda\Sigma} \\ \Phi_{NN\Xi} \end{pmatrix}, \tag{A.31}$$

with $T$ being a diagonal matrix

$$T = \begin{pmatrix} 2t_\Lambda + t_N & 0 & 0 & 0 \\ 0 & 2t_\Sigma + t_N & 0 & 0 \\ 0 & 0 & t_\Lambda + t_\Sigma + t_N & 0 \\ 0 & 0 & 0 & 2t_N + t_\Xi \end{pmatrix}, \tag{A.32}$$

and the symmetric potential matrix

$$V = \begin{pmatrix} 2\tilde{V}_{N\Lambda,N\Lambda} + \tilde{V}_{\Lambda\Lambda,\Lambda\Lambda} & \tilde{V}_{\Lambda\Lambda,\Sigma\Sigma} & \tilde{V}_{\Lambda\Lambda,\Lambda\Sigma} + \sqrt{2}\tilde{V}_{N\Lambda,N\Sigma} & \sqrt{2}\tilde{V}_{\Lambda\Lambda,N\Xi} \\ \tilde{V}_{\Sigma\Sigma,\Lambda\Lambda} & 2\tilde{V}_{N\Sigma,N\Sigma} + \tilde{V}_{\Sigma\Sigma,\Sigma\Sigma} & \tilde{V}_{\Sigma\Sigma,\Lambda\Sigma} + \sqrt{2}\tilde{V}_{N\Sigma,N\Lambda} & \sqrt{2}\tilde{V}_{\Sigma\Sigma,N\Xi} \\ \tilde{V}_{\Lambda\Sigma,\Lambda\Lambda} + \sqrt{2}\tilde{V}_{N\Sigma,N\Lambda} & \tilde{V}_{\Lambda\Sigma,\Sigma\Sigma} + \sqrt{2}\tilde{V}_{N\Lambda,N\Sigma} & \tilde{V}_{N\Lambda,N\Lambda} + \tilde{V}_{N\Sigma,N\Sigma} + \tilde{V}_{\Lambda\Sigma,\Lambda\Sigma} & \sqrt{2}\tilde{V}_{\Lambda\Sigma,N\Xi} \\ \sqrt{2}\tilde{V}_{N\Xi,\Lambda\Lambda} & \sqrt{2}\tilde{V}_{N\Xi,\Sigma\Sigma} & \sqrt{2}\tilde{V}_{N\Xi,\Lambda\Sigma} & \tilde{V}_{NN,NN} + 2\tilde{V}_{N\Xi,N\Xi} \end{pmatrix}. \tag{A.33}$$

Comparing Eqs. (A.31) to (A.33) with Eq. (A.19), one can now intuitively read off the combinatorial factors for two-body potentials present in the three-body Hamiltonian. A generalization to an $A$-body system with strangeness $S = -2$ is straightforward. General speaking, in the strangeness $S = 0$ sector, the combinatorial factor is simply the binomial coefficient of $\binom{A_{\text{nucl}}}{2} = A_{\text{nucl}}(A_{\text{nucl}} - 1)/2$, where, $A_{\text{nucl}}$ is the number of nucleons for the given state (i.e. $A - 2$ for states with two singly strange hyperons and $A - 1$ for states involved a $\Xi$ hyperon). For the $S = -1$ and $S = -2$ sectors, the corresponding factors are listed in Table A.1-A.2. The second row is the free-space two-body

potentials that appear in the two-body Schrödinger equation. The first column labels all possible transitions between many-particle states. Here, we omit the particle labels of A-1 (A-2) nucleons and only list the last two baryons of the states that involve in the interactions. To shorten the presentation, we only include particle transitions in one direction. The other one is given by the symmetry of the potentials.

| | $S = -1$ | | | |
|---|---|---|---|---|
| *YN* potential transition | $\tilde{V}_{N\Lambda,N\Lambda}$ | $\tilde{V}_{N\Lambda,N\Sigma}$ | $\tilde{V}_{N\Sigma,N\Lambda}$ | $\tilde{V}_{N\Sigma,N\Sigma}$ |
| $\Lambda\Lambda \to \Lambda\Lambda$ | $2(A-2)$ | - | - | |
| $\Lambda\Lambda \to \Lambda\Sigma$ | - | $\sqrt{2}(A-2)$ | - | |
| $\Lambda\Sigma \to \Lambda\Sigma$ | $A-2$ | - | - | $A-2$ |
| $\Lambda\Sigma \to \Sigma\Sigma$ | - | $\sqrt{2}(A-2)$ | - | - |
| $\Sigma\Sigma \to \Lambda\Sigma$ | - | - | $\sqrt{2}(A-2)$ | - |
| $\Sigma\Sigma \to \Sigma\Sigma$ | - | - | - | $2(A-2)$ |

Table A.1: Combinatorial factors of the two-body YN interactions embedded in the *A*-body space with strangeness $S = -2$.

| $YY$ potential transition | $\tilde{V}_{\Lambda\Lambda,\Lambda\Lambda}$ | $\tilde{V}_{\Lambda\Lambda,\Lambda\Sigma}$ | $\tilde{V}_{\Lambda\Lambda,\Sigma\Sigma}$ | $\tilde{V}_{\Lambda\Sigma,\Lambda\Sigma}$ | $\tilde{V}_{\Lambda\Sigma,\Sigma\Sigma}$ | $\tilde{V}_{\Sigma\Sigma,\Sigma\Sigma}$ | $\tilde{V}_{\Lambda\Lambda,N\Xi}$ | $\tilde{V}_{\Lambda\Sigma,N\Xi}$ | $\tilde{V}_{\Sigma\Sigma,N\Xi}$ | $\tilde{V}_{N\Xi,N\Xi}$ |
|---|---|---|---|---|---|---|---|---|---|---|
| $\Lambda\Lambda \to \Lambda\Lambda$ | 1 | - | - | - | - | - | - | - | - | - |
| $\Lambda\Lambda \to \Lambda\Sigma$ | - | 1 | - | - | - | - | - | - | - | - |
| $\Lambda\Lambda \to \Sigma\Sigma$ | - | - | 1 | - | - | - | - | - | - | - |
| $\Lambda\Sigma \to \Lambda\Sigma$ | - | - | - | 1 | - | - | - | - | - | - |
| $\Lambda\Sigma \to \Sigma\Sigma$ | - | - | - | - | 1 | - | - | - | - | - |
| $\Sigma\Sigma \to \Sigma\Sigma$ | - | - | - | - | - | 1 | - | - | - | - |
| $\Lambda\Lambda \to N\Xi$ | - | - | - | - | - | - | $\sqrt{A-1}$ | - | - | - |
| $\Lambda\Sigma \to N\Xi$ | - | - | - | - | - | - | - | $\sqrt{A-1}$ | - | - |
| $\Sigma\Sigma \to N\Xi$ | - | - | - | - | - | - | - | - | $\sqrt{A-1}$ | - |
| $N\Xi \to N\Xi$ | - | - | - | - | - | - | - | - | - | $A-1$ |

Table A.2: Combinatorial factors of the two-body $YY$ interactions embedded in the $A$-body space with trangeness $S = -2$.

## A.3 Four-body Schrödinger equation

To justify Table A.1, A.2, we also provide the symmetric Schrödinger equation for four-body basis states with $S = -2$. Based on the four-body Schrödinger equation, one can quickly determine the corresponding combinatorial factors and then compare with the ones listed in the tables. Since the kinetic operator is gain diagonal in the considered basis, we will focus on the potential matrix elements. The four-body basis states and their completeness relation are

$$|\{p_1 p_2 p_3 p_4\}\rangle \equiv a_{p_1}^\dagger a_{p_2}^\dagger a_{p_3}^\dagger a_{p_4}^\dagger |0\rangle; \qquad \sum_{p_1<p_2<p_3<p_4} |\{p_1 p_2 p_3 p_4\}\rangle\langle\{p_1 p_2 p_3 p_4\}| = \mathbb{1}. \qquad \text{(A.34)}$$

In the basis Eq. (A.34), the potential matrix elements becomes

$$\langle\{p_1' p_2' p_3' p_3'\}|V|\{p_1 p_2 p_3 p_4\}\rangle =$$
$$2\{V_{p_1'p_2',p_1p_2}\delta_{p_3'p_3}\delta_{p_4'p_4} + V_{p_1'p_2',p_1p_4}\delta_{p_3'p_2}\delta_{p_4'p_3} + V_{p_1'p_2',p_2p_3}\delta_{p_3'p_1}\delta_{p_4'p_4}$$
$$+ V_{p_1'p_2',p_3p_1}\delta_{p_3'p_2}\delta_{p_4'p_4} + V_{p_1'p_2',p_3p_4}\delta_{p_3'p_1}\delta_{p_4'p_2} + V_{p_1'p_2',p_4p_2}\delta_{p_3'p_1}\delta_{p_4'p_3}$$
$$+ V_{p_4'p_1',p_1p_2}\delta_{p_3'p_3}\delta_{p_2'p_4} + V_{p_4'p_1',p_1p_4}\delta_{p_2'p_3}\delta_{p_3'p_2} + V_{p_4'p_1',p_2p_3}\delta_{p_2'p_4}\delta_{p_3'p_1}$$
$$+ V_{p_4'p_1',p_3p_1}\delta_{p_2'p_4}\delta_{p_3'p_2} + V_{p_4'p_1',p_3p_4}\delta_{p_2'p_2}\delta_{p_3'p_1} + V_{p_4'p_1',p_4p_2}\delta_{p_3'p_1}\delta_{p_2'p_3}$$
$$+ V_{p_3'p_1',p_1p_2}\delta_{p_2'p_3}\delta_{p_4'p_4} + V_{p_3'p_1',p_1p_4}\delta_{p_2'p_2}\delta_{p_4'p_3} + V_{p_3'p_1p_2p_3}\delta_{p_2'p_1}\delta_{p_4'p_4}$$
$$+ V_{p_3'p_1',p_3p_1}\delta_{p_2'p_2}\delta_{p_4'p_4} + V_{p_3'p_1',p_3p_4}\delta_{p_2'p_1}\delta_{p_4'p_2} + V_{p_3'p_1',p_4p_2}\delta_{p_2'p_1}\delta_{p_4'p_3}$$
$$+ V_{p_3'p_4',p_4p_2}\delta_{p_1'p_1}\delta_{p_2'p_3} + V_{p_3'p_4',p_3p_4}\delta_{p_1'p_1}\delta_{p_2'p_2} + V_{p_3'p_4',p_1p_4}\delta_{p_1'p_2}\delta_{p_2'p_3}$$
$$+ V_{p_3'p_4',p_1p_2}\delta_{p_2'p_4}\delta_{p_1'p_3} + V_{p_3'p_4',p_3p_1}\delta_{p_1'p_2}\delta_{p_2'p_4} + V_{p_3'p_4',p_2p_3}\delta_{p_1'p_1}\delta_{p_2'p_4}$$
$$+ V_{p_2'p_3',p_1p_4}\delta_{p_4'p_3}\delta_{p_1'p_2} + V_{p_2'p_3',p_4p_2}\delta_{p_1'p_1}\delta_{p_4'p_3} + V_{p_2'p_3',p_1p_2}\delta_{p_1'p_3}\delta_{p_4'p_4}$$
$$+ V_{p_2'p_3',p_3p_1}\delta_{p_4'p_4}\delta_{p_1'p_2} + V_{p_2'p_3'p_2p_3}\delta_{p_1'p_1}\delta_{p_4'p_4} + V_{p_2'p_3'p_3p_4}\delta_{p_4'p_2}\delta_{p_1'p_1}$$
$$+ V_{p_4'p_2'p_2p_3}\delta_{p_3'p_4}\delta_{p_1'p_1} + V_{p_4'p_2'p_3p_1}\delta_{p_1'p_2}\delta_{p_3'p_4} + V_{p_4'p_2',p_1p_2}\delta_{p_1'p_3}\delta_{p_3'p_4}$$
$$+ V_{p_4'p_2',p_3p_4}\delta_{p_3'p_2}\delta_{p_1'p_1} + V_{p_4'p_2',p_4p_2}\delta_{p_3'p_3}\delta_{p_1'p_1} + V_{p_4'p_2',p_1p_4}\delta_{p_1'p_2}\delta_{p_3'p_3} \qquad \text{(A.35)}$$
$$+ V_{p_2'p_1',p_1p_2}\delta_{p_3'p_4}\delta_{p_4'p_3} + V_{p_2'p_1',p_1p_4}\delta_{p_3'p_3}\delta_{p_4'p_2} + V_{p_2'p_1',p_2p_3}\delta_{p_3'p_4}\delta_{p_4'p_1}$$
$$+ V_{p_2',p_1'p_3p_1}\delta_{p_3'p_4}\delta_{p_4'p_2} + V_{p_2'p_1',p_3p_4}\delta_{p_3'p_2}\delta_{p_4'p_1} + V_{p_2'p_1',p_4p_2}\delta_{p_3'p_3}\delta_{p_4'p_1}$$
$$+ V_{p_1'p_4',p_1p_2}\delta_{p_3'p_4}\delta_{p_2'p_3} + V_{p_1'p_4',p_1p_4}\delta_{p_2'p_2}\delta_{p_3'p_3} + V_{p_1'p_4',p_2p_3}\delta_{p_2'p_1}\delta_{p_3'p_4}$$
$$+ V_{p_1'p_4',p_3p_1}\delta_{p_2'p_2}\delta_{p_3'p_4} + V_{p_1'p_4',p_3p_4}\delta_{p_2'p_1}\delta_{p_3'p_2} + V_{p_1'p_4',p_4p_2}\delta_{p_3'p_3}\delta_{p_2'p_1}$$
$$+ V_{p_1'p_3',p_1p_2}\delta_{p_2'p_4}\delta_{p_4'p_3} + V_{p_1'p_3',p_1p_4}\delta_{p_2'p_3}\delta_{p_4'p_2} + V_{p_1'p_3'p_2p_3}\delta_{p_2'p_4}\delta_{p_4'p_1}$$
$$+ V_{p_1'p_3'p_3p_1}\delta_{p_2'p_4}\delta_{p_4'p_2} + V_{p_1'p_3'p_3p_4}\delta_{p_2'p_2}\delta_{p_4'p_1} + V_{p_1'p_3'p_4p_2}\delta_{p_2'p_3}\delta_{p_4'p_1}$$
$$+ V_{p_4'p_3'p_4p_2}\delta_{p_1'p_3}\delta_{p_2'p_1} + V_{p_4'p_3'p_3p_4}\delta_{p_1'p_2}\delta_{p_2'p_1} + V_{p_4'p_3'p_1p_4}\delta_{p_1'p_3}\delta_{p_2'p_2}$$
$$+ V_{p_4'p_3'p_1p_2}\delta_{p_2'p_3}\delta_{p_1'p_4} + V_{p_4'p_3',p_3p_1}\delta_{p_1'p_4}\delta_{p_2'p_2} + V_{p_4'p_3',p_2p_3}\delta_{p_1'p_4}\delta_{p_2'p_1}$$
$$+ V_{p_3'p_2',p_1p_4}\delta_{p_4'p_2}\delta_{p_1'p_3} + V_{p_3'p_2'p_4p_2}\delta_{p_1'p_3}\delta_{p_4'p_1} + V_{p_3'p_2',p_1p_2}\delta_{p_1'p_4}\delta_{p_4'p_3}$$
$$+ V_{p_3'p_2',p_3p_1}\delta_{p_4'p_2}\delta_{p_1'p_4} + V_{p_3'p_2',p_2p_3}\delta_{p_1'p_4}\delta_{p_4'p_1} + V_{p_3'p_2',p_3p_4}\delta_{p_4'p_1}\delta_{p_1'p_2}$$
$$+ V_{p_2'p_4',p_2p_3}\delta_{p_3'p_1}\delta_{p_1'p_4} + V_{p_2'p_4',p_3p_1}\delta_{p_1'p_4}\delta_{p_3'p_2} + V_{p_2'p_4',p_1p_2}\delta_{p_1'p_4}\delta_{p_3'p_3}$$
$$+ V_{p_2'p_4',p_3p_4}\delta_{p_3'p_1}\delta_{p_1'p_2} + V_{p_2'p_4',p_4p_2}\delta_{p_3'p_1}\delta_{p_1'p_3} + V_{p_2'p_4',p_1p_4}\delta_{p_1'p_3}\delta_{p_3'p_2}\},$$

which is a summation of total 72 two-body potential matrix elements[1]. In order to obtain the Schrödinger equation, we again project the equation Eq. (A.8) onto the state $|\{p_1' p_2' p_3' p_4'\}\rangle$, assuming $p_1' < p_2' < p_3' < p_4'$. Among the terms in Eq. (A.35), only the first 36 terms then contribute to the final Hamiltonian, the remaining 36 terms vanish because of the particle orderings. Furthermore, similar to the case of the 3-body basis, here every 6 of the first 36 terms in Eq. (A.35) can be combined together by renaming particles and using the antisymmetry of the potential. For example, the first 6 terms yields

$$
\sum_{p_1 < p_2 < p_3 < p_4} 2\{ V_{p_1' p_2', p_1 p_2} \delta_{p_3' p_3} \delta_{p_4' p_4} + V_{p_1' p_2', p_1 p_4} \delta_{p_3' p_2} \delta_{p_4' p_3} \underset{\substack{p_4 \leftrightarrow p_2 \\ p_3 \leftrightarrow p_4}}{} + V_{p_1' p_2', p_2 p_3} \delta_{p_3' p_1} \delta_{p_4' p_4} \underset{\substack{p_1 \leftrightarrow p_3 \\ p_1 \leftrightarrow p_2}}{}
$$

$$
+ V_{p_1' p_2' p_3 p_1} \delta_{p_3' p_2} \delta_{p_4' p_4} \underset{p_2 \leftrightarrow p_3}{} + V_{p_1' p_2', p_3 p_4} \delta_{p_3' p_1} \delta_{p_4' p_2} \underset{\substack{p_1 \leftrightarrow p_3 \\ p_2 \leftrightarrow p_4}}{} + V_{p_1' p_2', p_4 p_2} \delta_{p_3' p_1} \delta_{p_4' p_3} \underset{\substack{p_1 \leftrightarrow p_3 \\ p_4 \leftrightarrow p_1 \\ p_1 \leftrightarrow p_2}}{} \} \Psi(p_1 p_2 p_3 p_4)
$$

$$
= \sum_{p_1 < p_2 < p_3 < p_4} 2 V_{p_1' p_2', p_1 p_2} \delta_{p_3' p_3} \delta_{p_4' p_4} \Psi(p_1 p_2 p_3 p_4) + \sum_{p_1 < p_3 < p_4 < p_2} 2 V_{p_1' p_2', p_1 p_2} \delta_{p_3' p_3} \delta_{p_4' p_4} \Psi(p_1 p_3 p_4 p_2)
$$

$$
+ \sum_{p_3 < p_1 < p_2 < p_4} 2 V_{p_1' p_2', p_1 p_2} \delta_{p_3' p_3} \delta_{p_4' p_4} \Psi(p_3 p_1 p_2 p_4) + \sum_{p_1 < p_3 < p_2 < p_4} 2 V_{p_1' p_2', p_2 p_1} \delta_{p_3' p_3} \delta_{p_4' p_4} \Psi(p_1 p_3 p_2 p_4)
$$

$$
+ \sum_{p_3 < p_4 < p_1 < p_2} 2 V_{p_1' p_2', p_1 p_2} \delta_{p_3' p_3} \delta_{p_4' p_4} \Psi(p_3 p_4 p_1 p_2) + \sum_{p_3 < p_1 < p_4 < p_2} 2 V_{p_1' p_2', p_2 p_1} \delta_{p_3' p_3} \delta_{p_4' p_4} \Psi(p_3 p_1 p_4 p_2)
$$

$$
= \sum_{p_1 < p_2 < p_3 < p_4} 2 V_{p_1' p_2', p_1 p_2} \delta_{p_3' p_3} \delta_{p_4' p_4} \Psi(p_1 p_2 p_3 p_4) + \sum_{p_1 < p_3 < p_4 < p_2} 2 V_{p_1' p_2', p_1 p_2} \delta_{p_3' p_3} \delta_{p_4' p_4} \Psi(p_1 p_2 p_3 p_4)
$$

$$
+ \sum_{p_3 < p_1 < p_2 < p_4} 2 V_{p_1' p_2', p_1 p_2} \delta_{p_3' p_3} \delta_{p_4' p_4} \Psi(p_3 p_1 p_2 p_4) + \sum_{p_1 < p_3 < p_2 < p_4} 2 V_{p_1' p_2', p_2 p_1} \delta_{p_3' p_3} \delta_{p_4' p_4} \Psi(p_1 p_3 p_2 p_4)
$$

$$
+ \sum_{p_3 < p_4 < p_1 < p_2} 2 V_{p_1' p_2', p_1 p_2} \delta_{p_3' p_3} \delta_{p_4' p_4} \Psi(p_1 p_2 p_3 p_4) + \sum_{p_3 < p_1 < p_4 < p_2} 2 V_{p_1' p_2', p_1 p_2} \delta_{p_3' p_3} \delta_{p_4' p_4} \Psi(p_1 p_2 p_3 p_4)
$$

$$
= \sum_{p_1 < p_2} 2 V_{p_1' p_2', p_1 p_2} \sum_{p_3 < p_4} \delta_{p_3' p_3} \delta_{p_4' p_4} \Psi(p_1 p_2 p_3 p_4)
$$

$$
= \sum_{p_1 < p_2} 2 V_{p_1' p_2', p_1 p_2} \Psi(p_1 p_2 p_3' p_4').
$$

$$(A.36)$$

---

[1] In general, the total number of two-body potential matrix elements contributing to the many-body potential matrix elements in an $A$-body basis is given by $\left[\frac{A(A-1)}{2!}\right]^2 (A-2)!$.

Hence, the Schrödinger equation in the four-body basis Eq. (A.34) becomes

$$
\begin{aligned}
(t_{p'_1} + t_{p'_2} &+ t_{p'_3} + t_{p'_4})\Psi(p'_1 p'_2 p'_3 p'_4) \\
&+ \sum_{p_1 < p_2} 2V_{p'_1 p'_2, p_1 p_2}\Psi(p_1 p_2 p'_3 p'_4) + \sum_{p_1 < p_3} 2V_{p'_1 p'_3, p_1 p_3}\Psi(p_1 p'_2 p_3 p'_4) \\
&+ \sum_{p_1 < p_4} 2V_{p'_1 p'_4, p_1 p_4}\Psi(p_1 p'_2 p'_3 p_4) + \sum_{p_2 < p_3} 2V_{p'_2 p'_3, p_2 p_3}\Psi(p'_1 p_2 p_3 p'_4) \\
&+ \sum_{p_2 < p_4} 2V_{p'_2 p'_4, p_2 p_4}\Psi(p'_1 p_2 p'_3 p_4) + \sum_{p_3 < p_4} 2V_{p'_3 p'_4, p_3 p_4}\Psi(p'_1 p'_2 p_3 p_4) \\
&= E\Psi(p'_1 p'_2 p'_3 p'_4).
\end{aligned}
\tag{A.37}
$$

Let us consider an explicit basis consisting of four states, $|\{NN\Lambda\Lambda\}\rangle$, $|\{NN\Sigma\Sigma\}\rangle$, $|\{NN\Lambda\Sigma\}\rangle$ and $|\{NNN\Xi\}\rangle$. In this basis, the norm of the wavefunction $|\Psi\rangle$ can be expressed as

$$
\begin{aligned}
\langle\Psi|\Psi\rangle &= \int d^3\tilde{p}_1 d^3\tilde{p}_2 |\tfrac{1}{2}\Psi_{NN\Lambda\Lambda}(\tilde{p}_1\tilde{p}_2)|^2 + \int d^3\tilde{p}_1 d^3\tilde{p}_2 |\tfrac{1}{2}\Psi_{NN\Sigma\Sigma}(\tilde{p}_1\tilde{p}_2)|^2 + \\
&\int d^3\tilde{p}_1 d^3\tilde{p}_2 |\tfrac{1}{\sqrt{2}}\Psi_{NN\Lambda\Sigma}(\tilde{p}_1\tilde{p}_2)|^2 + \int d^3\tilde{p}_1 d^3\tilde{p}_2 |\tfrac{1}{\sqrt{6}}\Psi_{NNN\Xi}(\tilde{p}_1\tilde{p}_2)|^2.
\end{aligned}
\tag{A.38}
$$

The normalization in Eq. (A.38) leads to the introduction of a new set of the wavefunction components

$$
\begin{aligned}
\Phi_{NN\Lambda\Lambda} &= \frac{1}{2}\Psi_{NN\Lambda\Lambda}, \qquad \Phi_{NN\Sigma\Sigma} = \frac{1}{2}\Psi_{NN\Sigma\Sigma}, \\
\Phi_{NN\Lambda\Sigma} &= \frac{1}{\sqrt{2}}\Psi_{NN\Lambda\Sigma}, \qquad \Phi_{NNN\Xi} = \frac{1}{\sqrt{6}}\Psi_{NNN\Xi}.
\end{aligned}
\tag{A.39}
$$

Applying the coupled Schrödinger the equation Eq. (A.37) to these components yields

$$
(T + V)\begin{pmatrix} \Phi_{NN\Lambda\Lambda} \\ \Phi_{NN\Sigma\Sigma} \\ \Phi_{NN\Lambda\Sigma} \\ \Phi_{NNN\Xi} \end{pmatrix} = E\begin{pmatrix} \Phi_{NN\Lambda\Lambda} \\ \Phi_{NN\Sigma\Sigma} \\ \Phi_{NN\Lambda\Sigma} \\ \Phi_{NNN\Xi} \end{pmatrix},
\tag{A.40}
$$

with the kinetic matrix being diagonal

$$
T = \begin{pmatrix} 2t_N + 2t_\Lambda & 0 & 0 & 0 \\ 0 & 2t_N + 2t_\Sigma & 0 & 0 \\ 0 & 0 & 2t_N + t_\Sigma + t_\Sigma & 0 \\ 0 & 0 & 0 & 3t_N + t_\Xi \end{pmatrix},
\tag{A.41}
$$

and the potential matrix $V$ given in Eq. (A.42). It is now straightforwardly to verify that the combinatorial factors read off from the Hamiltonian Eq. (A.42) are exactly the same as those tabulated in Table A.1,A.2

$$V = \begin{pmatrix} \tilde{V}_{NN,NN} + 4\tilde{V}_{NA,NA} + \tilde{V}_{AA,AA} & \tilde{V}_{AA,\Sigma\Sigma} & \tilde{V}_{AA,A\Sigma} + 2\sqrt{2}\tilde{V}_{NA,N\Sigma} & \sqrt{3}\tilde{V}_{AA,N\Xi} \\ \tilde{V}_{\Sigma\Sigma,AA} & \tilde{V}_{NN,NN} + 4\tilde{V}_{N\Sigma,N\Sigma} + \tilde{V}_{\Sigma\Sigma,\Sigma\Sigma} & \tilde{V}_{\Sigma\Sigma,A\Sigma} + 2\sqrt{2}\tilde{V}_{N\Sigma,NA} & \sqrt{3}\tilde{V}_{\Sigma\Sigma,N\Xi} \\ \tilde{V}_{A\Sigma,AA} + 2\sqrt{2}\tilde{V}_{N\Sigma,NA} & \tilde{V}_{A\Sigma,\Sigma\Sigma} + 2\sqrt{2}\tilde{V}_{NA,N\Sigma} & V_{NN,NN} + 2\tilde{V}_{NA,NA} + 2V_{N\Sigma,N\Sigma} + \tilde{V}_{A\Sigma,A\Sigma} & \sqrt{3}\tilde{V}_{A\Sigma,N\Xi} \\ \sqrt{3}\tilde{V}_{N\Xi,AA} & \sqrt{3}V_{N\Xi,\Sigma\Sigma} & \sqrt{3}V_{N\Xi,A\Sigma} & 3\tilde{V}_{NN,NN} + 3\tilde{V}_{N\Xi,N\Xi} \end{pmatrix} . \tag{A.42}$$

# Momentum distribution and correlation functions

In this appendix, we derive the final expressions for the one-body nucleon distribution and two-body NN correlation functions in hypernuclei using Jacobi bases. The hyperon distribution and YN correlation functions are then obtained analogously.

## B.1 One-body nucleon distribution functions

Before evaluating the nucleon density function,

$$\mathcal{D}_N(\mathbf{p}) = \langle\Psi|\delta(\mathbf{p} - \mathbf{p}_N)P_N|\Psi\rangle, \qquad P_N = |tm_t\rangle_{NN}\langle tm_t|, \tag{B.1}$$

let us first summarize some relations between single-particle basis states in different representations, which will be employed for the evaluation. In momentum representation, single particle states are denoted as $|\mathbf{p}\rangle$. These states are related to the basis states in angular momentum representation specified by momentum $p'$, the orbital angular momentum $l$ and magnetic quantum number $m$, $|p'lm\rangle$, by

$$\langle\mathbf{p}|p'lm\rangle = \frac{\delta(p - p')}{pp'}Y_{lm}(\hat{p}). \tag{B.2}$$

Instead of momentum $p'$, one can also employ a set of the energy quantum number $n$ together with the orbital angular momentum $lm$, $|nlm\rangle$, to define single-particle (HO) basis states in the angular momentum representation. Similar to Eq. (B.2), one can also write

$$\langle\mathbf{p}|nlm\rangle = R_{nl}(p)Y_{lm}(\hat{p}), \tag{B.3}$$

and

$$\langle pl'm'|nlm\rangle = \delta_{ll'}\delta_{mm'}R_{nl}(p). \tag{B.4}$$

In the basis $|p'lm\rangle$, the Kronecker delta operator $\delta(\mathbf{p} - \mathbf{p}_N)$ can be easily evaluated

$$
\begin{aligned}
\langle p'lm|\delta(\mathbf{p} - \mathbf{p}_N)|p''l''m''\rangle &= \int d^3p_1 d^3p_2 \langle p'lm|\mathbf{p}_1\rangle\langle\mathbf{p}_1|\delta(\mathbf{p} - \mathbf{p}_N)|\mathbf{p}_2\rangle\langle\mathbf{p}_2|p''l''m''\rangle \\
&= \int d^3p_1 d^3p_2 \frac{\delta(p' - p_1)}{p'p_1} \frac{\delta(p'' - p_2)}{p''p_2} \langle\mathbf{p}_1|\delta(\mathbf{p} - \mathbf{p}_N)|\mathbf{p}_2\rangle Y_{lm}^*(\hat{p}_1)Y_{l''m''}(\hat{p}_2) \\
&= \int d^3p_1 d^3p_2 \frac{\delta(p' - p_1)}{p'p_1} \frac{\delta(p'' - p_2)}{p''p_2} \delta(\mathbf{p}_1 - \mathbf{p})\delta(\mathbf{p}_1 - \mathbf{p}_2)Y_{lm}^*(\hat{p}_1)Y_{l''m''}(\hat{p}_2) \\
&= Y_{lm}^*(\hat{p})Y_{l''m''}(\hat{p}) \frac{\delta(p' - p)}{p'p} \frac{\delta(p'' - p)}{p''p}.
\end{aligned}
$$
(B.5)

We now come back to the evaluation of Eq. (B.1). Remember that our wavefunctions $|\Psi\rangle$ are expanded in the NCSM basis $|\alpha^{*(Y)}\rangle$ ( see Eq. (3.2)),

$$
\begin{aligned}
|\Psi\rangle &= \sum_\alpha C_\alpha |\alpha^{*(Y)}\rangle \\
&= \sum_\alpha C_\alpha |\mathcal{N}JT, \alpha_{A-1}\, n_Y I_Y t_Y; (J_{A-1}(l_Y s_Y)I_Y)J, (T_{A-1}t_Y)T\rangle \\
&\equiv \sum_\alpha C_\alpha |\mathbf{\bullet\!-\!\bullet}\rangle.
\end{aligned}
$$
(B.6)

with the coefficients $C_\alpha$ determined from the Lanczos iterations. In order to operate the $\delta(\mathbf{p} - \mathbf{p}_N)$ operator on the states $|\alpha^{*(Y)}\rangle$, one needs to make use of a complete set of auxiliary states $|\beta\rangle$ defined in Eq. (B.7) that single out a nucleon as the outermost spectator,

$$
\begin{aligned}
|\beta\rangle &= |(\alpha^{*(Y)})^{*(1)}\rangle \\
&= |\mathcal{N}JT, \alpha_{A-1}^{*(Y)}\, n_N I_N t_N; (J_{A-1}^{*(Y)}(l_N s_N)I_N)J, (T_{A-1}^{*(Y)}t_N)T\rangle \\
&\equiv |\mathbf{\bullet_\top\!\bullet}\rangle.
\end{aligned}
$$
(B.7)

Note that the transition from $|\alpha^{*(Y)}\rangle$ to $|\beta\rangle$ states is given by Eqs. (3.30) and (3.31). Let us also introduce another set of auxiliary states $|\tilde{\beta}\rangle$ that are very similar to the $|\beta\rangle$ states in Eq. (B.7) but the outer nucleon is characterized by the orbital angular momentum $\tilde{l}_N$ and spin $s_N$ couple to the total angular momentum $\tilde{I}_N$, together with the momentum $p_N$ instead of the energy quantum number $n_N$

$$
|\tilde{\beta}\rangle = |JT, \tilde{\alpha}_{A-1}^{*(Y)}\, p_N \tilde{I}_N t_N; (\tilde{J}_{A-1}^{*(Y)}(\tilde{l}_N s_N)\tilde{I}_N)J, (\tilde{T}_{A-1}^{*(Y)}t_N)T\rangle.
$$
(B.8)

The completeness relation of the auxiliary states $|\tilde{\beta}\rangle$ reads

$$
\begin{aligned}
\sum_{\tilde{\beta}} |\tilde{\beta}\rangle\langle\tilde{\beta}| &= \sum_{\substack{\tilde{\alpha}_{A-1}^{*(Y)} \\ \tilde{l}_N, \tilde{I}_N}} \int dp_N p_N^2 |JT, \tilde{\alpha}_{A-1}^{*(Y)}\, p_N \tilde{I}_N t_N; (\tilde{J}_{A-1}^{*(Y)}(\tilde{l}_N s_N)\tilde{I}_N)J, (\tilde{T}_{A-1}^{*(Y)}t_N)T\rangle \\
&\qquad \langle JT, \tilde{\alpha}_{A-1}^{*(Y)}\, p_N \tilde{I}_N t_N; (\tilde{J}_{A-1}^{*(Y)}(\tilde{l}_N s_N)\tilde{I}_N)J, (\tilde{T}_{A-1}^{*(Y)}t_N)T| = \mathbb{1}.
\end{aligned}
$$
(B.9)

With the help of Eq. (B.3), the overlap between the two states $|\beta\rangle$ and $|\tilde{\beta}\rangle$ can be expressed as

$$\langle\beta|\tilde{\beta}\rangle = \delta_{\alpha^{*(Y)}_{A-1}\tilde{\alpha}^{*(Y)}_{A-1}}\delta_{I_N\tilde{I}_N}\delta_{l_N\tilde{l}_N}R_{n_N l_N}(p_N), \tag{B.10}$$

where the Kronecker symbol $\delta_{\alpha^{*(Y)}_{A-1}\tilde{\alpha}^{*(Y)}_{A-1}}$ imposes the equality of all quantum numbers charactering the $|\alpha^{*(Y)}_{A-1}\rangle$, and $|\tilde{\alpha}^{*(Y)}_{A-1}\rangle$ states, namely the total energy quantum nuber $\mathcal{N}_{A-1}$, angular momentum $J_{A-1}$, isospin $T_{A-1}$ as well as the state index. Now plugging Eq. (B.6) into Eq. (B.1) and then exploiting the completeness relations for $|\beta\rangle$ and $|\tilde{\beta}\rangle$, one has

$$D_N(\mathbf{p}) = \sum_{\alpha\alpha'}\sum_{\beta\beta'}\sum_{\tilde{\beta}\tilde{\beta}'}C_\alpha C_{\alpha'}\langle\alpha^{*(Y)}|\beta\rangle\langle\beta|\tilde{\beta}\rangle\langle\tilde{\beta}|\delta(\mathbf{p}-\mathbf{p}_N)P_N|\tilde{\beta}'\rangle\langle\tilde{\beta}'|\beta'\rangle\langle\beta'|\alpha'^{*(Y)}\rangle \tag{B.11}$$

We are now left to evaluate the remaining term $\langle\tilde{\beta}|\delta(\mathbf{p}-\mathbf{p}_N)P_N|\tilde{\beta}'\rangle$ in Eq. (B.11). For this, one first needs to decouple the orbital angular momentum of the outer nucleon $\tilde{l}_N$ from the total angular momentum $J$ and its isospin $t_N, m_{t_N}$ from the total isospin $T$, and then employ the relation Eq. (B.5)

$$\langle\tilde{\beta}|\delta(\mathbf{p}-\mathbf{p}_N)P_N|\tilde{\beta}'\rangle = \langle\tilde{\alpha}^{*(Y)}_{A-1}\,p_N\tilde{I}_N t_N; (\tilde{J}^{*(Y)}_{A-1}(\tilde{l}_N s_N)\tilde{I}_N)J, (\tilde{T}^{*(Y)}_{A-1}t_N)T|\delta(\mathbf{p}-\mathbf{p}_N)P_N|$$

$$\tilde{\alpha}'^{*(Y)}_{A-1}\,p'_N\tilde{I}'_N t_N; (\tilde{J}'^{*(Y)}_{A-1}(\tilde{l}'_N s_N)\tilde{I}'_N)J, (\tilde{T}'^{*(Y)}_{A-1}t_N)T\rangle$$

$$= \sum_{\substack{m_{\tilde{I}_N},m_{\tilde{I}'_N}\\ m_{\tilde{l}_N},m_{\tilde{l}'_N}}}\delta_{\alpha^{*(Y)}_{A-1}\tilde{\alpha}^{*(Y)}_{A-1}}(\tilde{T}^{*(Y)}_{A-1}\,t_N\,T, m_T-m_{t_N}m_{t_N}m_T)^2$$

$$\times(\tilde{J}^{*(Y)}_{A-1}\tilde{I}_N J, m_J-m_{\tilde{I}_N}m_{\tilde{I}_N}m_J)(\tilde{l}_N s_N\tilde{I}_N, m_{\tilde{l}_N}m_{\tilde{I}_N}-m_{\tilde{l}_N}m_{\tilde{I}_N})$$

$$\times(\tilde{J}'^{*(Y)}_{A-1}\tilde{I}'_N J, m_J-m_{\tilde{I}'_N}m_{\tilde{I}'_N}m_J)(\tilde{l}'_N s_N\tilde{I}'_N, m_{\tilde{l}'_N}m_{\tilde{I}'_N}-m_{\tilde{l}'_N}m_{\tilde{I}'_N})$$

$$\times\langle p_N\tilde{l}_N m_{\tilde{l}_N}|\delta(\mathbf{p}-\mathbf{p}_N)|p'_N\tilde{l}'_N m_{\tilde{l}'_N}\rangle \tag{B.12}$$

$$= \sum_{\substack{m_{\tilde{I}_N}\\ m_{\tilde{l}_N},m_{\tilde{l}'_N}}}\delta_{\tilde{\alpha}^{*(Y)}_{A-1}\tilde{\alpha}'^{*(Y)}_{A-1}}(\tilde{T}^{*(Y)}_{A-1}\,t_N\,T, m_T-m_{t_N}m_{t_N}m_T)^2$$

$$\times Y_{\tilde{l}_N m_{\tilde{l}_N}}(\hat{p})\,Y^\star_{\tilde{l}'_N m_{\tilde{l}_N}}(\hat{p})\frac{\delta(p_N-p)}{p_N p}\frac{\delta(p'_N-p)}{p'_N p}$$

$$\times(\tilde{J}^{*(Y)}_{A-1}\tilde{I}_N J, m_J-m_{\tilde{I}_N}m_{\tilde{I}_N}m_J)(\tilde{J}^{*(Y)}_{A-1}\tilde{I}'_N J, m_J-m_{\tilde{I}_N}m_{\tilde{I}_N}m_J)$$

$$\times(\tilde{l}_N s_N\tilde{I}_N, m_{\tilde{l}_N}m_{\tilde{I}_N}-m_{\tilde{l}_N}m_{\tilde{I}_N})(\tilde{l}'_N s_N\tilde{I}'_N, m_{\tilde{l}'_N}m_{\tilde{I}_N}-m_{\tilde{l}'_N}m_{\tilde{I}_N}).$$

Now plugging Eqs. (B.10) and (B.12) into Eq. (B.11), one obtains the final expression for the nucleon momentum distribution $D_N(\mathbf{p})$

$$
\begin{aligned}
D_N(\mathbf{p}) = \sum_{\alpha\alpha'}\sum_{\beta\beta'} C_\alpha C_{\alpha'}\, \delta_{\alpha^{*(Y)}_{A-1}\alpha'^{*(Y)}_{A-1}} \langle\alpha^{*(Y)}|\beta\rangle\langle\beta'|\alpha'^{*(Y)}\rangle \\
\times (T^{*(Y)}_{A-1}\, t_N\, T, m_T - m_{t_N} m_{t_N} m_T)^2 R_{n_N l_N}(p) R_{n'_N l'_N}(p) \\
\times \sum_{\substack{m_{I_N}\\ m_{l_N}, m_{l'_N}}} Y_{l_N m_{l_N}}(\hat{p}) Y^{\star}_{l'_N m_{l'_N}}(\hat{p}) \\
\times (J^{*(Y)}_{A-1} I_N J, m_J - m_{I_N} m_{I_N} m_J)(J^{*(Y)}_{A-1} I'_N J, m_J - m_{I_N} m_{I_N} m_J) \\
\times (l_N s_N I_N, m_{l_N} m_{I_N} - m_{l_N} m_{I_N})(l'_N s_N I'_N, m_{l'_N} m_{I_N} - m_{l'_N} m_{I_N}).
\end{aligned}
\tag{B.13}
$$

Likewise, an explicit expression for the hyperon momentum distribution function can be easily derived

$$
D_Y(\mathbf{p}) = \langle\Psi|\delta(\mathbf{p} - \mathbf{p}_Y)P_Y|\Psi\rangle, \quad \text{with} \quad P_Y = |tm_t\rangle_{YY}\langle tm_t|
\tag{B.14}
$$

Note that, the evaluation of $\mathcal{D}_Y(\mathbf{p})$ does not require any intermediate states because, by construction, the hyperon is already the outermost particle in our basis state $|\alpha^{*(Y)}\rangle$ (see Eq. (B.6)). Hence, the summations over $\beta$ and $\beta'$ are left out. One finally gets,

$$
\begin{aligned}
D_Y(\mathbf{p}) = \sum_{\alpha\alpha'} C_\alpha C_{\alpha'}\, \delta_{\alpha_{A-1}\alpha'_{A-1}} R_{n_Y l_Y}(p) R_{n'_Y l'_Y}(p) \\
\times (T_{A-1}\, t_Y\, T, m_T - m_{t_Y} m_{t_Y} m_T)^2 \\
\times \sum_{\substack{m_{I_Y}\\ m_{l_Y}, m_{l'_Y}}} Y_{l_Y m_{l_Y}}(\hat{p}) Y^{\star}_{l'_Y m_{l'_Y}}(\hat{p}) \\
\times (J_{A-1} I_Y J, m_J - m_{I_Y} m_{I_Y} m_J)(J_{A-1} I'_Y J, m_J - m_{I_Y} m_{I_Y} m_J) \\
\times (l_Y s_Y I_Y, m_{l_Y} m_{I_Y} - m_{l_Y} m_{I_Y})(l'_Y s_Y I'_Y, m_{l'_Y} m_{I_Y} - m_{l'_Y} m_{I_Y}).
\end{aligned}
\tag{B.15}
$$

## B.2  NN correlation function in momentum space

Intuitively, in order to evaluate the nucleon-nucleon correlation function

$$
\begin{aligned}
C_{NN}(\mathbf{p}) &= \langle\Psi|\delta(\mathbf{p} - \mathbf{p}_{NN})|\Psi\rangle \\
&= \sum_{\alpha,\alpha'} C_\alpha C_{\alpha'} \langle\alpha^{*(Y)}|\delta(\mathbf{p} - \mathbf{p}_{NN})|\alpha^{*(Y)}\rangle \\
&\equiv \sum_{\alpha,\alpha'} C_\alpha C_{\alpha'} \langle\bigcirc\!\!-\!\!\bullet|\delta(\mathbf{p} - \mathbf{p}_{NN})|\bigcirc\!\!-\!\!\bullet\rangle,
\end{aligned}
\tag{B.16}
$$

one will need to insert a complete set of the intermediate states $|\gamma\rangle = \left|(\alpha^{*(2)})^{*(Y)}\right\rangle$ that single out an NN pair,

$$
\begin{aligned}
\left|(\alpha^{*(2)})^{*(Y)}\right\rangle &= |\mathcal{N}JT, \alpha_{A-1}^{*(2)} \, n_Y(l_Y s_Y)I_Y t_Y; (J_{A-1}^{*(2)}(l_Y s_Y)I_Y)J, (T_{A-1}^{*(2)}t_Y)T\rangle \\
&\equiv \left|\, \vphantom{O} \right\rangle.
\end{aligned} \tag{B.17}
$$

These auxiliary states together with their transition coefficients $\langle \,\circ\!-\!\,\circ\,\rangle$ are already computed in Eqs. (3.9) and (3.11), which are intensively used when computing the Hamiltonian matrix elements in the $S = 0$ sector. Hence, the NN correlation function in Eq. (B.16) can be calculated straightforwardly

$$
\begin{aligned}
C_{NN}(\mathbf{p}) = \sum_{\alpha\alpha'} \sum_{\gamma\gamma'} &C_\alpha C_{\alpha'} \, \delta_{\alpha_{A-3}\alpha'_{A-3}} \, \delta_{YY'} \langle \alpha^{*(Y)}|\gamma\rangle\langle\gamma'|\alpha'^{*(Y)}\rangle \\
&\times R_{n_{NN}l_{NN}}(p) R_{n'_{NN}l'_{NN}}(p) \\
&\times \sum_{\substack{m_{I_{NN}} m_{J_{A-1}^{*(2)}} \\ m_{l_{NN}}, m_{l'_{NN}}}} Y_{l_{NN}m_{l_{NN}}}(\hat{p}) \, Y^\star_{l'_{NN}m_{l'_{NN}}}(\hat{p}) \\
&\times (I_Y J_{A-1}^{*(2)}J, m_J - m_{J_{A-1}^{*(2)}} m_{J_{A-1}^{*(2)}} m_J)(I_Y J_{A-1}^{*(2)\prime}J, m_J - m_{J_{A-1}^{*(2)}} m_{J_{A-1}^{*(2)}} m_J) \\
&\times (J_{A-3} I_{NN} J_{A-1}^{*(2)}, m_{J_{A-1}^{*(2)}} - m_{I_{NN}} m_{I_{NN}} m_{J_{A-1}^{*(2)}}) \\
&\times (J_{A-3} I_{NN} J_{A-1}^{*(2)\prime}, m_{J_{A-1}^{*(2)}} - m_{I_{NN}} m_{I_{NN}} m_{J_{A-1}^{*(2)}}) \\
&\times (l_{NN} s_{NN} I_{NN}, m_{l_{NN}} m_{I_{NN}} - m_{l_{NN}} m_{I_{NN}}) \\
&\times (l'_{NN} s_{NN} I_{NN}, m_{l'_{NN}} m_{I_{NN}} - m_{l'_{NN}} m_{I_{NN}}).
\end{aligned} \tag{B.18}
$$

Likewise, for calculating the YN correlation function

$$
C_{YN}(\mathbf{p}) = \langle \Psi | \delta(\mathbf{p} - \mathbf{p}_{YN}) P_{\tau_Y} | \Psi \rangle, \tag{B.19}
$$

one needs to employ the intermediate states $|\alpha^{*(YN)}\rangle$ which single out a YN pair

$$
\begin{aligned}
|\alpha^{*(YN)}\rangle &= |\mathcal{N}JT, \alpha_{YN}\,\alpha_{A-2}; ((l_{YN}S_{YN})J_{YN}(\lambda J_{A-2})J_{A-1})J, (t_{YN}T_{A-2})T\rangle \\
&\equiv \left|\, \vphantom{O} \right\rangle.
\end{aligned} \tag{B.20}
$$

Again, these intermediate states $|\alpha^{*(YN)}\rangle$ and the corresponding transition coefficients $\langle \alpha^{*(YN)}|\alpha^{*(Y)}\rangle = \langle \,\circ\!-\!\,\circ\,\rangle$ are already computed in Section 3.2.2 when evaluating the Hamiltonian matrix elements

in the $S = -1$ sector. The correlation function Eq. (B.19) finally reads

$$
\begin{aligned}
C_{YN}(\mathbf{p}) = \sum_{\substack{\alpha^{*(Y)}\ \alpha^{*YN} \\ \alpha'^{*(Y)}\ \alpha'^{*(YN)}}} & C_\alpha C_{\alpha'} \, \delta_{\alpha_{A-2}\alpha'_{A-2}} \langle \alpha^{*(Y)} | \alpha^{*(YN)} \rangle \langle \alpha'^{*(YN)} | \alpha'^{*(Y)} \rangle \\
& \times \delta_{t_Y t'_Y} R_{n_{YN} l_{YN}}(p) R_{n'_{YN} l'_{YN}}(p) \\
& \times \sum_{\substack{m_{I_{YN}} \\ m_{l_{YN}}, m_{l'_{YN}}}} Y_{l_{YN} m_{l_{YN}}}(\hat{p}) \, Y^\star_{l'_{YN} m_{l'_{YN}}}(\hat{p}) \\
& \times (J_{A-2} I_{YN} J, m_J - m_{I_{YN}} m_{I_{YN}} m_J)(J_{A-2} I'_{YN} J, m_J - m_{I_{YN}} m_{I_{YN}} m_J) \\
& \times (l_{YN} s_{YN} I_{YN}, m_{l_{YN}} m_{I_{YN}} - m_{l_{YN}} m_{I_{YN}}) \\
& \times (l'_{YN} s_{YN} I'_{YN}, m_{l'_{YN}} m_{I_{YN}} - m_{l'_{YN}} m_{I_{YN}}).
\end{aligned}
\tag{B.21}
$$

Based on the final expressions for the momentum distributions in Eqs. (B.13) and (B.15) and correlations in Eqs. (B.18) and (B.21), one quickly writes down similar formulas for the corresponding distributions $\mathcal{D}(\mathbf{r})$ and $C(\mathbf{r})$ in configuration space. Furthermore, It can be easily shown that the Jacobi coordinates of a nucleon $r_N$ and a hyperon ($r_Y$) are related to the their C.M. coordinates $R_N$ and $R_Y$ via

$$
R_N = \frac{m_N(A-1) + m_Y}{m_N(A-2) + m_Y} r_N,
\tag{B.22}
$$

and

$$
R_Y = \frac{m_N(A-1)}{m_N(A-1) + m_Y} r_Y.
\tag{B.23}
$$

where $m_N$ and $m_Y$ are nucleon and hyperon masses, respectively and $A$ is the total number of particles.

# Jacobi coordinates for an $A$-body system

The relative motions of an $A$-body system can generally be described by a set of $A - 1$ independent Jacobi vectors. Each of such a Jacobi vector represents the displacement of the c. m. of two different subsystems. In general for $A > 2$ there exists more than one set of the Jacobi coordinates which can be assigned to the system. One possible set of the Jacobi coordinates $\mathbf{r}_{12}, \mathbf{r}_3, \cdots, \mathbf{r}_{A-1}, \mathbf{r}_A$ is shown in Fig. C.1. These Jacobi vectors are related to the single-particle coordinates via[1]

$$
\begin{aligned}
\mathbf{r}_{12} &= \mathbf{x}_1 - \mathbf{x}_2, \\
\mathbf{r}_3 &= \mathbf{x}_3 - \frac{m_1\mathbf{x}_1 + m_2\mathbf{x}_2}{m_1 + m_2}, \\
&\vdots \\
\mathbf{r}_A &= \mathbf{x}_A - \frac{\sum_{i=1}^{A-1} \mathbf{x}_i m_i}{\sum_{i=1}^{A-1} m_i},
\end{aligned}
\tag{C.1}
$$

or in momentum space,

$$
\begin{aligned}
\mathbf{p}_{12} &= \frac{m_2}{m_1 + m_2}\mathbf{k}_1 - \frac{m_1}{m_1 + m_2}\mathbf{k}_2, \\
\mathbf{p}_3 &= \frac{m_1 + m_2}{m_1 + m_2 + m_3}\mathbf{k}_3 - \frac{m_3}{m_1 + m_2 + m_3}(\mathbf{k}_1 + \mathbf{k}_2), \\
&\vdots \\
\mathbf{p}_A &= \frac{\sum_{i=1}^{A-1} m_i}{\sum_{i=1}^{A} m_i}\mathbf{k}_A - \frac{m_A}{\sum_{i=1}^{A} m_i}\sum_{i=1}^{A-1}\mathbf{k}_i.
\end{aligned}
\tag{C.2}
$$

In general, different Jacobi-coordinate sets can be conveniently labeled using the Jacobi tree [170], and related to each other via an orthogonal transformation. An example of such a transformation for a 3-body system is shown in Appendix C.1.

---

[1] Note that one may employ different prefactors for the Jacobi coodinates.

$$(\text{C.3})$$
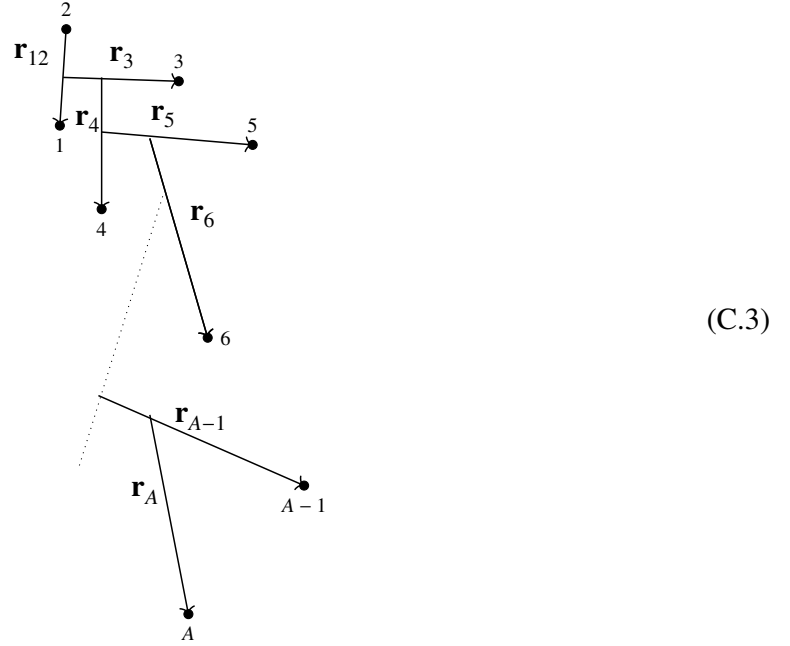
Figure C.1: A possible set of Jacobi coordinates for an *A*-body system

## C.1 Orthogonal transformation between two sets of three-cluster Jacobi coordinates

Generally, for describing a system of three clusters, for example 1,2 and 3, one can use different sets of Jacobi coordinates in which either cluster 1 or 2 or 3 is the outer spectator. These three different sets of intrinsic Jacobi coordinates are illustrated in Fig. C.2
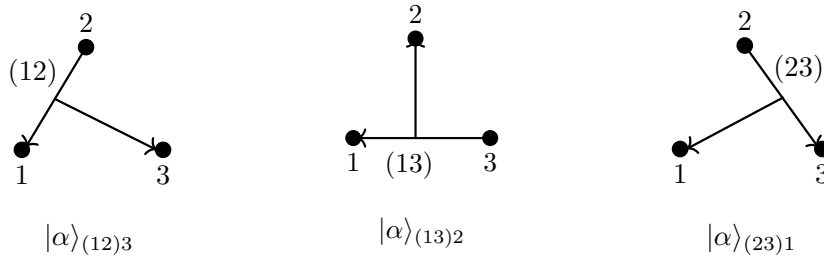


Figure C.2: Three different sets of three-clusters Jacobi coordinates. The left figure depicts a Jacobi set (denoted as $|\alpha\rangle_{(12)3}$), where the third particle is a spectator. The middle figure shows another set ($|\alpha\rangle_{(13)2}$) that singles out particle 2 as a spectator. In the third set (left figure) particle 1 is then an outer spectator, denoted as $|\alpha\rangle_{(23)1}$.

In terms of a single-particle HO basis, each set of Jacobi coordinates in Fig. C.2, for example

$|\alpha\rangle_{(12)3}$, can be expressed as follows

$$|\alpha\rangle_{(12)3} = \left|n_{12}n_3((l_{12}(s_1s_2)S_{12})J_{12}(l_3s_3)I_3)J;((t_1t_2)T_{12}t_3)T\right\rangle, \tag{C.4}$$

where $n_{12}$ and $n_3$ are the HO quantum numbers for the relative motion of clusters (12)and the spectator 3, respectively. $l_{12}$ and $S_{12}$ are the orbital angular momentum and total spin of the pair (12), which couple to the total angular momentum $J_{12}$. The orbital angular momentum of the spectator $l_3$ couples with its spin $s_3$ to the total angular momentum $I_3$. $J_{12}$ and $I_3$ finally couple to the total angular momentum of the system $J$. Similarly, the isospins of the pair couple to $T_{12}$ which combines with the isospin of the spectator particle $t_3$ to form the total isospin T. Likewise, the states $|\alpha\rangle_{(13)2}$ and $|\alpha\rangle_{(23)1}$ also read

$$
\begin{aligned}
|\alpha\rangle_{(13)2} &= \left|n_{13}n_2((l_{13}(s_1s_3)S_{13})J_{13}(l_2s_2)I_2)J;((t_1t_3)T_{13}t_2)T\right\rangle, \\
|\alpha\rangle_{(23)1} &= \left|n_{23}n_1((l_{23}(s_2s_3)S_{23})J_{23}(l_3s_3)I_3)J;((t_2t_3)T_{23}t_1)T\right\rangle.
\end{aligned} \tag{C.5}
$$

The transformation between two different sets of the three-cluster Jacobi coordinates, for example, between $|\alpha\rangle_{(12)3}$ and $|\alpha\rangle_{(13)2}$ is given by [83]

$$
\begin{aligned}
{}_{(13)2}\langle\alpha|\alpha\rangle_{(12)3} = &\langle n_{13}n_2((l_{13}(s_1s_3)S_{13})J_{13}(l_2s_2)I_2)J;((t_1t_3)T_{13}t_2)T \\
&\left|n_{12}n_3((l_{12}(s_1s_2)S_{12})J_{12}(l_3s_3)I_3)J;((t_1t_2)T_{12}t_3)T\right\rangle \\
= &\hat{J}_{13}\hat{I}_2\hat{J}_{12}\hat{I}_3\hat{S}_{13}\hat{S}_{12}\hat{T}_{13}\hat{T}_{12}(-1)^{l_2+l_3+S_{13}+s_2+S_{12}+s_3+T_{13}+t_2+T_{12}+t_3} \\
&\times \sum_{LS}\hat{L}^2\hat{S}^2
\left\{\begin{matrix} l_{13} & S_{13} & J_{13} \\ l_2 & s_2 & I_2 \\ L & S & J \end{matrix}\right\}
\left\{\begin{matrix} l_{12} & S_{12} & J_{12} \\ l_3 & s_3 & I_3 \\ L & S & J \end{matrix}\right\} \\
&\times \langle n_{13}\,l_{13},\,n_2\,l_2:L|n_{12}\,l_{12},n_3\,l_3:L\rangle_d \\
&\times \left\{\begin{matrix} s_2 & s_1 & S_{12} \\ s_3 & S & S_{13} \end{matrix}\right\}
\left\{\begin{matrix} t_2 & t_1 & T_{12} \\ t_3 & T & T_{13} \end{matrix}\right\}.
\end{aligned} \tag{C.6}
$$

Here, the HO bracket $\langle n_{13}\,l_{13},\,n_2\,l_2:L|n_{12}\,l_{12},n_3\,l_3:L\rangle_d$ follows the conventions in [105] with the mass ratio given by

$$d = \frac{m_2m_3}{m_1(m_1+m_2+m_3)}. \tag{C.7}$$

For a detailed derivation of Eq. (C.6) one can refer to [83]. Analogous expressions can be obtained for the transformations between the two other states, ${}_{2(13)}\langle\alpha|\alpha\rangle_{(23)1}$ and ${}_{3(12)}\langle\alpha|\alpha\rangle_{(23)1}$, using the symmetry of the two-cluster subsystem and appropriately renumbering the clusters.

# Bibliography

[1] H. D. Politzer, *Reliable Perturbative Results for Strong Interactions?*,
Phys. Rev. Lett. **30** (26 1973) 1346–1349,
URL: https://link.aps.org/doi/10.1103/PhysRevLett.30.1346.

[2] G. Prosperi, M. Raciti and C. Simolo, *On the running coupling constant in QCD*,
Progress in Particle and Nuclear Physics **58** (2007) 387–438, URL:
http://www.sciencedirect.com/science/article/pii/S0146641006000731.

[3] K. Nakamura et al., *Review of Particle Physics*,
Journal of Physics G: Nuclear and Particle Physics **37** (2010) 075021.

[4] E. Oset, P. de Córdoba, L. Salcedo and R. Brockmann,
*Decay modes of sigma and lambda hypernuclei*, Physics Reports **188** (1990) 79–145, URL:
http://www.sciencedirect.com/science/article/pii/037015739090091F.

[5] M. Danysz and J. Pniewski, *Delayed disintegration of a heavy nuclear fragment: I*,
The London, Edinburgh, and Dublin Philosophical Magazine and Journal of Science **44**
(1953) 348–350, URL: https://doi.org/10.1080/14786440308520318.

[6] D. Davis, *50 years of hypernuclear physics*, Nuclear Physics A **754** (2005) 3–13, URL:
http://www.sciencedirect.com/science/article/pii/S0375947405000047.

[7] A. Gal, E. V. Hungerford and D. J. Millener, *Strangeness in nuclear physics*,
Rev. Mod. Phys. **88** (2016) 035004.

[8] O. Hashimoto and H. Tamura, *Spectroscopy of hypernuclei*,
Progress in Particle and Nuclear Physics **57** (2006) 564–653, URL:
http://www.sciencedirect.com/science/article/pii/S0146641005000761.

[9] H. Tamura et al., *Observation of a Spin-Flip M1 Transition in $^{7}_{\Lambda}Li$*, Phys. Rev. Lett. (2000),
URL:
https://journals.aps.org/prl/abstract/10.1103/PhysRevLett.84.5963.

[10] B. C. Dover, *Open Problems and Future Prospects for Hypernuclear Physics*, (1992),
URL: https://inis.iaea.org/collection/NCLCollectionStore/_Public/23/
060/23060825.pdf.

[11] D. J. Millener, *Hypernuclear Gamma-Ray Spectroscopy and the Structure of p-shell Nuclei
and Hypernuclei*, arXiv (2009).

[12] D. J. Millener, A. Gal, C. B. Dover and R. H. Dalitz,
*Spin dependence of the $\Lambda N$ effective interaction*, Phys. Rev. C **31** (1985) 499–509,
URL: https://link.aps.org/doi/10.1103/PhysRevC.31.499.

[13] H. Hotchi et al., *Spectroscopy of medium-heavy $\Lambda$ hypernuclei via the $(\pi^+, K^+)$ reaction*, Phys. Rev. C **64** (4 2001) 044302, URL: https://link.aps.org/doi/10.1103/PhysRevC.64.044302.

[14] D. J. Prowse, $_{\Lambda\Lambda}^{6}$He *Double Hyperfragment*, Phys. Rev. Lett. **17** (14 1966) 782–785, URL: https://link.aps.org/doi/10.1103/PhysRevLett.17.782.

[15] R. H. Dalitz, D. H. Davis, P. H. Fowler, A. Montwill, J. Pniewski and J. A. Zakrzewski, *The Identified $\Lambda\Lambda$-Hypernuclei and the Predicted H-Particle*, Proceedings of the Royal Society of London. Series A, Mathematical and Physical Sciences **426** (1989) 1–17, URL: http://www.jstor.org/stable/2398533.

[16] H. Takahashi et al., *Observation of a $_{\Lambda\Lambda}^{6}$HeHe Double Hypernucleus*, Phys. Rev. Lett. **87** (2001) 212502.

[17] J. K. Ahn et al., *Double-$\Lambda$ hypernuclei observed in a hybrid emulsion experiment*, Phys. Rev. C **88** (1 2013) 014003, URL: https://link.aps.org/doi/10.1103/PhysRevC.88.014003.

[18] S. Durr et al., *Ab-Initio Determination of Light Hadron Masses*, Science **322** (2008) 1224–1227, arXiv: 0906.3599 [hep-lat].

[19] S. R. Beane, W. Detmold, K. Orginos and M. J. Savage, *Nuclear Physics from Lattice QCD*, Prog. Part. Nucl. Phys. **66** (2011) 1–40, arXiv: 1004.2935 [hep-lat].

[20] R. B. Wiringa, V. G. J. Stoks and R. Schiavilla, *Accurate nucleon-nucleon potential with charge-independence breaking*, Physical Review C **51** (1995) 38?51, URL: http://dx.doi.org/10.1103/PhysRevC.51.38.

[21] V. G. J. Stoks, R. A. M. Klomp, C. P. F. Terheggen and J. J. de Swart, *Construction of high-quality NN potential models*, Phys. Rev. C **49** (6 1994) 2950–2962, URL: https://link.aps.org/doi/10.1103/PhysRevC.49.2950.

[22] T. A. Rijken, H. Polinder and J. Nagata, *Extended-soft-core* NN *potentials in momentum space. II. Meson-pair exchange potentials*, Phys. Rev. C **66** (4 2002) 044009, URL: https://link.aps.org/doi/10.1103/PhysRevC.66.044009.

[23] R. Machleidt, *The High precision, charge dependent Bonn nucleon-nucleon potential (CD-Bonn)*, Phys. Rev. **C63** (2001) 024001, arXiv: nucl-th/0006014 [nucl-th].

[24] T. A. Rijken, M. M. Nagels and Y. Yamamoto, *Baryon-Baryon Interactions —Nijmegen Extended-Soft-Core Models—*, Progress of Theoretical Physics Supplement **185** (2010) 14–71, URL: https://ui.adsabs.harvard.edu/abs/2010PThPS.185...14R.

[25] J. Haidenbauer and U.-G. Meißner, *Jülich hyperon-nucleon model revisited*, Phys. Rev. C **72** (4 2005) 044005, URL: https://link.aps.org/doi/10.1103/PhysRevC.72.044005.

[26] T. A. Rijken, V. G. J. Stoks and Y. Yamamoto, *Soft-core hyperon-nucleon potentials*, Phys. Rev. C **59** (1 1999) 21–40, URL: https://link.aps.org/doi/10.1103/PhysRevC.59.21.

[27] S. Weinberg, *Nonlinear Realizations of Chiral Symmetry*,
Phys. Rev. **166** (5 1968) 1568–1577,
URL: https://link.aps.org/doi/10.1103/PhysRev.166.1568.

[28] S. Weinberg, *Phenomenological Lagrangians*,
Physica A: Statistical Mechanics and its Applications **96** (1979) 327–340, URL:
http://www.sciencedirect.com/science/article/pii/0378437179902231.

[29] C. Ordóñez, L. Ray and U. Van Kolck,
*Nucleon-nucleon potential from an effective chiral Lagrangian*, English (US),
Physical Review Letters **72** (1994) 1982–1985.

[30] N. Kaiser, R. Brockmann and W. Weise,
*Peripheral nucleon-nucleon phase shifts and chiral symmetry*,
Nucl. Phys. **A625** (1997) 758–788, arXiv: nucl-th/9706045 [nucl-th].

[31] E. Epelbaum, H. Hammer and U.-G. Meißner, *Modern Theory of Nuclear Forces*,
Rev. Mod. Phys. **81** (2009) 1773–1825, arXiv: 0811.1338 [nucl-th].

[32] D. R. Entem and R. Machleidt, *Accurate charge-dependent nucleon-nucleon potential at
fourth order of chiral perturbation theory*, Phys. Rev. C **68** (4 2003) 041001,
URL: https://link.aps.org/doi/10.1103/PhysRevC.68.041001.

[33] D. R. Entem, N. Kaiser, R. Machleidt and Y. Nosyk,
*Peripheral nucleon-nucleon scattering at fifth order of chiral perturbation theory*,
Phys. Rev. C **91** (1 2015) 014002,
URL: https://link.aps.org/doi/10.1103/PhysRevC.91.014002.

[34] E. Epelbaum, H. Krebs and P. Reinert,
*High-precision nuclear forces from chiral EFT: State-of-the-art, challenges and outlook*,
(2019), arXiv: 1911.11875 [nucl-th].

[35] P. Reinert, H. Krebs and E. Epelbaum,
*Semilocal momentum-space regularized chiral two-nucleon potentials up to fifth order*,
Eur. Phys. J. **A54** (2018) 86, arXiv: 1711.08821 [nucl-th].

[36] D. R. Entem, R. Machleidt and Y. Nosyk,
*High-quality two-nucleon potentials up to fifth order of the chiral expansion*,
Phys. Rev. C **96** (2 2017) 024004,
URL: https://link.aps.org/doi/10.1103/PhysRevC.96.024004.

[37] E. Epelbaum et al., *Few- and many-nucleon systems with semilocal coordinate-space
regularized chiral two- and three-body forces*, Phys. Rev. **C99** (2019) 024313,
arXiv: 1807.02848 [nucl-th].

[38] M. Piarulli et al., *Light-nuclei spectra from chiral dynamics*,
Phys. Rev. Lett. **120** (2018) 052503, arXiv: 1707.02883 [nucl-th].

[39] R. Roth, L. Joachim, C. Angelo, B. Sven and P. Navrátil, *Similarity-Transformed Chiral
NN + 3N Interactions for the Ab Initio Description of $^{12}$C and $^{16}$O*,
Phys. Rev. Lett. **107** (7 2011) 072501,
URL: https://link.aps.org/doi/10.1103/PhysRevLett.107.072501.

[40] A. Nogga, *Light hypernuclei based on chiral and phenomenological interactions*,
Nuclear Physics A **914** (2013) 140–150, XI International Conference on Hypernuclear and
Strange Particle Physics (HYP2012), URL:
http://www.sciencedirect.com/science/article/pii/S0375947413001693.

[41] R. Wirth, D. Gazda, P. Navrátil, A. Calci, J. Langhammer and R. Roth,
*Ab Initio Description of p-Shell Hypernuclei*, Phys. Rev. Lett. **113** (2014) 192502.

[42] E. Epelbaum, W. Gloeckle and U.-G. Meißner,
*The two-nucleon system at next-to-next-to-next-to-leading order*,
Nuclear Physics A **747** (2005) 362–424.

[43] E. Epelbaum, H. Krebs and U.-G. Meißner,
*Precision nucleon-nucleon potential at fifth order in the chiral expansion*,
Phys. Rev. Lett. **115** (2015) 122301, arXiv: 1412.4623 [nucl-th].

[44] E. Epelbaum, *Few-nucleon forces and systems in chiral effective field theory*,
Prog. Part. Nucl. Phys. **57** (2006) 654–741, arXiv: nucl-th/0509032 [nucl-th].

[45] H. Polinder, J. Haidenbauer and U.-G. Meißner,
*Hyperon-nucleon interactions: A Chiral effective field theory approach*,
Nucl. Phys. **A779** (2006) 244–266.

[46] J. Haidenbauer, S. Petschauer, N. Kaiser, U.-G. Meißner, A. Nogga and W. Weise,
*Hyperon-nucleon interaction at next-to-leading order in chiral effective field theory*,
Nucl. Phys. **A 915** (2013) 24–58.

[47] J. Haidenbauer, U.-G. Meißner and A. Nogga,
*Hyperon-nucleon interaction within chiral effective field theory revisited*,
Nucl. Phys. **A915** (2013) 24–58.

[48] J. Haidenbauer, U.-G. Meißner and S. Petschauer, *Strangeness S = −2 baryon-baryon
interaction at next-to-leading order in chiral effective field theory*,
Nucl. Phys. **A954** (2016) 273–293, arXiv: 1511.05859 [nucl-th].

[49] M. M. Nagels, T. A. Rijken and Y. Yamamoto,
*Extended-soft-core baryon-baryon model ESC16. II. Hyperon-nucleon interactions*,
Phys. Rev. C **99** (4 2019) 044003,
URL: https://link.aps.org/doi/10.1103/PhysRevC.99.044003.

[50] T. A. Rijken, *The Nijmegen hyperon-nucleon and hyperon-hyperon interactions*,
Nuclear Physics A **639** (1998) 29c–40c, Proceedings of the International Conference on
Hypernuclear and Strange Particle Physics, URL:
http://www.sciencedirect.com/science/article/pii/S0375947498002498.

[51] J. Haidenbauer and U.-G. Meißner,
*A study of hyperons in nuclear matter based on chiral effective field theory*,
Nuclear Physics A **936** (2015) 29–44, URL:
http://www.sciencedirect.com/science/article/pii/S0375947415000160.

[52] E. Epelbaum, "Nuclear Forces from Chiral Effective Field Theory: A Primer", 2010,
arXiv: 1001.3229 [nucl-th].

[53] V. Bernard, E. Epelbaum, H. Krebs and U.-G. Meißner,
*Subleading contributions to the chiral three-nucleon force. I. Long-range terms*,
Phys. Rev. **C77** (2008) 064004.

[54] V. Bernard, E. Epelbaum, H. Krebs and U.-G. Meißner, *Subleading contributions to the
chiral three-nucleon force II: Short-range terms and relativistic corrections*,
Phys. Rev. **C84** (2011) 054001.

[55] U.-G. Meißner, *A new tool in nuclear physics: Nuclear lattice simulations*,
Nucl. Phys. News. **24** (2014) 11–15, arXiv: 1505.06997 [nucl-th].

[56] T. Lähde and U.-G. Meißner, *Nuclear Lattice Effective Field Theory*, Springer, 2019.

[57] M. J. Savage, *Effective field theory for nuclear physics*, Nucl. Phys. **A721** (2003) 94–103,
arXiv: nucl-th/0301058 [nucl-th].

[58] G. Hagen, M. Hjorth-Jensen, G. R. Jansen, R. Machleidt and T. Papenbrock,
*Evolution of Shell Structure in Neutron-Rich Calcium Isotopes*,
Phys. Rev. Lett. **109** (3 2012) 032502,
URL: https://link.aps.org/doi/10.1103/PhysRevLett.109.032502.

[59] Y. Fujiwara, Y. Suzuki and C. Nakamoto, *Baryon-baryon interactions in the SU(6) quark
model and their applications to light nuclear systems*,
Prog. Part. Nucl. Phys. **58** (2007) 439–520, arXiv: nucl-th/0607013 [nucl-th].

[60] S. Petschauer and N. Kaiser,
*Relativistic SU(3) chiral baryon-baryon Lagrangian up to order $q^2$*,
Nucl. Phys. **A916** (2013) 1–29, arXiv: 1305.3427 [nucl-th].

[61] H. Polinder, J. Haidenbauer and U.-G. Meißner,
*Strangeness S = -2 baryon-baryon interactions using chiral effective field theory*,
Phys. Lett. **B653** (2007) 29–37, arXiv: 0705.3753 [nucl-th].

[62] J. K. Ahn et al., *Measurement of the $\Xi^- p$ scattering cross sections at low energy*,
Physics Letters B **633** (2006) 214–218, URL:
http://www.sciencedirect.com/science/article/pii/S0370269305018770.

[63] S. J. Kim, *presentation at the 12th International Conference on Hypernuclear and Strange
Particle Physics, Sendai, Japan, 2015*, (2015),
URL: http://lambda.phys.tohoku.ac.jp/hyp2015/.

[64] J. Haidenbauer, U.-G. Meißner, N. Kaiser and W. Weise,
*Lambda-nuclear interactions and hyperon puzzle in neutron stars*,
Eur. Phys. J. **A53** (2017) 121.

[65] L. Tolos and L. Fabbietti, *Strangeness in Nuclei and Neutron Stars*, (2020),
arXiv: 2002.09223 [nucl-ex].

[66] D. Chatterjee and I. Vidaña, *Do hyperons exist in the interior of neutron stars?*,
Eur. Phys. J. **A52** (2016) 29.

[67] P. B. Demorest, T. Pennucci, S. M. Ransom, M. S. E. Roberts and J. W. T. Hessels,
*A two-solar-mass neutron star measured using Shapiro delay*,
Nature **467** (2010) 1081–1083, arXiv: 1010.5788 [astro-ph.HE].

[68] J. Antoniadis et al., *A Massive Pulsar in a Compact Relativistic Binary*,
Science **340** (2013) 6131.

[69] A. Nogga, H. Kamada and W. Glöckle,
*The Hypernuclei $^4_\Lambda$He and $^4_\Lambda$H: Challenges for modern hyperon nucleon forces*,
Phys. Rev. Lett. **88** (2002) 172501.

[70] A. Nogga, *Light hypernuclei based on chiral and phenomenological interactions*,
Nuclear Physics A **914** (2013).

[71] E. Hiyama, M. Kamimura, T. Motoba, T. Yamada and Y. Yamamoto,
$\Lambda - \Sigma$ *conversion in $^4_\Lambda$He and $^4_\Lambda$H based on a four-body calculation*,
Phys. Rev. C **65** (1 2001) 011301,
URL: https://link.aps.org/doi/10.1103/PhysRevC.65.011301.

[72] H. Nemura, Y. Akaishi and Y. Suzuki, *Ab initio Approach to s-Shell Hypernuclei $^3_\Lambda$H, $^4_\Lambda$H, $^4_\Lambda$He, and $^5_\Lambda$He with a $\Lambda N - \Sigma N$ Interaction*, Phys. Rev. Lett. **89** (14 2002) 142504,
URL: https://link.aps.org/doi/10.1103/PhysRevLett.89.142504.

[73] E. Hiyama, M. Kamimura, T. Motoba, T. Yamada and Y. Yamamoto,
*Three body model study of A = 6, A = 7 hypernuclei: Halo and skin structures*,
Phys. Rev. C **53** (5 1996) 2075–2085,
URL: https://link.aps.org/doi/10.1103/PhysRevC.53.2075.

[74] E. Hiyama, M. Kamimura, Y. Yamamoto, T. Motoba and T. A. Rijken,
*S = -1 hypernuclear structure*, Prog. Theor. Phys. Suppl. **185** (2010) 106–151.

[75] E. Hiyama and T. Yamada, *Structure of light hypernuclei*,
Prog. Part. Nucl. Phys. **63** (2009) 339–395.

[76] A. Gal and D. J. Millener, *Neutron-rich hypernuclei: $^6_\Lambda$H and beyond*,
Phys. Lett. **B725** (2013) 445–450.

[77] D. Millener, *Shell-model calculations for p-shell hypernuclei*,
Nuclear Physics A **881** (2012) 298–309, Progress in Strangeness Nuclear Physics, URL:
http://www.sciencedirect.com/science/article/pii/S0375947412000504.

[78] P. Navratil, S. Quaglioni, I. Stetcu and Barrett,
*Recent developments in no-core shell-model calculations*, J. Phys. **G36** (2009) 083101.

[79] B. R. Barrett, P. Navrátil and J. P. Vary, *Ab initio no core shell model*,
Progress in Particle and Nuclear Physics **69** (2013) 131–181, URL:
http://www.sciencedirect.com/science/article/pii/S0146641012001184.

[80] P. Navrátil, J. P. Vary and B. R. Barrett,
*Properties of $^{12}$C in the Ab Initio Nuclear Shell Model*,
Phys. Rev. Lett. **84** (25 2000) 5728–5731,
URL: https://link.aps.org/doi/10.1103/PhysRevLett.84.5728.

[81] S. K. Bogner, R. J. Furnstahl, P. Maris, R. J. Perry, A. Schwenk and J. P. Vary,
*Convergence in the no-core shell model with low-momentum two-nucleon interactions*,
Nucl. Phys. **A801** (2008) 21–42, arXiv: 0708.3754 [nucl-th].

[82] P. Navrátil, G. P. Kamuntavičius and B. R. Barrett,
*Few-nucleon systems in translationally invariant harmonic oscillator basis*,
Phys. Rev. **C61** (2000) 044001.

[83]  S. Liebig, U.-G. Meißner and A. Nogga, *Jacobi no-core shell model for p-shell nuclei*,
Eur. Phys. J. **A52** (2016) 103.

[84]  R. Roth and P. Navrátil,
*Ab Initio Study of $^{40}Ca$ with an Importance Truncated No-Core Shell Model*,
Phys. Rev. Lett. **99** (9 2007) 092501,
URL: https://link.aps.org/doi/10.1103/PhysRevLett.99.092501.

[85]  M. K. G. Kruse, E. D. Jurgenson, P. Navrátil, B. R. Barrett and W. E. Ormand,
*Extrapolation uncertainties in the importance-truncated No-Core Shell Model*,
Phys. Rev. **C87** (2013) 044301.

[86]  D. Gazda, J. Mares, P. Navrátil, R. Roth and R. Wirth,
*No-Core Shell Model for Nuclear Systems with Strangeness*,
Few Body Syst. **55** (2014) 857–860, arXiv: 1312.0478 [nucl-th].

[87]  R. Wirth and R. Roth,
*Induced Hyperon-Nucleon-Nucleon Interactions and the Hyperon Puzzle*,
Phys. Rev. Lett. **117** (2016) 182501.

[88]  R. Wirth and R. Roth,
*Light Neutron-Rich Hypernuclei from the Importance-Truncated No-Core Shell Model*,
Phys. Lett. **B779** (2018) 336–341.

[89]  S. Y. Lee and K. Suzuki, *The effective interaction of two nucleons in the s-d shell*,
Physics Letters B **91** (1980) 173–176, URL:
http://www.sciencedirect.com/science/article/pii/0370269380904232.

[90]  S. Lee and K. Suzuki, *Convergent Theory for Effective Interaction in Nuclei*,
Progress of Theoretical Physics **64** (1980),
URL: https://doi.org/10.1143/PTP.64.2091.

[91]  S. Okubo, *Diagonalization of Hamiltonian and Tamm-Dancoff Equation*,
Prog. Theor. Phys. **12** (1954) 603.

[92]  P. Navratil, G. P. Kamuntavičius and B. R. Barrett,
*Few nucleon systems in translationally invariant harmonic oscillator basis*,
Phys. Rev. **C61** (2000) 044001, arXiv: nucl-th/9907054 [nucl-th].

[93]  A. Nogga, P. Navrátil, B. R. Barrett and J. P. Vary,
*Spectra and binding energy predictions of chiral interactions for $^7Li$*,
Phys. Rev. **C73** (2006) 064002.

[94]  H. Feldmeier, T. Neff, R. Roth and J. Schnack, *A unitary correlation operator method*,
Nuclear Physics A **632** (1998) 61–95, URL:
http://www.sciencedirect.com/science/article/pii/S0375947497008051.

[95]  D. Glazek and G. Wilson, *Perturbative renormalization group for Hamiltonians*,
Phys. Rev. D **49** (8 1994) 4214–4218,
URL: https://link.aps.org/doi/10.1103/PhysRevD.49.4214.

[96]  F. J. Wegner, *Flow equations for Hamiltonians*, Nuclear Physics B - Proceedings
Supplements **90** (2000) 141–146, Non-perturbative QCD and Hadron Phenomenology, URL:
http://www.sciencedirect.com/science/article/pii/S0920563200009117.

[97]   S. K. Bogner, R. J. Furnstahl and R. J. Perry,
       *Similarity Renormalization Group for Nucleon-Nucleon Interactions*,
       Phys. Rev. **C75** (2007) 061001, arXiv: `nucl-th/0611045 [nucl-th]`.

[98]   S. K. Bogner, R. J. Furnstahl, P. Maris, R. J. Perry, A. Schwenk and J. P. Vary,
       *Convergence in the no-core shell model with low-momentum two-nucleon interactions*,
       Nucl. Phys. **A801** (2008) 21–42.

[99]   S. K. Bogner, R. J. Furnstahl and R. J. Perry, *Three-Body Forces Produced by a Similarity
       Renormalization Group Transformation in a Simple Model*,
       Annals Phys. **323** (2008) 1478–1501, arXiv: `0708.1602 [nucl-th]`.

[100]  P. Navratil and B. R. Barrett, *Shell model calculations for the three nucleon system*,
       Phys. Rev. (1998), URL: `https://arxiv.org/pdf/nucl-th/9711027.pdf`.

[101]  P. Navrátil, G. P. Kamuntavičius and B. R. Barrett,
       *Few-nucleon systems in a translationally invariant harmonic oscillator basis*,
       Phys. Rev. C (2000).

[102]  S. Liebig, *Antisymmetrisation in a Jacobi coordinate based no-core shell model approach*,
       PhD thesis: Bonn University, 2013.

[103]  A. R. Edmonds, *Angular momentum in quantum mechanics*,
       Princeton, University press, 1957.

[104]  M. Moshinsky, *Transformation brackets for harmonic oscillator functions*,
       Nuclear Physics **13** (1959) 104–116, URL:
       `http://www.sciencedirect.com/science/article/pii/0029558259901439`.

[105]  G. P. Kamuntavičius, R. K. Kalinauskas, B. R. Barrett, S. Mickevičius and D. Germanas,
       *The general harmonic-oscillator brackets: compact expression, symmetries, sums and
       Fortran code*, Nucl. Phys. **A695** (2001) 191–201.

[106]  P. Pacheco, *Parallel Programming with MPI*, A Wiley-Interscience Publication, 1996.

[107]  C. Lanczos, *An iteration method for the solution of the eigenvalue problem of linear
       differential and integral operators*, J. Res. Natl. Bur. Stand. B **45** (1950) 255–282.

[108]  R. B. Lehoucq, D. C. Sorensen and C. Yang, *ARPACK Users' Guide: Solution of Large
       Scale Eigenvalue Problems with Implicitly Restarted Arnoldi Methods*,
       American Mathematical Society, 1997.

[109]  S. D. Watkins, *The Matrix Eigenvalue Problem GR and Krylov Subspace Method*,
       Society for Industrial and Applied Mathematics, 2007.

[110]  R. B. Wiringa, V. G. J. Stoks and R. Schiavilla,
       *An accurate nucleon-nucleon potential with charge independence breaking*,
       Phys. Rev. **C51** (1995) 38–51.

[111]  E. D. Jurgenson, P. Navrátil and R. J. Furnstahl,
       *Evolving nuclear many-body forces with the similarity renormalization group*,
       Phys. Rev. **C83** (2011) 034301.

[112]  S. Bogner, R. Furnstahl and A. Schwenk,
       *From low-momentum interactions to nuclear structure*,
       Progress in Particle and Nuclear Physics **65** (2010) 94–147, URL:
       `http://www.sciencedirect.com/science/article/pii/S0146641010000347`.

[113] A. Gal, *Charge symmetry breaking in Λ hypernuclei revisited*,
Phys. Lett. **B744** (2015) 352–357.

[114] E. Epelbaum, H. Krebs and U.-G. Meißner,
*Improved chiral nucleon-nucleon potential up to next-to-next-to-next-to-leading order*,
Eur. Phys. J. **A51** (2015) 53, arXiv: 1412.0142 [nucl-th].

[115] R. Wirth, D. Gazda, P. Navrátil and R. Roth, *Hypernuclear No-Core Shell Model*,
Phys. Rev. **C97** (2018) 064315, arXiv: 1712.05694 [nucl-th].

[116] A. R. Bodmer, Q. N. Usmani and J. Carlson,
*Binding energies of hypernuclei and three-body $\Lambda NN$ forces*,
Phys. Rev. C **29** (2 1984) 684–687,
URL: https://link.aps.org/doi/10.1103/PhysRevC.29.684.

[117] B. Gibson and E. Hungerford, *A survey of hypernuclear physics*,
Physics Reports **257** (1995) 349–388.

[118] B. F. Gibson, A. Goldberg and M. S. Weiss,
*Effects of lambda-sigma coupling in $_{\Lambda}^{4}H$, $_{\Lambda}^{4}He$, and $_{\Lambda}^{5}He$*, Phys. Rev. **C6** (1972) 741–748.

[119] H. Nemura, Y. Akaishi and Y. Suzuki, *Ab initio approach to s shell hypernuclei, $_{\Lambda}^{3}H$, $_{\Lambda}^{4}H$,
$_{\Lambda}^{4}He$ and $_{\Lambda}^{5}He$ with a realistic $\Lambda N$ - $\Sigma N$ interaction*, Phys. Rev. Lett. **89** (2002) 142504.

[120] H. Bando, T. Motoba and J. Zofka, *Production, structure and decay of hypernuclei*,
Int. J. Mod. Phys. **A5** (1990) 4021–4198.

[121] A. Gal, J. Soper and R. Dalitz, *A shell-model analysis of binding energies for the p-shell
hypernuclei III. Further analysis and predictions*, Annals of Physics **113** (1978) 79–97, URL:
http://www.sciencedirect.com/science/article/pii/0003491678902506.

[122] H. Mei, K. Hagino, J. M. Yao and T. Motoba,
*Microscopic study of low-lying spectra of Λ hypernuclei based on a beyond-mean-field
approach with a covariant energy density functional*, Phys. Rev. C **91** (6 2015) 064305,
URL: https://link.aps.org/doi/10.1103/PhysRevC.91.064305.

[123] T. O. Yamamoto et al., *Observation of Spin-Dependent Charge Symmetry Breaking in $\Lambda N$
Interaction: Gamma-Ray Spectroscopy of $_{\Lambda}^{4}He$*, Phys. Rev. Lett. **115** (22 2015) 222501,
URL: https://link.aps.org/doi/10.1103/PhysRevLett.115.222501.

[124] R. Dalitz and AGal, *The formation of, and the γ-radiation from, the p-shell hypernuclei*,
Annals of Physics **116** (1978) 167–243, URL:
http://www.sciencedirect.com/science/article/pii/0003491678900088.

[125] R. Wirth and R. Roth,
*Similarity renormalization group evolution of hypernuclear Hamiltonians*,
Phys. Rev. **C100** (2019) 044313, arXiv: 1902.03324 [nucl-th].

[126] D. R. Tilley, C. M. Cheves, J. L. Godwin, G. M. Hale, H. M. Hofmann, J. H. Kelley,
C. G. Sheu and H. R. Weller, *Energy Levels of Light Nuclei A=6*, Nucl. Phys. (2017),
URL: http://www.tunl.duke.edu/nucldata/ourpubs/06_2002.pdf.

[127] J. Tjon, Physics Letters B **56** (1975) 217–220, URL:
http://www.sciencedirect.com/science/article/pii/0370269375903780.

[128]  N. Klein, S. Elhatisari, T. A. Lähde, D. Lee and U.-G. Meißner,
*The Tjon Band in Nuclear Lattice Effective Field Theory*, Eur. Phys. J. **A54** (2018) 121.

[129]  A. R. Bodmer and Q. N. Usmani,
*Coulomb effects and charge symmetry breaking for the A=4 hypernuclei*,
Phys. Rev. C **31** (4 1985) 1400–1411,
URL: https://link.aps.org/doi/10.1103/PhysRevC.31.1400.

[130]  A. Nogga, *Charge-symmetry breaking in light hypernuclei based on chiral and similarity renormalization group-evolved interactions*, AIP Conf. Proc. **2130** (2019) 030004.

[131]  B. Povh, *Nuclear Physics With Strange Particles*,
Prog. Part. Nucl. Phys. **18** (1987) 183–216.

[132]  M. Agnello et al., *New results on mesonic weak decay of p-shell $\Lambda$-hypernuclei*,
Phys. Lett. **B681** (2009) 139–146.

[133]  H. Tamura et al., *Observation of a Spin-Flip M1 Transition in $^{7}_{\Lambda}Li$*, Phys. Rev. Lett. (2000),
URL:
https://journals.aps.org/prl/abstract/10.1103/PhysRevLett.84.5963.

[134]  R. C. Herndon and Y. C. Tang, *Phenomenological $\Lambda$-Nucleon Potentials from S -Shell Hypernuclei. I. Dependence on Hard-Core Size*, Phys. Rev. **153** (4 1967) 1091–1099,
URL: https://link.aps.org/doi/10.1103/PhysRev.153.1091.

[135]  B. F. Gibson, I. R. Afnan, J. A. Carlson and D. R. Lehman,
*Importance of baryon baryon coupling in hypernuclei*,
Prog. Theor. Phys. Suppl. **117** (1994) 339–350.

[136]  H. Le, J. Haidenbauer, U.-G. Meißner and A. Nogga,
*Implications of an increased $\Lambda$-separation energy of the hypertriton*,
Physics Letters B **801** (2020) 135189, URL:
http://www.sciencedirect.com/science/article/pii/S0370269319309116.

[137]  M. Jurič et al.,
*A new determination of the binding-energy values of the light hypernuclei (A $\leq$ 15)*,
Nuclear Physics B **52** (1973) 1–30, URL:
http://www.sciencedirect.com/science/article/pii/0550321373900849.

[138]  J. Adam et al., *Precise measurement of the mass difference and the binding energy of hypertriton and antihypertriton*, (2019), arXiv: 1904.10520 [hep-ex],
URL: https://arxiv.org/abs/1904.10520.

[139]  J. Adam et al., $^{3}_{\Lambda}H$ and $^{3}_{\Lambda}\bar{H}$ production in $Pb - Pb$ collisions at $\sqrt{s_{NN}}$ = 2.76TeV,
Physics Letters B **754** (2016) 360–372, URL:
http://www.sciencedirect.com/science/article/pii/S0370269316000575.

[140]  P. Braun-Munzinger and B. Dßonigus,
*Loosely-bound objects produced in nuclear collisions at the LHC*,
Nucl. Phys. **A987** (2019) 144–201, arXiv: 1809.04681 [nucl-ex].

[141]  A. Gal and H. Garcilazo, *Towards resolving the $^{3}_{\Lambda}H$ lifetime puzzle*,
Phys. Lett. **B791** (2019) 48–53, arXiv: 1811.03842 [nucl-th].

[142] D. Gazda and A. Gal,
*Ab initio Calculations of Charge Symmetry Breaking in the A = 4 Hypernuclei*,
Phys. Rev. Lett. **116** (2016) 122501.

[143] D. Davis, *"50 years of hypernuclear physics: I. The early experiments"*,
Nuclear Physics A **754** (2005) 3–13, URL:
http://www.sciencedirect.com/science/article/pii/S0375947405000047.

[144] T. Gogami et al.,
*Spectroscopy of the neutron-rich hypernucleus $^7_\Lambda$He from electron scattering*,
Phys. Rev. **C94** (2016) 021302,
URL: http://inspirehep.net/record/1473001?ln=en.

[145] A. Nogga, *Nuclear and Hypernuclear Three- and Four-Body Bound States*,
PhD thesis, 2001.

[146] E. Botta, T. Bressani and A. Feliciello,
*On the binding energy and the charge symmetry breaking in $A \leq 16$ $\Lambda$-hypernuclei*,
Nucl. Phys. (2016),
URL: https://inspirehep.net/search?p=find+eprint+1608.07448.

[147] I. Stetcu, B. R. Barrett, P. Navrátil and J. P. Vary,
*Effective operators within the ab initio no-core shell model*, Phys. Rev. **C 71** (2005) 044325.

[148] G. Audi, A. Wapstra and C. Thibault,
*The Ame2003 atomic mass evaluation: (II). Tables, graphs and references*,
Nuclear Physics A **729** (2003) 337–676, The 2003 NUBASE and Atomic Mass Evaluations,
URL:
http://www.sciencedirect.com/science/article/pii/S0375947403018098.

[149] I. Angeli and K. Marinova,
*Table of experimental nuclear ground state charge radii: An update*,
Atomic Data and Nuclear Data Tables **99** (2013) 69–95, ISSN: 0092-640X, URL:
http://www.sciencedirect.com/science/article/pii/S0092640X12000265.

[150] A. Ekström et al., *Accurate nuclear radii and binding energies from a chiral interaction*,
Phys. Rev. **C91** (2015) 051301, arXiv: 1502.04682 [nucl-th].

[151] S. Binder et al., *Few-nucleon systems with state-of-the-art chiral nucleon-nucleon forces*,
Phys. Rev. C **93** (4 2016) 044002,
URL: https://link.aps.org/doi/10.1103/PhysRevC.93.044002.

[152] Z.-T. Lu, P. Mueller, G. W. F. Drake, W. Nörtershäuser, S. C. Pieper and Z.-C. Yan,
*Colloquium: Laser probing of neutron-rich nuclei in light atoms*,
Rev. Mod. Phys. **85** (4 2013) 1383–1400,
URL: https://link.aps.org/doi/10.1103/RevModPhys.85.1383.

[153] J. J. Li, W. H. Long and A. Sedrakian,
*Hypernuclear stars from relativistic Hartree-Fock density functional theory*,
Eur. Phys. J. **A54** (2018) 133.

[154] H. Mei, K. Hagino, J. M. Yao and T. Motoba,
*Microscopic study of low-lying spectra of $\Lambda$ hypernuclei based on a beyond-mean-field approach with a covariant energy density functional*, Phys. Rev. **C91** (2015) 064305.

[155]  H. Nemura, Y. Suzuki, Y. Fujiwara and C. Nakamoto, *Study of Light Λ- and ΛΛ-Hypernuclei with the Stochastic Variational Method and Effective ΛN Potentials*, Progress of Theoretical Physics **103** (1999) 929–958, URL: https://inspirehep.net/search?p=find+eprint+nucl-th/9912065.

[156]  J. Haidenbauer and U.-G. Meißner, *In-medium properties of a ΞN interaction derived from chiral effective field theory*, Eur. Phys. J. **A55** (2019) 23, arXiv: 1810.04883 [nucl-th].

[157]  K. Nakazawa et al., *The first evidence of a deeply bound state of Xi$^-$ $-^{14}$N system*, PTEP **2015** (2015) 033D02.

[158]  T. A. Rijken and Y. Yamamoto, *Extended-soft-core baryon-baryon model III: S=-2 hyperon-hyperon/nucleon interaction*, (2006), arXiv: nucl-th/0608074 [nucl-th].

[159]  H. Nemura, S. Shinmura, Y. Akaishi and K. S. Myint, *Full-coupled channel approach to doubly strange (s)-shell hypernuclei*, Phys. Rev. Lett. **94** (2005) 202502, arXiv: nucl-th/0407033 [nucl-th].

[160]  E. Hiyama and K. Nakazawa, *Structure of S = −2 Hypernuclei and Hyperon-Hyperon Interactions*, Ann. Rev. Nucl. Part. Sci. (2018).

[161]  I. N. Filikhin and A. Gal, *Faddeev-Yakubovsky Search for $_{\Lambda\Lambda}^{4}$H*, Phys. Rev. Lett. **89** (17 2002) 172502, URL: https://link.aps.org/doi/10.1103/PhysRevLett.89.172502.

[162]  I. N. Filikhin and A. Gal, *Faddeev-Yakubovsky calculations for light ΛΛ hypernuclei*, Nucl. Phys. **A707** (2002) 491–509, arXiv: nucl-th/0203036 [nucl-th].

[163]  S. Nakaichi-Maeda and Y. Akaishi, *Lightest double Lambda hypernucleus*, Prog. Theor. Phys. **84** (1990) 1025–1029.

[164]  E. Hiyama, M. Kamimura, T. Motoba, T. Yamada and Y. Yamamoto, *Four-body cluster structure of A = 7 − 10 double-Λ hypernuclei*, Phys. Rev. C **66** (2 2002) 024007, URL: https://link.aps.org/doi/10.1103/PhysRevC.66.024007.

[165]  A. Gal, *Strangeness nuclear physics - 2010: Overview of strangeness nuclear physics*, Prog. Theor. Phys. Suppl. **186** (2010) 270–281, URL: http://inspirehep.net/record/865809?ln=en.

[166]  A. Gal, *Recent progress on hypernuclei*, "arXiv" (2019), URL: http://arxiv.org/abs/arXiv:1909.11400.

[167]  J. K. Ahn et al., *Production of $_{\Lambda\Lambda}^{4}$H Hypernuclei*, Phys. Rev. Lett. **87** (13 2001) 132504, URL: https://link.aps.org/doi/10.1103/PhysRevLett.87.132504.

[168]  S. D. Randeniya and E. V. Hungerford, *Reevaluation of the reported observation of the $_{\Lambda\Lambda}^{4}$H hypernucleus*, Phys. Rev. C **76** (6 2007) 064308, URL: https://link.aps.org/doi/10.1103/PhysRevC.76.064308.

[169]   M. M. Nagels, T. A. Rijken and Y. Yamamoto, *Extended-soft-core Baryon-Baryon ESC08 model III. S=-2 Hyperon-hyperon/nucleon Interaction*, (2015), arXiv: 1504.02634 [nucl-th].

[170]   G. P. Kamuntavičius, *Simple functional-differential equations for the bound-state wave-function components*, Few-Body Systems **1** (1986) 91–109, URL: https://doi.org/10.1007/BF01277077.

# Acronyms

| | |
|---|---|
| **QCD** | Quantum Chromodynamics |
| **J-NCSM** | Jacobi no-core shell model |
| **IT-NCSM** | Importance-truncated no-core shell model |
| **SRG** | Similarity Renormalization Group |
| **GEM** | Gaussian expansion method |
| **C.M.** | Center of mass |
| **$\chi$EFT** | Chiral effective field theory |
| **EFT** | Effective field theory |
| **LEC** | Low energy constant |
| **LO** | Leading order |
| **NLO** | Next-to-leading order |
| **$N^2LO$** | Next-to-next-to-leading order |
| **$N^3LO$** | Next-to-next-to-next-to-leading order |
| **$N^4LO$** | Next-to-next-to-next-to-next-to-leading order |
| **NN** | Nucleon-nucleon |
| **YN** | Hyperon-nucleon |
| **YY** | Hyperon-hyperon |
| **YNN** | Hyperon-nucleon-nucleon |
| **YYN** | Hyperon-hyperon-nucleon |
| **BB** | Baryon-baryon |
| **3N** | Three-nucleon |
| **CSB** | Charge symmetry breaking |
| **HO** | Harmonic oscillator |

| | |
|---|---|
| **SMS** | Semi-locdal momentum-space-regularized |
| **RMS** | Root mean square |
| **CFP** | Coefficient of fractional parantage |
| **HDF5** | Hierarchical Data Format 5 |

# Acknowledgements

# Curriculum Vitae

---

**Personal data**

Hoai Le Thi

Geb. am 05.07.1987, Nam Dinh

Email: h.le@fz-juelich.de

**Education**

| | |
|---|---|
| 1993 - 2002 | Elementary school, Hong Quang, Nam Dinh |
| 2002 -2005 | High school, Le Hong Phong, Nam Dinh |
| 2005 -2006 | Bachelor study, Hanoi National University of Education |
| 2006 -2011 | Bachelor of Science, Physics, Belgorod National Research University |
| 2011 -2013 | Master of Science, Physics, Belgorod National Research University |
| 2013 -2015 | Master of Science, Simulation Science, GRS, RWTH Aachen University |
| 2016 - 2020 | PhD study, Physics, Bonn University |